Development of High Seismic Performance Integrated Bridge Pier Connected by Hysterical Damper

2018

Angga FAJAR Setiawan

Abstract

Angga FAJAR Setiawan

Development of High Seismic Performance Integrated Bridge Pier Connected by Hysterical Damper

The pier is one of the main components of the bridge which supports the structure of the bridge so that the bridge can stand. If it occurs failure, the whole bridge structure will collapse and it needs to be replaced with the new structure. The earthquake occurrence is one of the most damageable to the bridge pier. This phenomenon occurs in conventional pier systems which adopts the concept "weak-column", unlike the frame system of the building which implements approach "strong-column weak-beam". In the conventional column concept, the plastic hinge is formed on the bottom part of the pier. In the severe earthquake event, if the strength and ductility of the pier sufficient with the earthquake demand, it occurs cracks or spalls in the plastic hinge and residual deformation. While the strength and ductility of the structure are insufficient with the earthquake demand, the pier will fail and cause the whole bridge structure to collapse. Plastic hinge is an important part to generate energy dissipation to dampen the seismic vibration, but the leniency of the plastic hinge system in the column portion is the residual deformation. Residual deformation poses challenges of post-quake structural restoration, time consumption, and traffic closure that leads to economic problems. This study discusses the development of high seismic performance integrated bridge pier with multiple columns connected by hysterical dampers. The integrated pier consists slender columns which are expected to have a large elastic or slight-elastic deformation. Below the deformation limit capacity, the hysterical dampers expected to produce sufficient energy dissipation and to quench the structural vibration due to earthquake excitation. In the severe earthquake event, the column element is in the near to elastic behavior. So that the damage can be limited, the restoration challenge and its cost are reduced, also the structure can still operate immediately after the earthquake. After the Great East Japan earthquake in 2011, the earthquake was not

the main cause of the bridge bearing support damaged, but it is possible due to the deterioration subjected by the frequent lateral deformation or daily load. The idea to prevent the damaged bearing support is by removing the bearing support which connects the pier and the superstructure integrally. Application of the gap in the hysterical damper expected to realize the high flexibility of the piers to accommodate deformation due to the superstructure elongation. The gap can also delay the hysterical damper work at the small deformation. In the shear panel damper (SPD) case, the gap appearance capable of reducing the SPD stress under frequent lateral deformation event for example triggered by; small earthquake, wind, and thermal expansion, creep and shrinkage of the superstructure. The SPD stress reduction will increase the N-value of the high-cyclic fatigue phenomena. So that it can improve the structural lifetime and reduce the life-cycle cost of the structure. The study scopes are described in the chapters below.

Chapter 1 introduces the concept of integrated pier with multiple column connected by a hysterical damper, the deteriorated of rubber bearing support phenomenon, the important points of high seismic performance bridge pier, the bridge damaged statistic under severe earthquake, the life-cycle cost reduction of structure that installed by the damper under earthquake event, and the development storyline of the high seismic performance bridge pier. Finally, the research objective to be presented in this chapter.

Chapter 2 discusses the numerical analysis and dissipated energy optimization of reinforced concrete columns connected by friction damping mechanism under cyclic loading which is the basic philosophy of this study. The structure contained three concrete columns connected by friction devices using pre-stressed concrete bolts for confinement. This structure that has distributed configuration of damper along the columns height expected realize more robustness than the pier that uses concentrated damper. When the contribution of a damper is absent due to losing, the other dampers still can resist the external force. In this study, non-linear finite element analysis is performed by modeling the column with a fiber section element and the friction devices with link elements. The optimum energy dissipation in the elastic state is investigated by applying regular patterns of incremental confinement force and varying the confinement force in each friction device. Based on the hysteresis loops comparisons, the friction coefficient and slip deformation value of the friction device were the important parameters in the numerical analysis. Comparison of numerical and experimental hysteresis loops and curvature distributions showed good agreement. The optimum energy dissipation in the elastic state is investigated successfully using two methods. Finally, it is found that the confinement force pattern and magnitude governed the hysteresis loop shape and curvature distribution along the column height.

Chapter 3 discusses the structural concept of integrated bridge pier with triple reinforced concrete column connected by friction damper plus gap (FGD). This proposed structural system substitutes the conventional bridge pier structural system by eliminates the bearing support of the bridge. The bridge bearing support has deterioration problem under frequent small lateral deformation which is triggered by the mentioned of the first paragraph. Numerical analysis is performed for this system with fiber element model including non-linear static and dynamic. The parallel combination of the bilinear and stopper material idealization is implemented to the FDG. The structural simulations with different limit state of column location and the different yield strength of reinforcing steel configuration are conducted to get the better structural cost-performance option. It shows that the some proposed structures have an excellent performance not only under frequent lateral load in the small deformation range but also under severe seismic load.

Chapter 4 discusses dissipated energy and seismic performance enhancement of integrated steel pipes bridge pier connected by shear panel damper (SPD) which conducted with numerical analysis. The pier structure that has been developed and implemented by the Hanshin Expressway is installed with SPD along its height. The SPDs connect the steel pipe columns at certain intervals with a uniform distribution of strength and stiffness. The connection between the bottom and top end of the steel pipe columns are fix-fix. In this study, the dissipated energy enhancement of the structure is performed through four scenarios with two different structural configurations. To prevent significant residual deformation under severe earthquake, the limit state of the structure under severe earthquake is proposed through restricting the lateral deformation limit of the structure with 90% yield-stiffness of the steel pipe. In the proposed deformation limit, the optimization capable of increasing the dissipated energy up to 272% of the initial design structure configuration. Under severe earthquake excitation (called Level 2), the structure response that has the best-energy dissipation still below the deformation limit of the proposed performance criteria.

Chapter 5 study the experiments and numerical analysis of Shear Panel Damper plus Gap (SPDG). The gap appearance of the SPDG is expected to generate flexible stiffness under frequent small lateral deformation of the pier. The experiment is performed by subjecting the specimens which have scale 0.5 with cyclic loading. Based on the experiment result which also considering the friction effect of sliding surface, the proposed behavior of the SPDG capable to be achieved. The mechanism and parameter of the SPDG verified by numerical analysis including simplified spring model and FEM model. The spring model verification is conducted with dynamic analysis which uses displacement excitation based on the experimental loading protocol. While the FEM verification that implements three-dimensional shell element is conducted by static pushover analysis. The stiffness and strength factor is determined by matching the skeleton of the experimental hysteresis loop and analysis to the theoretical value. The FEM simulation gives verification about the gap mechanism and the strength factor by monitoring the stress distribution in the web panel of SPDG. The experimental result seems the expected behavior of the SPDG can be accomplished. The hysteresis loops of the spring model have good agreement with experimental results as well as the skeleton curve of the FEM results have good agreement with the experimental and the spring model.

Chapter 6 discusses the implementation shear panel damper plus gap (SPDG) in the integrated steel pipes pier is conducted. The structural model that has the best seismic performance in Chapter 4 is carried out in this study. The additional gap is implemented in the SPDG device which is idealized as series-parallel of spring element combination. The friction effect of the sliding surface also to be considered based on the experimental and numerical analysis investigation of Chapter 5. The behavior and the seismic performance of the proposed structure are examined by static and dynamic analysis. In the dynamic analysis, the proposed structure subjected by the both of two-level ground motion input. The results show that the proposed structure capable generates expected behavior and achieves Performance 2a under Level 2 of earthquake excitation. The friction part also capable of reducing the seismic response of the structure under Level 1 of earthquake excitation. While the additional gap in the SPDG system taking some consequent to the structure including dissipated energy decrement and seismic response enlargement.

Chapter 7 concludes and recommends the accomplishment of this research.

Acknowledgements

This dissertation was completed with advice and support of individuals and groups who proved help and their valuable assistance during the time of conducting this study.

It was my honor to spend my cherished 3 years in the Earthquake and Lifeline Laboratory, Department of Urban Management, Graduate school of Engineering at Kyoto University, the acknowledgement is my deepest sincere to thank for those whom I do really want to express for their collaboration. Thanks a lot to the blessing of the Almighty God (Allah SWT), due to the blessings and graces, I have the power to finish this doctoral study.

First and foremost, my debt of gratitude must go to my advisor, Prof. Junji Kiyono. He patiently provided the inspiration, encouragement and advice necessary for me to proceed through the doctoral course and complete my dissertation, I want to thank Prof. Kiyono for his persistent encouragement, kindness and serving as an exemplar to me as a great exemplar to me as a great mentor. He has been a strong and supportive adviser to me throughout my graduate school career, but he has always given me great freedom to pursue independent work. Also, he likes my father to me while I sped my years in Japan.

I would like to express my deepest appreciation to Prof. Yoshikazu Takahashi. He sincerely provided the vision to give me advices for the research way, encouragement and counsel necessary for me to conquer through all obstacles in the completion this research work. Also, Prof. Sumio Sawada who provided some idea about my doctoral research with nice discussion.

Special thanks to my committee, Prof. Junji Kiyono, Prof. Takahashi, and Assoc. Prof. Aiko Furukawa, for their guidance and helpful suggestions. Their comment has served me well and I owe them my heartfelt appreciation. Very high appreciation must be delivered to all members in Hanshin Expressway Limited Company, especially Dr. Kanaji shared me knowledge about high seismic performance of bridge pier.

I also wish to thank Assoc. Prof. Okumura (Kansai Univerisity), The discussion with them really pushed my research going smoothly. I would like to express my appreciation to these members. My gratefully acknowledge should sent to my wife (Nana Diana), my son (Akio) and my family members, their encouragements and prays are always inspired me to go ahead, and just focusing on my research. I do really want to say 'I love you so much'. Members of earthquake and lifeline engineering laboratory, especially, the secretariat Ms. Yoshida and Ms. Taki, also deserve my sincerest thanks, their friendship and assistance has meat more to me than I could ever express. I could not complete my work without invaluable friendly assistance of the participants of those.

I should also mention Ms. Wu, Ms. Yotsui, and Mr. Nishikawa they and me are in the same grade, their impairments and encouragement helped me in completion of this research even they are also very busy with their research. I sincerely wish everything will go well for you. Also my senior in Kiyono laboratory; Rishi san, Dohi san, and Budha san who have shared their experience in the doctoral study.

I should also mention Mr. Goto, Mr. Iwahashi, Mr. Goto, Mr. Toyoda, Mr. Mori who helped me to translate my thesis abstract in Japanese version. Finally, an honorable mention goes to JICA (Japan International Corporation Agency) for their financial support granted throughout my doctoral course. Also, especially Ms. Miyashita and Ms. Yuko who guided me during study in Japan.

Contents

*

List of Figures

List of Tables

Chapter 1

Introduction

1.1 Background

1.1.1 General problem

A pier is one of the main components of the bridge which supports the structure of the bridge so that the bridge can stand. If it occurs failure, the whole bridge structure may be collapse and needs to be replaced with the new structure. The pier structure not only supports the gravitational load of upper structures and traffic loads, but also resists the lateral loads caused by traffic loads, environmental actions, and natural disasters. In the cases of lateral load, the traffic load action that contains brake force and the centrifugal force of the vehicle is not significant. While the environmental events are driven by the flow of water (for bridges over water) and scouring. Furthermore, in natural disasters occurrence, lateral loads are caused by strong wind (i.e. typhoon, cyclone, and hurricane), earthquake excitation, and flood events or Tsunami. Even though the disaster occurrence is rare but it rises high vulnerability to the bridge structure.

An earthquake occurrence is one of the most damageable to the bridge pier. Usually, in the conventional pier systems which adopts the concept "weak column" [32], the plastic hinge formed on the bottom part of the pier occurs damage, as shown in Figure 1.1A. Because the conventional pier system is unlike the frame system of the building which implements approach "strong-column weak-beam". In the severe earthquake event, if the strength and ductility of the pier sufficient with the earthquake demand, it occurs cracking or spalling in the plastic hinge and residual deformation. While if the strength and ductility of the structure are insufficient with the earthquake demand, the pier may be fail and cause the whole bridge structure

(A) (B) (C)

FIGURE 1.1: Illustration of: (A) the formation of plastic hinge in the conventional pier, (B) the bridge collapse [33], and (C) residual deformation of the pier due to Kobe earthquake in 1995 [17].

to collapse [32], as shown in Figure 1.1B. Plastic hinge is a vital part to generate dissipation energy to dampen the seismic vibration, but the leniency of the plastic hinge system in the bridge pier structure, as shown in Figure 1.1C is the residual deformation. Residual deformation poses challenges of post-quake structural restoration, time consumption, and traffic closure that leads to economic problems [31].

Since Hyogo-ken Nanbu earthquake in 1995, the seismic coefficient for the bridge design that has been determined by the Japan Road Association (JRA) [23] contains two level of seismic design (Level 1 and Level 2), as shown in Figures (A.1-A.3). Based on the JRA criteria [23], under the Level 1 of earthquake occurrence which frequent probable occurrence, the structure should remain to behave elastically. While under Level 2 of seismic occurrence, the plastic behavior of the pier member is allowed but the collapse of the structure should be avoided or the structural damage should be limited. However, even though ductility concept has been implemented with the plastic hinge in the conventional pier system, the problem mentioned in the second paragraph above remains difficult to be solved.

Furthermore, based on the observations of Takahashi et al. [48] after the Great East Japan earthquake in 2011, the earthquake was not the main cause of the bridge bearing support damage, but it might be caused by the deterioration, as shown in Figure 1.2A. Probably, the deterioration occurrence due to the aging [21, 14], the compression fatigue [13, 6], or frequent lateral deformation of the daily load [49], as shown in Figure 1.2B. The frequent lateral deformation that inflicts the fatigue damage might be triggered by the thermal expansion, creep, and shrinkage of the superstructure, traffic load, wind load, and small to the medium earthquake occurrences.

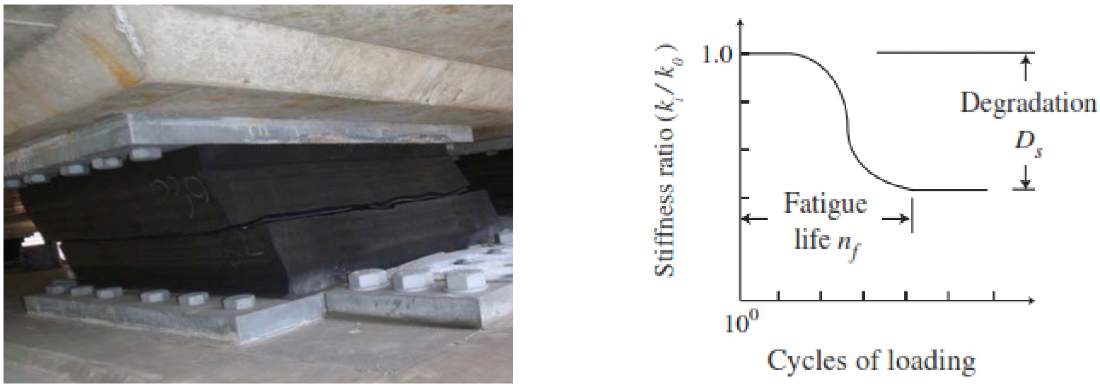

(A) (B)

FIGURE 1.2: Rubber bearing problem: (A) lost seismic performance of deteriorated rubber bearing [48] and (B) compressive cyclic fatigue curve of rubber bearing [6].

1.1.2 Research motivation

In the previous study [35], an experiment was performed on a high seismic performance RC column accompanied by friction damper under cyclic loading. The structure contained three concrete columns connected by the friction dampers and pre-stressed concrete (PC) bolts, as shown in Figure 1.3A. Based on the experiment result of the reference [35], this structure had sufficient energy dissipation due to the achievement of elastic-plastic behavior with large enough elastic deformation capacity, as shown in Figure 1.3B. The elastic deformation capacity was about 2% of drift ratio and the restoring force was fairly constant up to 10% drift. Also, by considering the difference confinement force distribution pattern the friction damper in the structural system can achieve different hysteresis loop shape and different curvature distribution along the column height, as shown in Figure 1.4. On the other hand, the previous study [35] just considered the experimental result which the numerical parameters of the structure have not yet to be calibrated. Also, there was lack of structural confinement force distribution patterns to investigate the influenced structural behavior which just considering uniform and triangular pattern. Furthermore, the optimum energy dissipation related the confinement force distribution pattern of the friction damper is a demand for the high seismic performance bridge pier development.

In the case steel bridge pier, an integrated pier with multiple steel pipe columns connected by shear panel damper (SPD) has been developed and applied by Hanshin Expressway, as shown in Figure 1.5A. At the top and bottom of steel pipes is connected to the pile cap and head pier with fix connection, respectively. While the SPDs are installed at along the pier height with

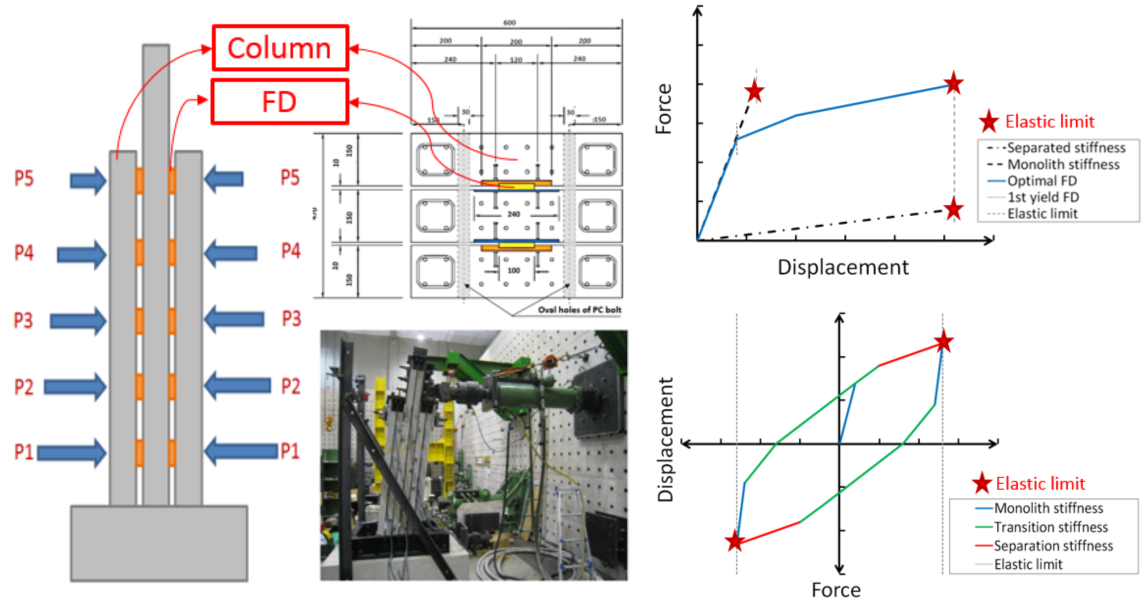

(A) (B)

FIGURE 1.3: Columns connected by the friction dampers (FD) [35]: (A) specimen of the structure and (B) the structural concept.

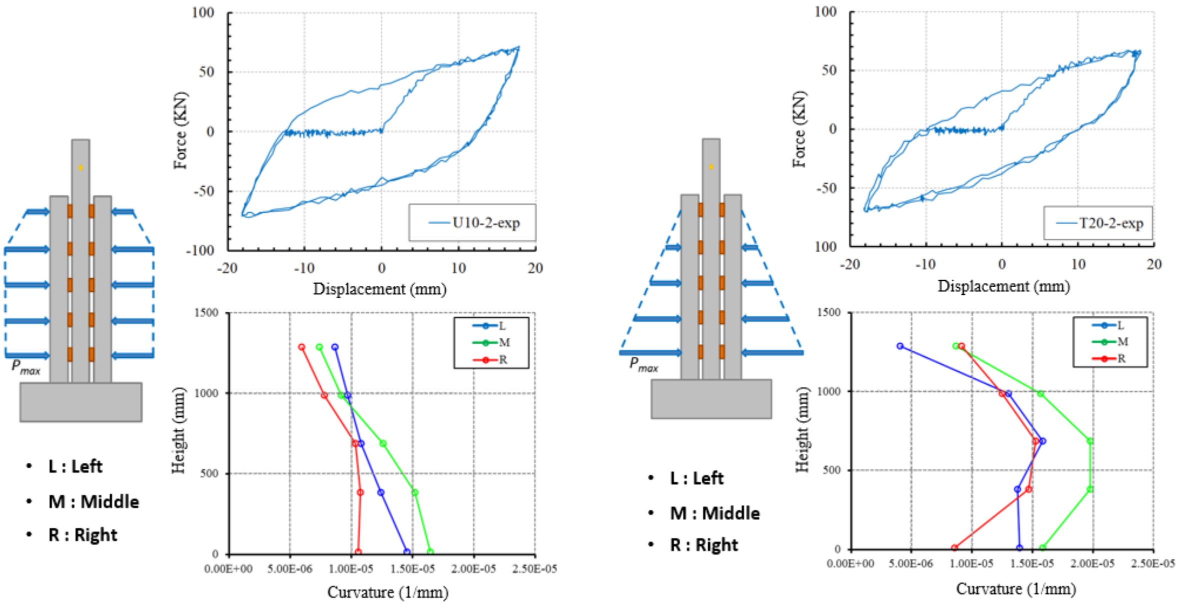

(A) (B)

FIGURE 1.4: Experiment results [36] with different confinement force of FD in the structural system of: (A) uniform pattern and (B) triangular pattern.

certain intervals of a uniform distribution in its strength and stiffness terms, as shown in Figure 1.5B. With the dissipated energy capacity of the SPD, high seismic performance structure can be achieved. As a result, the damage possibility caused by severe earthquake excitation can be reduced. In the less of structural damage, the life-cycle-cost of the structure that built in the high seismic zone can be descended [37]. Furthermore, this kind of the structure has a great

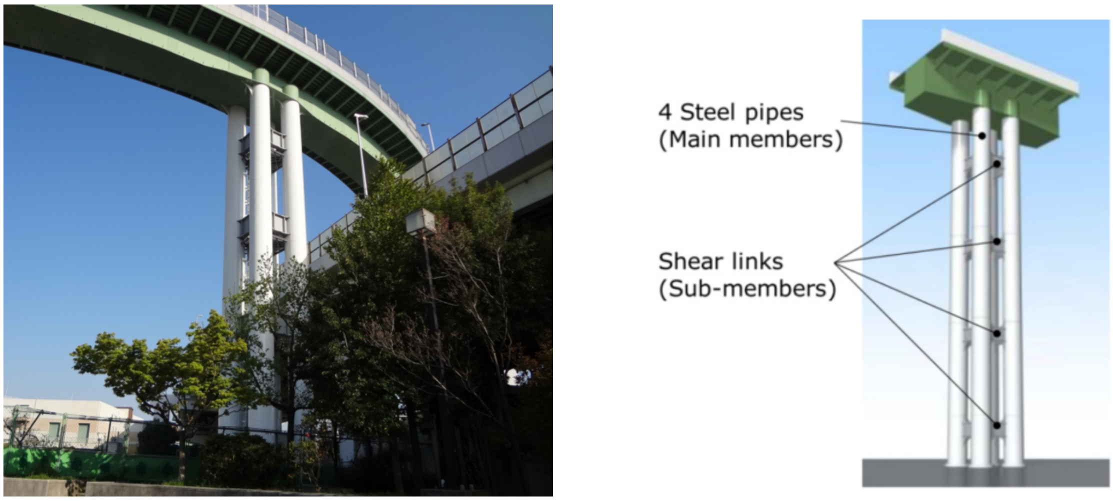

(A) (B)

FIGURE 1.5: The integrated bridge pier with steel pipe column connected by shear panel damper [37]: (A) the implementation and (B) the concept.

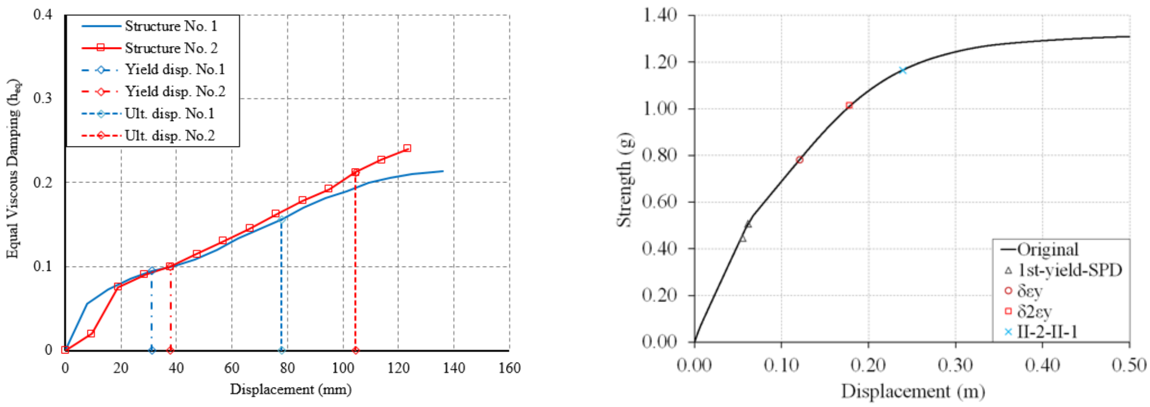

(A) (B)

FIGURE 1.6: Structural seismic performance of integrated steel pipe bridge pier connected by SPD: (A) the relation of displacement and the equal damping based on the experiment result [26] and (B) the maximum response and limit state [45].

potential to be implemented for bridge structures not only in Japan but also in another country which has high seismic hazard. However, based on the study results of the reference [26], the dissipated energy that was produced by the SPD has not yet achieved the optimum. There was not significant dissipated energy production of its SPD (around 10% of the equivalent damping ratio value) on the elastic deformation range. Also at deformations over the yielding limit of steel pipe column, the dissipated energy was dominantly produced by the yielding of steel pipe column. At the maximum load resistance capacity, the damping ratio value was about 21%, as shown in the Figure 1.6A. Based on the reference [37], the structure enriched the Performance 2b (the structures occur medium-damaged by severe earthquakes) for the Importance Bridge category, as shown in Figure 1.6B. Even though some predecessor studies of the structure that mentioned in sub-chapter "High performance of bridge pier structures" have contributed many knowledge about the structural parameter and the structural behavior, the seismic performance has not yet achieved the Performance 2a (Small damage under Level 2 of seismic excitation).

Furthermore, based on the observed problem of the rubber bearing lost performance due to suspected the deterioration which mentioned in sub-chapter "General problem", a development of modified seismic device need to be conducted. By keeping the structural seismic performance before the predicted severe earthquake occurs, the structure could achieve the expected performance in a real upcoming great earthquake event. One of solution option maybe delaying of the seismic device contribution under daily load to reduce its cyclic stress. By proposing this solution option, the more efficient of the life-cycle cost of the bridge structure could be realized.

1.2 Literature Review

1.2.1 The records of bridge damages due to big earthquake

Based on the various history of devastating earthquake occurrence in the community area, bridge damages need to be studied and evaluated to avoid structural failure under seismic occurrences. In the structural failure prevention, the sustainable development and implementation of high seismic performance bridge technology needs to be conducted. The design codes should be continuously improved following technological developments.

The various bridge damages due to the earthquake which occurred in various countries were mentioned here. The Niigata Earthquake (1964) inflicted intensive damage in the city of Niigata, Yamagata, and Akita [39]. In the western part of the USA, the Loma Prieta earthquake (1989) and Notridge (1994) are the boundaries of the Pacific plate the North American plate [28]. Loma Prieta earthquake that is triggered by slip between the plates on the border of San Andreas Fault occurred and destroyed the infrastructure and life line in the area of San Francisco's Marina. The Northridge earthquake also caused various structural damage to buildings and infrastructure in the Los Angeles area [1]. Furthermore, the Kobe earthquake is an "inland crustal earthquake" type [23] which it's acceleration was very large and devastating character [53] because the earthquake location was close to the city center and most of the area in Kobe city has been a reclaimed land. Land reclamation has had a firmness and a low natural period,

TABLE 1.1: The data of the damaged bridge due to big earthquake [39, 28, 1, 23, 52, 53].

No.	Earthquake events	M_W	Depth (KM)	Damage level of the bridges					
				Caltrans (2008)					Total
				I	II	III	IV	V	
				None	Minor	Moderate	Major	Collapse	
				JSCE (1996)					
				D	C	B	A	As	
				None	Mild	Severe	Very severe	Collapse	
1	Niigata 1964	7.5	40.0	N/A	N/A	N/A	13	3	16
2	Loma Prieta 1989	6.9	13.0	N/A	80	10	10	3	103
3	Nothrige 1994	6.7	18.4	N/A	85	95	47	6	233
4	Kobe 1995	6.9	17.6	184	8	13	4	7	216
5	Chichi 1999	7.6	7.0	N/A	N/A	16	9	5	30
6	Great East Japan 2011	9.0	24.4	N/A	N/A	N/A	N/A	N/A	312
	Percentage			30.8%	28.9%	22.4%	13.9%	4.0%	100.0%

thus a large earthquake amplification factor. In Taiwan (1999), a severe earthquake occurred. Namely Chichi earthquake that is caused by an active fault on land is one of the most devastating earthquakes in Taiwan. Then in 2011, there was an earthquake in the Tohoku region of Great East Japan Earthquake. Such a typical "interplate earthquake" [23] not only inflicted the damage to buildings and infrastructure but also triggered a tsunami.

The above earthquake events caused damage to the bridge structure with different levels of damage. Each of the damages that were caused by the earthquake is shown in Table 1.1. It can be seen that there were about 40 percent of bridge damage with the moderate up to the collapse level occurred under the big earthquake events.

1.2.2 The relationship of seismic performance and the life-cycle cost of the structure

In a bridge design stage on the high seismic zone, the desired seismic performance of the structure takes the consequent which affects the life-cycle cost. In the concept of conventional structures, the performance of the structure is determined by its strength and ductility. In the philosophy of high-performance structure , after a severe earthquake occurred the structure only needs a light restoration and the bridge remains operated. The consequence is the initial construction cost may be relatively more expensive. On the other hand, if a moderate performance is chosen, the appearance of a big earthquake may evoke intensive restoration, a lot of restoration costs, and closing the bridge service during recovery time.

Some of the following studies below explain the structural performance enhancement. The installation of damper devices raises the significant contribution reducing the total cost during life-cycle time in the moderate to high seismic zones. Tiflanidis and Beck [47] performed a cost-effectiveness analysis of the performance of a four-story non-ductile RC structure retrofitted with the viscous fluid damper under earthquake events. The result showed that the total of life-cycle cost can be significantly reduced with the optimum reinforcement scenario. Further, Gidaris and Tafanidlis [12] conducted the assessment and optimization of the viscous fluid damper design of a three-story office building structure covering the cost criteria of the service scope with considering the influence of different seismicity characters. The result showed that the design optimizing of the life-cycle cost on the mild up to severe earthquake occurrence produced significantly structural response reduction and consequently minimized the loss cost.

1.2.3 High performance of bridge pier structures

In this decade, there is a lot of high seismic performance bridge pier with different concepts and mechanisms. Among these are the un-bonded bar reinforced concrete (UBRC) system where structures have stable post-yield stiffness. Also, self-centering system is a bridge pier which has a well re-centering capacity and capable reduce the damage level. Furthermore, the isolation system with high damper rubber bearing, lead rubber bearing, and friction pendulum bearing which can extend the natural period structure and also provide sufficient damping. Besides, there is a development of an integrated bridge pier with multiple columns connected by the hysterical dampers. In this system, the additional structural damping is generated by the dissipated energy of the damper, so that the damage of the column components due to seismic excitation can be reduced.

The high-performance bridge pier with unbonded bar reinforced concrete (UBRC) that was studied by Iemura et al. [19] can realize stable stiffness in post-yield states. Also, by applying the smaller cross-section of the proposed pier than the conventional pier [20], the more economical structure can be realized. Furthermore, the study of self-centering system with un-bonded post-tensioned was proposed by Mander and Cheng [30]. The seismic performance of this structure was studied by the reference [42]. Also, the development of the pier with UBPT was carried out by applying a ductile fiber-reinforced concrete by Billington and Yoon [2] and the further development with the application of fiber tubes and GFRP tubes to their plastic hinges in reference [8, 5]. Then, the behavior and the seismic performance of UBPT piers with the segmental system were investigated in reference[9, 4, 40, 41]. Moreover, the seismic performance investigation with shaking table test and numerical analysis of self-centering reinforced concrete bridge pier was conducted in reference [24]. The study about seismic performance based evaluation from the reference [27] concluded that the self-centering centering RC pier needs total cost almost equal with the conventional RC pier, it's benefit needs downtime shorter. The concept of self-centering piers with the additional damper on self-centering steel plate shear wall has been studied by reference [3], which can improve the seismic performance of frame structure in the form of good re-centering capacity. This system also adopted in the truss pier structure in reference [43]. Furthermore, the pillar structure system with UBPT combined with hysteresis and viscous damper was performed by Gunay and Mosalam [25].

The implementation of the isolation system on the bridge structure is one of the methods of improving the bridge pier seismic performance. Also, the design of a highway bridge based-isolation system was carried out by reference [11]. Design by considering nonlinear behavior between piers and high damping rubber bearing (HDRB) isolation devices was investigated experimentally by Shoji et al. [10]. Iemura et al. [18] conducted a study of the proportion of energy dissipation by taking into account the interaction of columns and isolation devices with sliding rubber bearings (SRB). Moreover, the isolation effectiveness of lead rubber bearing (LRB) to damp the bridge structure seismic response is carried out in reference [38, 22]. On the other studies, the experiment and numerical analysis of implementation high-performance isolation friction pendulum (IFP) on bridge structures to damp seismic excitation were studied respectively by Tsopelas et al. [50] and Wang et al. [51].

The high seismic performance of the integrated multiple columns connected by shear link dampers or shear panel dampers (SPD) has been developed and implemented in the structure. This typical structure has been proposed not only for the building but also for the bridge pier. Shear panel damper is an option of the several passive damper types for reducing earthquake load due to easy installation, maintenance, and affordability. The experiment study was conducted on a high-performance seismic column accompanied by friction dampers under cyclic loading by the reference [35]. Also, the studies of such structure was conducted, for example, the research about self-centering steel plate shear wall [3]. The structure can improve the seismic performance of frame structure in the contributions of the excellent re-centering capability. Secondly, the study of seismic response evaluation of the linked column frame system (LCF) was conducted [29]. In the event of a moderate earthquake, a quick reparation can be conducted to the damper devices that are damaged, in addition, this system realized collapse prevention conditions in the structure under great earthquake. Furthermore, the experimental study of the bridge pier with structural fuses and bi-steel columns was conducted [7]. While the result showed that the elastic deformation state of the steel columns and the energy dissipation were still limited. Also, the structure of a self-anchorage suspension cable bridge in San Fransisco-Oakland Bay was built by applying shear link damper within the main pylon. Based on the reference [34], the seismic performance of this bridge pylon was controlled by safety-evaluation earthquakes (SEE) with 1500 years of earthquake return-period which applied six inputs of earthquake load following the characters of San Andreas Fault and Hayward Fault. The structural simulations of pushover analysis and non-linear time history analysis showed that the main pylon was remaining in the elastic state, also shear link damper yielded below the strain limit. Moreover, the integrated bridge pier with multiple steel pipe columns connected by shear panel damper (SPD) has been developed and applied by Hanshin Expressway. The top and bottom of steel pipes were connected to the pile cap and head pier respectively with fix connection. While the SPDs were installed at along the pier height with certain intervals of a uniform distribution in its strength and stiffness terms. With the dissipated energy capacity of the its SPD, this structure has been enriched as high seismic performance structure which has enriched the Performance 2b (the structures occur medium-damaged by severe earthquakes) for the Importance Bridge category [37]. As the study result, the damage possibility caused by severe earthquake excitation has been reduced. In the less of structural damage, the life-cycle-cost of the structure that built in the high seismic zone can be descended [37].

The study of integrated bridge pier with multiple steel pipes connected by SPD was also commenced by several predecessor research. For example, the experimental study on seismic performance of an integrated column by multi steel pipes with hysteric damper was conducted [26]. Secondly, the basic property of an integrated column by multiple steel pipe columns with hysterical shear panel damper [45] was studied. Furthermore, to improve the seismic force reduction also to reduce the cost of the structure that was in the case of the foundation, the proposal of the bridge column integrated by multiple steel pipe columns with a direct-connected pile and seismic response analysis was conducted [46]. As well as research on the mechanical behavior of the pier with integrated steel pipe columns subjected to axial, torque, and cyclic loads on horizontal direction [15], and also the effect of structural parameters of SPD on the performance of multi-pipe integrated bridge pier [16] were investigated.

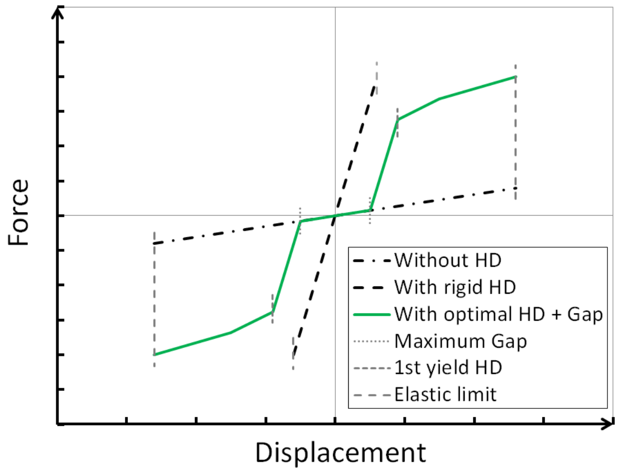

FIGURE 1.7: The proposed concept of an additional gap on the hysterical damper.

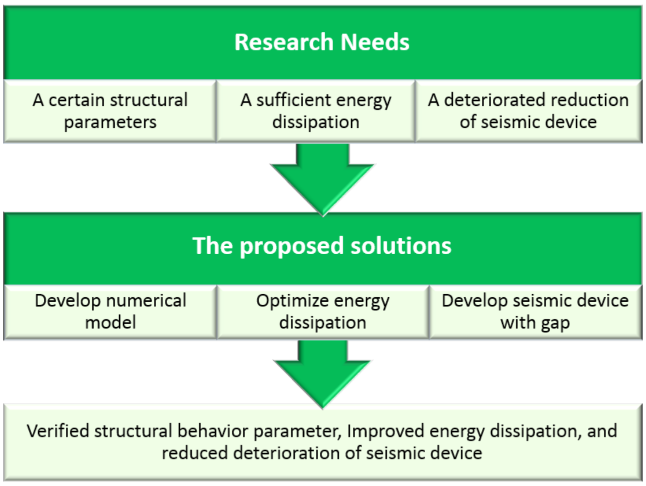

(A)

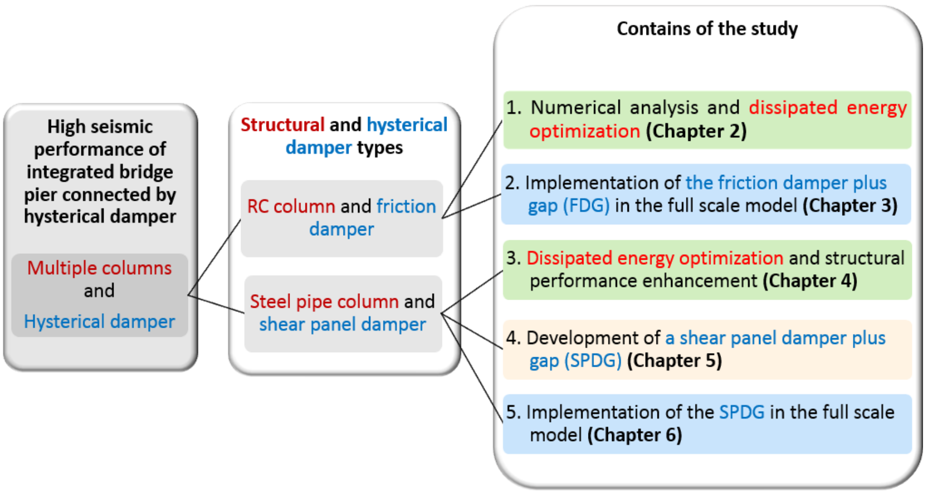

(B)

FIGURE 1.8: The illustration of: (A) the objective research and (B) thesis organization.

1.3 Objective

The goal of this study is the achievement of high seismic performance bridge pier. In the term of high seismic performance in this study, the structure can realize limited damage and reduce residual deformation under Level 2 [23] of earthquake excitation. The implementation of the multiple columns could improve the deformation limit capacity which near to the elastic behavior. Also, the hysterical damper appearance could absorb effectively vibration energy of the structure under seismic excitation. Furthermore, the additional gap existence could provide sufficient structural flexibility to accommodate frequent lateral deformation, as illustrated in Figure 1.7. The illustration of the of research objective is shown in Figure 1.8A. More ever, the specific objectives are:

- Numerical analysis of integrated triple RC columns connected by friction dampers: it calibrated the appropriate friction damper parameters and verified the structural behavior. The parameter calibration of the friction damper was conducted by the matching analysis not the hysteresis loops but also the curvature distributions of the columns. While, the structural behavior verification was performed by the monitoring of the hysteresis loops, the curvature distributions, the sensitivity of the friction dampers deformation related the confine force distribution of the friction damper along the column height.
- Dissipated energy optimization of integrated triple RC columns connected by friction dampers: it optimized the dissipated energy of the existing structural configuration by changing the confinement force value and the distribution pattern of the friction damper based on the calibrated parameters of the friction damper. Also, the best optimal confinement force pattern, the characteristic of hysteresis loop, the elastic deformation capacity, and the damping energy related the deformation were examined in the numerical model.
- The implementation of the proposed friction damper plus gap (FDG) to the integrated triple RC columns: The full scale numerical model of the structure was developed. Also the numerical analysis including static and dynamic were include in this part. The skeleton curve, the structural stiffness and the limit state of the structure examined by the static pushover analysis. Then, the dissipated energy to be examined by the static cyclic analysis. Finally, the structural performance verification was conducted by dynamic analysis by applying the Level 2 of earthquake excitation based on the [23]. The proposed structure can not only behave near elastic behavior under Level 2 of seismic excitation but also has sufficient flexibility for the frequent lateral deformation.

- The seismic performance enhancement of integrated bridge pier with multiple steel pipes connected by shear panel damper: By redistributing the strength and the stiffness of the shear panel damper along the steel pipes height and proposing the pin connection between the top end of the steel pipes and head pier, the seismic performance enhancement of the structure was conducted by numerical analysis. This enhancement could not only improve the dissipated energy of the structure but also increase the deformation limit capacity of the structure. Finally, the seismic performance was increased from Performance 2b to be Peformance IIa.
- The development of a shear panel damper plus gap (SPDG): Experiment of four SPDG specimens was conducted by considering the effect of friction force of sliding surface. Also, the numerical analysis with spring model and 3D model of shell element were conducted to calibrate the structural parameters and examine the structural behavior. The SPDG could produce not only sufficient flexibility under deformation below the gap length but also raise sufficient dissipated energy.
- The proposal of integrated bridge pier with steel pipes connected by shear panel damper plus gap: The SPDG following the calibrated experimental result was implemented in the structure. Numerical analysis was conducted to examine not only the structural performance under Level 1 and Level 2 of earthquake excitation but also the structural behavior. In the proper friction force of SPDG's sliding surface the structure could not only realize performance 2a under Level 2 of seismic excitation but also has better flexibility under deformation below the gap length.

1.4 Thesis Organization

This study discussed the development of an integrated bridge pier with multiple columns connected by hysterical dampers (HD). The integrated pier consists slender columns which are expected to have a large elastic or a slight elastic deformation capacity. Below the deformation capacity limit, the hysterical damper could to produce sufficient energy dissipation to quench the vibration due to earthquake excitation. In the severe earthquake event, the column element was in the near to elastic behavior. So that the damage can be limited, the restoration challenge and it's cost can be reduced, also the structure can still operate immediately after the earthquake.

In this thesis, there are two structural types of bridge pier that to be developed as high seismic performance structure. The first one is the RC columns connected by friction dampers

(FD) while the other one is the steel pipes columns connected by shear panel dampers (SPD). The illustration of the thesis organization is shown in Figure 1.8B. The first chapter discussed about the introduction. In addition, numerical analysis and dissipated energy optimization of integrated triple RC columns connected by friction damper was discussed in the second chapter. This chapter's scopes included the numerical analysis method of the structure, the influence of friction force distribution to the structural behavior and dissipated energy capacity, as well as the optimum dissipated energy. In the third chapter, the concept of high seismic performance of the integrated pier with triple RC columns connected by friction damper plus gap was proposed. Numerical analysis was performed to simulate structures including static analysis and dynamic analysis. The structure could not only accommodate the frequent lateral deformation with sufficient flexibility but also behave elastic or near to elastic under Level 2 of seismic excitation based on JRA 2012 code. In the fourth chapter, seismic performance enhancement of integrated pier with multiple steel pipe columns connected by shear panel damper was conducted. In this chapter, the SPD strength distribution is varied to obtain the optimum dissipation energy. The pin connection system based on the reference [44] is also adopted in the top connection of the steel pipe columns, to achieve significant dissipated energy improvement and elastic deformation capacity. The fifth chapter discussed the development of shear panel damper plus gap (SPDG) which was conducted by experimental and numerical analysis. The sixth chapter described the structural concept of an integrated pier with multiple steel pipe columns connected by shear panel damper plus gap. This structural concept is similar to the third chapter wherein the small deformation (below the gap) of the structure has sufficient flexibility while in the large deformation the damper device works and the structural stiffness increases as main stiffness.

Bibliography

[1] Basoz, N.I., Kiremidjian, A.S., King, S.A. and Law, K.H.: Statistical Analysis of Bridge Damage Data from the 1994 Northridge, CA, Earthquake, Earthquake Spectra, volume 15, no. 1:25–54, 1999.

[2] Billington, S.L. and Yoon, J.K.: Cyclic Response of Unbonded Posttensioned Precast Columns with Ductile Fiber-Reinforced Concrete, Journal of Bridge Engineering, volume 9, no. 4:353–363, 2004.

[3] Clayton, P., Berman, J.W. and Lowes, L.: Seismic design and performance of self-centering steel plate shear walls, Journal of Structural Engineering, volume 1, no. JANUARY:22–30, 2011.

[4] Dawood, H., ElGawady, M. and Hewes, J.: Behavior of Segmental Precast Posttensioned Bridge Piers under Lateral Loads, Journal of Bridge Engineering, volume 17, no. 5:735–746, 2012.

[5] Dawood, H.M. and Elgawady, M.: Performance-based seismic design of unbonded precast post-tensioned concrete filled GFRP tube piers, Composites Part B: Engineering, volume 44, no. 1:357–367, 2012.

[6] Deng, P. and Warn, G.P.: Modeling the Compression Stiffness Degradation in Circular Elastomeric Bearings due to Fatigue, Journal of Engineering Mechanics, volume 142, no. 1:1–11, 2016.

[7] El-Bahey, S. and Bruneau, M.: Bridge Piers with Structural Fuses and Bi-Steel Columns. I: Analytical Investigation, Journal of Bridge Engineering, volume 17, no. 1:36–46, 2012.

[8] ElGawady, M., Booker, A. and Dawood, H.: Seismic behavior of posttensioned concrete-filled fiber tubes, Journal of Composites for Construction, volume 14, no. 5:616–628, 2010.

[9] ElGawady, M.A. and Sha'lan, A.: Seismic Behavior of Self-Centering Precast Segmental Bridge Bents, Journal of Bridge Engineering, volume 16, no. 3:328–339, 2011.

[10] Gaku Shoji, Kazuhiko Kawashima, A.S.: Cyclic Loading Test to Clarify Nonlinear Behavior of an Isolated Bridge Supported by High Damping Rubber Bearings, Journal of JSCE, volume I, no. 56:81–100, 1995.

[11] Ghobarah, A. and Ali, H.: Design of Base-isolated Highway Bridges, in *Ninth world conference on Earthquake Engineering*, pages 615–620, Ninth world conference on Earthquake Engineering, Tokyo, 1988.

[12] Gidaris, I. and Taflanidis, A.A.: Performance assessment and optimization of fluid viscous dampers through life-cycle cost criteria and comparison to alternative design approaches, Bulletin of Earthquake Engineering, volume 13, no. 4:1003–1028, 2015.

[13] Guo, C., Zhou, L. and Lv, J.: Fatigue Life Prediction for Circular Rubber Bearings Subjected to Cyclic Compression, Journal of Applied Polymer Science, volume 123, no. 7:2194–2203, 2011.

[14] Hamaguchi, H., Samejima, Y. and Kani, N.: A study of aging effect on rubber bearings after about twenty years in use, in *11th World Conference on Seismic Isolation, Energy Dissipation Control of Structures*, pages 1–16, World Conference on Seismic Isolation, Energy Dissipation and Active Vibration Control of Structures, Guangzhou, 2009.

[15] Hashimoto, K., Sugiura, K., Nishioka, T. and Tamba, Y.: Mechanical Behavior of Steel Pier Integrated Steel Pipes Subjected to Axial, Torsional and Cyclic Horizontal Load, Journal of JSCE, volume 70, no. 1:80–93, 2014.

[16] Hashimoto, K. et al.: Effect of Structural Parameters of Shear Panel Damper on Seismic Performance of Multi-pipe Integrated Bridge Pier, Journal of JSCE, volume 72, no. 1:75–91, 2016.

[17] Hashimoto, S., Abe, M. and Fujino, Y.: Damage Analysis of Hanshin Expressway Viaducts during 1995 Kobe Earthquake. III: Three-Span Continuous Girder Bridges, Journal of Bridge Engineering, volume 10, no. 1:61–68, 2005.

[18] Iemura, H., Takahashi, Y. and Chen, Y.: Control of Seismic Energy Partitioning of Bridge Piers with Sliding Rubber Bearing, Technical report, Kyoto University, Kyoto, 2008.

[19] Iemura, H., Takahashi, Y. and Sagobe, N.: Development of Unbonded Bar Reinforced Concrete Structure, in *13 th World Conference on Earthquake Engineering*, 1537, page 15, 13 th World Conference on Earthquake Engineering, British Columbia, 2004.

[20] Iemura, H., Takahashi, Y. and Sogabe, N.: Two-level seismic design method using post-yield stiffness and its application to unbonded bar reinforced concrete piers, Journal of JSCE, volume 23, no. 1:109–116, 2006.

[21] Itoh, Y., Gu, H., Satoh, K. and Yamamoto, Y.: Long-Term Deterioration of High Damping Rubber Bridge Bearing, Doboku Gakkai Ronbunshuu A, volume 62, no. 3:595–607, 2006.

[22] Jangid, R.S.: Seismic Response of Isolated Bridges, volume 9, no. 2:156–166, 2004.

[23] Japan Road Association: *Specifications for Highway Bridges: Part V Seismic Design*, Maruzen Co. Ltd., Tokyo, 2012.

[24] Jeong, H.I., Sakai, J. and Mahin, S.a.: Shaking Table Tests and Numerical Investigation of Self-Centering Reinforced Concrete Bridge Columns Shaking Table Tests and Numerical Investigation of Self-Centering Reinforced Concrete Bridge Columns, Technical Report 06, Pasific Earthquake Engineering, Berkeley, 2008.

[25] Kam, W.Y., Pampanin, S., Palermo, A. and Carr, A.J.: Self-centering structural systems with combination of hysteretic and viscous energy dissipations, Earthquake Engineering and Structural Dynamics, volume 39, no. January:1083–1108, 2010.

[26] Kanaji, H. et al.: Experimental Study on Seismic Performance of an Integrated Column by Multi Steel Pipes with Hysteretic Damper, Journal of JSCE, volume 13, no. 49:59–72, 2006.

[27] Lee, W.K. and Billington, S.L.: Performance-based earthquake engineering assessment of a self-centering, post-tensioned concrete bridge system, Earthquake Engineering and Structural Dynamics, volume 40, no. November 2010:887–902, 2010.

[28] Mahin, S.A.: The Loma Prieta Earthquake : Implications of Structural Damage The Loma Prieta Earthquake : Implications of Structural Damage, in *Second International Conferences on Recent Advances in Geotechnical Earthquake Engineering and Soil Dynamics*, pages 1–14, Missouri, 1991.

[29] Malakoutian, M., Berman, J.W. and Dusicka, P.: Seismic response evaluation of the linked column frame system, Earthquake Engineering and Structural Dynamics, volume 6, no. May 2013:795–814, 2012.

[30] Mander, J.B. and Cheng, C.: Seismic resistance of bridge piers based on damage avoidance design, Technical report, State University of New York at Buffalo, Buffalo, 1997.

[31] Mitoulis, S.A. and Rodriguez Rodriguez, J.: Seismic Performance of Novel Resilient Hinges for Columns and Application on Irregular Bridges, Journal of Bridge Engineering, volume 22, no. 2:1–12, 2017.

[32] Moehle, J.P. and Eberhard, M.O.: Bridge Engineering Handbook: Earthquake Damage to Bridges, chapter 34, page 34, CRC Press, Boca Raton, 2000.

[33] Mylonakis, G.: The Collapse of Fukae (Hanshin Expressway) Bridge , Kobe , 1995 : The Role of Soil and Soil- Structure Interaction, in *Fifth International Conference on Case Histories in Geotechnical Engineering*, pages 0–12, Missouri University of Science and Technology, New York, 2004.

[34] Nader, M., Maroney, P. and Eng, P.: Seismic Design for the Self Anchored Suspension Bridge–San Francisco Oakland Bay Bridge, IABSE Symposium Report, volume 102, no. 2014-09-01T00:00:00:1307–1314, 2014.

[35] Nakamura, H., Takahashi, Y. and Sawada, S.: *The Elasto-Plastic Behavior of the Rectangular RC Column Accompanied with Friction Damping Mechanism with Complex Confinement*, Undergraduate thesis, Kyoto University, 2011.

[36] Nakamura, H., Takahashi, Y. and Sawada, S.: The Elasto-plastic Behavior of the Rectangular RC Column Accompanied with Friction Damping Mechanism, Journal of JSCE, volume 68, no. 4:577–583, 2012.

[37] Nakamura, R., Kanaji, H. and Kosaka, T.: Development and Design of New Steel Pipe Integrated Pier with Shear Link, Technical report, Hanshin Expressway Company Limited, Osaka, 2014.

[38] Neethu, B. and Das, D.: Influence of Passive Isolator Parameters on Seismic Response Control of Multi-Span Bridges, International Journal of Scientific and Research Publications, volume 5, no. 1:2250–3153, 2015.

[39] on Earthquakes, J.N.C.: Seismological Aspects of the Niigata Earthquake, 1975.

[40] Ou, Y.c.: *Precast Segmental Post-tensioned Concrete Bridge Columns for Seismic Regions*, Ph.D. thesis, State University of New York, 2007.

[41] Ou, Y.C., Chiewanichakorn, M., Aref, A.J. and Lee, G.C.: Seismic Performance of Segmental Precast Unbonded Posttensioned Concrete Bridge Columns, Journal of Structural Engineering, ASCE, volume 133, no. 4:484–494, 2007.

[42] Palermo, A., Pampanin, S. and Calvi, G.M.: Use of "Controlled Rocking" in the seismic design of Bridges, in *13th World Conference on Earthquake Engineering*, 4006, page Paper No. 4006, World Conference on Earthquake Engineering, British Columbia, 2004.

[43] Pollino, M. and Bruneau, M.: Seismic retrofit of bridge steel truss piers using a controlled rocking approach, Journal of Bridge Engineering, volume 12, no. 5:600–610, 2007.

[44] Saiidi, S. and Mehrsoroush, A.: Earthquake-Resistant Telescopic Pipe Pin Column Base Connections for Accelerated Bridge Construction, in *10th U.S. National Conference on Earthquake Engineering*, Frontiers of Earthquake Engineering, Anchorage, 2014.

[45] Shinohara, M., Kanaji, H., Oniki, K. and Sugiura, K.: Basic Properties of an Integrated Column by Multiple Steel Pipes with Hysteretic Shear Damper, Journal of JSCE, volume 58A:471–483, 2012.

[46] Shinohara, M., Kanaji, H., Oniki, O. and Kimura, M.: A Proposal of a Bridge Column Integrated by Multiple Steel Pipes with Directly-connected Piles and a Seismic Response Analysis, Journal of JSCE, volume 69, no. 3:312–325, 2013.

[47] Taflanidis, A.A. and Beck, J.L.: Life-cycle cost optimal design of passive dissipative devices, Structural Safety, volume 31, no. 6:508–522, 2009.

[48] Takahashi, Y. and Hoshikuma, J.i.: Damage to Road Bridges Induced by Ground Motion in the 2011 Great East Japan Earthquake, Journal of JSCE, volume 1:398–410, 2013.

[49] Taylor, A.W., Lin, A.N. and Martin, J.W.: Performance of Elastomers in Isolation Bearings: A Literature Review, Earthquake Spectra, volume 8, no. 2:279–303, 1992.

[50] Tsopelas, P., Constantinou, M.C., Kim, Y.S. and Okamoto, S.: Experimental Study of FPS System in Bridge Seismic Isolation, Earthquake Engineering and Structural Dynamics, volume 25, no. 4:65–78, 1996.

[51] Wang, Y.P., Chung, L.L. and Liao, W.H.: Seismic response analysis of bridges isolated with friction pendulum bearings, Earthquake Engineering and Structural Dynamics, volume 27, no. 10:1069–1093, 1998.

[52] Weinni, D.: Chi-Chi, Taiwan Earthquake Event Report, Technical report, Risk Management Solution Inc., California, 2000.

[53] Yamazaki, F., Motomura, H. and Hamada, T.: Damage Assessment of Expressway Networks in Japan Based on Seismic Monitoring, in *12th World Conference on Earthquake Engineering*, January 2000, pages 1–8, New Zealand Society for Earthquake Engineering, Auckland, 2000.

Chapter 2

Numerical Analysis and Dissipated Energy Optimization of the Integrated RC Columns Connected by Friction Dampers

2.1 General Remarks

The integrated triple RC columns connected by friction dampers has high-potential to be developed as high seismic performance bridge pier. The distributed friction dampers system of the bridge pier might be more robustness than that uses the concentrated damper system. Based on the experimental study of the reference [11], the structure can achieve sufficient energy dissipation with large elastic deformation capacity. This study examined the structural behavior and dissipated energy optimization of such structure by numerical analysis in the experiment results of the reference [10]. The important material parameters of the FD and the RC column were investigated by matching the hysteresis loops and the curvature distribution patterns between numerical and experimental results. Also, the optimum energy dissipation in the elastic state was investigated by applying regular patterns of incremental confinement force and varying the confinement force in each friction damper using a number of confinement force combinations. As the results, the friction coefficient and slip deformation value of the friction damper have been the important parameters in the numerical analysis. Also, comparison of numerical and experimental hysteresis loops and curvature distributions has shown good agreement. Furthermore, a different type of confinement force pattern treatment resulted in different hysteresis loops and curvature distributions. Finally, in the best optimum confinement force pattern of the structure, there have been 40% times dissipated energy enhancement from the original uniform confinement pattern and the 25% or larger of damping ratio could be achieved around the elastic deformation limit.

2.2 Background

The using of a frictional damper is one of the alternatives to improve the seismic performance of the structure. Its existence can support the plastic hinge contribution in absorbing the vibration energy of the structure during the earthquake occurrence. So that, the reduced plastic hinge results the descended of the structural damage. There are some studies about the using of the frictional damper to the structure including, a large cantilever panel structure connected by limited slip bolt joints for seismic control of buildings was developed by Pall [14]. Also, the concept of the friction-damped braced frame for steel structures was proposed by Pall and Marsh [15]. Furthermore, Mualla and Belev [9] developed a rotational FDD with a V-bracing shape for seismic control of steel structures. However, all of the predecessor studies have not yet considered the keeping the main structural member remains elastic behavior. While an integrated multiple RC columns connected by friction dampers has high-potential to be developed as high seismic performance bridge pier. It can achieve sufficient energy dissipation with large elastic deformation capacity [10]. Also, the distributed friction dampers system of the bridge pier has more robustness than that uses the concentrated damper. When the contribution of a part of the dampers is absent due to losing, the others damper still present to resist the external force and to absorb the vibration energy. In addition, the using of concrete material for pier has the advantages in the term of easy affordability and maintenance.

In the previous study [10], experiment was performed on a high seismic performance RC column accompanied by friction damper under cyclic loading. The structure contained three concrete columns connected by the friction dampers and pre-stressed concrete (PC) bolts, as shown in Figure 2.1. Based on the experiment result of the reference [10], this structure had sufficient energy dissipation due to the achievement of elastic-plastic behavior with large enough elastic deformation capacity, as shown in Figure 2.2. The elastic deformation capacity was about 2% of drift ratio and the restoring force was fairly constant up to 10% drift. Based on the FEMA 356 standard [3] for Immediate Occupancy performance, the limitations on the primary RC column structure are minor hairline cracking, limited yielding possible at a few locations,

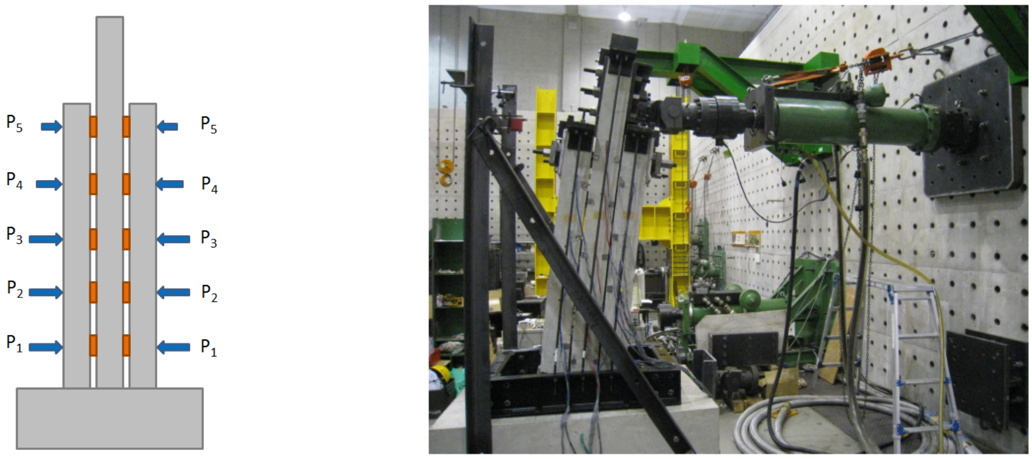

(A) (B)

FIGURE 2.1: Columns connected by the friction dampers (FD) [10]: (A) the structural concept and (B) the experimental setup.

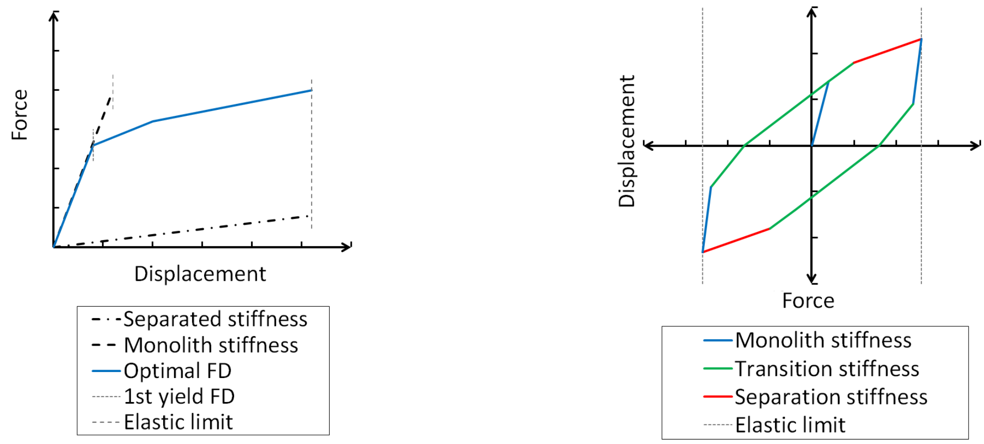

(A) (B)

FIGURE 2.2: Columns connected by the friction dampers (FD) behavior [10]: (A) skeleton curve and (B) hysteresis loop.

and no crushing. Also, the drift limit is 1% in transient events and no permanent drift may occur. This column type may be used in essential or hazardous facilities that must reach the Immediate Occupancy performance category in a severe earthquake. With its sufficient elastic deformation capacity and energy dissipation, the proposed structure is expected to remain an elastic behavior under Level 2 of seismic excitation [5]. Also, by considering the difference confinement force distribution pattern the friction damper in the structural system can achieve different hysteresis loop shape and different curvature distribution along the column height, as shown in Figure 2.3.

The other hand, the previous study [10] just considered the experimental result which the numerical parameters of the structure have not yet to be calibrated. Also, there was lack of

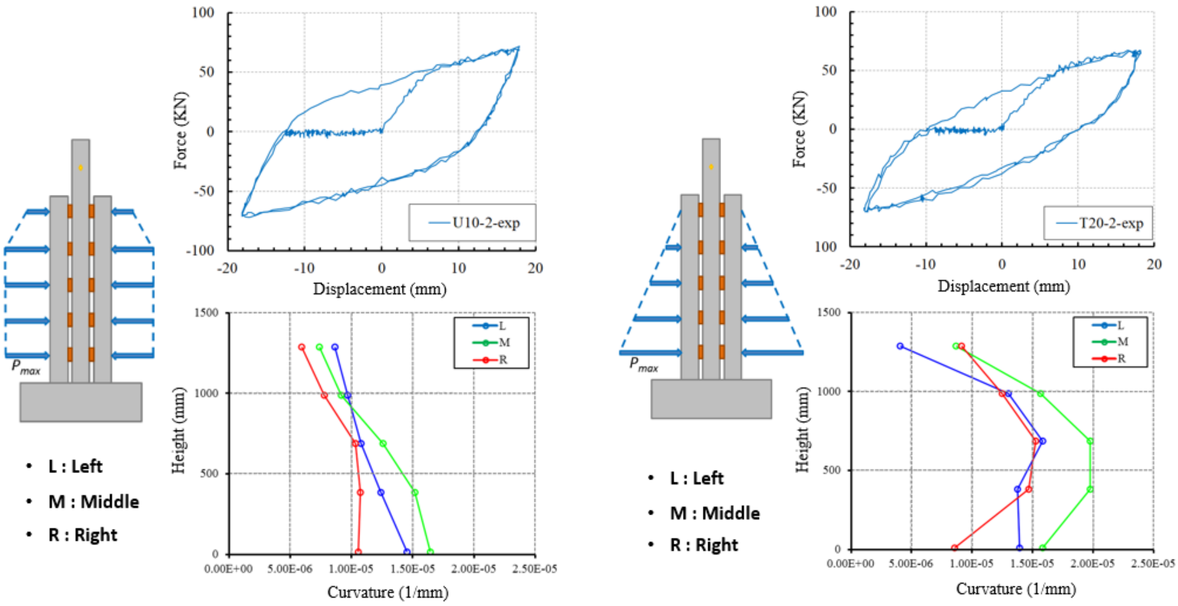

(A) (B)

FIGURE 2.3: Experiment results [11] with different confinement force of FD in the structural system of: (A) uniform pattern and (B) triangular pattern.

structural confinement force distribution patterns to investigate the influenced structural behavior which just considering uniform and triangular pattern. Furthermore, the optimum energy dissipation related the confinement force distribution pattern of the friction damper is a demand for the high seismic performance bridge pier development.

This study examined the structural behavior and dissipated energy optimization of integrated triple columns connected by friction dampers by numerical analysis. Numerical analysis is one of the appropriate ways to verify the structural response in cases of the complex nonlinearity. The experiment results of the reference [10] were chosen to calibrate the numerical model by matching the hysteresis loops and the curvature distributions. So that the calibrated of the structural parameters could be used for the dissipated energy optimization and numerical simulation of such a full-scale structural model. Also, the seismic performance of a structure could be improved by optimizing the energy dissipation in the elastic state. Based on the predecessor study, the dissipated energy optimization method in which minimizing the energy input and maximizing the energy dissipation was proposed by Pall [1]. Also, Mualla and Belev [9] implemented the SPI minimization method to improve their proposed structural system. In this study, the optimization method of Pall [1] was implemented by measuring the maximum energy dissipation with a regular confinement force pattern and varying the confinement force value in each friction damper over multiple static cyclic analysis. As the result, the numerical analysis calibration has good agreement with the experimental result in the term of hysteresis loops and curvature distributions. Also, The behavior of the structure with the optimum energy dissipation was also captured to show the causality. Furthermore, the confinement force distribution pattern and its value governed the dissipated energy, the elastic deformation capacity, and the shape of the hysteresis loop and the curvature distribution. Finally, in the best optimum confinement force pattern of the structure, the dissipated energy enhancement was about 1.40% from the uniform of original confinement pattern.

2.3 Integrated triple columns connected by friction dampers

2.3.1 Friction damper characteristics

Pall [14], Mualla and Belev [9], and Moralez et al. [16] implemented an idealized elastic-plastic model of the friction damper in numerical analysis based on experiment results. The friction damper followed the Coulomb dry friction law, with the friction force in both static and slip conditions assumed to be constant because they were subjected to pressure high enough to produce excessive deformation with low relative velocity [4]. The friction coefficient (μ) can be determined as Equation (2.1). The F_{max} is maximum shear force and the N is normal force.

$$\mu = \frac{\mathrm{F}_{max}}{N} \tag{2.1}$$

Mualla and Belev [9] performed experiments and numerical analysis of a steel frame with an FDD that contained an asbestos-free friction pad material and steel. The cyclic test with 400 cycles showed that almost no damage occurred on the FDD. Nakamura [12] conducted experiments on friction dampers that contained friction material made of SS400 steel connected by a couple made of SUS304 steel. Experiment results showed that the friction coefficient increased almost linearly with slip increment, starting from about 0.2 at first slip until about 0.5 at the end of the loading. The force and displacement curves are shown in Figure 2.4.

2.3.2 The specimen properties of the integrated RC columns connected by FD

The structure contained three RC columns with fixed supports at the base and free of constraints at the top. The three columns were connected to the friction damper with PC bolts at 300 mm intervals over the 1500 mm column height. The PC bolts that have 30 mm of diameter confined each friction damper. The column section was 600 mm wide and 150 mm deep, and

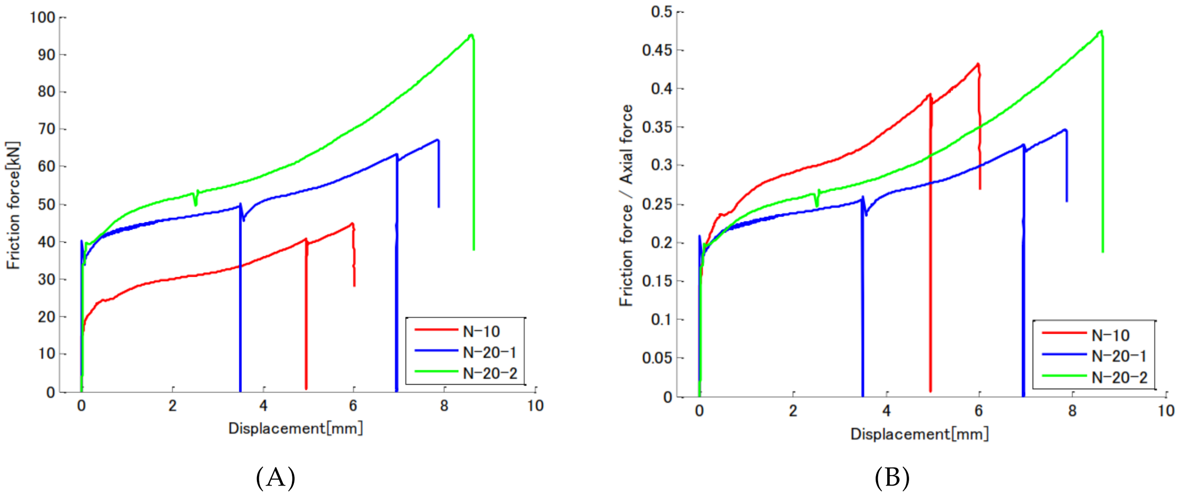

FIGURE 2.4: Experiment results [12] of: (A) Friction force and (B) Friction coefficient.

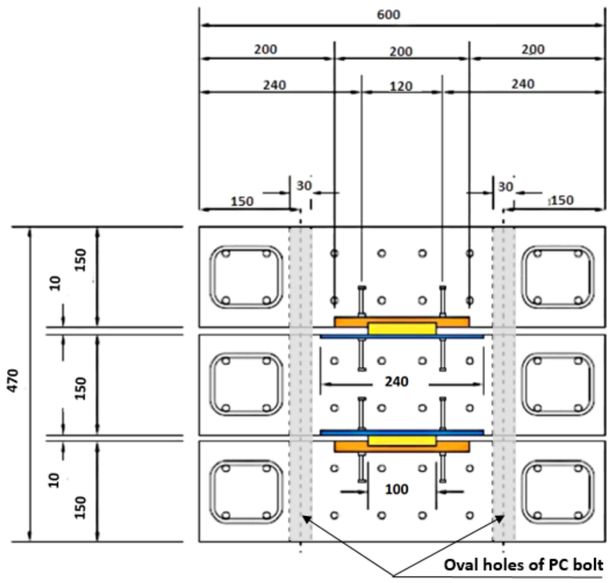

FIGURE 2.5: The cross section of the integrated RC columns connected by FD [11] (units in mm).

contained 16D10 longitudinal reinforcement bars and 2D6 transversal reinforcement with 50 mm spacing, as shown in Figure 2.5. The longitudinal reinforcement was SD345 steel and the transversal reinforcement was SD295 steel. The compressive strength of the concrete column specimen was 37 MPa.

2.3.3 The principle concept of the integrated RC columns connected by FD

The purpose of the integrated RC columns connected by FD is the achievement of sufficient energy dissipation during elastic deformation. The structure was composed of three thin columns to achieve large elastic deformation capacity. The friction dampers connected each

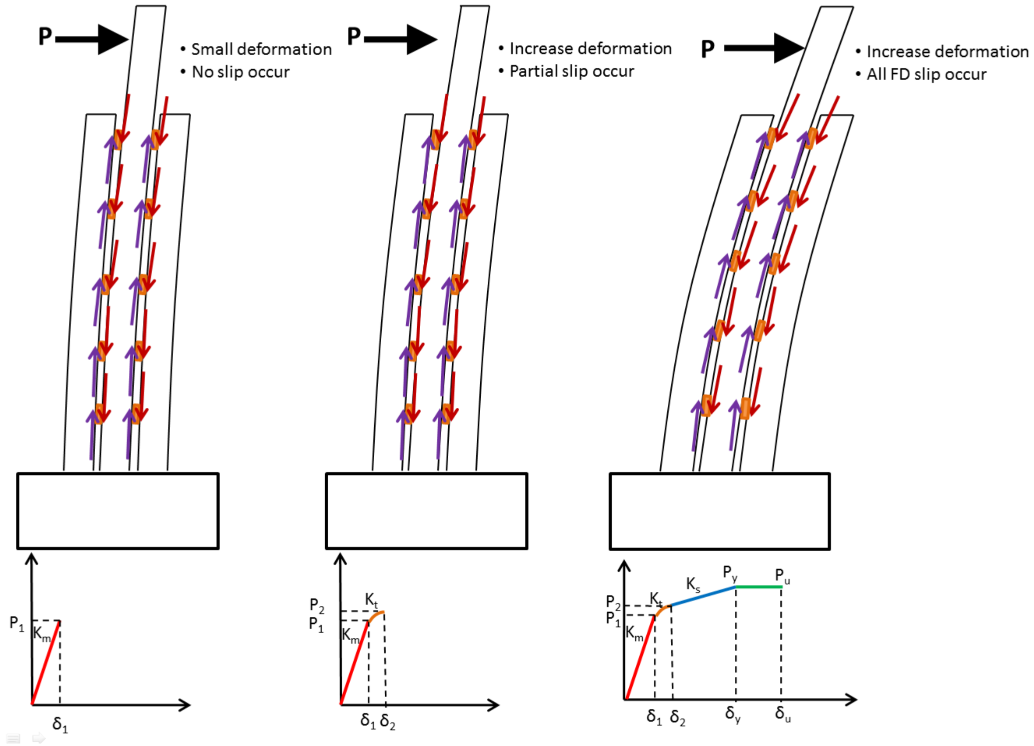

FIGURE 2.6: Force and deformation characteristics of the integrated RC columns connected by FD.

TABLE 2.1: Confinement force distributions of the friction dampers [10].

		Conf. force (Tonf)			
No	Elevation (mm)	U10	T10	T20	T40
1	300	10	10	20	40
2	600	10	7.5	15	30
3	900	10	5	10	20
4	1200	10	2.5	5	10
5	1500	5	0	0	0

TABLE 2.2: Cyclic loading scenarios [10].

No	Scenario	δ_{max} (mm)
1	U10	-9 to 9
2	T10	-7 to 7
3	T20	-8 to 8
4	U10-2	-17.5 to 17.5
5	T20-2	-17.5 to 17.5
6	T20-3	-200 to 200
7	T40	-160 to 200

column with the horizontal confining forces of the PC bolts to realize the structural unity. Energy dissipation is achieved when the slip deformation of each friction damper occurs during lateral deformation of the structure [11]. The implementation of the non-linearity concept and advanced numerical analysis improved Pall's [1] optimization method, which only considered

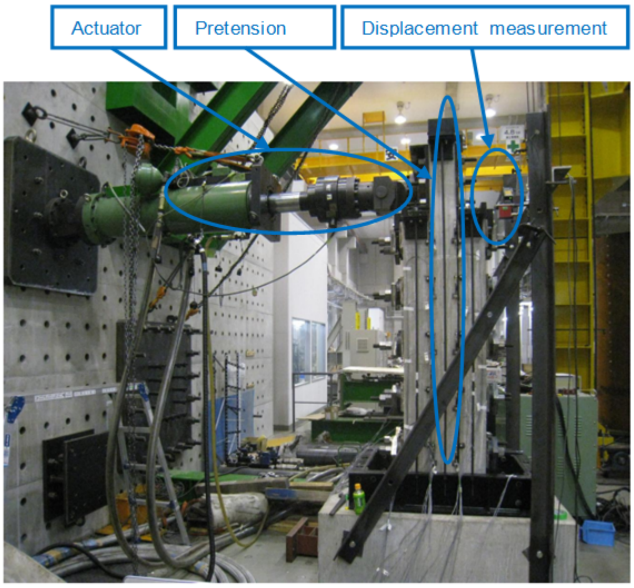

FIGURE 2.7: Experimental setup of the integrated RC columns connected by FD [10].

linear behavior of the cross section of the concrete structure and uniform slipping force distribution along the structural height.

The structure had four distinct stiffness stages. When a small lateral force (P) was applied to the top of the column, small lateral deformation occurred, and slip did not yet occur on the friction dampers. In this stage, the stiffness of the column was the monolithic stiffness (K_m). With increasing lateral force, the deformation of the column increased. Slip occurred at some parts of the friction dampers, and the stiffness of the column decreased to the transition stiffness (K_t). Further increases in the lateral deformation propagated the slip to all friction dampers, and the stiffness decreased to the separated stiffness (K_s). The separated stiffness was valid in the elastic range before the reinforcing yielded. After the reinforcing steel yielded, the stiffness continued to decline to the plastic stiffness K_p. The illustration of the four stages is shown in Figure 2.6.

2.4 Previous experimental study of the structure

The main focus of the experiments was to investigate the influence of the confinement force distribution of the friction dampers on the structure's behavior. Two specimens were tested. Specimen 1 was confined by two PC bolts outside of the friction damper, while specimen 2 was confined by one buried PC bolt in the centre of the friction damper. There were four variations of the confinement force distribution, which are shown in Table 2.1.

Seven variations of cyclic loadings were performed, as shown in Table 2.2. Specimen 1 was used in all cases except T20-3, which used specimen 2. The cyclic loading test was implemented with displacement control. Axial stress of 1 MPa was applied on each column to simulate the self-weight of the superstructure. The experimental setup is shown in Figure 2.7.

2.5 Numerical analysis method

2.5.1 Structural idealization

The integrated RC columns connected by FD was modeled as a frame element in the two-dimensional model with three degrees of freedom. The numerical analysis was conducted with Opensees, which is able to solve highly non-linear structural problems [7]. Selecting the appropriate element types depends on the problem conditions. The upper end of the middle column was idealized as an elastic frame because it was used as the loading point support covered with a steel plate.

The force-based beam-column element with a fiber section was used for the other column elements following [19]. Based on [22] and [21], the fiber section of the element can be used to solve distributed plasticity problems. The interaction between the reinforcing steel and the concrete to be idealized as perfect bond. This chapter also improved the previous study [20], which implemented displacement-based elements as force-based elements because of the better accuracy and the cheaper computation time [13]. There were two Gauss-Legendre integration points [18], which were located in each segment of the column to obtain an accurate model, as shown in Figure 2.8. Concrete material (named Concrete02) and smoothed bi-linear material (named Steel02) are used for the RC column sections. The friction dampers were modeled as two-node link elements with bi-linear material (named Steel01) in the transverse direction and elastic material properties in the perpendicular direction of the column height.

2.5.2 Concrete material parameters

The Concrete02 constitutive model was used for the concrete material. The model adopts the Kent-Park concept modified by Scott [17] and the hysteresis behavior following the reference [23]. The parameters were adjusted to match the post-peak stress measured from the T20-3 and T40 loading scenarios. The parameter adjustment was done by performing a multi-simulation analysis to match the ultimate stress and strain variables of the concrete material.

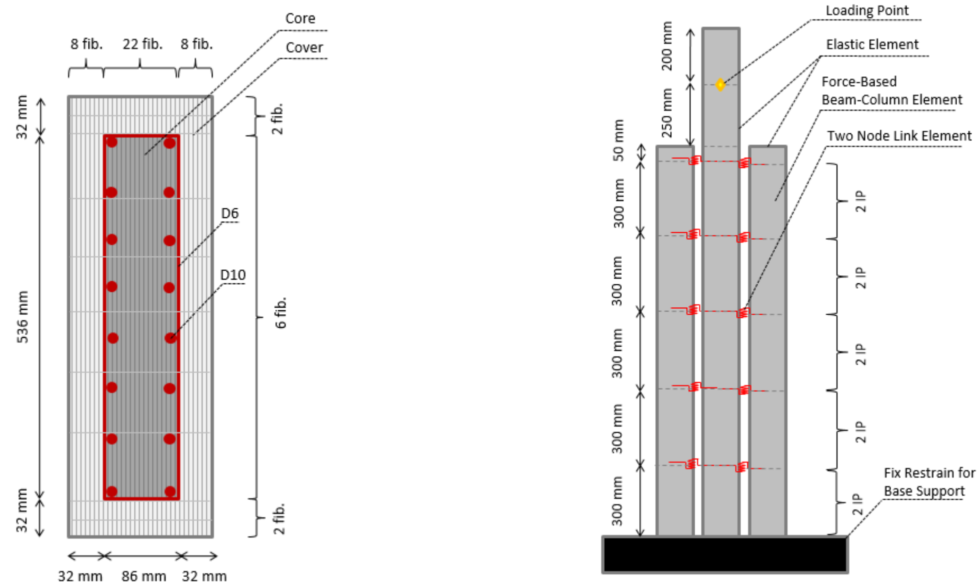

(A) (B)

FIGURE 2.8: The numerical model: (A) RC column cross section and (B) the structural idealization of the whole model.

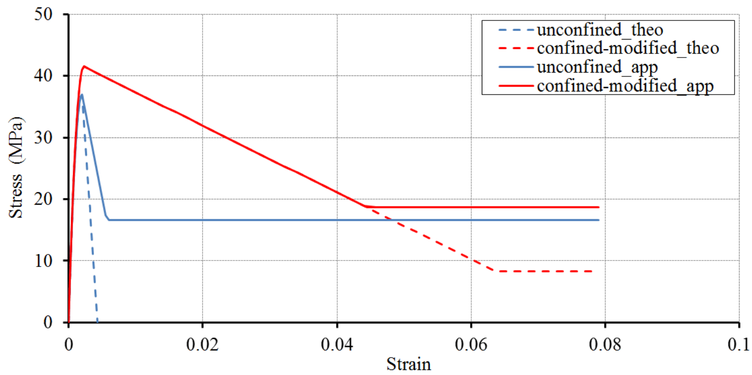

FIGURE 2.9: The constitutive model of concrete material in the numerical model.

TABLE 2.3: Input parameters of the longitudinal reinforcing steel.

f_y(MPa)	E(MPa)	b	R_0	cR_1	cR_2
345	200000	0.04	19.50	0.925	0.50

TABLE 2.4: Input parameters of the friction damper with the T10 confinement force configuration.

Conf. force (KN)	f_y(MPa)	E(MPa)	b
100.0	50.0	2000.0	1.0e-8
75.0	37.5	1500.0	1.0e-8
50.0	25.0	1000.0	1.0e-8
25.0	12.5	500.0	1.0e-8
0.0	0.0	0.0	0.0

Based on the multi-simulation analysis, the concrete had a peak stress (σ_0) of 37.00 MPa at 0.002 strain and the ultimate stress of $0.45\sigma_{c0}$ at 0.00562 strain. With the confinement effect of the transversal reinforcement, the core concrete had peak stress (σ_{cc}) of 41.50 MPa at 0.00224 strain and the ultimate stress of ($0.45\sigma_{cc}$) at 0.0446 ultimate strain, as shown in Figure 2.9. The concrete tensile strength was assumed to be zero.

2.5.3 Steel material parameters

The smoothed bi-linear material (Steel02) constitutive model based on the Giuffre-Menegotto-Pinto theory [8] was used for the reinforcing steel material. The input parameters were the yield strength f_y, the elastic modulus E, the hardening ratio b, and the parameters controlling the transition between elastic and plastic branches were R_0, c_{R1}, and c_{R2}. The material parameters were chosen based on the recommendations of reference [6] as shown in Table 2.3.

2.5.4 Friction damper parameters

The friction dampers were modeled with a bi-linear material model in which the elastic state represents the stick stage, and the post-yield state represents the slip stage. The bi-linear material was used to model the uniaxial bi-linear steel material with kinematic hardening and optional isotropic hardening based on the Finite Elements for Design, Evaluation, and Analysis of Structures (FEDEAS) [2]. The perfect plastic consideration is chosen in the reason after several time lateral deformation the friction force will be constant.

The friction coefficient was assumed to be 0.5 with a hardening ratio near zero and the slip deformation was 0.025 mm. The friction damper parameters were determined from numerical trials. Based on this analysis, the friction coefficient and the slip deformation were the key parameters that determined the column stiffness. The input parameters of the friction dampers with Steel01 material for case T10 are shown in Table 2.4.

2.5.5 Numerical analysis

The numerical analysis were adjusted to match the experimental setup. An equivalent gravity load, the structure self-weight, and the axial force of the pretension bar were included in the model. The structure self-weight was idealized as a point load with a density of 25 KN/m^3 at every node. The axial load of the pretension bar simulated the dead load of the superstructure, and was idealized as a compressive point load of 1.00 MPa at the top of each column component. The cyclic load was idealized as a cyclic displacement load at the node located 1.80 m from the bottom as shown in Figure 2.8.

Two load stages were implemented. First was the equivalent gravity load in the form of a constant nodal load pattern and the second was the cyclic load in the form of a linear nodal displacement pattern. The equivalent gravity load implemented the load control integrator fwith the Newton algorithm, and the cyclic load implemented the displacement control integrator with the Newton algorithm [6]. The equivalent gravity load was given directly without increment while the cyclic load used 0.10 mm displacement increments.

The experimental scenarios that are shown in Table 2.2 were numerically simulated. The U10, T10, and T20 patterns had 1 mm increments of cyclic loading in each loop, while the T20-3 and T40 patterns had gradually changing increments. The U10-2 and T20-2 patterns had only one loop of cyclic loading.

2.6 Numerical calibration results

The numerical analysis results reveal the hysteresis loops of the structure under cyclic loading, the curvature distribution of each column, the force and displacement relationship of the friction dampers, and the optimum energy dissipation of the structure.

2.6.1 Hysteresis loops of the structure

The hysteresis loop comparisons in the elastic condition are shown in Figures (2.10–2.13). The condition of the structure in which remains elastic behavior can be observed from the monitoring of the maximum stress-strain response of the reinforcing steel of the columns section, as shown in Figure 2.14. It can be seen that the numerical and experimental results have similar separated stiffness (K_s), unloading stiffness, and peak force at each loading cycle. However, the monolith stiffness (Km) at the initial loading and reloading is higher in the numerical model. Differences in the monolith stiffness probably occurred because the numerical model implements bi-linear material with perfect plastic behavior which has equal yield strength in the both small deformation and large deformation. While the real condition of the hysteresis loop of FD behave isotropic hardening in the small deformation and kinematic hardening in the large deformation.

The post-yield state was reached in cases T20-3 and T40, and the numerical and experimental results have similar separated stiffness (K_s) and unloading stiffness. The numerical results

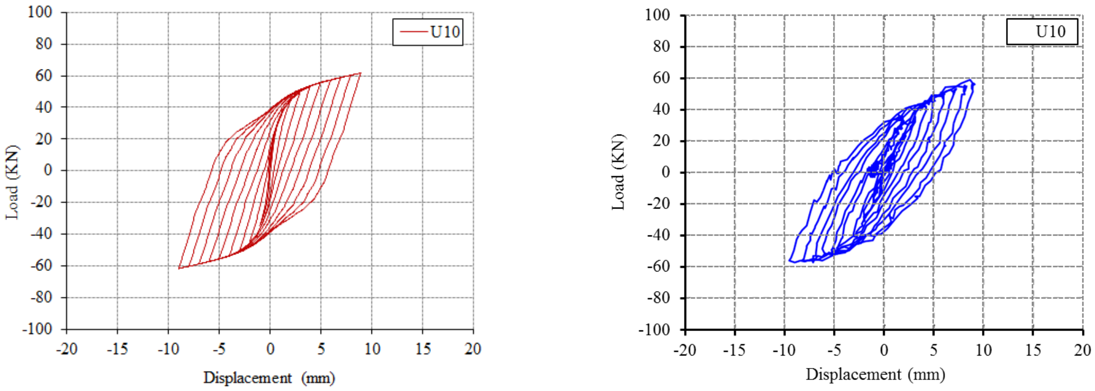

(A) (B)

FIGURE 2.10: Comparison of the U10 hysteresis loops: (A) numerical result and (B) experimental result [10].

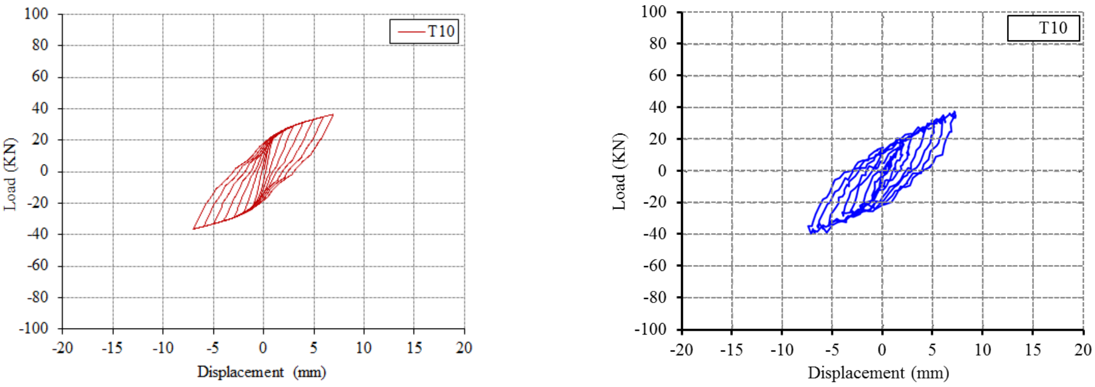

(A) (B)

FIGURE 2.11: Comparison of the T10 hysteresis loops: (A) numerical result and (B) experimental result [10].

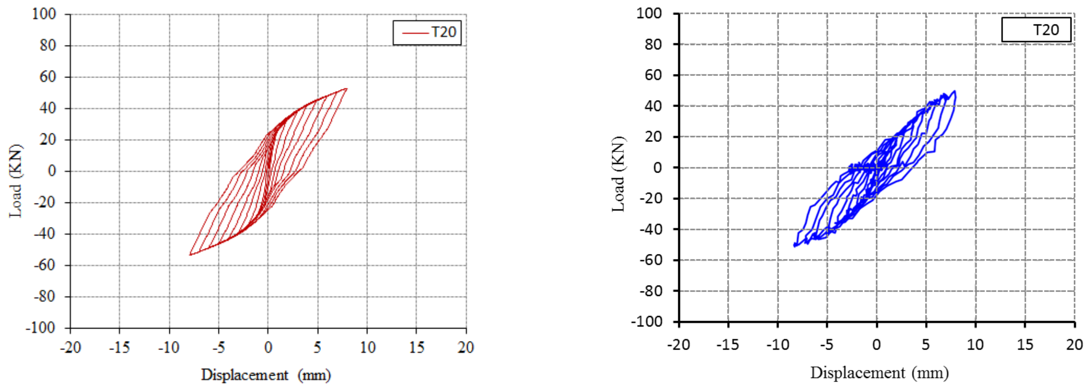

(A) (B)

FIGURE 2.12: Comparison of the T20 hysteresis loops: (A) numerical result and (B) experimental result [10].

for both T20-3 and T40 show larger loading and reloading stiffness values than the experimental results are shown in Figures (2.15 and 2.16). This is probably because the large deformation and the high non-linearity of the whole structure meant the interaction of the friction dampers

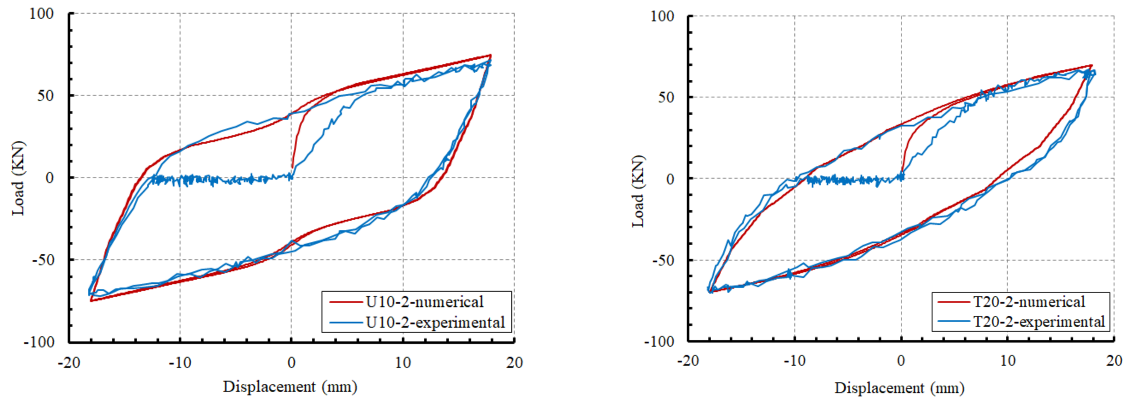

(A) (B)

FIGURE 2.13: Comparison of the numerical and experimental hysteresis loops: (A) U10-2 and (B) T20-2.

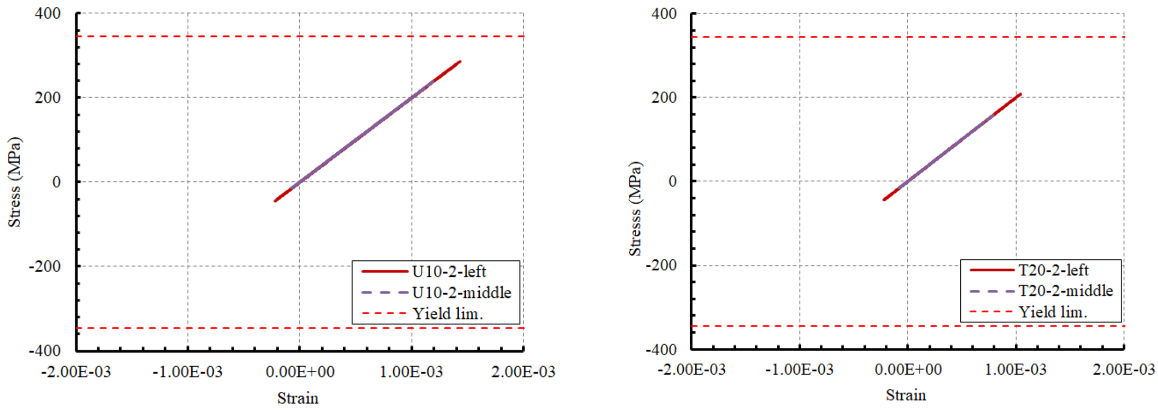

(A) (B)

FIGURE 2.14: The maximum strain and stress of the column sections: (A) uniform pattern (U10-2) and (B) triangular pattern (T20-2).

and columns was not considered in the numerical model, which utilized only beam and link elements.

2.6.2 Curvature distributions

The sectional curvature that was monitored in each of the columns at the maximum displacement for scenarios U10-2 and T20-2 shows that the numerical and experimental results had the same curvature distribution pattern. However, the numerical results had adjacent curvature values in each column instead of the experimental results, as shown in Figures (2.17 and 2.18). The curvature differences probably arose from the interaction of the friction dampers pate and the columns, which influenced the column stiffness, and was not considered in the numerical model. In in Figures (2.17 and 2.18).

The maximum sectional curvature of scenario U10-2 occurred at the bottom of the column

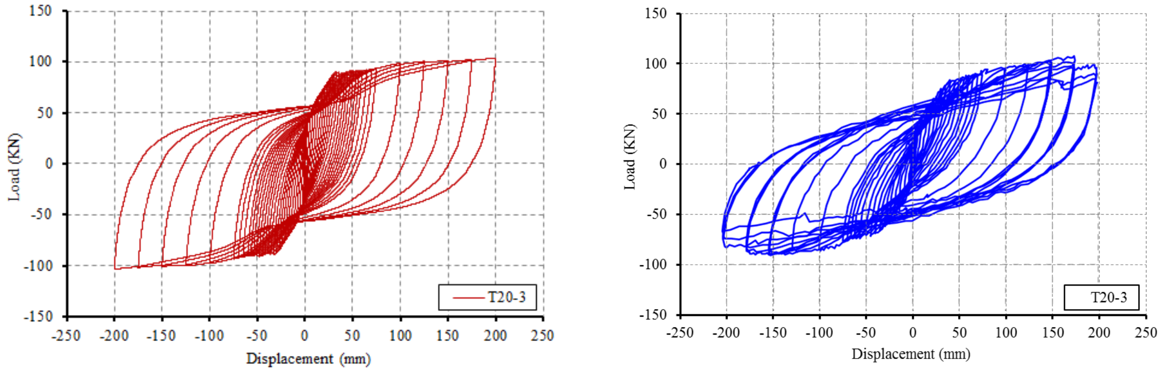

(A) (B)

FIGURE 2.15: Comparison of the T20-3 hysteresis loops: (A) numerical result and (B) experimental result [10].

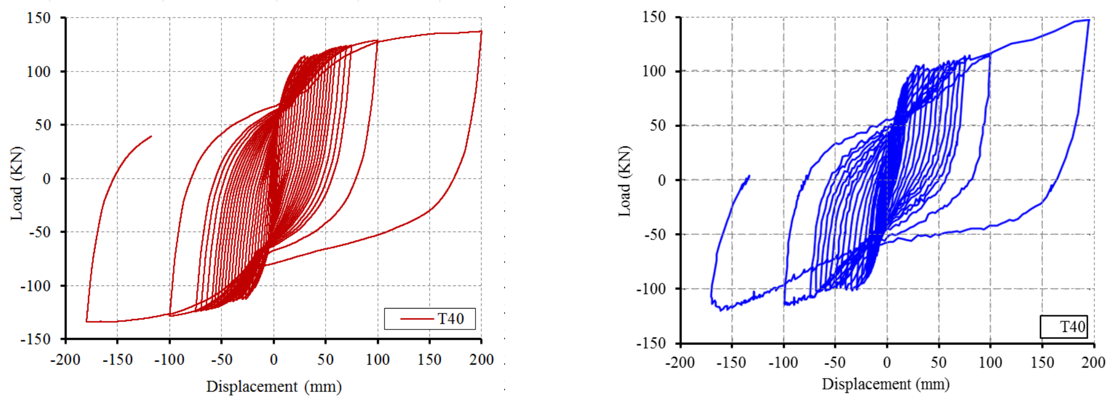

(A) (B)

FIGURE 2.16: Comparison of the T20 hysteresis loops: (A) numerical result and (B) experimental result [10].

(triangular curvature distribution), while in scenario T20-2 it occurred at the middle of the column (parabolic curvature distribution). Scenario U10-2 had uniform stiffness distribution so that its weakest point is the bottom region. However, scenario T20-2 had a triangular stiffness distribution with the largest stiffness in the bottom region and the smallest stiffness in the top region. The global bending moment distribution of an external load for this type of cantilever structure is triangular. In this situation, the middle region is the weakest point for resisting the lateral load, and a parabolic curvature distribution is generated. Theoretically, the optimum elastic deformation capacity will be achieved if the column curvature distribution is uniform. Uniform curvature distribution can be realized in the simply-supported beam with two couple bending moments with single curvature in each beam end. In the case of the RC integrated RC columns connected by FD, the elastic deformation capacity can be increased by varying the confinement force distribution to achieve a nearly uniform curvature distribution.

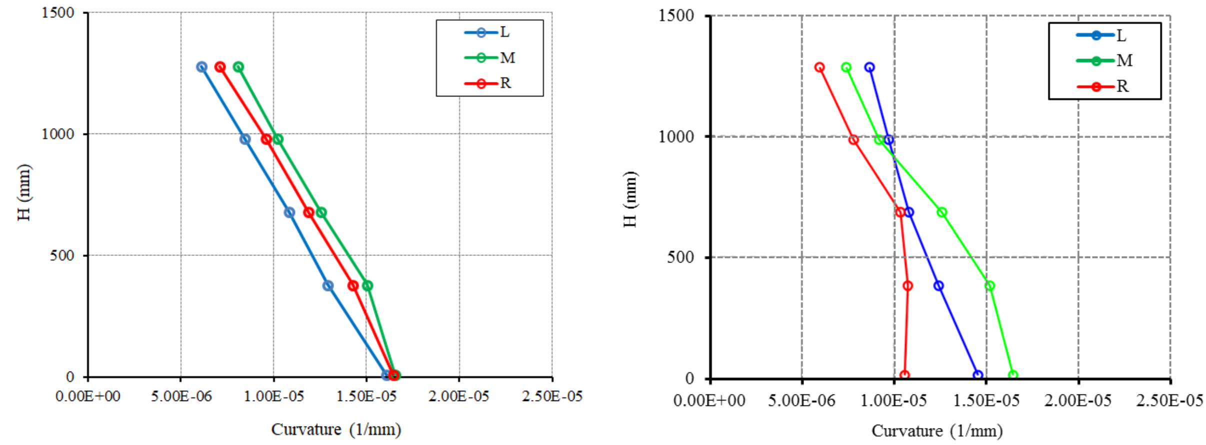

(A) (B)

FIGURE 2.17: Comparison of the U10-2 curvature distributions: (A) numerical result and (B) experimental result [10]. H: Height; L: left-side column; M: middle-side column; R: right-side column.

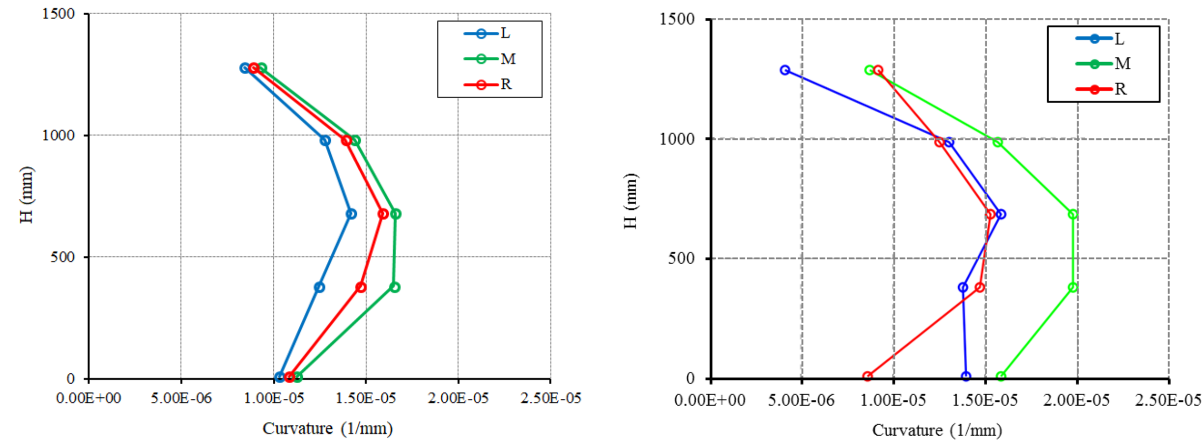

(A) (B)

FIGURE 2.18: Comparison of the T20-2 curvature distributions: (A) numerical result and (B) experimental result [10]. H: Height; L: left-side column; M: middle-side column; R: right-side column.

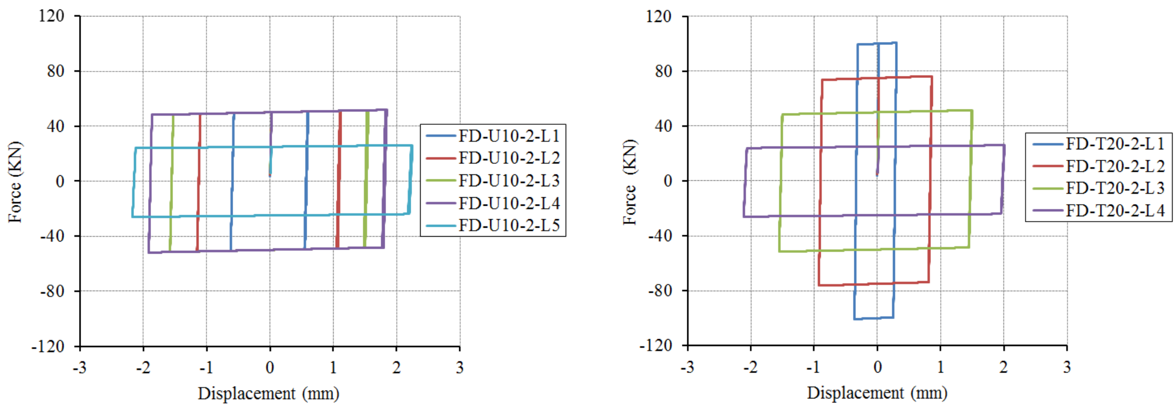

(A) (B)

FIGURE 2.19: Comparison of the T20 hysteresis loops: (A) numerical result and (B) experimental result [10]. FD-U10-2-L1: friction device number 1 on the left-side of the U10-2 confinement force pattern; FD-T20-2-L1: friction device number 1 on the left-side of the T20-2 confinement force pattern.

2.6.3 Friction damper force and displacement characteristics

The force and displacement of the friction dampers were monitored to determine how each friction damper works under different confinement force distributions. Comparisons between scenarios U10-2 and T20-2 were made. Monitoring was applied with full cyclic loading to quantify the maximum sliding displacement and friction resistance of each friction damper. Based on Figure 2.19, friction dampers 1 and 2 in scenario U10-2 had larger slip displacement than in scenario T20-2, and friction dampers 4 and 5 in scenario U10-2 had smaller sliding displacements than in scenario T20-2. The column with the uniform confinement distribution had smaller displacement variations of the friction damper along the column height than the column with the triangular confinement distribution. It can be concluded that the uniform confinement distribution generated sharper transitional stiffness than the triangular confinement distribution, which corresponds to the characteristics of the hysteresis loops that were discussed previously.

2.7 Dissipated energy optimization

2.7.1 Optimization method

After the parameters used in the numerical analysis were verified, the energy dissipation was optimized. There are two methods that were used to find the optimum energy dissipation. The first is a regular determined pattern and the second is an arbitrary pattern. In the numerical analysis, three cyclic loading steps with displacement load control were performed to measure the energy dissipation in each hysteresis loop. All steps were implemented in the elastic limit of the RC column structure. The energy dissipation of each hysteresis loop was calculated with a rectangular segmental numerical integration method. While the elastic behavior was confirmed upon the reinforcing steel strain remained under the yield strain. Furthermore, he energy dissipation was calculated from the second step until the third step, which is the shaded area shown in Figure 2.20.

2.7.2 Regular determined confinement force pattern (first method)

The first method defined 22 regular confinement force distribution patterns of the friction dampers are shown in Figures (2.21A–2.21E). Each confinement force was varied incrementally 40 times, producing 880 total variations of the confinement force pattern. As the results, the

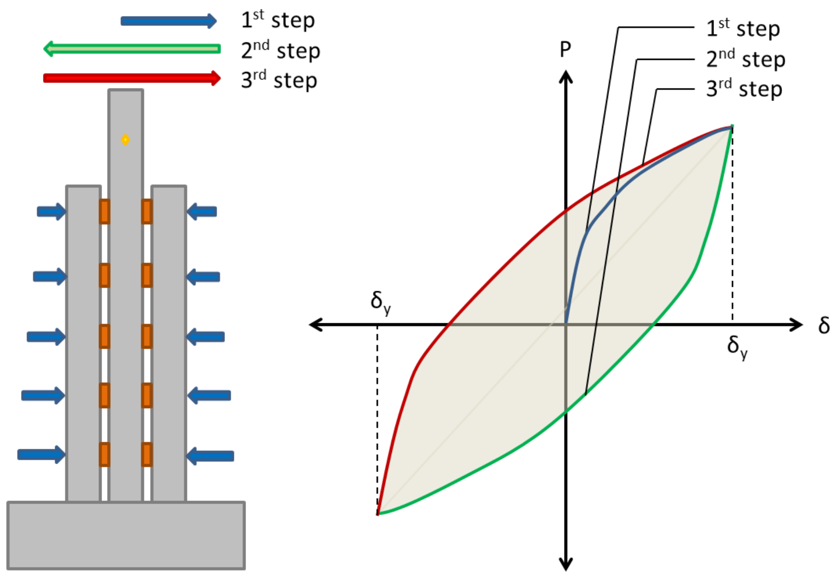

FIGURE 2.20: The dissipated energy calculation method of the integrated RC columns connected by FD.

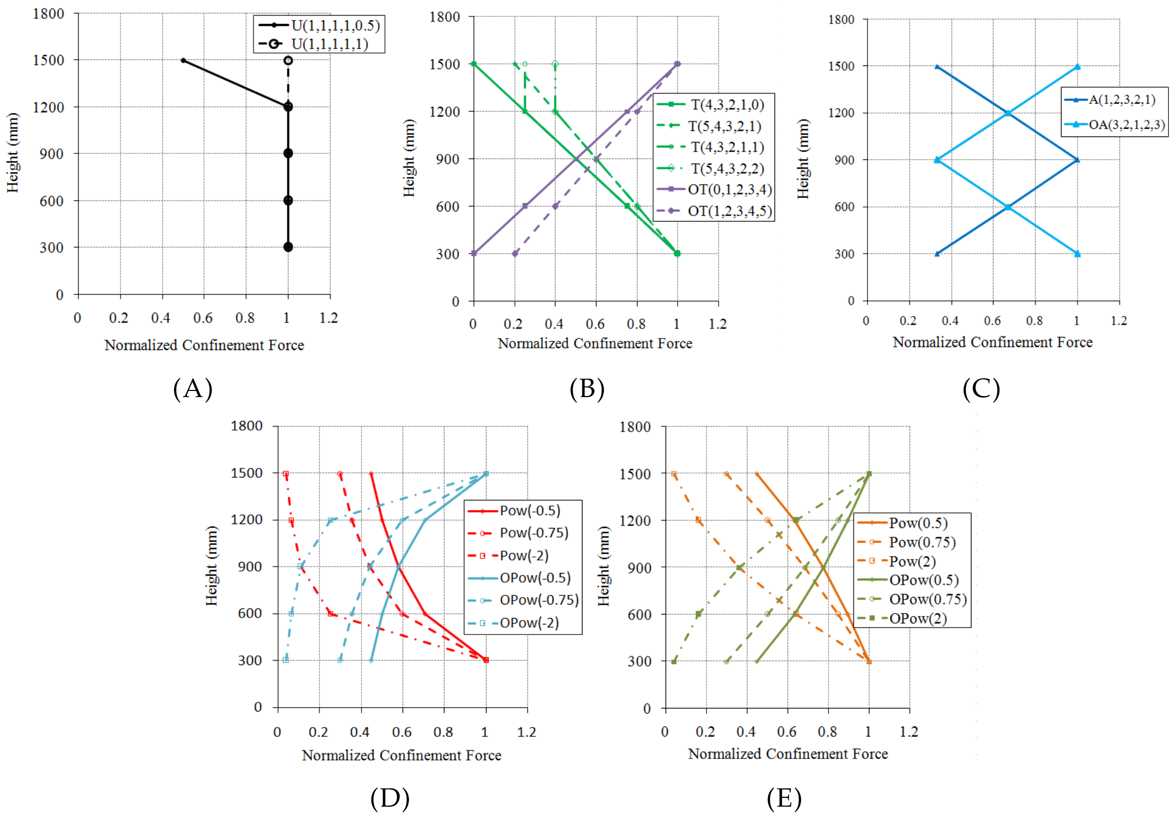

FIGURE 2.21: The friction damper confinement force pattern for finding the optimum energy dissipation: (A) uniform pattern, (B) triangular pattern, (C) arrow pattern, (D) power negative pattern, and (E) power positive pattern.

largest optimum energy dissipation in the elastic range was the triangular T(5,4,3,2,1)-230KN pattern with the energy dissipation value of 4.32 KJ or equal to 0.28 of the damping ratio, which was about 36% larger than for U(2,2,2,2,1)-100KN. At the optimum point, the maximum

TABLE 2.5: The structural behavior parameters related to the confinement force pattern in the elastic displacement limit of the first dissipated energy optimization method.

No	Conf. pattern	Max. conf. force (KN)	Displacement (mm)	Force (KN)	Dissip. enrg. (KJ)	Equal damping ratio (ζ)
1	T(5,4,3,2,1)-230KN	230.00	24.80	96.31	4.32	0.28
2	T(5,4,3,2,2)-210KN	210.00	23.50	95.33	4.30	0.30
3	Pow(-0.5)-210KN	210.00	22.50	95.85	4.29	0.31
4	T(4,3,2,1,1)-260KN	260.00	24.30	98.43	4.28	0.27
5	Pow(-0.75)-280KN	280.00	22.90	99.08	4.25	0.29
6	Pow(0.75)-210KN	210.00	22.80	96.84	4.23	0.30
7	Pow(0.5)-180KN	180.00	21.50	95.43	4.12	0.31
8	OA(3,2,1,2,3)-180KN	180.00	19.40	94.90	3.94	0.34
9	U(1,1,1,1,0.5)-150KN	150.00	19.60	95.48	3.86	0.32
10	U(1,1,1,1,1)-130KN	130.00	18.30	93.98	3.72	0.34
11	T(4,3,2,1,0)-250KN	250.00	25.40	87.37	3.39	0.23
12	A(1,2,3,2,1)-190KN	190.00	18.30	88.10	3.27	0.32
13	U(1,1,1,1,0.5)-100KN	100.00	22.10	78.96	3.19	0.29
14	OPow(-0.5)-170KN	170.00	16.70	86.91	3.10	0.34
15	OPow(0.5)-140KN	140.00	17.10	84.95	3.10	0.34
16	T(4,3,2,1,0)-200KN	200.00	26.30	79.89	3.06	0.22
17	Pow(2)-290KN	290.00	23.70	84.47	2.88	0.22
18	OPow(0.75)-160KN	160.00	15.60	85.59	2.83	0.33
19	OPow(-0.75)-190KN	190.00	15.90	83.90	2.80	0.33
20	OT(1,2,3,4,5)-150KN	150.00	16.30	79.21	2.66	0.33
21	OT(0,1,2,3,4)-150KN	150.00	15.80	73.18	2.26	0.31
22	OPow(2)-170KN	170.00	15.70	73.22	2.21	0.30
23	OPow(-2)-230KN	230.00	15.90	70.19	2.00	0.28
24	Pow(-2)-250KN	250.00	21.60	59.48	1.33	0.16

T(5,4,3,2,1)-230KN: triangular of the regular determined pattern with the confinement force configuration $P_{FD1} = 5/5\ x\ 230\ KN, P_{FD2} = 4/5\ x\ 230\ KN, P_{FD3} = 3/5\ x\ 230\ KN, P_{FD4} = 2/5\ x\ 230\ KN$, and $P_{FD5} = 1/5\ x\ 230\ KN$.

confinement force was 230 KN and the elastic deformation capacity was 24.80 mm (1.4% of drift ratio). It is observed in Table 2.5 that the eight confinement force patterns that produced the largest energy dissipation have a decreasing confinement force pattern from friction damper 1 to 4, while the eight confinement force patterns that achieved the smallest energy dissipation have an increasing confinement force pattern from friction damper 1 to 5.

The confinement force increment for pattern U(1,1,1,1,0.5) generated elastic deformation capacity decrease in general, while the resisting force rose smoothly until some point and continued with almost a constant value, as shown in Figure 2.22A. The energy dissipation had a similar trend with the parabolic curve that had an extreme point. The maximum energy dissipation was observed at a confinement force of 150 KN, above which the elastic displacement

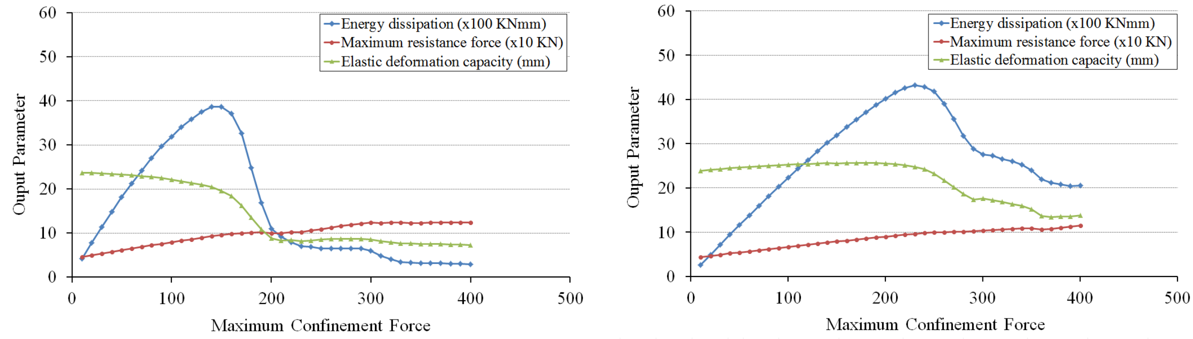

(A) (B)

FIGURE 2.22: Output parameters at each confinement force increments: (A) uniform pattern and (B) triangular pattern.

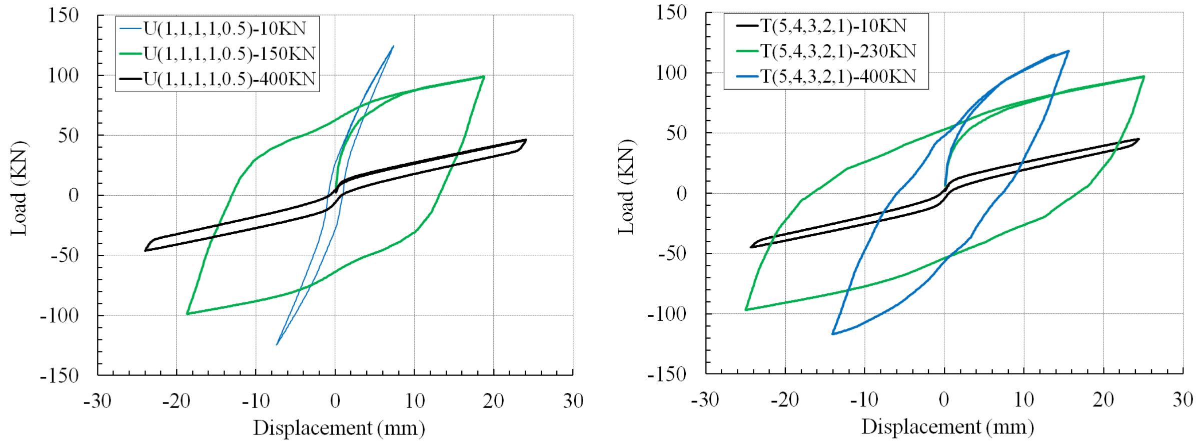

(A) (B)

FIGURE 2.23: Hysteresis loops for each confinement force increment: (A) uniform pattern and (B) triangular pattern.

capacity decreased sharply. The hysteresis loops of pattern U(1,1,1,1,0.5) for the smallest confinement force, the optimum dissipated energy, and the largest confinement force are shown in Figure 2.23A.

The confinement force increment for pattern T(5,4,3,2,1) generated a smooth elastic deformation capacity increase until a maximum point and decreased with a sharper gradient, while the resisting force increased smoothly, as shown in Figure 2.22B. The energy dissipation trend had a similar trend with the parabolic curve that had an extreme point. The largest energy dissipation was achieved at a confinement force of 230 KN, when the elastic displacement capacity was also starting to decrease sharply. The hysteresis loop of pattern T(5,4,3,2,1) for the smallest confinement force, the optimum dissipated energy, and the largest confinement force are shown in Figure 2.23B.

The elastic deformation capacity and peak resisting force as a function of the confinement

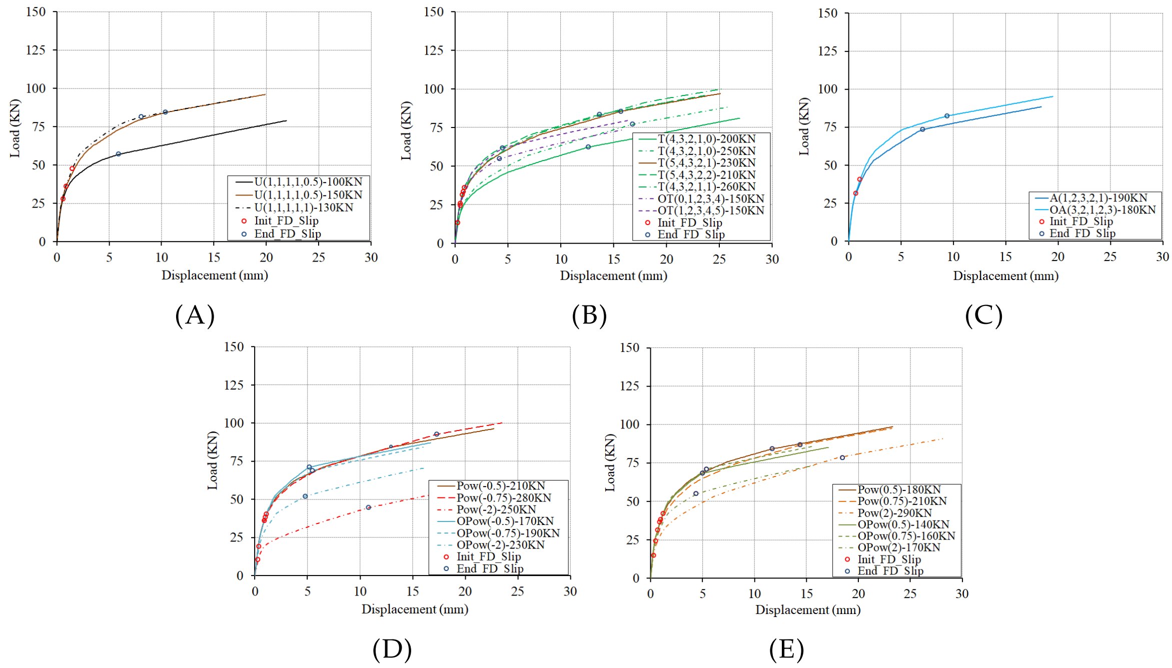

FIGURE 2.24: Force and deformation curves showing the slip state of the friction dampers related the confinement force pattern: (A) uniform pattern, (B) triangular pattern, (C) arrow pattern, (D) power negative pattern, and (E) power positive pattern.

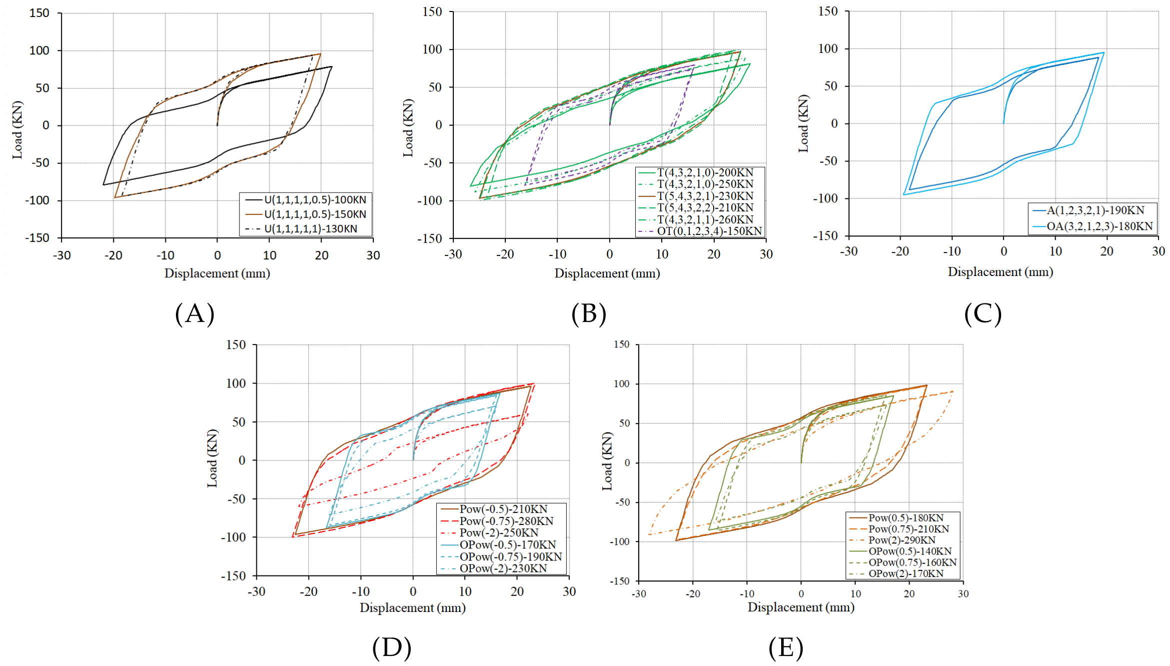

FIGURE 2.25: Hysteresis loops shape related the confinement force pattern: (A) uniform pattern, (B) triangular pattern, (C) arrow pattern, (D) power negative pattern, and (E) power positive pattern.

force are shown in Table 2.5. The data are sorted based on the magnitude of the energy dissipation. The force-deformation curves are shown in Figure 2.24, with the first-last sliding deformation of the friction damper indicating transitional stiffness (K_t) denoted by a blue dot.

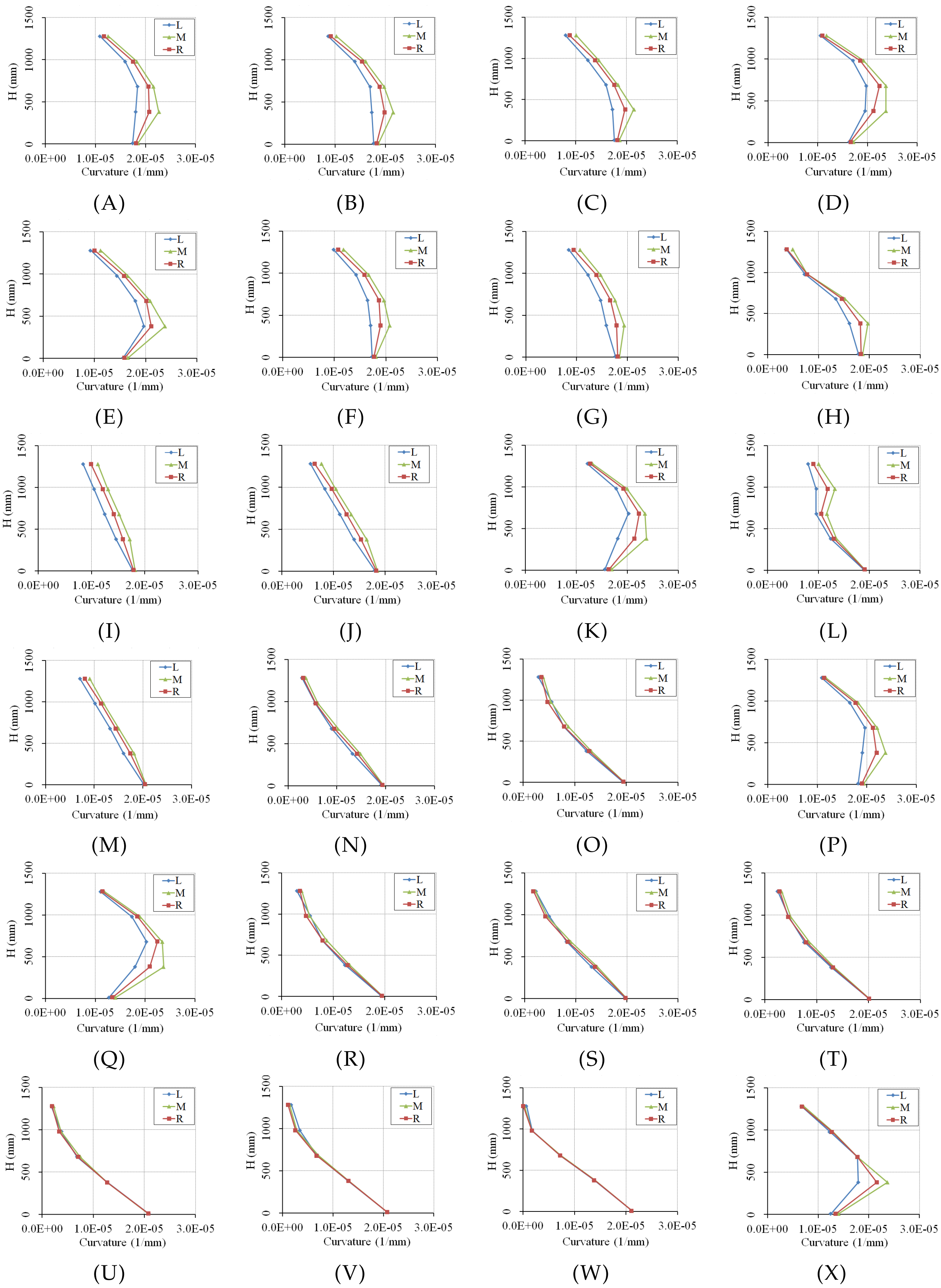

FIGURE 2.26: Curvature distributions with regular determined confinement force pattern: (A) T(5,4,3,2,1)-230KN, (B) T(5,4,3,2,2)-210KN, (C) Pow(-0.5)-210KN, (D) T(4,3,2,1,1)-260KN, (E) Pow(-0.75)-280KN, (F) Pow(0.75)-210KN, (G) Pow(0.5)-180KN, (H) OA(3,2,1,2,3)-180KN, (I) U(1,1,1,1,0.5)-150KN, (J) U(1,1,1,1,1)-130KN, (K) T(4,3,2,1,0)-250KN, (L) A(1,2,3,2,1)-190KN, (M) U(1,1,1,1,0.5)-100KN, (N) OPow(-0.5)-170KN, (O) OPow(0.5)-140KN, (P) T(4,3,2,1,0)-200KN, (Q) Pow(2)-290KN, (R) OPow(0.75)-160KN, (S) OPow(-0.75)-190KN, (T) OT(5,4,3,2,1)-150KN, (U) OT(0,1,2,3,4)-150KN, (V) OPow(2)-170KN, (W) OPow(-2)-230KN, and (X) Pow(-2)-250KN.

Patterns T(5,4,3,2,1)-230KN had relatively large value in therms of the resisting force, the elastic deformation capacity, and the last sliding displacement of the friction damper among the other proposed confinement force patterns. Patterns such as T(5,4,3,2,2)-210KN, Pow(-0.5)-210KN, and T(4,3,2,1,1)-260KN, which also produced relatively large energy dissipation, have similar conditions.

The optimizing confinement force from the experimental patterns increased the resisting force in the separated stiffness (K_s), increased the sliding deformation state, which impacts the transition stiffness (K_t) state, and decreased the elastic deformation capacity. However, the monolith stiffness (K_m) and separated stiffness (K_s) showed almost no differences. This statement is supported by Figures (2.24A and 2.24B), which show the transformations of the force-deformation shapes from the original confinement pattern of the experiments, which are U(1,1,1,1,0.5)-100KN and T(4,3,2,1,0.0)-200KN to U(1,1,1,1,0.5)-150KN and T(4,3,2,1,0.0)-270KN.

Other patterns proposed to achieve the optimum energy dissipation in the elastic deformation capacity from the original experimental pattern include U(1,1,1, 1,1)-130KN, T(5,4,3,2,1)-230KN, T(4,3,2,1,0.4)-210KN, T(4,3,2,1,0.25)-260KN, OT(1,2,3,4,0)-150KN, and OT (1,2,3,4,5)-150KN. The U(1,1,1,1,1)-130KN pattern had similar characteristics with the U(1,1,1,1,0.5)-150KN pattern, but it had a smaller elastic deformation capacity and a larger sliding deformation state. For the power confinement force pattern, the Pow(-0.75)-280KN pattern provided the largest resisting force, while the OT(4,3,2,1)-150KN and OT(1,2,3,4,5)-150KN patterns had smaller sliding deformation state and elastic deformation capacity than the original triangular pattern.

The confinement force pattern produced various hysteresis loop shapes. The large value of the last sliding displacement of the confinement force pattern as mentioned in section (4) produced gradual transition stiffness (K_t) and large elastic deformation capacity in the triangular pattern, and power pattern. The reverse condition occurred in the uniform pattern, opposite triangular pattern, arrow pattern, and opposite power pattern. This statement is clarified with Figure 2.25.

The confinement force pattern of the friction damper also produced various curvature distributions in the structure. The linear gradient of the curvature distribution patterns occurred on the uniform confinement force distribution patterns, as shown in Figures (2.26I, 2.26J, and 2.26M). The arch shape of the curvature distribution was observed on the triangular pattern, and power pattern, as shown in Figures (2.26A, 2.26B, 2.26C, 2.26D, 2.26E, 2.26F, 2.26G, 2.26H, 2.26K, 2.26P, 2.26Q, and 2.26X), and from the grand optimum pattern as shown in Figure 2.27C.

TABLE 2.6: The confinement force variable of the arbitrary pattern optimization method.

FD no.	Confinement force range (KN)
1	140-280 incr. 20
2	140-240 incr. 20
3	100-240 incr. 20
4	60-160 incr. 20
5	20-120 incr. 20

TABLE 2.7: The structural behavior parameter related to the confinement force pattern in the elastic displacement limit of the second dissipated energy optimization method.

No	Conf. pattern	Max. conf. force (KN)	Displacement (mm)	Force (KN)	Dissip. enrg. (KJ)	Equal damping ratio (ζ)
1	GO(12,7,7,3,6)-240KN	240.00	23.20	97.28	4.45	0.31

GO(12,7,7,3,6)-240KN: grand optimum of the arbitrary pattern with the confinement force configuration $P_{FD1} = 12/12\ x\ 240\ KN, P_{FD2} = 7/12\ x\ 240\ KN, P_{FD3} = 7/12\ x\ 240\ KN, P_{FD4} = 3/12\ x\ 240\ KN$, and $P_{FD5} = 6/12\ x\ 240\ KN$.

The opposite arch shape of the curvature distribution is formed by the opposite triangular pattern and opposite power pattern, as shown in Figures (2.26N, 2.26O, 2.26R, 2.26S, 2.26T, 2.26U, 2.26V, and 2.26W). Other curvature distributions that formed were the S-shape from the opposite arrow confinement force distribution pattern and opposite S-shape from the arrow confinement force pattern, as shown in Figures (2.26H and 2.26L). The various curvature distributions formed because the column regions that were relatively weak produced larger curvatures than the other column regions.

2.7.3 Arbitrary pattern (second method)

The second method, which is named the arbitrary pattern, determined the confinement force range in each friction damper in increments of 20 KN, as shown in Table 2.6, producing 13,824 total variations of the confinement force pattern. As the results mentioned in Table 2.7, the grand optimum (GO) of the arbitrary confinement force pattern optimization method generated the largest overall optimum energy dissipation, which was 40% larger than for U(1,1,1,1,0.5)-100KN. Also, its energy dissipation was 4.95 KJ or equal to 0.31 of the damping ratio, and its elastic deformation capacity was 23.20 mm (about 1.3% of drift ratio). In this best optimum result, the confinement force pattern is (12,7,7,3,6) with the maximum confinement force is 240 KN, as shown in Figure 2.27A.

Generally, the largest dissipated energy achievement of GO(12,7,7,3,6)-240KN in case of relatively large resisting force, elastic deformation capacity, and the last sliding displacement

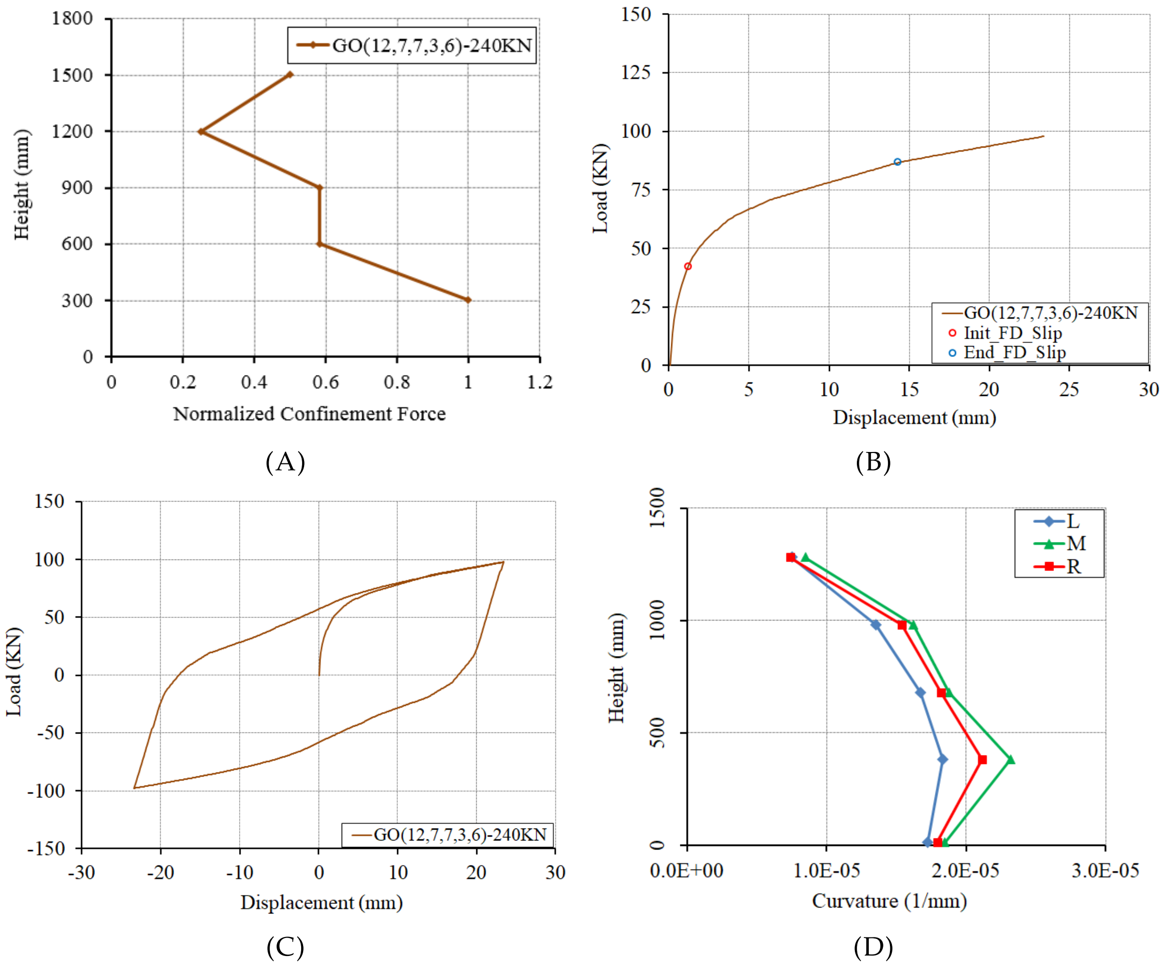

FIGURE 2.27: Output parameter of the structure with grand optimum confinement force pattern (GO(12,7,7,3,6)-240KN): (A) optimum confinement force, (B) skeleton curve, (C) hysteresis loop, and (D) curvature distribution.

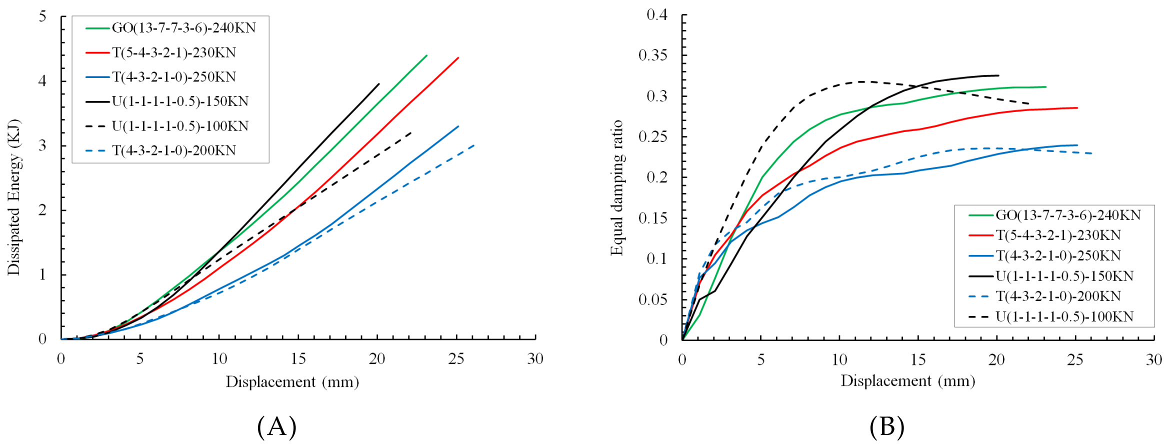

FIGURE 2.28: Dissipated energy properties related structural displacement: (A) dissipated energy and (B) equal damping ratio.

(transitional stiffness) of the friction damper among the other proposed confinement force patterns, as shown in Figure 2.27B. Compared to the T(5,4,3,2,1)-230KN pattern, the GO(12,7,7,3,6)-240KN pattern has equal tendency of the confinement force distribution in the term of the friction device number 1 up to number 4. While, it is found that the using larger confinement force in the friction device number 5 of GO(12,7,7,3,6)-240KN pattern resulted larger resisting force rate and slightly smaller elastic deformation capacity than T(5,4,3,2,1)-230KN pattern, as shown in Figure 2.27C. So that the different confinement force treatment of the most free location from the constraint point of friction device (FD number 5) results significant different energy dissipation achievement. Because based on the friction deformation device monitoring in Figure 2.11, it has the most sensitive sliding deformation. Furthermore, the curvature distribution of the GO(12,7,7,3,6)-240KN pattern is parabolic pattern which near the same with the triangular confinement force pattern, as shown in Figure 2.27D.

2.7.4 The relation of deformation to the dissipated energy and the structural damping

Based on the observation of the Figure 2.28A, the dissipated energy achievement progress increase more rapidly as the deformation increment. The optimized uniform pattern confinement force distribution which implements U(1,1,1,1,0.5)-150KN has larger dissipated energy rate than the grand optimum and the optimized triangular pattern which are underneath, respectively. However, due to the larger elastic deformation capacity, the GO(12,7,7,3,6)-240KN and T(5,4,3,2,1)-230KN patterns have larger energy dissipation than the U(1,1,1,1,0.5)-150KN pattern in the elastic deformation limit state. These phenomena correspond the hysteresis loop shape of each structure which mentioned before. Furthermore, the damping ratio trend increases drastically in the small deformation (less than 0.5% of drift), small alteration around the yield state, as shown in Figure 2.28B.

2.8 Conclusions

After determining the appropriate constitutive material parameters of the friction damper, concrete, and reinforcing steel, a fiber section of beam element model was successfully used to simulate experiments of RC columns connected by the FD under cyclic loading. As the results, comparisons between numerical and experimental hysteresis loops and curvature distributions showed satisfactory outcomes. Finally, dissipated energy optimization was conducted successfully to improve energy dissipation of the existing structural confinement force configuration. Some important notes are explained below:

(a) The proper friction coefficient and sliding displacement of the friction damper were the most important factors. In the elastic perfect plastic idealization, the appropriate of friction coefficient and the sliding displacement of the friction damper were 0.5 and 0.025 mm, respectively.

(b) Force and displacement monitoring were useful for elucidating the role the confinement distribution had in the slip distribution of each friction damper. The uniform confinement force pattern generated sharper transitional stiffness than the triangular confinement distribution, which fit the characteristics of the measured hysteresis loops.

(c) The energy dissipation of the RC integrated RC columns connected by FD was optimized with two methods. The first applied regular confinement force patterns on the friction dampers with incremental confinement forces, and the second prescribed the confinement force increment in each friction damper with a specific pre-determined range. The optimum pattern of the first method was the T(5,4,3,2,1)-230KN pattern, which produced energy dissipation 36% larger than the uniform pattern of U(1,1,1,1,0.5)-100KN from the experimental set. While the overall optimum pattern was the GO(12,7,7,3,6)-240KN of the arbitrary pattern (second method), with 40% larger energy dissipation of the U(1,1,1,1,0.5)-100KN pattern.

(d) The increment of confinement force in each pattern affected the elastic deformation capacity, resisting force, and the last sliding deformation state of the friction damper, which impacted the transition stiffness (K_t) transformation. Nevertheless, the monolith stiffness and the separated stiffness were not sensitive with the increment of the confinement force. The larger the elastic deformation capacity and resisting force of the structure, the more the energy dissipation was enriched.

(e) The confinement force pattern of the friction dampers influenced the hysteresis loop shape and curvature distribution of the structure. The hysteresis loop shape was dominated primarily by the transition stiffness (K_t) and secondarily by the elastic deformation capacity and resisting force capacity.

(f) The various confinement force distribution patterns generated various curvature distributions along the column height. Larger curvatures were produced in column regions that were relatively weak.

(g) By implementing the best optimum of dissipated energy, the 25% or larger of damping ratio can be achieved around the elastic deformation state of the structure. The elastic deformation capacity of the structure is around the 1.3 to 1.4% of drift ratio. With such kind of high damping capability in the sufficient elastic deformation capacity, the integrated triple RC columns connected by friction damper has a great potential to be developed for the high seismic performance bridge pier structure.

Bibliography

[1] Aavtar.S. Pall, C.M.: Optimum Seismic Resistance of Large Panel Structures Using Limited Slip Bolted Joints, in *Proceedings, 7th World Conference on Earthquake Engineering*, pages 177–184, World Conference on Earthquake Engineering, Istambul, 1980.

[2] F.C. Filippou: FEDEAS - Finite Elements for Design, Evaluation, and Analysis of Structures Theory, Reference Manual and Example, Technical report, Department of Civil Engineering, University of California, California, 1996.

[3] FEMA: *Prestandard and Commentary for the Seismic Rehabilitation of Buildings*, 1, Federal Emergency Management Agency, Washington, D.C., 2000.

[4] Hockett, C.F. and Chomsky, N.: The State of the Art, chapter 2, pages 23–48, 1968.

[5] Japan Road Association: *Specifications for Highway Bridges: Part V Seismic Design*, Maruzen Co. Ltd., Tokyo, 2012.

[6] Mazzoni, S., McKenna, F., Scott, M.H. and Fenves, G.L.: OpenSees Command Language Manual, 2007.

[7] Mckenna, F., Scott, M.H. and Fenves, G.L.: Nonlinear Finite-Element Analysis Software Architecture Using Object Composition, Journal of Computing in Civil Engineering, volume 24, no. 1:95–107, 2010.

[8] Menegotto, G., Pinto, M. and Emilio, P.: Method of Analysis for Cyclically Loaded R.C. Plane Frames Including Changes in Geometry and Non-Elastic Behavior of Elements under Combined Normal Force and Bending, in *Proceedings of IABSE Symposium on Resistance and Ultimate Deformability of Structures Acted on by Well Defined Loads*, pages 15–22, Zurich, 1973.

[9] Mualla, I. and Belev, B.: Performance of Steel Frames with a New Friction Damper Device under Earthquake Excitation, Engineering Structures, volume 24, no. 3:365–371, 2002.

[10] Nakamura, H., Takahashi, Y. and Sawada, S.: *The Elasto-Plastic Behavior of the Rectangular RC Column Accompanied with Friction Damping Mechanism with Complex Confinement*, Undergraduate thesis, Kyoto University, 2011.

[11] Nakamura, H., Takahashi, Y. and Sawada, S.: The Elasto-plastic Behavior of the Rectangular RC Column Accompanied with Friction Damping Mechanism, Journal of JSCE, volume 68, no. 4:577–583, 2012.

[12] Nakamura, H., Takahashi, Y. and Sawada, S.: *The Study on Earthquake Response Mechanism of Set RC Columns with Unity of Frictional Damping Mechanism*, Ph.D. thesis, Kyoto University, 2013.

[13] Neuenhofer, A. and Filippou, F.C.: Evaluation of Nonlinear Frame Finite-Element Models, Journal of Structural Engineering, volume 123, no. May:583–590, 1997.

[14] Pall, A.: *Limited Slip Bolted Joints : a Device to Control the Seismic Response of Large Panel Structures*, Doctoral thesis, Concordia University, 1979.

[15] Pall, A.S. and Marsh, C.: Response of Friction Damped Braced Frames, Journal of Structural Engineering, volume 108, no. June:1313–1323, 1982.

[16] Ramirez, J.D.M. and Tirca, L.: Numerical Simulation and Design of Friction- Damped Steel Frame Structures damped, in *15th World Conference in Earthquake Engineering*, Lisboa, 2012.

[17] Scott, B.D.: *Stress-Strain Relationships for Confined Concrete : Rectangular Sections*, Master thesis, University of Canterbury, 1980.

[18] Scott, M.H.: Numerical Integration Options for the Force-Based Beam-Column Element in OpenSees, 2011.

[19] Scott, M.H., Fenves, G.L., McKenna, F. and Filippou, F.C.: Software Patterns for Nonlinear Beam-Column Models, Journal of Structural Engineering, volume 134, no. 4:562–571, 2008.

[20] Setiawan, A.F., Takahashi, Y., Kiyono, J. and Sawada, S.: Numerical Analysis of RC Columns Accompanied with Friction Damping Mechanism under Cyclic Loading, in *Procedia Engineering*, volume 171, pages 821–835, Denpasar, 2017.

[21] Spacone, E., Filippou, F.C. and Taucer, F.F.: Fibre Beam-Column Model for Non-Linear Analysis of R/C Frames : Part II. Applications, Earthquake Engineering and Structural Dynamics, volume 25, no. January:727–742, 1996.

[22] Taucer, F.F. and Spacone, E.: Aa Fiber Beam-Column Element for Seismic Response Analysis of Reinforced Concrete Structures, Technical Report December 2014, Earthquake Engineering Research Center College of Engineering University of California, Berkeley, California, 1991.

[23] Yassin, M.H.M.: *Nonlinear analysis of prestressed concrete sructures under monotonic and cyclic loads*, University of California, Berkeley, 1994.

Chapter 3

A High Seismic Performance Concept of Integrated Bridge Pier with Triple RC Columns Connected by FDG

3.1 General Remarks

After Kobe earthquake 1995, the structural performance concept of a bridge in Japan considers two levels of seismic excitation which are named as Level 1 and Level 2. However, the Level 2 of ground motion input is a large seismic coefficient demand. Also, the problem of bridge rubber bearing support which commonly is used in Japan lost expected seismic performance due to the deterioration. Some possible causes of the deterioration are the aging, the compression fatigue, or the frequent lateral deformation which triggered by traffic load, wind load, thermal expansion, creeps, and shrinkages phenomena of daily load. While the behavior and the parameter of reinforced concrete (RC) column connected with friction device were determined successfully based on the experiment and numerical analysis. This study proposed the structural system of integrated bridge pier with triple RC column connected by friction damper plus gap which is expected to substitute the conventional bridge pier system avoiding the use of rubber bearing. In the investigation of its behavior and seismic performance, numerical analysis was performed with fiber cross-section of non-linear beam-column-based element model on the longitudinal direction of the bridge structure. As the analysis result, the proposed structure had an excellent performance not only under small deformation to allocate frequent lateral deformation but also under seismic load. Furthermore, in the structural simulations, the different limit state of column location and the various yield strength of reinforcing steel configuration were considered to obtain a better structural cost-performance option.

3.2 Background

The earthquake occurrence is one of the most damageable to the bridge pier. This phenomenon occurs in conventional pier systems which adopts the concept "weak column" [14], unlike the frame system of the building which implements approach "strong-column weak-beam". In the conventional column concept, the plastic hinge is formed on the bottom part of the pier. In the severe earthquake event, if the strength and ductility of the pier sufficient with the earthquake demand, it occurs cracking or spalling in the plastic hinge and residual deformation, as shown in Figure 3.1A. While the strength and ductility of the structure are insufficient with the earthquake demand, the pier may fail and cause the whole bridge structure to collapse [14]. Plastic hinge is a vital part to generate dissipation energy to dampen the seismic vibration, but the leniency of the plastic hinge system in the bridge pier structure is the residual deformation. Residual deformation poses challenges of post-quake structural restoration, time consumption, and traffic closure that leads to economic problems [13]. Since Hyogo-ken Nanbu earthquake in 1995, the seismic coefficient for the bridge design that has been determined by the Japan Road Association (JRA) [10] contains two level seismic input (Level 1 and Level 2). However, the Level 2 of ground motion input is a large seismic coefficient demand. Furthermore, based on the damaged bridge's observation of Takahashi et al. [28] after the Great East Japan earthquake in 2011, there are some rupture occurrences of rubber bearing supports even though its were designed following the post-1995 design specifications. Probably, it might be caused by the deterioration due to the aging [9, 7], the compression fatigue [6, 1], or frequent lateral deformation of the daily load [30], as shown in Figure 3.1B. The frequent lateral deformation that inflicts the fatigue damage, as shown in Figure 3.1C may be triggered by the thermal expansion, creep, and shrinkage of the superstructure, traffic load, wind load, and small to the medium earthquake occurrences. So that the development of high-performance bridge pier that could limit damage under Level 2 of seismic excitation and reduce the deterioration of seismic device in Japan is a challenging research.

The previous researcher below proposed some kinds of passive energy dissipated for seismic control of structure which implement friction device. A large cantilever panel structure connected with limited slip bolt joints for seismic control of building was developed by Pall [20]. Also, the concept of the friction damped braced frame of steel structure was proposed by

Pall and Marsh [22]. Mualla and Belev [15] developed rotated friction damping device (FDD) with a V-bracing shape for seismic control of steel structure. Furthermore, the experiments of high seismic performance column under cyclic loading have been performed by Nakamura et al. [17]. This structure consists of three parts of thin concrete columns linked to friction devices with prestressed bolts shown in Figure 3.2A. Based on the experimental results, this structure has a considerable deformation capacity elasticity with high energy dissipation. The elastic deformation capacity of the structure is about 2.0% of drift ratio. Also, it has a fairly constant resistance up to a 10.0% of drift ratio [16]. According to FEMA 356 [3], in the performance of Immediate Occupancy, the limitation of the main reinforced concrete column structure is small hairline cracks, the possibility of limited plasticization in some locations and no damage to the 1.0% drift ratio under temporary conditions and no permanent drift. This structure type is expected to correspond to important or dangerous facility categories that achieve Immediate Occupancy performance under severe earthquakes with a small probability of occurrence. Furthermore, the numerical analysis that was conducted by the reference [25] has good agreement results of calibrated numerical model parameters, as shown in Figure 3.2B. So that the reinforced concrete column connected by this friction damper has high potential to be implemented on the bridge pier structure. With large elastic deformation capacity and sufficient energy dissipation, this structure is capable of behaving elastically at Level 2 of seismic design based on JRA standard [10].

The objective of this research is to develop modified reinforced concrete columns connected by frictional damper with an additional gap on the friction damper. This structural system is expected to replace conventional bridge pier consisting of a column and bearing support. The expectation is that this structure can be implemented for future generation of the short-medium span bridges by removing bearing support, as shown in Figure 3.3. Even though the new seismic performance requirement of the rubber bearing support was upgraded by the Japanese Public Work Research Institute (PWRI) [26], some problems of the rubber bearing implementation may be remain occurred. The friction damper plus gap (FDG) is expected to realize high flexibility in small deformations. When the seismic load design occurs, the friction damper works to absorb the vibrational energy under the condition of the structure still below its limit state of the performance target. The application of reinforcing steel materials and the location of different limit states is expected to consider regarding cost and structural performance relationship. The expected performance target is the structure behaving elastically (called Performance I) under severe earthquake excitation (called Level 2). In this study, the implementation

(A) (B) (C)

FIGURE 3.1: The illustration of: (A) conventional pier under earthquake, (B) lost seismic performance of deteriorated rubber bearing [28], and (C) compressive cyclic fatigue curve of rubber bearing [1].

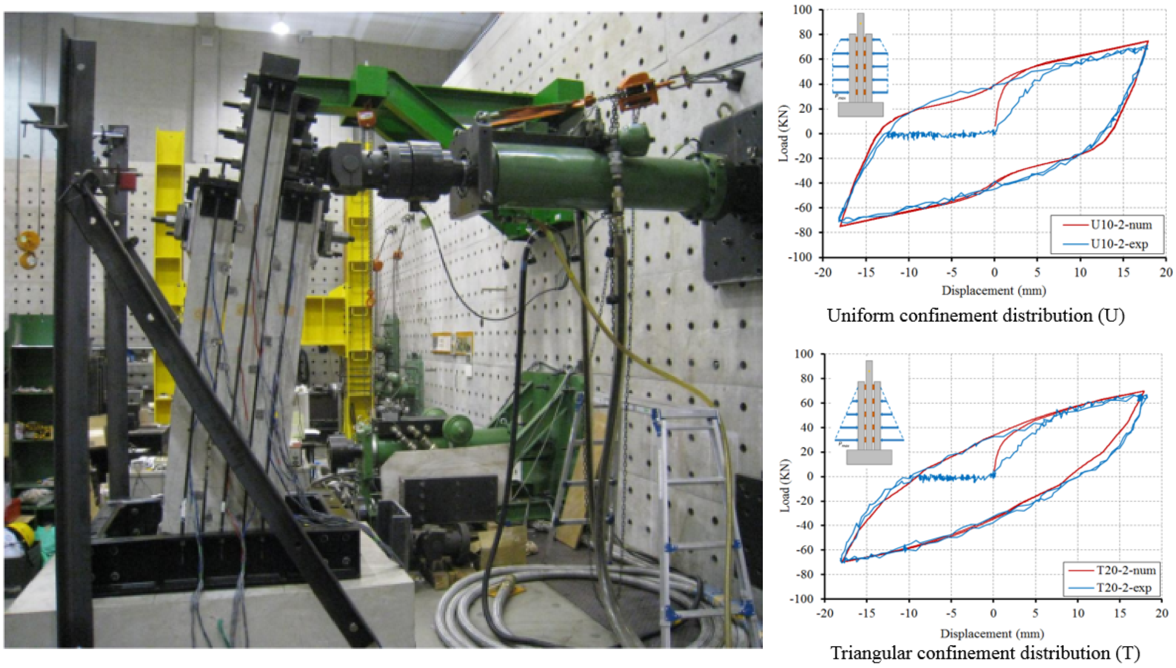

(A) (B)

FIGURE 3.2: The previous study of RC column connected by friction damper: (A) experimental study [16] and (B) numerical verification study [25].

RC pier connected with FDG just focused on the case longitudinal direction of the bridge structure. Numerical analysis with non-linear static and dynamic was performed to simulate this proposed structure by implementing the fiber section of force-based beam-column elements model. As the analysis results, the proposed structure had an excellent performance not only under small deformation to allocate frequent lateral deformation but also under the Level 2 of seismic excitation.

3.3 RC Column Accompanied by Friction Damper plus Gap

3.3.1 Friction damper

Pall et al. [21], Mualla and Belev [15] and Moralez et al. [23] implemented the elastoplastic idealization of friction damper in the numerical analysis based on experimental results. In the study above, the friction device follows the Coulomb rule of with dry friction law, the frictional force in both conditions of sticky and slip is assumed to be constant. The friction coefficient (μ) is the friction force ratio (F_{max}) with normal force (N) which can be determined as:

$$\mu = \frac{\mathrm{F}_{max}}{N} \tag{3.1}$$

Mualla and Belev [15] conducted experiments and numerical analysis of steel portal structures with friction damper devices (FDD) containing friction material (free friction asbestos material plus high-performance steel materials). With the 400 cycles of the load test, the result was almost no damage to FDD. Nakamura et al. [18] conducted a friction device testing experiment consisting of SS400 steel type friction material paired with SUS304 steel type material. The experiment results showed that along with the increase in the slip the coefficient value of friction increases close to linear, starting from about 0.2 at the beginning of slide occurs reaching approximately 0.5 at the end of loading.

3.3.2 The proposed seismic device mechanism of friction damper plus gap (FDG)

The friction damper plus gap is expected to achieve perfect sliding without force resistance under determined gap length. While under deformation larger than the gap space, it can achieve sufficient friction resistance that triggers energy dissipation. In the idealization, the mechanical behavior of FDG is a combination of series of stopper material as named Elastic Perfect Plastic Gap (EPPGap) and bi-linear (named Steel01) material models as shown in Figure 3.4A. So that, the global response of the proposed structure can behave small stiffness in the small deformation and sufficient energy dissipation achievement under large deformation, as shown in Figure 3.4B. In the seismic device design proposal, to accommodate sliding and bearing action at the gap space, FDG is composed of a slip surface connected to a base plate with a slit retaining and steel plate with *polytetrafluoroethylene* (PFTE) surface. To produce friction of the friction surface connected by a top plate with a SUS304 steel type paired with a steel plate with SS400, as shown in Figure 3.5.

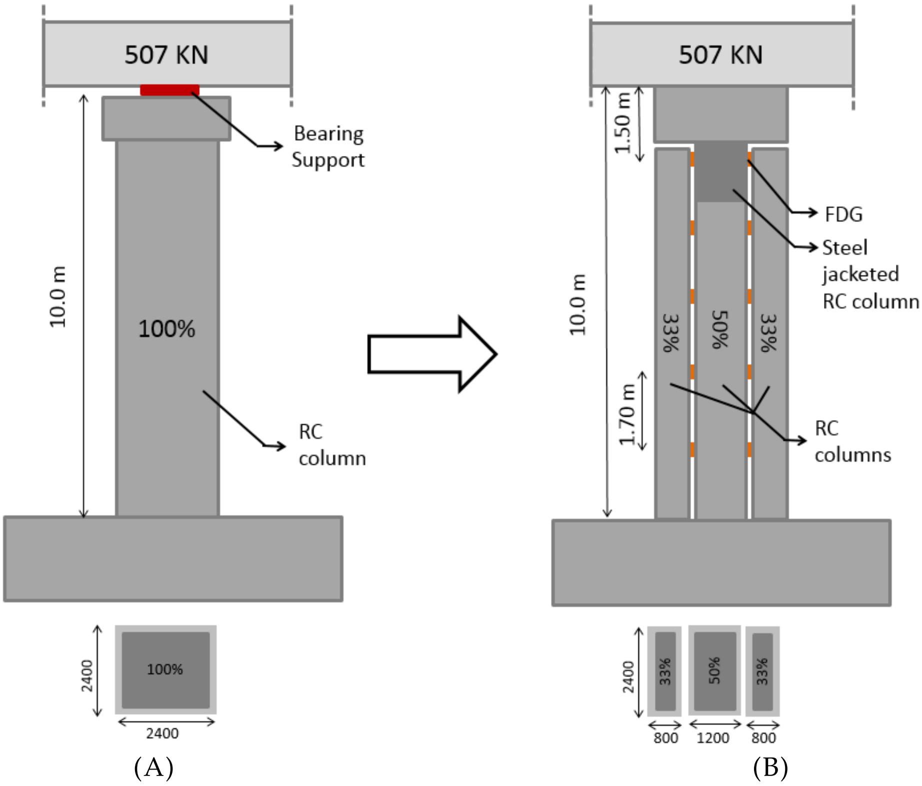

FIGURE 3.3: (A) The conventional bridge pier (with 100% cross-section area of the reference [8]) and (B) the proposed bridge pier connected by FDG (with 116% cross-section area of the conventional bridge pier).

3.3.3 The structural concept of RC pier connected by FDG

The principle of the column connected by the FDG is that the structure still behaves elastically in small deformation conditions due to an expansion of the bridge structure as well as to large deformations due to seismic loads with sufficient energy dissipation. To achieve a large elastic deformation capacity, the column structure is composed of three thin columns. The friction device unifies each component of the column through the bolts prestressed in the lateral direction. The energy of dissipation is produced by the slip deformation of the friction device due to the lateral deformation of the structure [16].

The RC column connected by friction damper without the gap has four stages of stiffness. When small lateral loads (P) work to the top of the column, minor lateral deformations occur, slippage has not occurred in the friction damper. At this stage, the stiffness of the column is the stiffness of the monolith (K_m). On the other hand, the larger lateral force (P) induces greater deformation of the column; the slip occurs in some portion of the friction damper, the column stiffness decreases to the transition stiffness (K_t). Increased column lateral deformation will induce all friction damper to slip so that separate stiffness (K_s) is formed. Separate stiffness is expected to occur in elastic fixed structural conditions before longitudinal steel reinforcements are yielding. After the yielding of the longitudinal steel reinforcement, the stiffness continues to experience plastic stiffness (K_p). The illustration of the stiffness stage of the structure is shown in Figure 3.6A. When comparing the four different structural systems as shown in Figure 3.6B, the column structure behaves in a monolithic manner having greater stiffness and strength than the separate parts, whereas the part that the group structure of the columns behaves separately has a greater elastic deformation capacity.

The RC column connected by FDG has the same initial stiffness as the group of columns behaving separately, while the ultimate strength approaches the monolithic group of columns behaving. The elastic deformation capacity looks like a structure that has separate stiffness as shown in Figure 3.6B.

3.3.4 The proposed bridge pier structure connected by FDG

A gap in the FDG expected to realize separated-section stiffness of the integrated pier among the gap range. When the deformation of the structure has exceeded gap length, the structure will behave as a monolith-section stiffness, the illustration of the mechanism can be seen in Figure 3.6B.

The seismic performance target of this structure is the seismic response of the structure still below its limit state under Level 2 of the earthquake excitation. The limit state on this proposed structure is to embody structures which behave closely to the elastic behavior with a sufficiently separated (post-sliding) stiffness. This determination was aimed at preventing residual deformation and structural damage during and after the earthquake as an effort to alleviate recovery work and restoration times demand.

There are four limiting scenarios which the different reinforcing steel grade configuration in the middle and side columns been implemented, as shown in Table 3.1. A strict limit state (full elastic conditions) was proposed by the elastic restriction on the side column. While a more loosely (semi-elastic) limit state was proposed by applying the elastic limits in the middle of the column section, which means that reinforcing steel in the side part of column occur yield, but the middle column remains elastic condition. The purpose of using structural configurations with different reinforced steel material grades (SD345 and USD685) is to achieve the best cost-performance of the structure. The high strength reinforcing steel expected to produce

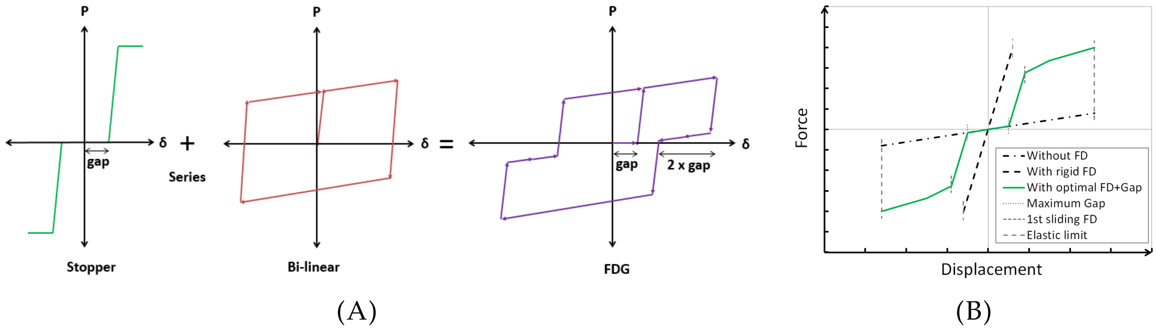

FIGURE 3.4: The proposed FDG behavior: (A) the constitutive mechanism of the device and (B) the global response of influenced pier structure.

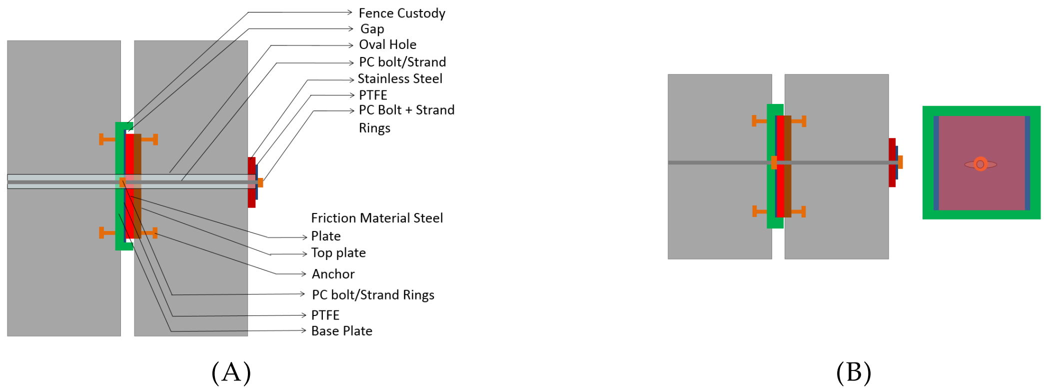

FIGURE 3.5: The component of proposed FDG: (A) side view and (B) top view.

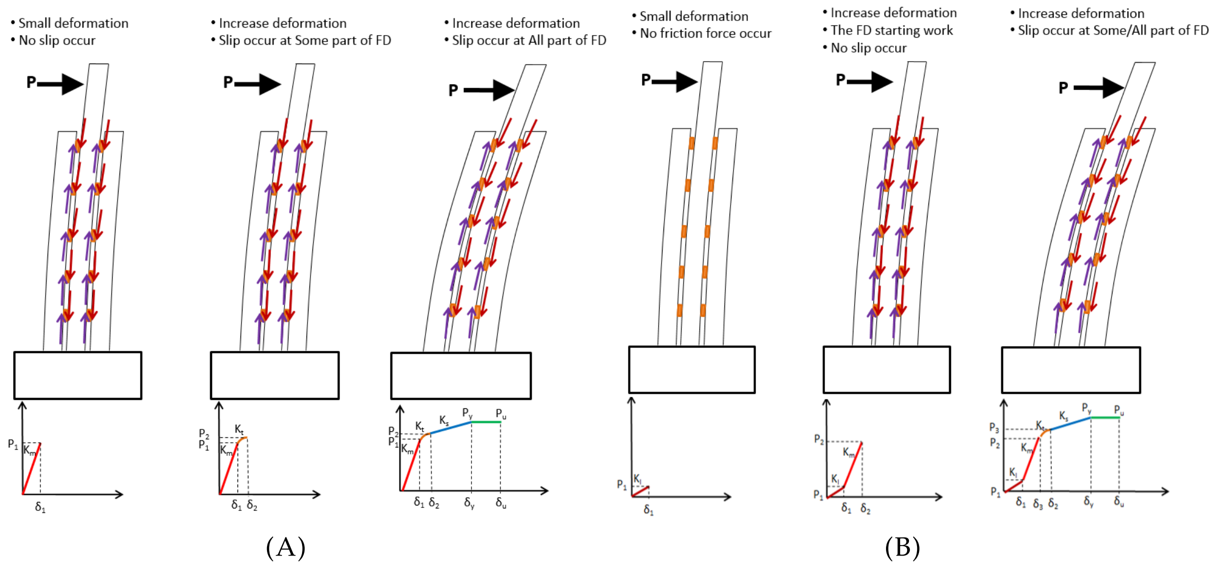

FIGURE 3.6: The mechanism of RC columns connected by friction damper: (A) without gap [16] and (B) with gap.

large elastic deformation capacity, while the ordinary strength of one expected to reduce the construction cost.

3.4 Numerical Analysis Method

In this study, each of the structural model variation was on the optimum energy dissipation state. The dissipated energy optimization was conducted by calculating energy dissipation in each increment of FDG's confinement force magnitude with static cyclic analysis. Also, the static pushover analysis was conducted to investigate not only the structural behavior but also the limit state of the structure. Furthermore, the non-linear dynamic analysis was performed to verify the seismic performance of the structures.

3.4.1 Structural idealization

The reinforced concrete pier connected by FDG to be idealized as frame elements in a two-dimensional model with three degrees of freedom. The appropriate element type needs to be considered based on its behavior. The upper end of the center column was idealized as an elastic element to simulate the support of the loading point which should have elastic behavior with the provision of a steel jacket structure system. For dynamic analysis, concentrated mass idealization is expected to achieve the ease of numerical convergence. Also, the upper structure masses of bridges and piers were placed at 10.0 m height. While the implementation of a Force-based Beam-column element with a fiber cross-section applied to the main column element [5, 29, 27, 19, 24]. In obtaining a convergent and accurate result, the number of sufficient integration points of the frame element and the number of fibers in the column cross section should be determined.

The friction device was idealized as a link element (called Two-node link element) that was coupled in series of bi-linear (called Steel01) and stopper (called EPPGap) material in the vertical direction. While an elastic material was applied in the perpendicular direction of the column height as the embodiment of the PC bar behavior. The FDG material parameters will be discussed in the sub-section of the FDG material parameters below.

3.4.2 Steel and concrete material parameters

The reinforcing steel materials modeling applies smoothed bi-linear material model (called Steel02) based on Giuffre-Menegotto-Pinto theory [12]. The reinforcing steel material input parameters include; f_y is the yield strength, E is the modulus of elasticity, b is the hardening ratio and the parameters for controlling the transition between the elastic branches to the plastic

TABLE 3.1: The variable of structural parameters.

Str. Name	Scenario	Gap (mm)	Reinforcing steel yield stregth (MPa)		Yield lim. loc.
			MC	SC	
Str1	1	0.00	345	345	MC
Str2	1	10.00	345	345	MC
Str3	1	20.00	345	345	MC
Str4	1	30.00	345	345	MC
Str5	1	w/o FD	345	345	MC
Str6	1	Rigid FD	345	345	MC
Str7	2	0.00	685	345	MC
Str8	2	10.00	685	345	MC
Str9	2	20.00	685	345	MC
Str10	2	30.00	685	345	MC
Str11	2	w/o FD	685	345	MC
Str12	2	Rigid FD	685	345	MC
Str13	3	0.00	685	685	MC
Str14	3	10.00	685	685	MC
Str15	3	20.00	685	685	MC
Str16	3	30.00	685	685	MC
Str17	3	w/o FD	685	685	MC
Str18	3	Rigid FD	685	685	MC
Str19	4	0.00	685	685	SC
Str20	4	10.00	685	685	SC
Str21	4	20.00	685	685	SC
Str22	4	30.00	685	685	SC
Str23	4	w/o FD	685	685	SC
Str24	4	Rigid FD	685	685	SC
Str25	CRC	-	345	-	-
Str26	CRC	-	685	-	-

SC: side column; MC: middle column; CRC: conventional reinforced concrete.

branches are R_0, c_{R1} and c_{R2}. The reinforced steel material parameters are selected following the recommendations of reference [4] as shown in Table 3.2. While the column elemental concrete material was modeled as a concrete material (called Concrete02) based on the reference [11] to a material constituted by reference [10]. In this study, concrete grade was assumed as C30 ($f_c{}'$ = 30 MPa).

3.4.3 Friction damper plus gap parameters

The friction material was idealized as a bi-linear material model, the elastic condition describing the sticky state, whereas the post-yielding state indicates that the slip state has occurred. In the numerical model, bi-linear (named Steel01) material could simulate isotropic

TABLE 3.2: The variable of the FDG confinement force.

Variable no.	Maximum confinement force (KN)
1	0
2 to 41	4200-12000 incr. 200
42	very large

TABLE 3.3: The reinforcing steel parameter input.

f_y(MPa)	E(MPa)	b	R_0	c_{R1}	c_{R2}
345	200000	0.02	19.5	0.925	0.5
685	200000	0.02	19.5	0.925	0.5

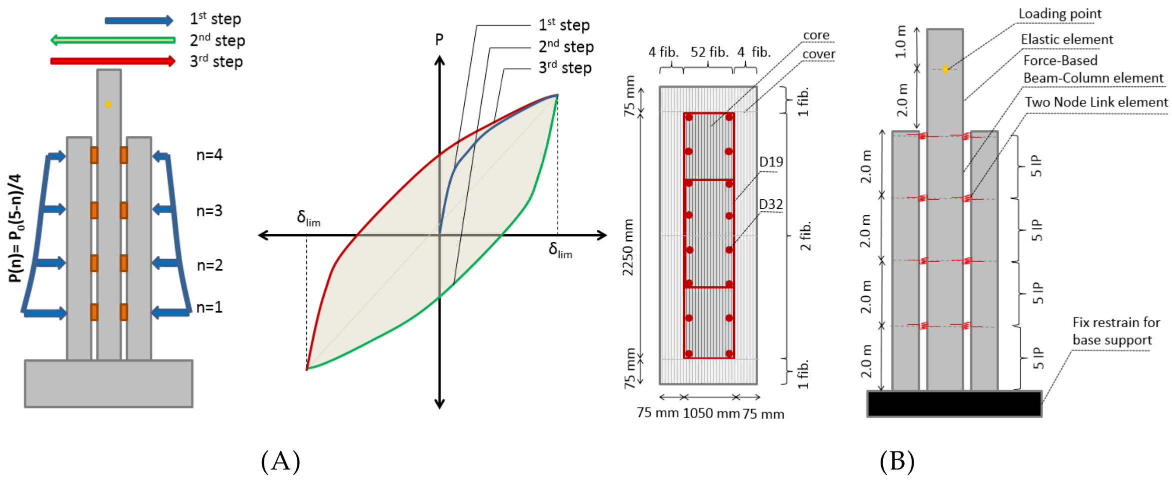

FIGURE 3.7: The confinement force distribution and the dissipated energy calculation method of the structure and (B) the structural idealization in the numerical model.

and kinematic hardening behavior based on Fedeas [2]. In this study, the behavior of cyclic hardening of FDG materials was only idealized as kinematic hardening.

The friction coefficient value was adjusted to be 0.5 with the hardening ratio close to zero and the slip deformation is 0.025 mm. Friction device parameters were achieved as a result of a numerical analysis calibration of the experiment from previous study [25]. Based on previous numerical analysis study, the friction coefficient and slip deformation were the most important parameters that play an important role in the formation of hysteretic curves and the distribution of curvatures along the column heights [25].

The frictional component of FDG is a series combination of a stopper material which idealized as Elastic Perfect Plastic Gap (EPPGap) material and bi-linear material which idealized as Steel01 material, as in Figure 3.4A. The stopper material works to simulate slip action across the gap. At the end position of the gap length, the stiffness and the strength of the EPPGap material were defined sharply greater than the steel material parameters (Steel01) on the friction device to reflect the slip deformation determined by the dominant friction surface.

3.4.4 The structural behavior investigation method

The structural behavior that needs to be investigated including the structural stiffness at the small deformation (accommodating the frequent lateral deformation), the deformation limit capacity, and also energy dissipation quantity of the structure. Static pushover analysis in each gap length variation (10 mm, 20 mm, and 30 mm) was performed including structural stiffness observation and comparison without the use of a gap (0 mm of a gap). Also, the effectiveness of gaps implementation in reducing the initial stiffness of the structure can be evaluated. More ever, the dissipated energy is also an important parameter of structural behavior because it involves the significance of structures in dampening seismic excitation. However, the existence of the gap could reduce the energy dissipation, then the gap length determination should pay attention to the impact of energy dissipation reduction. In this study, the significance of gap length effect to the dissipated energy was also carried out.

3.4.5 The structural performance investigation method

To examine structural performance, the full-scale model of the structure was simulated by numerical analysis. This study refers to the reference design of Iemura et. al. [8] which the designed conventional reinforced concrete structures following JRA code [10] was applied as a benchmark of the proposed structure. The bridge pier properties are; 9.6 m of height, 507 tons of superstructure mass, 5.0 of the ductility factor. The column has a 2.4 x 2.4 m^2 of the cross section with 1.20% of longitudinal reinforcement (72D35, 345 MPa). Also, it was assumed that the concrete has a compressive strength of 30 MPa. Furthermore, the transversal reinforcing steel consists of 4D19 with a distance of 150 mm. The conventional RC pier was simulated to make structural performance comparisons. In this study, there are two types of conventional structures, the structure that followed the reference [8] is varied again with different steel reinforcing grades, namely SD345 and USD685.

The performance of the proposed structures were compared with conventional reinforced concrete piers which were modified to 10.0 m in height by 1.40%, 1.51%, and 1.62% of the reinforcement range with 0 mm, 10 mm, 20 mm, and 30 mm in 42 variations of friction damper confinement force are shown in Table 3.1. The reinforced concrete column section connected by FDG was designed with a total area of 116% of the conventional column with a 33%-50%-33% configuration as shown in Figure 3.3. The structural configuration was determined with an area greater than 100% of the structure in reference [8] because, in theory, it's strength is smaller than the monolith column structure, as illustrated in Figure 3.4B.

In this study, structural parameters that were estimated to have significant influence i.e., the confinement force of the friction device, the reinforcing steel area demand, and the gap length. The structure was designed to accommodate thermal deformation up to 20 mm (40 m of bridge span, Δt = 40 $^\circ$ C, α = 1.2e-5 m/m $^\circ$ C). In this case, the triangular confinement distribution pattern was implemented along the height of the pier, as shown in Figure 3.7A. The optimum largest energy dissipation in the optimum FDG confinement force was selected and verified its seismic performance.

A non-linear analysis includes static pushover and dynamic time history was performed to observe the structural behavior and performance, respectively. The structural seismic performance verification was conducted by applying a Level 2 of earthquake excitation with Type I and Type II in which consists of three different excitation types of ground. The response spectra of the earthquake excitation inputs were presented in Figures (A.2 and A.3). Also, the residual deformations of the structure after the earthquake excitation were examined to confirm the re-centering capability.

3.4.6 Numerical analysis scenarios

The numerical analysis consists of three stages; static cyclic analysis, static pushover analysis, and dynamic analysis with earthquake excitation. The static cyclic analysis was conducted to investigate structural behavior including force and deformation relationships as well as the dissipated energy capacity under proposed deformation limit. Also, the static pushover analysis to examine the skeleton curve characteristic and the limit state of the structure. Furthermore, the dynamic analysis to find out the structure response and to verify the performance of the structure under Level 2 of the seismic excitation.

In the cyclic loading analysis, there are two stages of the loading pattern. The first is the equivalent gravitational load in the form of a constant nodal load pattern in the gravity direction. While the second is a cyclic load with displacement loading protocol in the lateral-longitudinal direction of the bridge structure. In the cyclic loading analysis, there are 3 steps of displacement loading protocol to the center of the mass of the structure at a height of 10.0

m as shown in Figure 3.7A. During cyclic loading under proposed deformation limit, energy dissipation was calculated by integrated the hysteresis loop area formed by the second and the third step, as shown in Figure 3.7A. In the equivalent gravity load, Newton's algorithm [11] of load integrator was adopted. While in the cyclic load, Newton algorithm [11] of displacement integrator was implemented. Equivalent gravity loads to be applied directly without increment, while the cyclic load to be implemented with increment 0.1 mm. Otherwise, the dynamic excitation load implements Newmark integration a time interval of 0.001 s.

To examine the re-centering capability of the structure, the residual deformations after an earthquake were recorded in the state before and after the confinement force of FDG to be released. Each residual deformation that the average deformations of the structure were calculated to be recorded in duration 5 seconds. There are two types of post-earthquake structural deformation records namely; the FDG condition still merges with structure, and the FDG contribution has been removed from the structure (confinement force released after earthquake event). The recording of the two deformation records were performed at (T_{eq} to T_{eq}+5) and (T_{eq}+15 to T_{eq}+20), respectively. While at the time (T_{eq}+15), the FDG was released under free vibration.

3.5 Results and Discussion

3.5.1 Structural behavior

As the result of the dissipated energy optimization that is shown in Figure 3.8, the greater the proportion of reinforced steel cross-section resulted the greater the energy dissipation produced. While the optimum confinement force magnitude could achieve the largest energy dissipation. The structural variation number 19 configured with 1.62% reinforcing steel and 10200 KN strength force that achieve the largest dissipated energy capacity in the scenario was chosen for the structural performance examination. The other hand, based on Figure 3.9, the longer the gap was applied resulted the smaller the energy dissipation to be achieved. The reduced energy dissipation occurs due to the descended area of each friction device hysteresis loop. Based on the friction devices hysteresis loop monitoring Figure 3.10, the gap existence reduces the hysteresis loop area of the friction device.

The stiffness ratios of the proposed structure with gaps and without gaps are shown in Table 3.4. The proposed structure had small initial stiffness and large elastic deformation limit capacity, thus having the ability to accommodate frequent lateral deformation. The structure

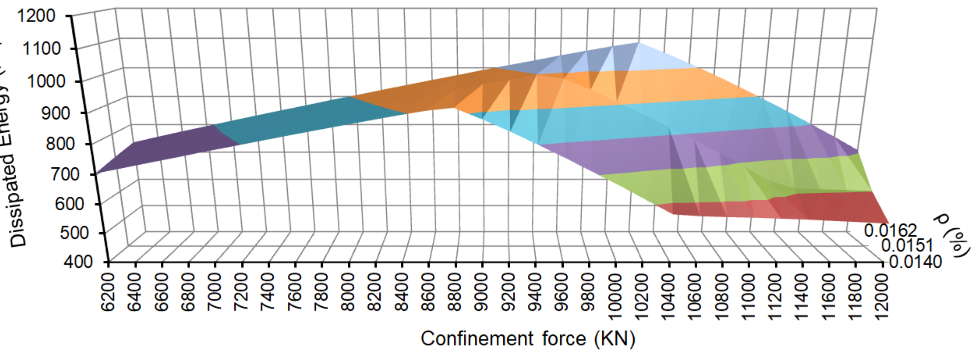

FIGURE 3.8: The dissipated energy influenced by the FDG confinement force and the proportion of reinforcing steel.

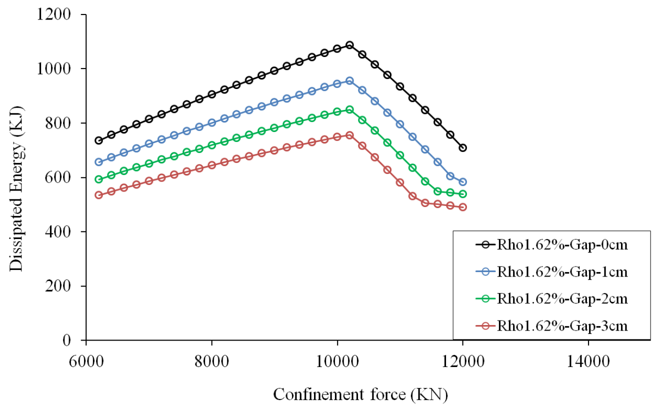

FIGURE 3.9: The dissipated energy influenced by the gap length.

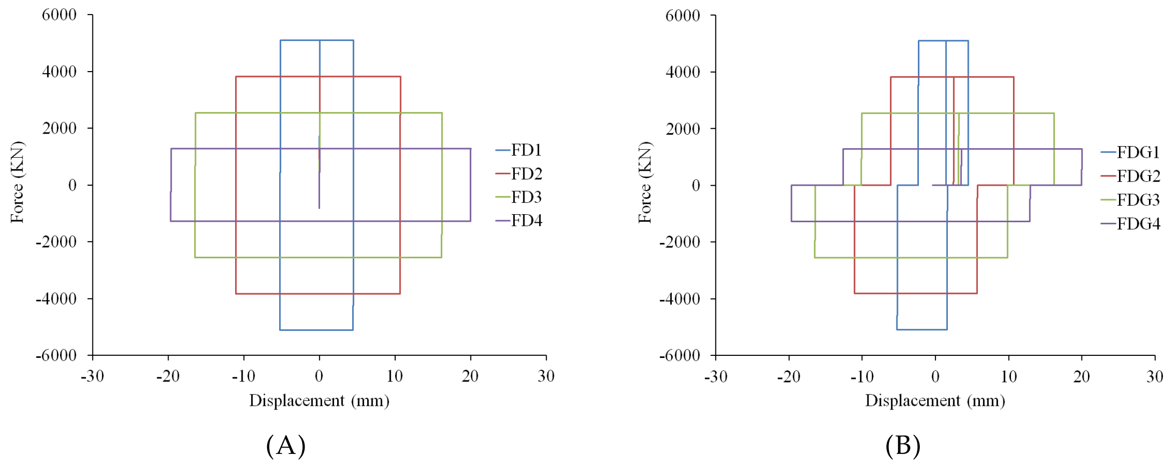

FIGURE 3.10: The SPD hysteresis curves of: (A) Str19 and (B) Str21.

that implements a 20 mm gap has a stiffness of 0.26 times compared to the structure which did not consider the gap.

As analysis result, the proposed structure with scenario 1 had a deformation limit capacity 0.75% of drift ratio. In the scenario 2, a significant improvement to be enriched which is 1.30% of drift ratio. Furthermore, both proposed structures with scenarios 3 and 4 achieved a

TABLE 3.4: The stiffness comparison at the small deformation.

Disp. (mm)	The structural stiffness with the gap length (K_{ef}, KN/m)				The structural stiffness ratio with the gap length (ratio K_{ef})			
	0 mm	10 mm	20 mm	30 mm	0 mm	10 mm	20 mm	30 mm
0.10	434083.47	45254.56	45254.56	45254.56	1.00	0.10	0.10	0.10
10.00	147214.38	38426.31	35829.41	35829.41	1.00	0.26	0.24	0.24
20.00	110595.51	69624.47	28570.04	28387.38	1.00	0.63	0.26	0.26
30.00	90735.87	76979.29	51619.02	25611.03	1.00	0.85	0.57	0.28

TABLE 3.5: The seismic performance of the structures.

Str. Name	Max. conf. force (KN)	Total energy dissi-pation (KJ)	Percentage dissipated energy of FDG	Equal damp-ing ratio (ζ_{eq}%)	Maximum deformation response of earthquake (mm)			Residual deformation (mm)		
					Max.	Ratio	Eq. no.	Before realeased	After realeased	Eq. no.
Str1	7400	332.73	0.96	0.21	107.87	1.48	II-I-1	10.68	9.21	II-I-1
Str2	6000	232.79	0.98	0.17	156.49	2.15	II-III-1	19.50	15.75	II-III-1
Str3	6000	171.11	0.97	0.12	172.69	2.37	II-II-1	27.65	24.23	II-III-1
Str4	5600	117.30	0.96	0.09	208.52	2.87	II-II-1	18.90	18.92	II-I-1
Str5	0	2.27	0.00	0.00	260.59	3.93	I-II-1	22.24	22.21	I-II-1
Str6	∼	9.13	0.00	0.01	64.53	1.89	II-II-1	6.13	6.99	II-I-1
Str7	10400	875.33	0.65	0.22	99.46	0.76	II-I-1	8.49	6.16	II-I-1
Str8	10200	760.85	0.65	0.19	128.98	0.98	II-I-1	7.74	5.09	I-II-1
Str9	8800	709.36	0.83	0.18	141.59	1.05	II-III-1	7.00	3.18	I-II-1
Str10	8600	626.11	0.84	0.16	162.05	1.20	I-II-1	7.58	7.09	I-II-1
Str11	0	16.79	0.00	0.01	151.94	1.23	I-I-1	1.20	1.26	I-I-1
Str12	∼	7.29	0.00	0.01	68.78	2.10	II-I-1	2.49	5.33	II-I-1
Str13	13800	1220.04	0.97	0.22	85.52	0.61	II-I-1	6.33	4.02	II-I-1
Str14	13000	1048.47	0.97	0.20	120.97	0.85	II-I-1	5.22	5.41	II-II-1
Str15	12000	918.56	0.97	0.18	123.44	0.86	II-III-1	4.23	3.04	II-III-1
Str16	11800	809.41	0.97	0.16	148.65	1.03	I-II-1	4.73	3.22	I-II-1
Str17	0	10.65	0.00	0.01	285.68	2.18	I-III-1	30.67	30.97	II-I-1
Str18	∼	13.69	0.00	0.01	71.74	1.33	II-I-1	1.13	1.65	II-I-1
Str19	10200	1086.84	0.98	0.23	98.31	0.69	II-I-1	4.62	2.69	II-I-1
Str20	10200	955.50	0.98	0.20	126.76	0.89	II-I-1	5.58	4.44	II-II-1
Str21	10200	849.94	0.98	0.18	131.12	0.92	II-III-1	5.56	4.12	I-II-1
Str22	10200	755.77	0.97	0.16	153.82	1.08	I-II-1	6.57	4.16	I-II-1
Str23	0	10.65	0.00	0.01	285.68	2.18	I-III-1	30.67	30.97	II-I-1
Str24	∼	13.69	0.00	0.01	71.74	1.33	II-I-1	1.13	1.65	II-I-1
Str25	-	-	-	-	129.13	3.85	II-I-1	15.01	-	II-III-1
Str26	-	-	-	-	128.36	2.14	II-I-1	11.41	-	I-II-1

deformation capacity limit about 1.40% of drift ratio. The use of high-strength steel (USD685) of reinforcement just in the middle column could significantly increase the deformation limit capacity. While the use of this in the middle and side of the column is just slightly improved of

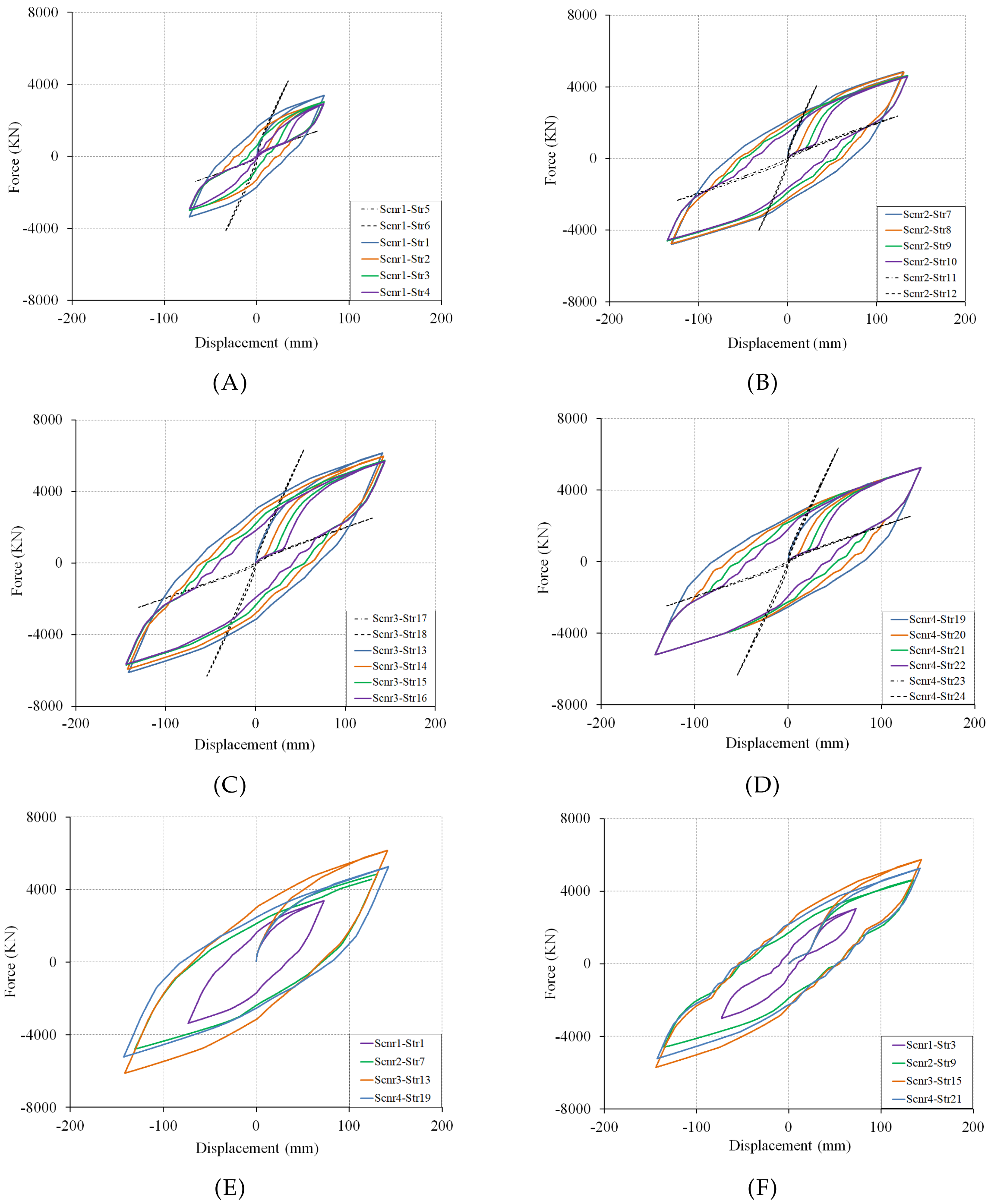

FIGURE 3.11: The hysteresis curve comparisons under static cyclic analysis: (A) Scenario1, (B) Scenario2, (C) Scenario3, (D) Scenario4, (E) structure without gap, and (F) structure with 20 mm gap.

the using high-strength steel in the middle column only. The use of high-strength steel materials also significantly increases structural strength both in the occurrence of FDG post-slip and at deformation limit. This reason will be explained in the next paragraph below. The structural behavior in the entity of deformation limit capacity and structural strength could be observed in Figure 3.11.

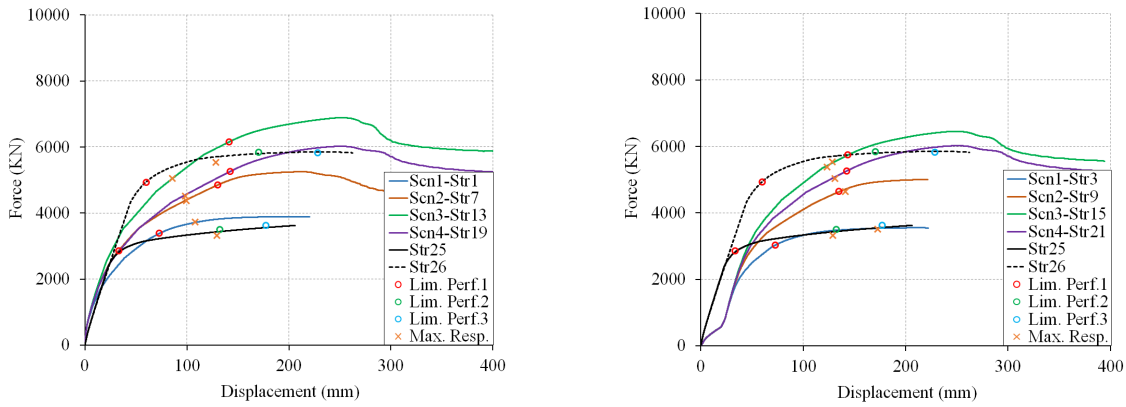

(A) (B)

FIGURE 3.12: The skeleton curve also its limit state under static pushover analysis and the maximum response under Level 2 of seismic excitation: (A) structure without gap and (B) structure with 20 mm gap.

The use of reinforcement with high-strength steel (USD685) material is expected to increase the dissipated energy. The reason is increased deformation limit capacity is as well as increased structural strength. As the result, the implementation of high-strength reinforcing steel in the middle column and ordinary-grade reinforcing steel in the side column with is significant enough to achieve large dissipated energy. Although the dissipated energy of this structure (Scnr2) is slightly smaller than that implements all reinforcing bars using high-grade steel (Scnr3 and Scnr4), it makes prosper in terms of the construction cost. While the damping ratio of the structures with Scnr2, Scntr3, and Scnr4 in the equal gap length were near to the same; this statement is supported by the data in column fifth of Table 3.5 and Figure 3.11.

The determination of deformation limit based on yielding stress of reinforcing steel in different column positions could achieve in nearly equal deformation capacity but different strength. The limit state of scenario 4 (Scnr4) is more stringent than scenario 3 (Scnr3). In the scenario 4 the structure was expected to behave fully elastic. Envisaged in scenario 3, the structure still occurring plastic deformation on the side column. The dissipated energy optimization of the scenario 3 required a larger FDG confinement force than the scenario 4. The larger the FDG confinement force resulted the larger the structural strength, but the elastic limit of the deformation capacity of the center column is almost identical, as shown in Figure 3.12. Based on the comparison the energy dissipation scenario 3 and scenario 4 of the structure that is shown in column third of Table 3.5, the scenario 3 achieved larger energy dissipation compared to the scenario 4. While in the scenario 4, the maximum strength of the proposed structures with different gap were adjacent rather than the scenario 1, 2, and 3. Also, the scenario 4 (perfect elastic

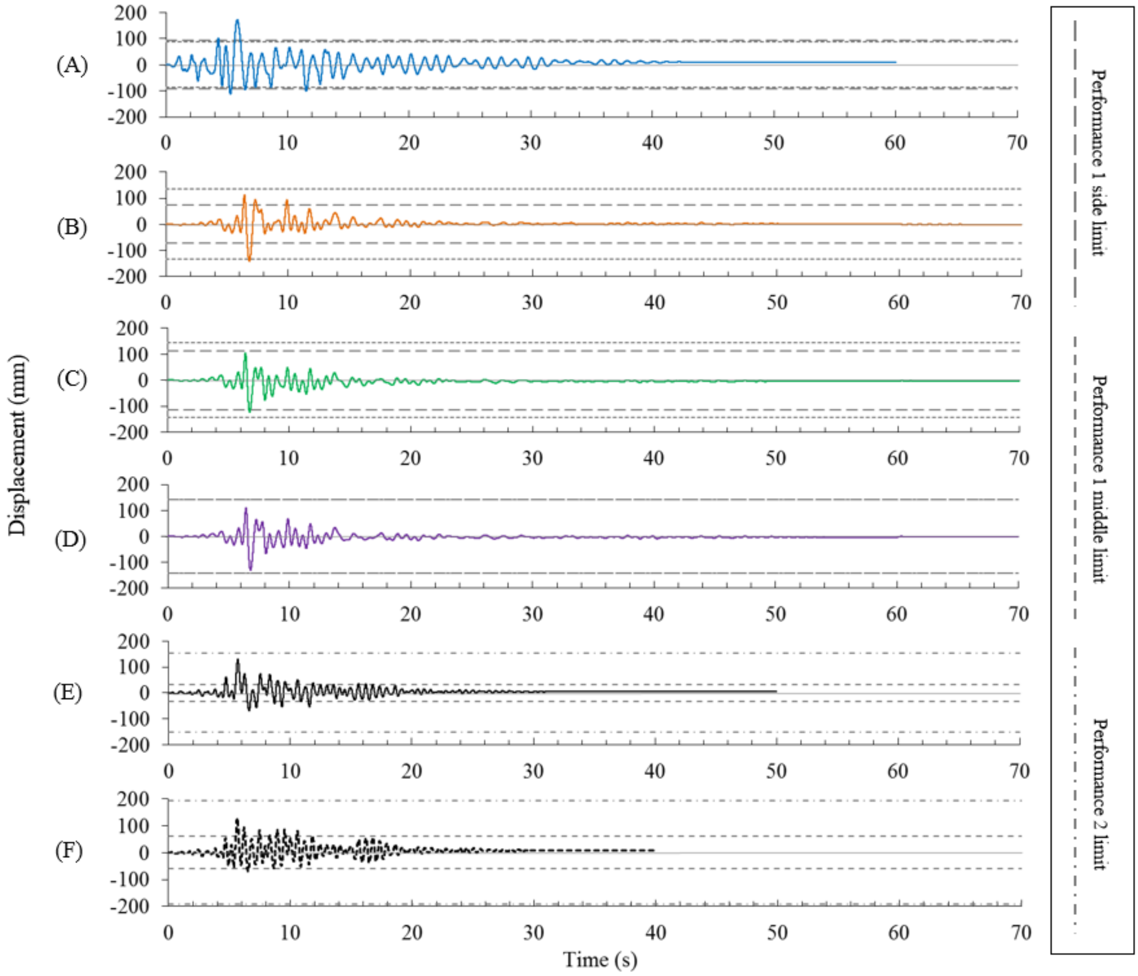

FIGURE 3.13: The maximum displacement response of the structure under seismic load level 2: (A) Str3, (B) Str9, (C) Str15, (D) Str21, (E) Str25, and (F) Str26.

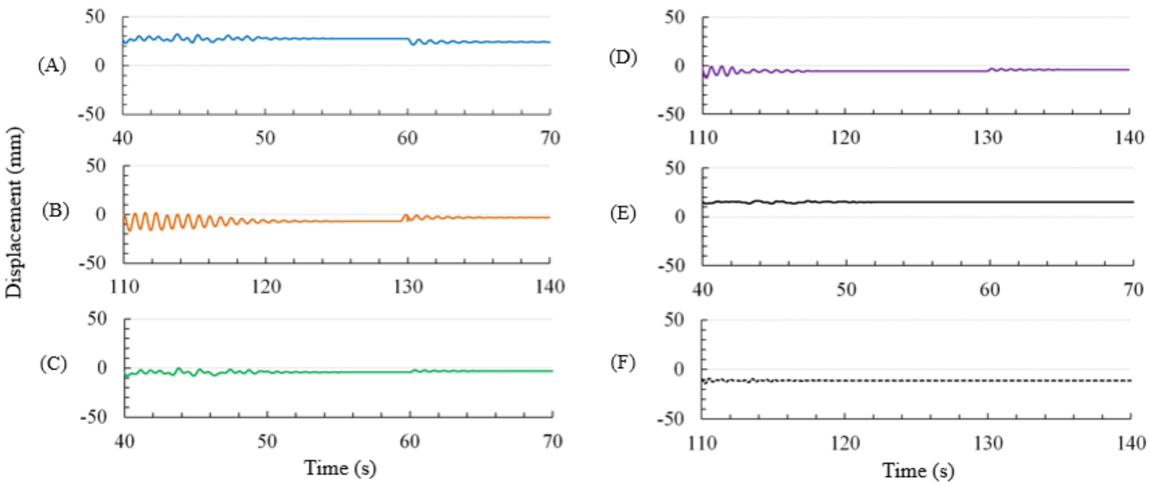

FIGURE 3.14: The maximum residual displacement response of the structure under seismic load level 2: (A) Str3, (B) Str9, (C) Str15, (D) Str21, (E) Str25, and (F) Str26.

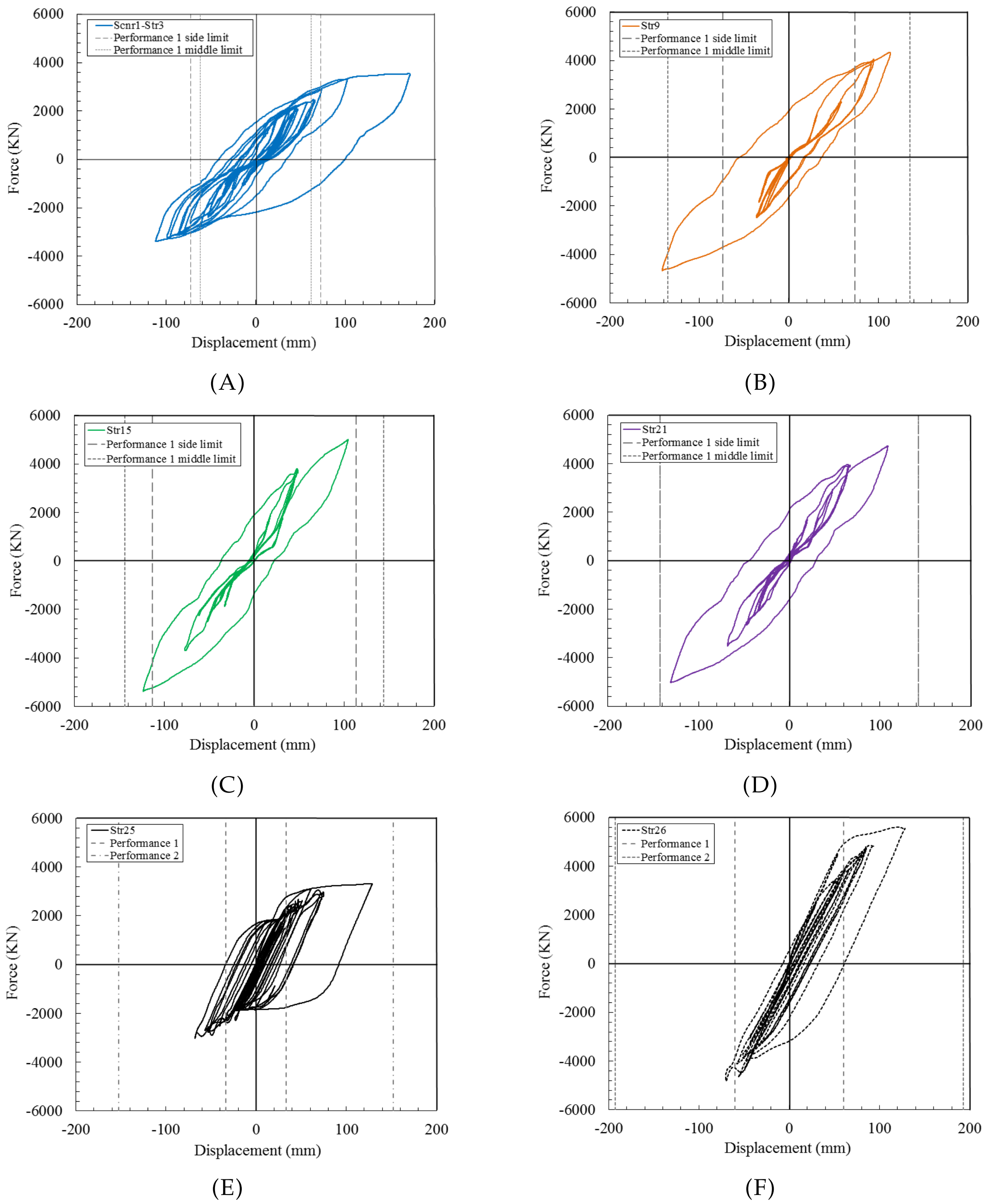

FIGURE 3.15: The force and displacement seismic response under Level 2 of earthquake excitation: (A) Str3, (B) Str9, (C) Str15, (D) Str21, (E) Str25, and (F) Str26.

deformation limit) had same confinement magnitude in the optimum energy dissipation, the other hand the scenario 1, 2, and 3 had different confinement force magnitude, as shown in Table 3.5. However, in the term friction device proportion of the dissipated energy achievement to the whole proposed structural system, the scenario 2 achieved the smallest value, as shown in column fourth of Table 3.5. The reason is the using high strength of reinforcing steel and the limiting state just on the middle column resulted in the significant yielding occurrence of the side part column.

3.5.2 Structural seismic performance

As the seismic performance verification with six input of Level 2 ground motion excitation, the structural performance target that remains elastic behavior could be achieved in several structural variations. All structures with scenario 1 (Scnr1) were not capable of enriching performance target. While the structures with scenario 2 (Scnr2) were deformed below the deformation limit in the application of a gap less than 10 mm. Finally, the structures with scenario 3 and 4 were capable of achieving the performance target up to 20 mm gap, as shown in column seventh of Table 3.5. Under earthquake excitation, the time history deformations of the proposed structures correspond to the deformation limit are shown in Figure 3.13.

Based on the skeleton curve with its limit state and maximum response of structure under Level 2 of earthquake excitation, the additional 20 mm of gap increase structural response. Consequently, it made some structures decrease its performance, as shown in Figure 3.12. Furthermore, the proposed structure (with 20 mm gap) of Str15 and Str21 were below the deformation limit (behave elastic or near to elastic) under Level 2 of earthquake excitation with a maximum displacement near to the conventional structure response, as shown in Figure 3.13. While the proposed structure that implements combination with ordinary-strength and high-strength of column reinforcement (Str9) in the scenario 2 slightly exceeded its deformation limit with a deformation ratio 1.05. The maximum response and the limit state of the structure are described in Figure 3.13 and Table 3.5. So that the application of high-strength steel reinforcement was required to achieve sufficient dissipated energy and deformation limit of the structure with elastic behavior (Performance I).

The proposed structures in scenarios 2, 3, and 4 produced smaller residual deformations than conventional pier structures, as shown in Figure 3.14. This happens because, in the scenario 2 and 3, the middle structure remained elastic behavior, while in scenario four all structure columns still experienced the elastic behavior. Hence, the structure that behaves elastically could have a good re-centering ability.

The force and deformation relation of the maximum response under seismic excitation of the structure are shown on Figure 3.15. The maximum resisting force of proposed structure (Str3) is near to the conventional pier with ordinary-strength reinforcing steel to all columns section (Str25), while in the case Str9, Str15, and Str21 is near to the conventional pier with high-strength reinforcing steel on the middle column (Str26). However the proposed structure with high-strength reinforcing steel in the middle part behave remains elastic under Level 2 of earthquake excitation while the conventional column (Str26) over the elastic deformation limit.

3.6 Conclusions

The integrated bridge pier with triple RC column connected by friction damper plus gap was successfully proposed to accommodate a 20 mm length of the frequent lateral deformation due to daily load. This structure could behave elastic or near elastic condition under severe earthquake excitation. Also, the remaining elastic behavior of the structure manifested small residual deformations. Based on the analysis, the structure had the following behaviors and performances:

(a) The gap length, the proportional cross-sectional area of the reinforcing steel, and friction damper strength should be determined proportionately. The longer of the gap resulted the smaller of the dissipated energy. The greater the reinforcing steel proportion obtained the greater the strength and the dissipated energy. While the friction force value needed to be determined at the optimum dissipated energy.

(b) In the optimum dissipated energy, the implementation of different location limits could affect the strength and the dissipated energy of the structure significantly. While deformation limit capacity was not affected significantly.

(c) The use of high strength steel reinforcement on the middle column could increase the deformation limit capacity, strength, and dissipated energy. While the application of high-strength steel reinforcement for all columns was slightly better in improving the performance of the structure than the application that was only in the middle of the column.

(d) The application of the 20 mm gap length of the FDG on the structure resulted in 0.26 times smaller stiffness than without the gap.

(e) The structure without and with gap can achieve the equivalent damping ratio 22%-23% and 18%, respectively.

(f) The maximum structural response of high strength reinforcing steel implementation in all of the column section was below the deformation limit under Level 2 of seismic excitation, while the maximum structural response of ordinary strength reinforcing steel implementation in all of the column section was over the deformation limit.

(g) The maximum structural response of high and ordinary strength reinforcing steel implementation slightly exceeded the limit state. It had potential and more economical to be improved and to be implemented in the real structure.

(h) The residual deformation of the structure which implemented high-strength reinforcing steel in the middle column was smaller than the conventional column structures. While the residual deformation of the structure which implemented ordinary strength reinforcing steel in all column was the largest. The re-centering capability of the structure which implemented ordinary strength reinforcing steel in all column might be lost due to all the column section was over the elastic state.

(i) The implementation of ordinary-strength reinforcing steel on the all of the column of the proposed structure resulted in almost equal lateral force resistance compared to the conventional RC pier with ordinary-strength reinforcing steel. The equal relation also was obtained on the high-strength steel material implementation.

Bibliography

[1] Deng, P. and Warn, G.P.: Modeling the Compression Stiffness Degradation in Circular Elastomeric Bearings due to Fatigue, Journal of Engineering Mechanics, volume 142, no. 1:1–11, 2016.

[2] F.C. Filippou: FEDEAS - Finite Elements for Design, Evaluation, and Analysis of Structures Theory, Reference Manual and Example, Technical report, Department of Civil Engineering, University of California, California, 1996.

[3] FEMA: *Prestandard and Commentary for the Seismic Rehabilitation of Buildings*, 1, Federal Emergency Management Agency, Washington, D.C., 2000.

[4] Filippou, F.C. and Issa, A.: Nonlinear Analysis of Reinforced Concrete Frames under Cyclic Load Reversals, Technical Report December, Earthquake Engineering Research Center College of Engineering University of California, Berkeley, California, 1988.

[5] Filippou, F.C., Popov, E. and Bertero, V.: Effects of Bond Deteroriation on Hysteretic Behavior of Renforce Concrete Joint, Technical Report August, Earthquake Engineering Research Center, California, 1983.

[6] Guo, C., Zhou, L. and Lv, J.: Fatigue Life Prediction for Circular Rubber Bearings Subjected to Cyclic Compression, Journal of Applied Polymer Science, volume 123, no. 7:2194–2203, 2011.

[7] Hamaguchi, H., Samejima, Y. and Kani, N.: A study of aging effect on rubber bearings after about twenty years in use, in *11th World Conference on Seismic Isolation, Energy Dissipation Control of Structures*, pages 1–16, World Conference on Seismic Isolation, Energy Dissipation and Active Vibration Control of Structures, Guangzhou, 2009.

[8] Iemura, H., Takahashi, Y. and Sogabe, N.: Two-level seismic design method using post-yield stiffness and its application to unbonded bar reinforced concrete piers, Journal of JSCE, volume 23, no. 1:109–116, 2006.

[9] Itoh, Y., Gu, H., Satoh, K. and Yamamoto, Y.: Long-Term Deterioration of High Damping Rubber Bridge Bearing, Doboku Gakkai Ronbunshuu A, volume 62, no. 3:595–607, 2006.

[10] Japan Road Association: *Specifications for Highway Bridges: Part V Seismic Design*, Maruzen Co. Ltd., Tokyo, 2012.

[11] Mazzoni, S., McKenna, F., Scott, M.H. and Fenves, G.L.: OpenSees Command Language Manual, 2007.

[12] Menegotto, G., Pinto, M. and Emilio, P.: Method of Analysis for Cyclically Loaded R.C. Plane Frames Including Changes in Geometry and Non-Elastic Behavior of Elements under Combined Normal Force and Bending, in *Proceedings of IABSE Symposium on Resistance and Ultimate Deformability of Structures Acted on by Well Defined Loads*, pages 15–22, Zurich, 1973.

[13] Mitoulis, S.A. and Rodriguez Rodriguez, J.: Seismic Performance of Novel Resilient Hinges for Columns and Application on Irregular Bridges, Journal of Bridge Engineering, volume 22, no. 2:1–12, 2017.

[14] Moehle, J.P. and Eberhard, M.O.: Bridge Engineering Handbook: Earthquake Damage to Bridges, chapter 34, page 34, CRC Press, Boca Raton, 2000.

[15] Mualla, I. and Belev, B.: Performance of Steel Frames with a New Friction Damper Device under Earthquake Excitation, Engineering Structures, volume 24, no. 3:365–371, 2002.

[16] Nakamura, H., Takahashi, Y. and Sawada, S.: *The Elasto-Plastic Behavior of the Rectangular RC Column Accompanied with Friction Damping Mechanism with Complex Confinement*, Undergraduate thesis, Kyoto University, 2011.

[17] Nakamura, H., Takahashi, Y. and Sawada, S.: The Elasto-plastic Behavior of the Rectangular RC Column Accompanied with Friction Damping Mechanism, Journal of JSCE, volume 68, no. 4:577–583, 2012.

[18] Nakamura, H., Takahashi, Y. and Sawada, S.: *The Study on Earthquake Response Mechanism of Set RC Columns with Unity of Frictional Damping Mechanism*, Ph.D. thesis, Kyoto University, 2013.

[19] Neuenhofer, A. and Filippou, F.C.: Evaluation of Nonlinear Frame Finite-Element Models, Journal of Structural Engineering, volume 123, no. May:583–590, 1997.

[20] Pall, A.: *Limited Slip Bolted Joints : a Device to Control the Seismic Response of Large Panel Structures*, Doctoral thesis, Concordia University, 1979.

[21] Pall, A., Marsh, C. and Fazio, P.: Friction Joints for Seismic Control of Large Panel Structures, PCI Journal, volume 25, no. 6:38–61, 1980.

[22] Pall, A.S. and Marsh, C.: Response of Friction Damped Braced Frames, Journal of Structural Engineering, volume 108, no. June:1313–1323, 1982.

[23] Ramirez, J.D.M. and Tirca, L.: Numerical Simulation and Design of Friction- Damped Steel Frame Structures damped, in *15th World Conference in Earthquake Engineering*, Lisboa, 2012.

[24] Scott, M.H. and Hamutçuoğlu, O.M.: Numerically Consistent Regularization of Force-based Frame Elements, International Journal for Numerical Methods in Engineering, volume 76, no. 10:1612–1631, 2008.

[25] Setiawan, A.F., Takahashi, Y., Kiyono, J. and Sawada, S.: Numerical Analysis of RC Columns Accompanied with Friction Damping Mechanism under Cyclic Loading, in *Procedia Engineering*, volume 171, pages 821–835, Denpasar, 2017.

[26] Shinohara, M., Sakai, J. and Hoshikuma, J.i.: Seismic requirements for laminated elastomeric bearings and test protocol for verification, Technical report, Public Work Research Institute (PWRI), Tokyo, 2012.

[27] Spacone, E., Filippou, F.C. and Taucer, F.F.: Fibre Beam-Column Model for Non-Linear Analysis of R/C Frames : Part II. Applications, Earthquake Engineering and Structural Dynamics, volume 25, no. January:727–742, 1996.

[28] Takahashi, Y. and Hoshikuma, J.i.: Damage to Road Bridges Induced by Ground Motion in the 2011 Great East Japan Earthquake, Journal of JSCE, volume 1:398–410, 2013.

[29] Taucer, F.F. and Spacone, E.: Aa Fiber Beam-Column Element for Seismic Response Analysis of Reinforced Concrete Structures, Technical Report December 2014, Earthquake Engineering Research Center College of Engineering University of California, Berkeley, California, 1991.

[30] Taylor, A.W., Lin, A.N. and Martin, J.W.: Performance of Elastomers in Isolation Bearings: A Literature Review, Earthquake Spectra, volume 8, no. 2:279–303, 1992.

Chapter 4

Seismic Performance Enhancement of Integrated Steel Pipes Bridge Pier Connected by SPD

4.1 General Remarks

The high seismic performance of integrated steel pipes bridge pier connected by shear panel damper (SPD) has been developed and implemented by the Hanshin Expressway. However, under severe seismic design (called Level 2), the current structure only attains lack of satisfied high seismic performance (named Performance 2b) that is probably due to the less significant achievement of deformation limit capacity and dissipated energy capacity. In this chapter, the seismic performance enhancement of such structure was conducted by considering the combinations of significant influential factors. These factors including the SPD distribution at along structural height, the segment number of the pier, and the proposed pin connection between the top part of the steel pipe columns and the head of the pier. Furthermore, the limit state of the structure under severe earthquake was proposed through restricting the lateral deformation limit of the structure with 90% yield-stiffness of the steel pipe column. As the results of the best seismic performance enhancement, the seismic performance of the structure was improved significantly, which was the achievement of Performance 2a under Level 2 of seismic excitation. Moreover, the deformation limit capacity was improved 1.63 times, the dissipated energy under deformation limit was increased 272% with equal damping ratio was 22.28%, the maximum deformation response was less than proposed deformation limit, and it had a better re-centering capability than the original structural configuration. Furthermore, the lateral seismic force demand could be decreased up to 22%.

4.2 Background

In the recent decade, the high seismic performance of the integrated multiple columns connected by shear link dampers or shear panel dampers (SPD) has been developed and has been implemented in the structure. This typical structure has been studied not only for the building but also for the bridge pier. Shear panel damper is an option of the several passive damper types for reducing earthquake load due to easy installation, maintenance, and affordability. The studies such structure were conducted, for example, the research about self-centering steel plate shear wall [7]. Based on its study, the structure improved the seismic performance of frame structure in the contributions of the excellent re-centering capability. Secondly, the study of seismic response evaluation of the linked column frame system (LCF) was developed [16]. In the event of a moderate earthquake, a quick reparation can be conducted to the damper devices that are damaged, in addition, this system realized collapse prevention conditions in the structure under great earthquake. Furthermore, the experimental study of the bridge pier with structural fuses and bi-steel columns was conducted [8]. While the result showed that at the elastic deformation state of the steel pipe columns, the energy dissipation was still limited. Also, the structure of a self-anchorage suspension cable bridge in San Fransisco-Oakland Bay was built by applying shear link damper within the main pylon. Based on the reference [21], the seismic performance of this bridge pylon is controlled by safety-evaluation earthquakes (SEE) with 1500 years of earthquake return-period which applies six inputs of earthquake load following the characters of San Andreas Fault and Hayward Fault. The structural simulations of pushover analysis and non-linear time history analysis showed that the main pylon remains in the elastic state, also shear link dampers yield below the strain limit. Moreover, an integrated bridge pier with multiple steel pipe columns connected by shear panel damper (SPD) has been developed and applied by Hanshin Expressway, as shown in Figure 4.1A. At the top and bottom of steel pipes is connected to the pile cap and head pier with fix connection, respectively. While the SPDs are installed at along the pier height with certain intervals of a uniform distribution in its strength and stiffness terms, as shown in Figure 4.1B. With the dissipated energy capacity of the SPD, high seismic performance structure can be achieved. As a result, the damage possibility caused by severe earthquake excitation can be reduced. In the less of structural damage, the life-cycle-cost of the structure that built in the high seismic zone can be descended [22].

The integrated bridge pier with multiple steel pipes connected by SPD has a great potential to be implemented for bridge structures not only in Japan but also in another country which has high seismic hazard. However, based on the study results of the reference [15], the dissipated energy that was produced by the SPD has not yet achieved the optimum. There was not significant dissipated energy production of its SPD (around 10% of the equivalent damping ratio value) on the elastic deformation range. Also at deformations over the yielding limit of steel pipe column, the dissipated energy was dominantly produced by the yielding of steel pipe column. At the maximum load resistance capacity, the damping ratio value was about 21%, as shown in the Figure 4.2A. Based on the reference [22], the structure enriched the Performance 2b (the structures occur medium-damaged by severe earthquakes) for the Importance Bridge category, as shown in Table 4.1. The study of integrated bridge pier with multiple steel pipes connected by SPD was also commenced by several predecessor research. For example, the basic property of an integrated column by multiple steel pipe columns with hysterical shear panel damper was studied [27]. Furthermore, to improve the seismic force reduction and to reduce the cost of the structure by the foundation case, the proposal of the bridge column integrated by multiple steel pipe columns with a direct-connected pile and seismic response analysis was conducted [28]. As well as research on the mechanical behavior of the pier with integrated steel pipe columns subjected to axial, torque, and cyclic loads on horizontal direction [10], and also the effect of structural parameters of SPD on the performance of multi-pipe integrated bridge pier [11] were investigated. Even though the predecessor studies of the structure in above have contributed many knowledge about the structural parameter and the structural behavior, the seismic performance has not yet achieved the Performance 2a (Small damage under Level 2 of seismic excitation)

This study discusses the seismic performance enhancement of integrated bridge pier with multiple steel pipes connected by SPD. In addition, the research object was taken from one of the structural variations based on reference [27]. The object of structure number II has 20 m of height with three segments of the pier, as shown in Figure 4.3A. There were four scenarios to increase those performance parameters of the structure which is shown in the Figure 4.3B. The four scenarios contain the combination of possible factors that have a significant contribution to improve the deformation limit capacity and the energy dissipation. These factors including SPD distribution (strength and stiffness) along the structural height, segment number of the pier, and the proposed pin connection between the top part of the steel pipe columns and the head of the pier. To achieve the significant seismic performance enhancement, the deformation limit of the structure was proposed by restricting the structural deformation limit at 90% yield

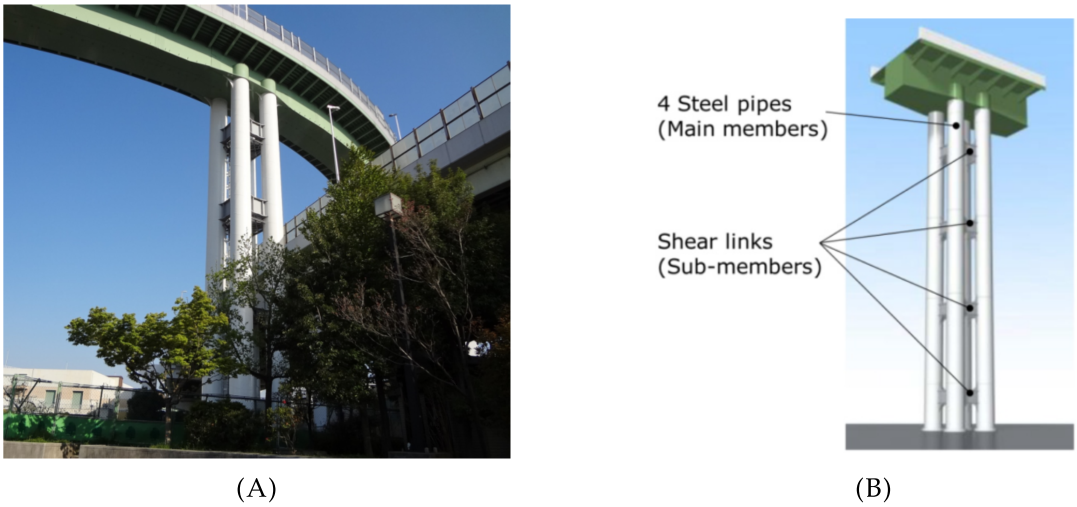

FIGURE 4.1: The integrated bridge pier with steel pipe column connected by shear panel damper [22]: (A) the implementation and (B) the concept.

stiffness of steel pipe column under seismic excitation design (named Level 2) based on JRA code [14]. Consequently, the proposed limit state is more stringent than the limit state of Performance 2a [22]. With this proposed deformation limit, the structural response under severe seismic design can be near to the elastic behavior. The near elastic behavior of the structure is intended to has a fair re-centering ability after major earthquake occurrences, in addition, easier refurbishment. As the result of the best seismic performance enhancement, the deformation limit capacity could be improved 1.63 times, the dissipated energy under deformation limit could be increased 272% with equal damping ratio was 22.28%, the maximum deformation response was less than the proposed deformation limit (satisfy with the Performance 2a [22]), and it had a better re-centering capability than the original structural configuration. Furthermore, the lateral seismic force demand could be decreased up to 22%.

4.3 Integrated Steel Pipes Bridge Pier connected by SPD

4.3.1 Shear panel damper

Shear panel damper consists of a low yield strength steel material of panel plate confined by the surrounding flanges part on the all of its edges, as shown in Figure 4.4A. On the small deformations, this device quickly reaches its yielding point due to shear deformation. Series of the development of the SPD device was started from the experimental study of thin steel shear wall damper by Takahashi et.al. [30], then the analysis method of it was developed by Thorburn et.al [32]. Also, the study of the hysteretic behavior of thin plate shear wall panels was proposed [23], and more about the cyclic behavior investigation of it was examined by reference [3]. Furthermore, the SPD behavior that is subject to axial load has been put forward by references [4, 5]. Moreover, the application of low-grade SPD steel material to seismic design was presented [34] and for the seismic design on the large deformations was studied by reference [1]. In this study, the shear panel damper behavior was idealized as a bilinear material model with hysteretic behavior following the reference [6], and the ultimate deformation capacity of SPD was adopted the reference [11]. Hence, the SPD hysteretic parameters are determined by the formulation as follows Equations (5.1-5.9).

$$Q_n = \tau_w.b_w.t_w,\ \Delta = \gamma_s.b_w \tag{4.1}$$

$$\tau_u = \tau_f + \tau_w \tag{4.2}$$

$$\frac{\tau_w}{\tau_{wy}} = 0.918 + \frac{0.038}{R_w^2} \leq 1.2 \tag{4.3}$$

$$\frac{\tau_f}{\tau_{fy}} = 0.0287\,\frac{b_f}{b_w}.\frac{t_f}{t_w}\left(\frac{t_f}{t_w}4..\frac{d_w}{(n_L+1)\,R_w b_w} + 2\right) \tag{4.4}$$

$$\tau_{wy} = \frac{\sigma}{\sqrt{3}} \tag{4.5}$$

$$R_w = \frac{b_w}{(n_L + 1)\ t_w}\sqrt{\frac{12\,(1-\nu)\ \tau_y}{K\pi^2 E}} \tag{4.6}$$

$$K = 5.35 + 4.\left(\frac{b}{d}\right)^2 for.\left(\frac{d}{b}\right) \geq 1 \tag{4.7}$$

$$K = 5.35\,.\left(\frac{b}{d}\right)^2 + 4for.\left(\frac{d}{b}\right) < 1 \tag{4.8}$$

$$\begin{aligned}\frac{\overline{\gamma_{su}}}{\gamma_{sy}} &= 20\ (\alpha \leq 0.8)\\ &= \frac{7.034}{(R_\tau+0.54)^{8.0}} + 4,\ (0.8 \leq \alpha \leq 1.5)\end{aligned} \tag{4.9}$$

With b is the component width, d is the component depth, t is the component thickness, n_L is the number of the stiffener flanges, E is the elastic modulus of steel material, Q_n is the shear force of the SPD, Δ is the displacement of the SPD, τ is shear stress of the steel material, γ_s is a shear strain of the steel material, and σ is an axial stress of the steel material.

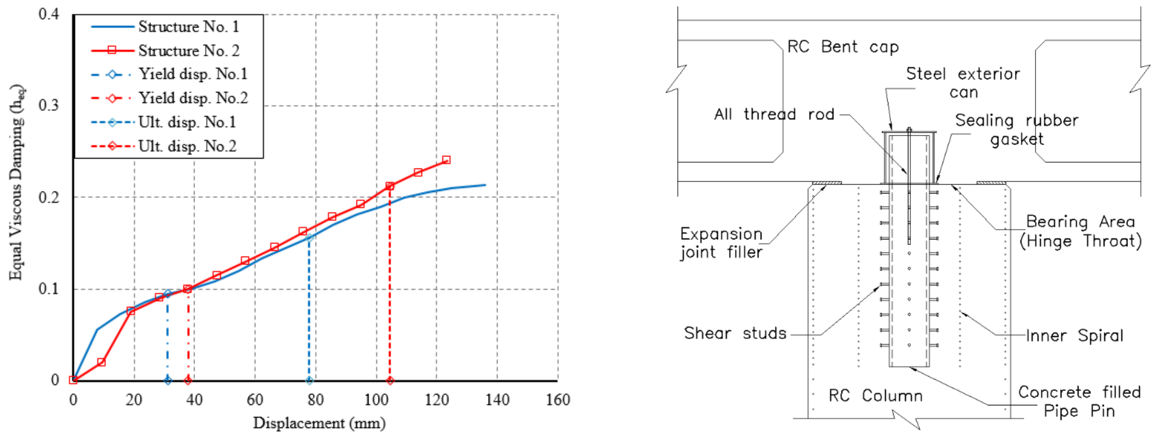

(A) (B)

FIGURE 4.2: (A) The relation of displacement and the equal damping based on the experiment result [15] and (B) the concept of pipe-pin connection of top end column connection [33].

TABLE 4.1: The required seismic performance matrix of integrated bridge pier with multiple steel pipes [22].

Seismic Performance Level / Earthquake	Performance I	Performance IIa	Performance IIb	Performance III	-
	[Structure safety performance]				
	Safety				Failure
	[Usability after earthquake]				
	No damage	Small damage	Medium damage	Big damage	
Level 1			Unacceptable		
Level 2					

Importance bridge (Ordinary design condition)
Importance bridge (To keep small damage is illogical subject to special design condition)
Ordinary bridge

4.3.2 The structural concept

The existing bridge pier that comprises four steel pipes is rigidly connected to the base and top of the column ends. The shear panel dampers are connected to the steel pipes with certain intervals to realize the integrated pier system, as shown in Figure 4.1A. During a lifetime, the vertical loads including self-weight and vehicles are supported by the axial resistance of the steel pipes, while the lateral loads are resisted by the interaction of the moment resistance of the steel pipes and the shear resistance of the SPD. When the pier structure undergoes lateral deformation, the SPD works in favor of shear forces and yields earlier than the steel pipe column elements. The vibration energy due to the seismic excitation to be absorbed by the dissipated

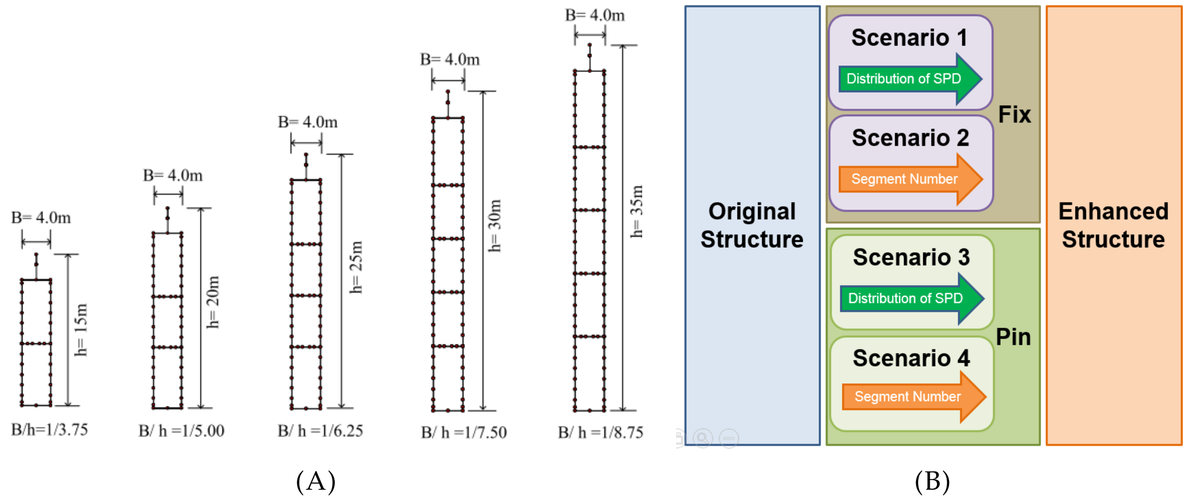

FIGURE 4.3: (A) The variable of the bridge pier height 8):structure I, structure II, structure III, structure IV, and structure V [27] and (B) the schematic of dissipated energy and seismic performance enhancement.

TABLE 4.2: The existing data of the structure [27].

(A)

h (mm)	B (mm)	D_p (mm)	t_p (mm)	f_{yp} (MPa)	W_s (KN)
20.0	4.0	1200.0	22.0	315.0	4369.0

(B)

d_w (mm)	b_w (mm)	t_w (mm)	b_f (mm)	t_f (mm)	f_{yw} (MPa)	f_{yf} (MPa)
700.0	700.0	22.0	200.0	50.0	225.0	345.0

h: height of the pier; B: with of the integrated pier; D_p: steel pipe diameter; t_p: steel pipe thickness; f_{yp}: yield strength of steel pipe steel material; W_s: weight of the superstructure; d_d: depth of SPD web; b_w: width of SPD web; t_w: thickness of SPD web; b_f: width of SPD flange; t_f: thickness of SPD flange; f_{yw}: yield strength of SPD web material; f_{yf}: yield strength of SPD flange material.

energy of the yielding SPD. So that the steel pipe damage due to severe earthquake excitation can be reduced, consequently, the life-cycle-cost of the structure can be improved [22].

In this study, the dissipated energy and structural seismic performance enhancement were performed on the structure II of reference [27], as shown in Figure 4.3A. In this case, a 4369 KN of the superstructure weight that is supported by the pier was chosen. The structure has a 4 m of outer width and a 20 m of height. Along the pier height, there are two SPDs that connect each steel pipes and divide it into three segments. The filled concrete steel pipes are installed along a third of the total height. The steel pipe column and the SPD are fixedly connected by the welded joint, as shown in Figure 4.4A. The entire structural properties are listed in Table 4.2.

TABLE 4.3: The SPD variables of the dissipated energy and seismic performance enhancement.

No.	Str. name	Scn.	SPD dist.	n_{segm}	n_{SPD}	Top con.	SPD dimension (mm) t_w	d_w	b_w	t_f	b_f
1	Str0	-	U	3	2	Fix	22	700	700	50	200
2	Str1	Scn1	NU	3	2	Fix	29-17, incr. -12	700	700	Min(2*t_w, 50)	200
3	Str2	Scn3	U	3	2	Pin	29	700	700	Min(2*t_w, 50)	200
4	Str3	Scn3	NU	3	2	Pin	35-29, incr. -6	700	700	Min(2*t_w, 50)	200
5	Str4	Scn3	U	3	3	Pin	19	700	700	Min(2*t_w, 50)	200
6	Str5	Scn3	NU	3	3	Pin	23-19, incr. -2	800-540, incr. -130	540-800, incr. 130	Min(2*t_w, 50)	200
7	Str6	Scn2	U	4	3	Fix	17	700	700	Min(2*t_w, 50)	200
8	Str7	Scn4	U	4	3	Pin	24	700	700	Min(2*t_w, 50)	200
9	Str8	Scn4	NU	4	3	Pin	25	800-540, incr. -130	540-800, incr. 130	Min(2*t_w, 50)	200
10	Str9	Scn4	U	4	4	Pin	17	700	700	Min(2*t_w, 50)	200
11	Str10	Scn4	NU	4	4	Pin	24-15, incr. -3	800-545, incr. -65	545-800, incr. 65	Min(2*t_w, 50)	200
12	Str11	Scn2	U	5	4	Fix	14	700	700	Min(2*t_w, 50)	200
13	Str12	Scn4	U	5	4	Pin	20	700	700	Min(2*t_w, 50)	200
14	Str13	Scn4	NU	5	4	Pin	21	800-545, incr. -65	545-800, incr. 65	Min(2*t_w, 50)	200
15	Str14	Scn4	U	5	5	Pin	16	700	700	Min(2*t_w, 50)	200
16	Str15	Scn4	NU	5	5	Pin	22-18, incr. -2	800-540, incr. -65	540-800, incr. 65	Min(2*t_w, 50)	200
17	Str16	Scn2	U	6	5	Fix	14	700	700	Min(2*t_w, 50)	200
18	Str17	Scn4	U	6	5	Pin	17	700	700	Min(2*t_w, 50)	200
19	Str18	Scn4	NU	6	5	Pin	18	800-540, incr. -65	540-800, incr. 65	Min(2*t_w, 50)	200
20	Str19	Scn4	U	6	6	Pin	15	700	700	Min(2*t_w, 50)	200
21	Str20	Scn4	NU	6	6	Pin	19-14, incr. -1	800-550, incr. -50	550-800, incr. 50	Min(2*t_w, 50)	200

Scn.: Scenario; U: Uniform strength distribution of SPD along pier height; NU: Non-uniform strength distribution of SPD along pier height; n_{SPD}: number of SPD in the pier structure; n_{SPD}: segment number of the pier structure.

4.4 Methodology

4.4.1 Numerical modeling of the structures

The seismic performance enhancement that was conducted by numerical analysis adopted the existing structural configuration of the reference [27]. Structure II was selected and simulated, as shown in Figure 4.3A. With the structural properties as shown in Table 4.2, the structure was modeled with Opensees software in the two dimensional and three degrees of freedom. The superstructure was idealized as lumped mass at an elevation position of 20 m from the base in the two directions (horizontal and vertical), as illustrated in Figure 4.4A. While the steel pipe column components were modeled as force-based beam-column with fiber section by applying the regularized plastic hinge with five integration points based on the references [17, 24, 25, 31, 29]. The steel pipe column material was modeled as smoothed bilinear (named Steel02) material by applying a combination of isotropic and kinematic hardening based on the references [17, 20]. While the steel pipe filling material on a third of the height of the pier

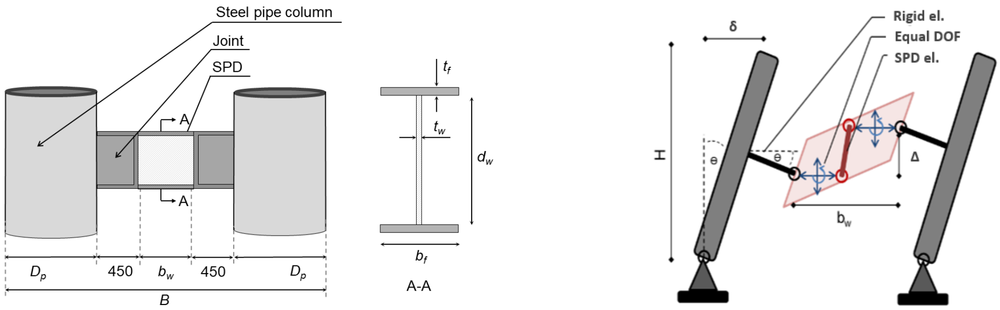

(A) (B)

FIGURE 4.4: The SPD modeling: (A) the SPD details [27] and (B) the SPD idealization in the numerical model.

was modeled as a concrete (named Concrete02) material based on the reference [17]. Also, the concrete constitutive material following the reference [14].

The SPD was modeled as link element based on the references [26, 2]. In the numerical model, each nodal of link element was positioned almost at one point at the center of the SPD location. Furthermore, the connection element between the SPD and the steel pipe column was idealized as a rigid elastic element. While the connection of SPD and join element were idealized as equal-DOF in all three degree of freedom. The connection of the SPD, the joint, and the steel pipes are illustrated in Figure 4.4B. The SPD constitutive material was idealized as bilinear (Steel01) material by applying kinematic hardening based on the reference [17]. The hysterical parameter of SPD was determined following the Equations ((5.1) - (5.9)) which is specified in the references [6, 11].

Before the seismic performance of the original structure to be enhanced by optimizing its energy dissipation, the calibration analysis was performed by matching the proposed model result to the previous model of the reference [27]. The matched parameter contains the skeleton curve, the SPD's yielding state, and the steel pipe yielding state.

4.4.2 Seismic performance enhancement scenarios

There are four scenarios to improve the seismic performance by increasing the energy dissipation of the structure, as illustrated in Figures (4.3B and 4.5). The first (Scn1), the strength and the stiffness of the SPD along the original pier height was redistributed with triangular pattern. This scenario is illustrated in Figure 4.6A. The second (Scn2), the addition of the SPD member along the pier height was applied on the original structural system (called fix-fix connection).

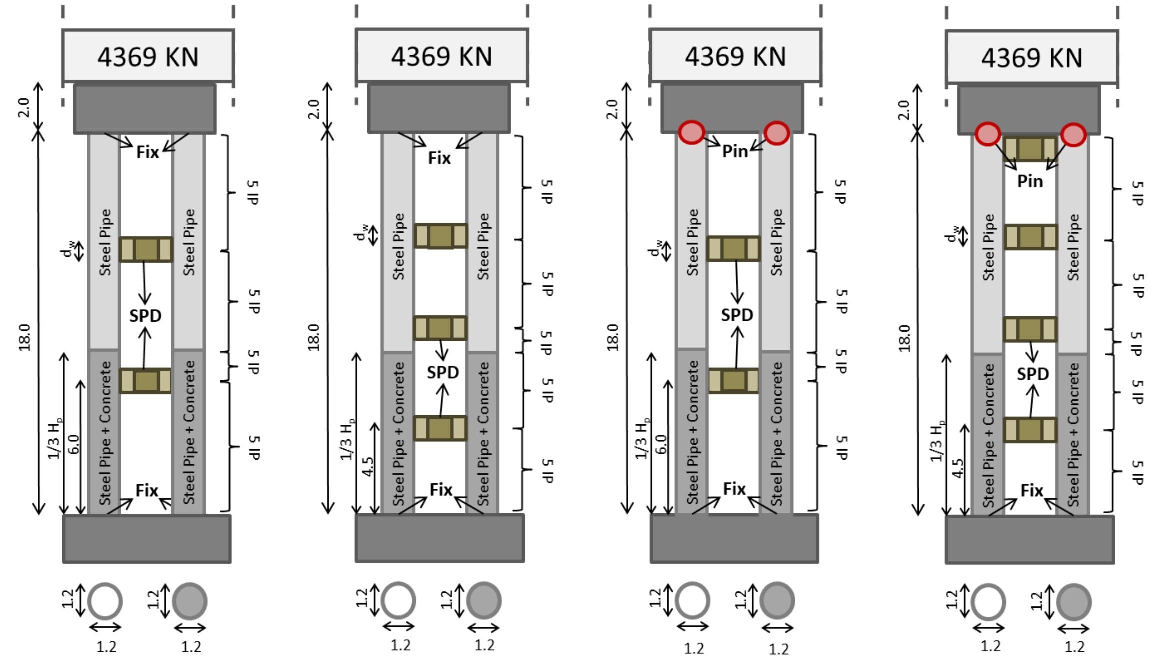

(A) (B) (C) (D)

FIGURE 4.5: The scenario of dissipated energy and seismic performance enhancement (the unit is in meter): (A) scenario 1, (B) scenario 2, (C) scenario 3, and (D) scenario 4.

The third scenario (Scn3) is basically same method with the first scenario, while the pin connection of the top end of the steel pipe to the pier head that adopts the references [33, 19, 18] was proposed with perfect pin idealization (called fix-pin connection). Also, the fourth method (Scn4) is essentially the combination of the Scn1, the Scn2, and the Scn3 which implemented the redistribution of SPD's strength and stiffness, additional SPD's member, and pin connection between top end steel pipe to the pier head. The scenario and structural configuration of the seismic performance enhancement is shown in Table 4.3. The proposed of pin connection implementation that follows the reference [33], is expected to achieve not only the larger deformation limit capacity but also more sensitive deformation of the SPD, as shown in Figure 4.2B. The more sensitive deformation of the SPD can obtain the better dissipated energy achievement.

The SPD that located in the top of the pier with fix-pin connection might need larger ultimate deformation capacity (Δ_{ult3}) than the SPD that to be implemented in the pier with fix-fix connection. So that, the SPD's installation with gradual increment of ultimate deformation capacity from the bottom to the top position of the pier was conducted in the case of Scn3 and Scn4 (pin connection on the top end of steel pipe). For example on the implementation of Str5, Str8, Str10, Str13, Str15, Str18 and Str20, in which the SPD's length (b_w) is shown in Table 4.3.

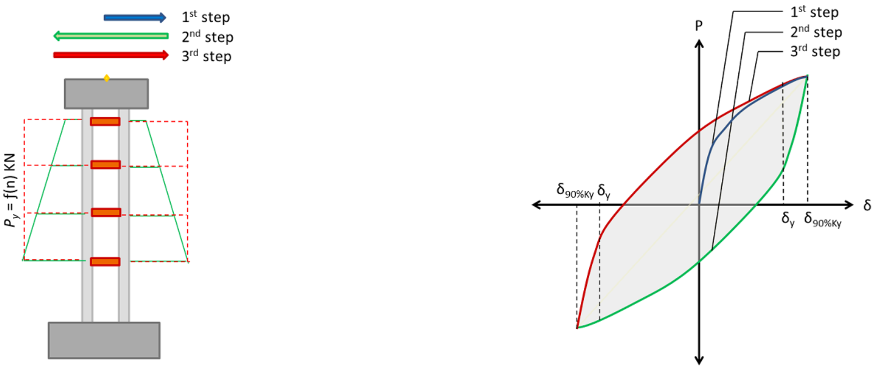

(A) (B)

FIGURE 4.6: (A) The step of cyclic loading and (B) the method of dissipated energy calculation.

The other hand, the SPD's shear force capacity that occurs in near to the fix connections of the column end might be the opposite with it's deformation sensitivity. The structures with fix-fix connections extensive SPD's shear force capabilities at the top and bottom ends, whereas in structures with fix-pin connections, this ability occurs at the bottom end of the column. This phenomenon happens because the part of the column that is located close to the fix constraint point has a greater rotational stiffness than the column portion on the free end. In this study, the several scenarios of dissipated energy improvement of the structure were conducted by keeping the deformation limit capacity value through the redistribution of SPD's strength proportional with to the rotational stiffness of the columns. The gradual strength distribution was applied in the several cases of Scn1, Scn3 and Scn4, for example Str5, Str8, Str10, Str13, Str15, Str18, and Str20.

In this analysis, the dissipated energy of the structures with each SPD strength configuration was calculated by a three-step of static analysis at the proposed limit state following the reference [13], as illustrated in Figure 4.6B. The largest energy dissipation in each structural configuration was obtained by calculating the energy dissipation based on the thickness variation of the topmost located SPD. The parameters of SPD dimension with the largest energy dissipation in each structural configuration that include the length (b_w), the height (d_w), and the thickness (t_w) are shown in Table 4.3.

In this study, the limit state of the structure was improved with some additional criteria. The first, the deformation limit of the structure was determined with the 90% stiffness of steel pipe column yielding. This limit state determination is expected to control the accumulation of the plasticized steel pipe cross-section so that the structure can achieve near to elastic behavior. While based on the reference [22], the maximum strain limit of steel pipe cross section that was determined by Hanshin Expressway is $2\varepsilon_y$. In the reference [22] criteria, the limit states and the soundness of the element members related the structural performance are shown in Figures (B.1-B.3). Also, in this proposed limit state, it was conceived that the largest deformation of the SPD is still below the limit criteria with the Soundness 3 ($20\gamma_{sy}$) based on references [6, 11].

4.4.3 The structural performance verification method

The structural performance was verified by non-linear static pushover and dynamic analysis. Static pushover analysis was performed to observe not only the behavior of the structure but also the limit state of the structure. In a static pushover analysis, the loading was applied by the displacement increment with Newton algorithm up to a maximum deformation of 0.5 m. In the dynamic analysis, there were two types ground motion excitation of the severe earthquake acceleration records (Type I and Type II of Level 2) which are based on reference [14]. From the two types of the ground motion excitation, three acceleration input of it were selected which considers the different soil conditions. The ground acceleration records is shown in Figures (A.5 and A.6) and the response spectra is shown in Figures (A.8 and A.9). Each of the maximum displacement responses of the structure was recorded and presented together with the skeleton curve and the limit state point. This dynamic analysis applies Newmark integration (β = 0.25 and γ = 0.5) with time interval of 0.001.

The residual deformation of the structure was measured by recording after the ground motion excitation finished. During the recording of residual deformation, the average deformation of the structure was calculated. The two types of post-earthquake structural deformation records were defined i.e. the SPD condition still connected with structure, and the SPD state was removed from the structure. The recording of the two residual deformation records was performed at (T_{eq} to T_{eq}+5) and (T_{eq}+15 to T_{eq}+20), respectively. When at the time (T_{eq}+15), the SPD was released during the free vibration. In the numerical simulation of Opensees, "UpdateParameter" command [9] was implemented to release of the SPD. The objective of deformation observation with two different methods is to observe the residual deformation and the structural to monitor of re-centering ability before and after structural refurbishment of severe earthquake occurrence.

4.5 Results and Discussion

In several sub-sections of this section, the structural characteristics, the structural energy dissipation, and the structural seismic performance were discussed. The structural characteristic scope includes the the limit state, the deformation capacity, the strength and stiffness, and the SPD deformation sensitivity. Also, the quantity of energy dissipation and equal damping of the structure were discussed in sub-section of the structural energy dissipation. Furthermore, in the structural seismic performance sub-section, the linkage of the strength, the deformation limit capacity and the dissipated energy capacity to the seismic response of the structure were discussed.

In the study of Shinohara et.al. [27], the influence of the pier basic properties to the structural behavior and seismic performance was examined by numerical analysis. In that numerical analysis, the fiber section of frame element was implemented with the material parameters followed the JRA 2002 code [14]. Also, the other structural parameters was adopted from the typical studies [12, 15]. In this study, the structural model calibration was conducted by matching the structural output parameters. As the results, it has a good agreement with the previous study [27]. The skeleton curve and the limit point comparison as shown in Figure 4.7A. Based on this comparison, it is clear that the skeleton curve and the yielding point of the SPD and the steel pipe column coincide. As this calibration result, the proposed numerical model is quite close to the numerical model of the reference [27].

The optimum dissipated energy in each proposed structural configuration was searched by varied the thickness of the determined SPD distribution along the pier height. As the result of the dissipated energy optimization in Figure 4.7B, the strength of the SPD that is influenced by the SPD thickness gives substantial contribution in the optimum dissipated energy enrichment. Also it was investigated that the implementation fix-pin connection system in the top end of the steel pipe has more significant dissipated energy achievement than the implementation of the fix-fix of one.

4.5.1 The structural behavior

In the Performance 2a of Hanshin Expressway's criteria [22], the maximum strain limit of steel pipe column shall be less than $2\varepsilon_y$. In this study, the deformation limit of the structure was determined with the 90% stiffness of steel pipe column yielding (the blue circle point), as shown Figure 4.7A. As the pushover analysis result, in the proposed deformation limit, the

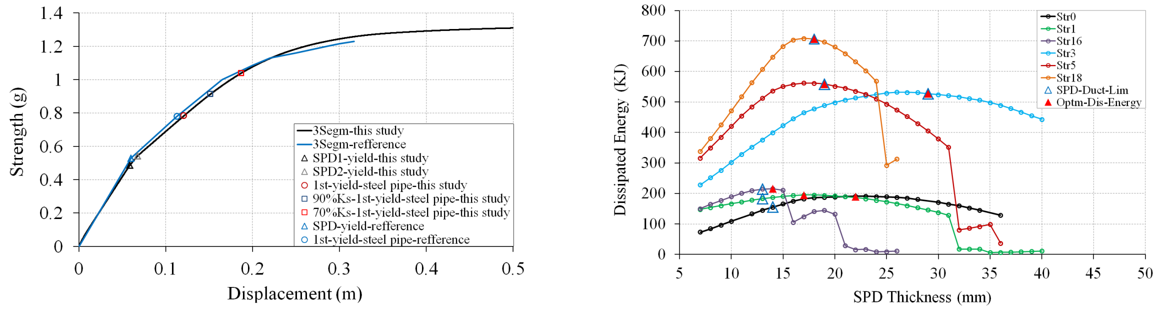

(A) (B)

FIGURE 4.7: The curve of: (A) calibration skeleton of the structural model and (B) dissipated energy optimization.

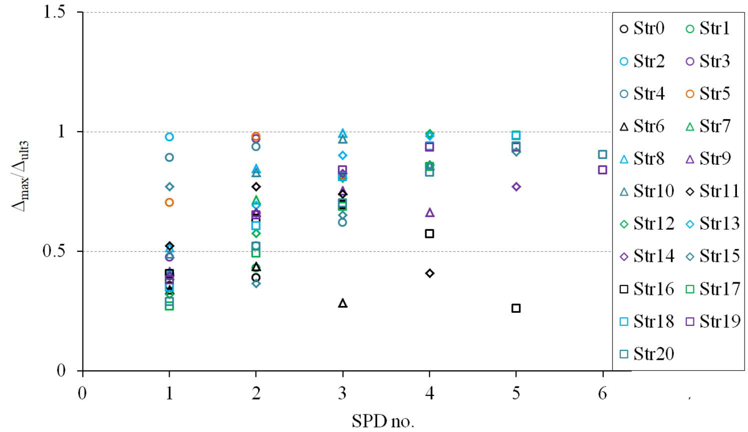

FIGURE 4.8: The SPD deformation ratio between maximum and ultimate value in the soundness 3 and Performance IIa.

steel pipe section was plasticized at a 116° of mean angle (the plastic area of the steel pipe column below 1/3 of the total area) and at a $1.44\varepsilon_y$ of average maximum strain. The tabular data of deformation limit related the cross section strain can be seen in Table 4.4. Hence, the proposed deformation limit still below the Performance 2a limit which is determined by Hanshin Expressway. Also, it was confirmed that the largest deformation of the SPD is still below the limit criteria with the Soundness 3 ($20\gamma_{sy}$) based on reference [6, 11]. The value of the SPD deformation ratio to the ultimate deformation limit is shown in Figure 4.8. So, it can be guaranteed that the SPD performance can remain stable in the Performance 2a.

California Department of Transportation has been determined the pipe-pin connection system between the top end RC pier and the pier head. Furthermore, the seismic performance and the behavior of this system was deeply studied by the reference [33]. This connection system can reduce the bending moment of the top end pier substantially [19] due to the single curvature achievement of the column on the bent system. The other hand, the integrated bridge pier with multiple steel pipes that developed by the Hanshin Expressway just implements fix-fix connection on the top and bottom of steel pipes end. Consequently, it only achieves limited of the dissipation energy and the deformation limit capacity. In this study, the adoption of the pipe-pin connection is expected to achieve single curvature of the steel pipe member so that the deformation limit capacity and the dissipated energy of the structure can be improved. The dissipated energy improvement can be achieved by the increasing of SPD's deformation sensitivity due to the single curvature behavior of the steel pipe.

As the analysis result that is shown in Table 4.4 and the Figure 4.9, the differences of the steel pipe top end connection systems (scenarios 1 and 2 compared scenarios 3 and 4) result the different deformation limit capacity. On the deformation limit of the 90% stiffness of yielding deformation, the fix connection at the top end of steel pipe achieves average deformation limit about 15.2 cm which is 1.27 times of the yielding deformation. Whereas in the proposed pin connection, the structure without SPD at the top end of the steel pipe produces the deformation limit in the average range of 24.9 cm which is about 1.32 times of the yielding deformation. While the average deformation limit capacity of the pier with the addition of SPD at the end of the steel pipe is 22.6 cm which is about 1.36 times of the yielding deformation. The addition of SPD at the top end of the steel pipe increases the deformation limit capacity less than the structure without and with the addition of the SPD. Thus, the implementation of pin connection in the top end of the column without additional SPD increases the deformation limit capacity 1.63 and 1.48 times than the structure which implements the fix connection, respectively. The fix connection implementation on the top end of the pier insults the double curvature distribution of the steel pipe, as shown in the Figures (4.10A and 4.10B). While the implementation of pin connection on it achieve single curvature distribution, as shown in Figures (4.10C and 4.10D). Therefore, the implementation of pin connection can enhance the deformation limit capacity of the structure. The other hand, the smaller deformation limit capacity improvement of the added SPD on top end column due to the restraint effect of the SPD to the top end of the steel pipe. The SPD's restraint effect results semi-rigid (between the perfect pin and the rigid connection) character of the top end steel pipe connection.

As way as the hypothesis, the structures with fix connections at the top end of the columns raises the most sensitive deformation of SPD at the central location of the column height. Whereas in the implementation of pin connections, it raises the most SPD's sensitivity at the top to the column and significantly achieve more sensitive deformation than the fix connection system. The comparison of the SPDs response under cyclic loading are shown in Figure 4.11. This phenomenon happens because the difference curvature distribution that mentioned above

TABLE 4.4: The parameter of the structural behavior and seismic performance.

Str. name	Structural behavior at the deformation limit						Structural performance					
							Max. deformation response (mm)			Max. residual deformation (mm)		
	δ_y (mm)	$\delta_{lim90\%}$ (mm)	Sector angle of plastic arch (°)	$\varepsilon/\varepsilon_y$	Diss. enrg. (KJ)	ζ_{eq} (%)	δ_{max}	$\delta_{max}/\delta_{lim90\%}$	Earthquake. no.	δ_{res1}	δ_{res2}	Earthquake. no.
Str0	123.60	153.90	111.86	1.40	195.30	9.92%	239.0	1.55	2-II-II-1	20.92	14.23	2-II-III-1
Str1	120.90	151.40	111.39	1.39	191.01	10.05%	238.3	1.57	2-II-II-1	20.31	14.73	2-II-III-1
Str2	195.70	252.60	110.10	1.41	527.53	19.27%	321.0	1.27	2-II-III-1	18.92	6.93	2-II-II-1
Str3	195.20	249.20	108.72	1.39	527.67	18.93%	309.1	1.24	2-II-III-1	17.08	0.80	2-I-III-1
Str4	124.90	155.40	108.59	1.41	205.49	10.71%	232.5	1.50	2-II-II-1	22.21	18.04	2-II-III-1
Str5	177.90	235.70	112.31	1.41	558.87	20.90%	271.3	1.15	2-II-II-1	26.46	9.57	2-II-III-1
Str6	119.20	151.90	115.78	1.43	206.62	10.67%	228.5	1.50	2-II-II-1	19.69	10.78	2-II-III-1
Str7	179.10	241.30	118.50	1.47	597.16	21.17%	272.4	1.13	2-II-II-1	30.22	6.17	2-II-III-1
Str8	201.90	261.90	114.57	1.43	625.92	20.05%	284.6	1.09	2-II-II-1	20.53	7.80	2-II-III-1
Str9	150.60	211.90	117.78	1.47	527.63	21.60%	255.7	1.21	2-II-II-1	49.60	6.63	2-II-III-1
Str10	176.00	239.20	120.22	1.47	640.07	21.75%	246.0	1.03	2-II-II-1	50.28	4.00	2-II-III-1
Str11	120.30	154.00	117.97	1.45	210.76	10.60%	225.9	1.47	2-II-II-1	18.50	10.80	2-II-III-1
Str12	172.50	236.10	120.75	1.48	634.03	22.19%	249.0	1.05	2-II-II-1	53.15	3.42	2-II-III-1
Str13	194.40	254.80	115.91	1.42	672.05	21.48%	262.3	1.03	2-II-II-1	42.06	3.79	2-II-III-1
Str14	147.90	210.30	120.78	1.49	546.85	21.70%	239.0	1.14	2-II-II-1	58.59	5.26	2-II-III-1
Str15	172.10	233.50	120.17	1.44	662.12	22.15%	234.9	1.01	2-II-I-1	52.78	3.27	2-II-III-1
Str16	116.60	150.30	120.24	1.44	215.53	10.66%	213.5	1.42	2-II-II-1	15.33	3.30	2-II-III-1
Str17	170.00	233.40	120.11	1.46	657.41	22.83%	237.5	1.02	2-II-I-1	58.87	3.24	2-II-III-1
Str18	192.50	252.80	115.79	1.41	706.89	22.28%	247.5	0.98	2-II-II-1	54.51	3.44	2-II-III-1
Str19	142.70	203.40	122.04	1.47	533.48	20.98%	234.0	1.15	2-II-I-1	47.93	3.10	2-II-III-1
Str20	164.00	224.70	120.84	1.45	658.10	22.26%	218.6	0.97	2-II-I-1	48.74	2.92	2-II-III-1

h: height of the pier; δ_y: yielding deformation; $\delta_{lim90\%}$: 90% yielding stiffness deformation; δ_{max}: maximum deformation response; δ_{res1}: natural residual deformation response; δ_{res2}: residual deformation response after SPD to be released; ε: ratio of strain at the proposed deformation limit to the yield strain; ε_y: yield strain; ζ_{eq}: equal damping ratio.

triggers different response to the SPD. The single curvature formation produce more accumulative deformation due to all the part of the steel pipe has the same rotation direction. While the double curvature formation achieve smaller cumulative deformation due to the difference rotation direction of each steel pipe part. Therefore, in the implementation of pin connection, the SPD deformation located in the upper region of the column should satisfied with the deformation limit of soundness 3.

In the theory of pure column stiffness comparison with fix-pin and fix-fix of the end moment restraint, the fix-pin connection has a stiffness about 0.25 times than the fix-fix connection. The structures that implement fix-pin connections have smaller second stiffness than the structure which adopts fix-fix connections. This statement was evidenced by the analysis results in the Figure 4.9 where the average stiffness ratio of the two structure types in Scn3 with Scn1 and

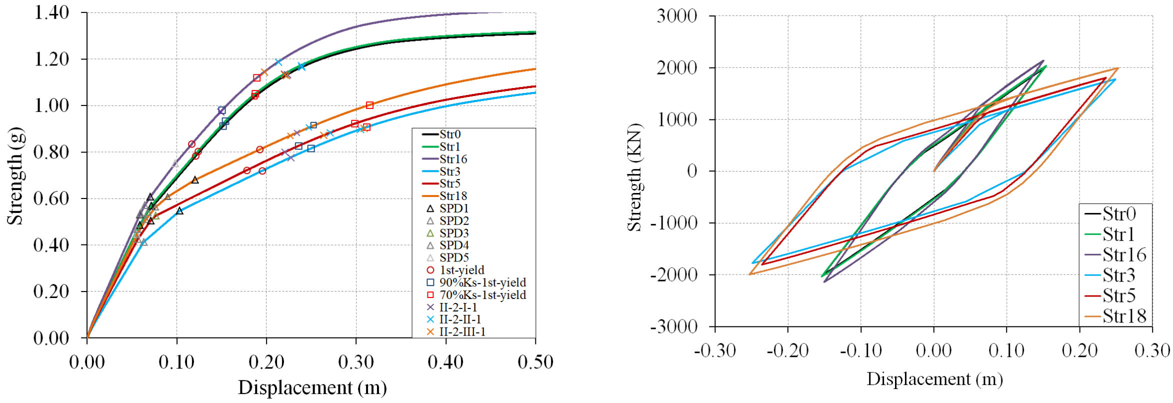

(A) (B)

FIGURE 4.9: The comparison of enhanced structure with the original designed structure in the terms of (A) skeleton curves and (B) hysteresis loops.

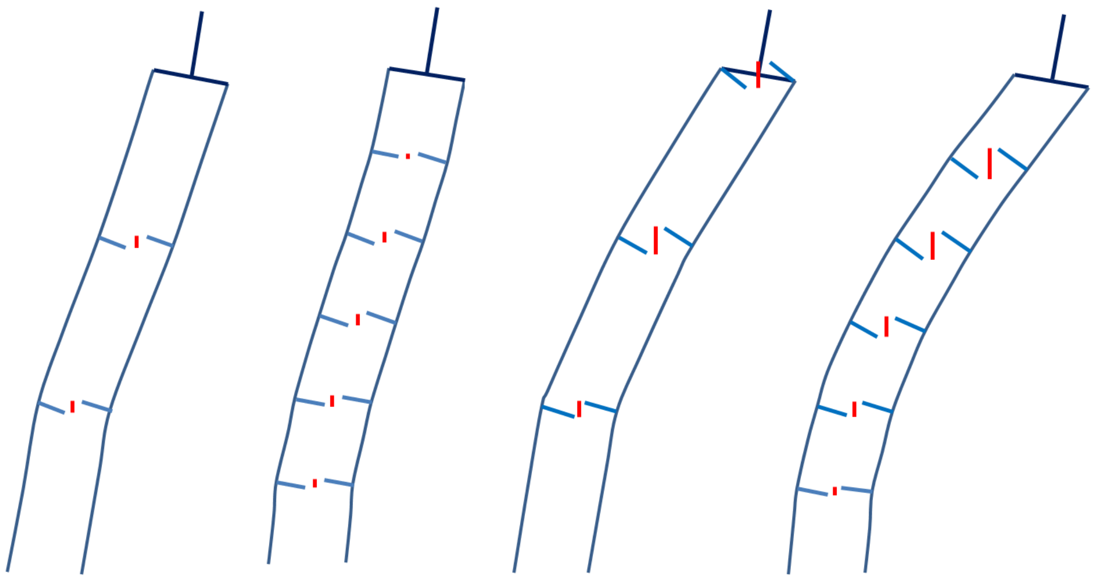

(A) (B) (C) (D)

FIGURE 4.10: The structural deformed shape under lateral load: (A) Str0, (B) Str16, (C) Str5, and (D) Str18.

Scn4 with Scn2 is about 0.4 times. While, the effect of post-yield stiffness of the SPD make the stiffness difference than the condition without SPD, so the stiffness ratio between the structure with SPD and without SPD is different. The other hand, the first stiffness of the structure at the best optimum energy dissipation (Str18) is slightly different. This condition occurs because when all SPD is still elastic, the structure behaves close to the monolithic conditions along the column height, while when all SPD occurs yield, the structural stiffness near to the pure column contribution. Besides, the transitional deformation values (the first transition stiffness

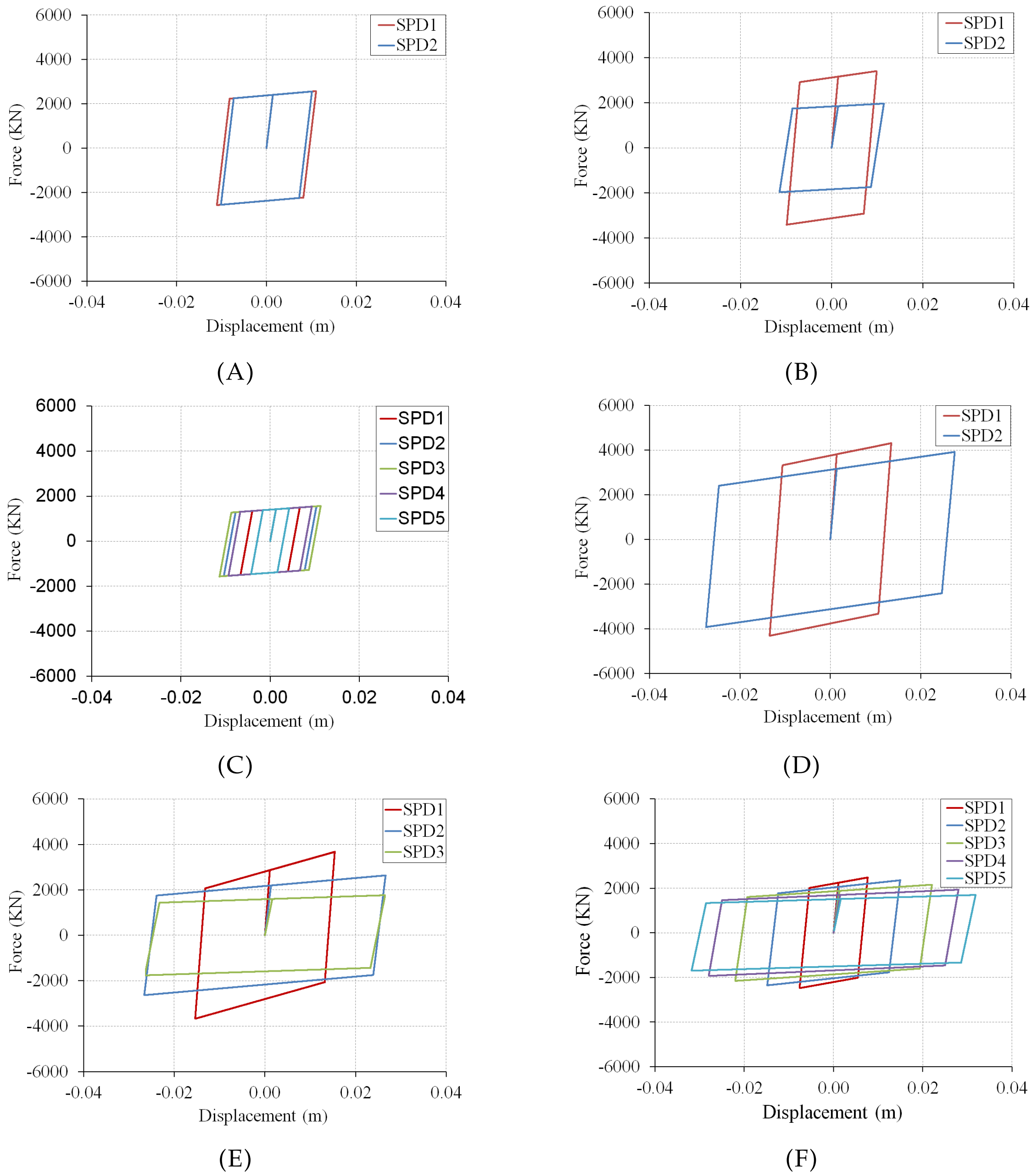

FIGURE 4.11: The SPD hysteresis curves of: (A) Str0, (B) Str1, (C) Str16, (D) Str3, (E) Str5, and (F) Str18.

point with the second stiffness) in all structural variations that under optimum conditions of dissipation energy are almost equal. The transition stiffness triggered by the sequence of the yielding SPD.

The length of the column segment can affect the strength and stiffness of the structure at the deformation limit. This statement was evidenced by the analysis results in Figure 4.9. For example, Str16 has strength and stiffness greater than Str0. Also, in the case of structures which implement pin connection in the top-end, Str18 also has strength and stiffness larger than Str5.

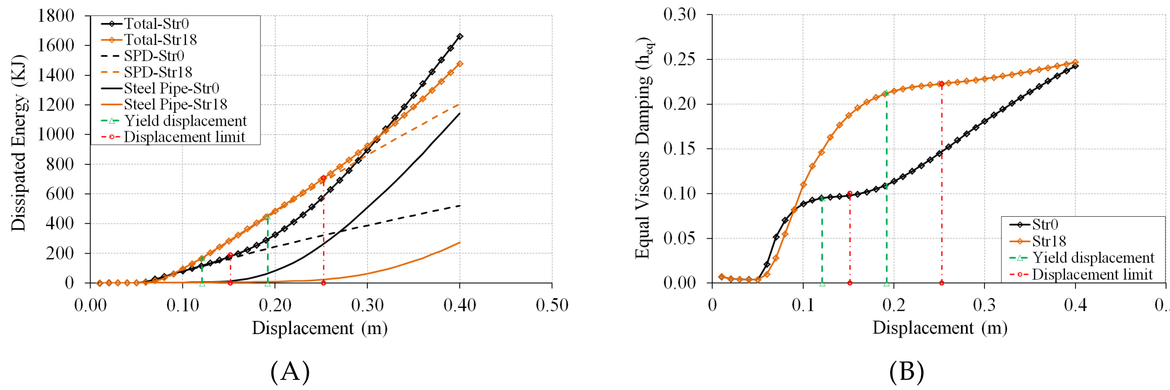

FIGURE 4.12: The dissipated energy comparison of Str18 to the Str0: (A) the dissipated energy composition and (B) the equal damping.

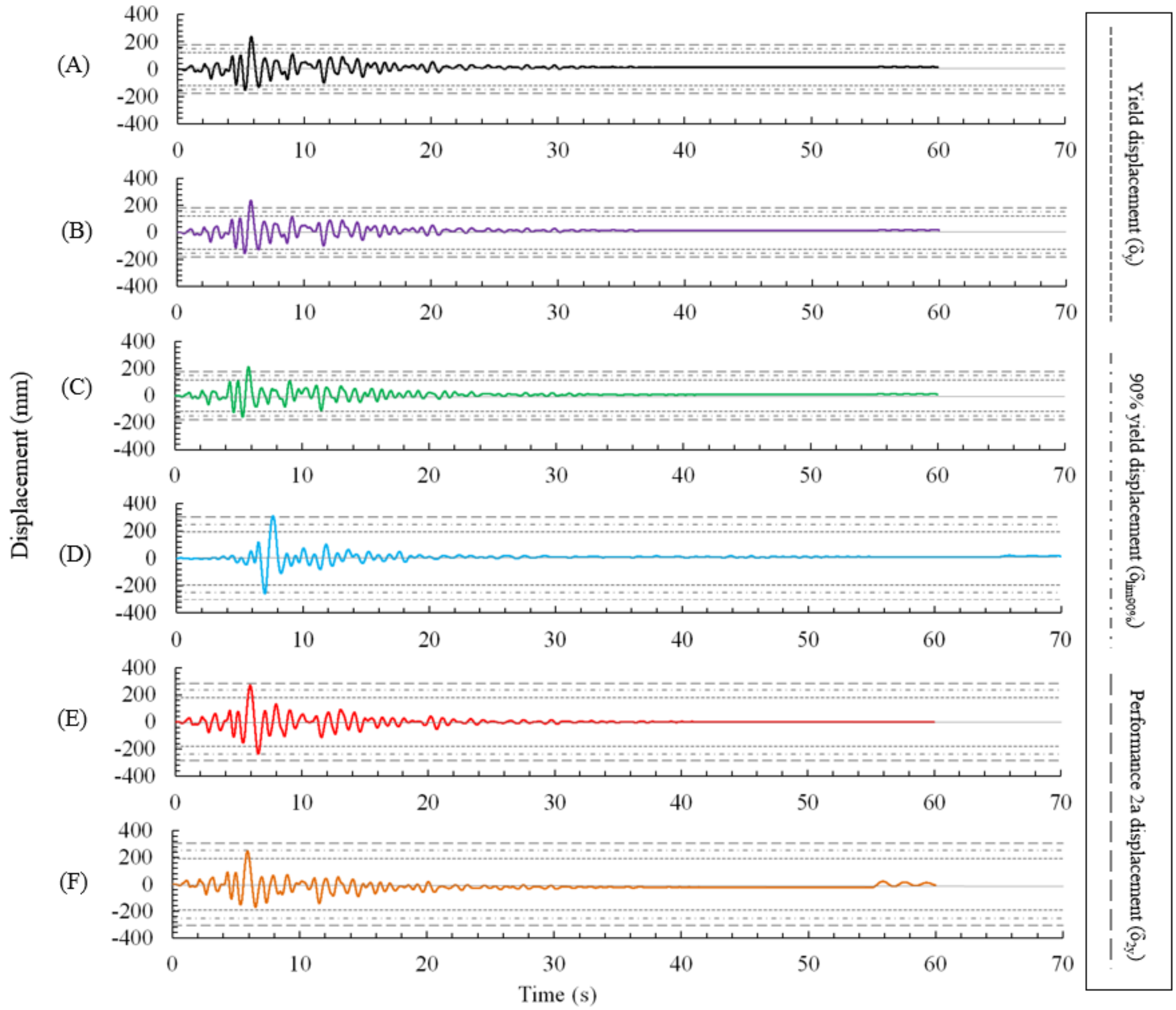

FIGURE 4.13: Maximum displacement responses of the structure under seismic excitation Level 2 of: (A) Str0, (B) Str1, (C) Str16, (D) Str3, (E) Str5, and (F) Str18.

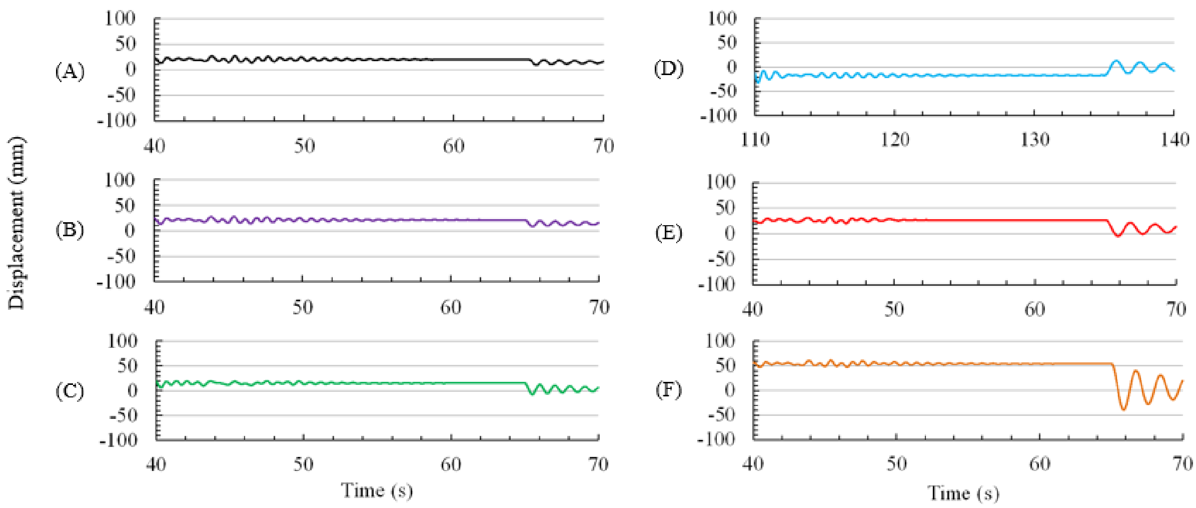

FIGURE 4.14: Maximum residual displacement responses of the structure under seismic excitation Level 2 of: (A) Str0, (B) Str1, (C) Str16, (D) Str3, (E) Str5, and (F) Str18.

In both examples, the deformation capacity ratio of each compared structural case is almost the same. This condition occurs due to the shorter of the column segment has the greater column stiffness in carrying the moment triggered by the SPD shear force. So that, to achieve the optimum dissipated energy, it requires more SPD number along the pier height with smaller shear strength.

4.5.2 The dissipated energy of the structure

Based on the observation of Table 4.4, the structures with the fix-fix connection on the top end of the steel pipe (the first scenario (Scn1) and the second scenario (Scn2)) have less significant dissipated energy. In this case, the greatest dissipated energy enhancement is the Str16 which is 14% with the dissipated energy value is 215.53 KJ. The damping ratio that generated on this system is 10.66%. As described in the previous sub-section, the implementation fix-fix connection of the structure causes the limited deformation of the SPD and also results in a small global deformation limit capacity of the structure.

Structures that implement fix-pin connections on the top end of the steel pipe achieve significant dissipated energy enhancement. In the third scenario (Scn3), the dissipated energy of Str5 reaches 558.87 KJ or equal to 194% times of the Str0 improvement. While in the fourth scene (Scn4), the dissipated energy increase proportional to the number of the pier segments. For example, the Str18 that applies 6 segments and 5 SPD produces dissipated energy 272% greater

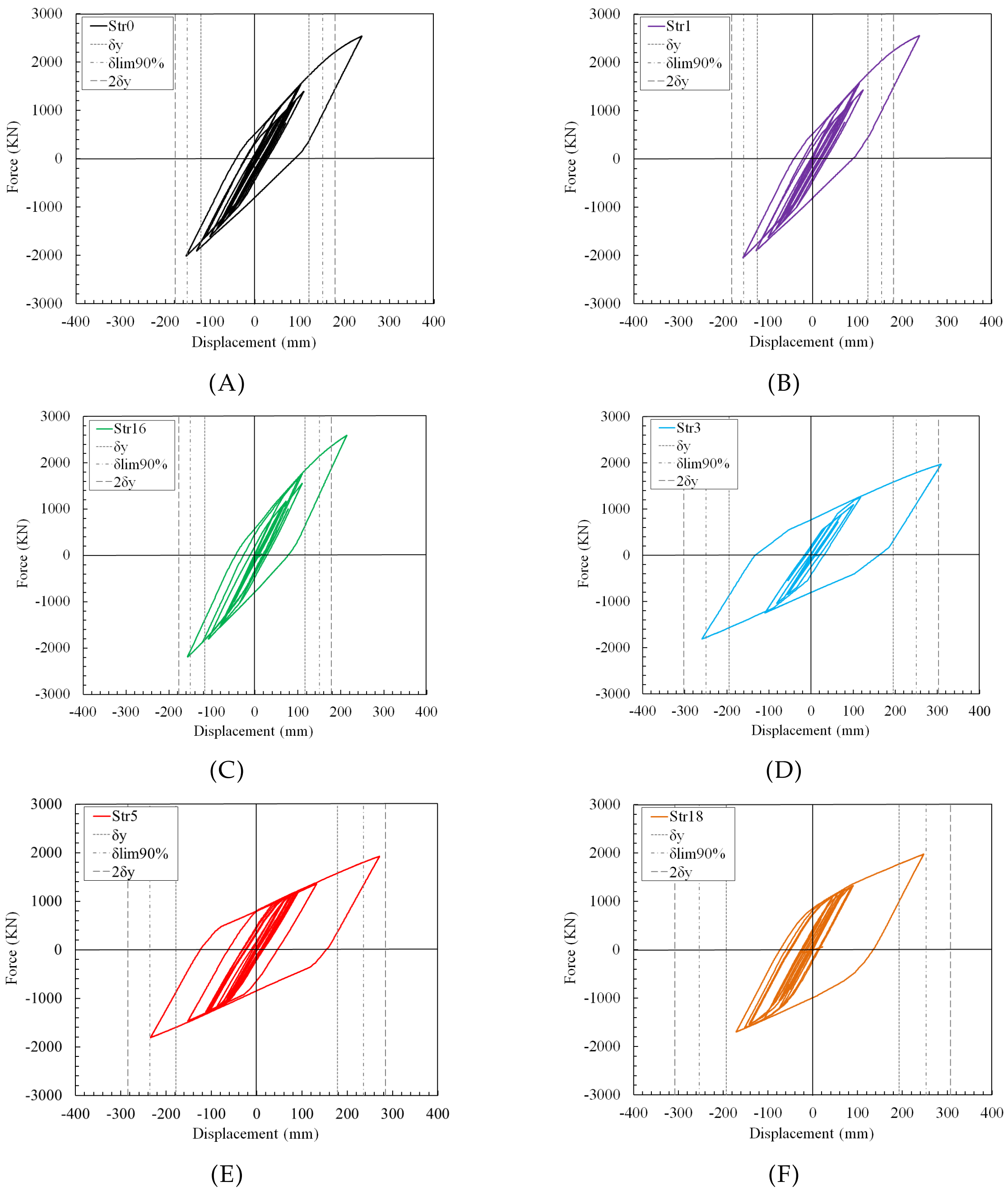

FIGURE 4.15: The force and displacement seismic response of: (A) Str0, (B) Str1, (C) Str16, (D) Str3, (E) Str5, and (F) Str18.

than the Str0. The Str18 achieves an equal damping ratio of 22.28%. The optimized structural properties and dissipated energy are shown in Table 4.4 and Figure 4.7B, respectively.

Furthermore, based on the analysis result of Table 4.4, with equal number of the SPD, the deformation limit and the dissipated energy of the structure that the SPD distribution proportional to the column stiffness (Non-Uniform; NU) will be greater than the structures which implement the uniform SPD distribution (U). For example, the deformation limit capacity and the dissipated energy of Str4 with Str5, Str7 with Str8, Str9 with Str10, Str12 compared Str13, Str14 with Str15, Str17 with Str18, and, Str19 with Str20 were observed, as shown in Table 4.4. Except in the case of comparisons Str2 with Str3, this occurs because the structure has only 2 SPDs mounted at 1/3h and 2/3h. In this condition, the steel pipe columns still has great potential to shift SPD number 2 with greater strength. The strength of SPD number 2 on uniform distribution (U) is greater than uniform (NU).

The dissipated energy quantity that could be represented visually by the hysteresis loop shape in Figure 4.10B is affected by the transition stiffness, strength, and deformation limit capacity of the structure. Structures that have short-range transition stiffness, sufficient strength, and large deformation limit capacity will produce significant dissipated energy. Therefore, dissipated energy enhancement was conducted by solving the best solution for three conditions to enrich optimal result.

In the monitoring of energy dissipation related the structural deformation, below proposed deformation limit, there is a more accelerated energy achievement of the best enhanced structure (Str18) compared to the original configuration of the structure (Str0), as shown in Figure 4.12A. While over the deformation limit, the dissipated energy achievement of the Str0 increase faster than the Str18. Generally, both the compared structures that which implement the fix and pin connection rise significantly on the 7 cm deformation upwards. Then, the total dissipated energy of both structural systems increase linearly up to the deformation limit. This phenomena occur because the SPD dominates the dissipated energy generation below the deformation limit. Furthermore, the energy dissipation rises more significant over the deformation limit because the yielding of steel pipe column contributes to adding structural significant energy dissipation. In the larger deformation, the significant dissipated energy increment occurs on the Str0 rather than the Str18 in case the top plastic hinge formation of the steel pipe to produce energy dissipation.

On the equal damping ratio observation of Figure 4.12B, there are a small equal damping achievement under the 7 cm deformation. These damping are only triggered by a concrete material that has an opening when it has a tensile strain. There are the nearly constant equal damping between the yielding point and the proposed deformation limit of the structure. On the proposed deformation limit of the best optimization, the equal damping value of each structure that implement the fix-fix and fix-pin connections are 10.03% and 22.28%, respectively. After the deformation limit exceeded, the damping value increases sharper linearly as the structural deformation increases.

4.5.3 The structural performance verification

Based on the study of the Nakamura et. al. [22], the pier structure only capable to achieve the Performance IIb under Level 2 of seismic excitation. In this study, the seismic performance verification was conducted by dynamic analysis by implementing the two types of Level 2 of earthquake excitation [14]. The structural response including the maximum response and the residual deformation before and after the releasing of SPD are shown in Table 4.4.

As the performance verification results, the structure that implements fix-fix connections averagely has a smaller maximum deformation response than the structure with the structure which implements fix-pin connection. Even though the displacement response is relatively smaller than the structure which implements fix-pin connection, all structures that implement the fix-fix connection have been exceeded the proposed deformation limit. The maximum displacement time history response and proposed deformation limit of the structures are shown in Figure 4.13. The occurrence of displacement response structures that implement fix-fix connection have relatively smaller than the one with fix-pin connection due to the greater strength and stiffness as described in the previous section. Besides, the effect of increased structural attenuation due to steel pipe column yielding also contributes to reducing the deformation response of structures that apply fix-fix connections. Based on the maximum response of the structure that is shown in Table 4.4 which is matched with the Figure 4.12B, the structure with fix-fix connection achieve an equal damping of about 14%. Furthermore, in the best dissipated energy improvement of the Scn1 and Scn2 (Str16), the lateral force demand is slightly increase, as shown in Figure 4.9A.

Although the deformation response of structures that apply fix-pin connection is relatively larger than the structure that implements the fix-fix connections, the maximum deformation ratio to the deformation limit $\delta_{max}/\delta_{lim90\%}$ of the structures are smaller than the structures which implement fix-fix connection. In the case of Str18 and Str20, the structure have a maximum response below the proposed deformation limit. This occurrence is influenced by not only the large deformation limit capacity but also the significant equal damping. By observing and matching the deformation response of the structure in Table 4.4 and the Figure 4.12B, the structure that applies fix-pin connection averagely has an equal damping of about 22%. Furthermore, in the best dissipated energy improvement of the Scn3 and Scn4 case (Str18), the lateral force demand could be decreased up to 22%, as shown in Figure 4.9A.

The addition of the number of segments along the height of the structure also improves the performance of the structure both in the structure that implements fix-fix connection and fix-pin connections. Based on Table 4.4, the maximum displacement response of the structure is getting smaller as the number of column segments increases. It caused by the dissipated energy and strength of the structure are the growth in line with the number of column segments. The best seismic performance for the structure that implements fix-fix connections is Str16 with a maximum response ratio of 1.42 whereas the structure with the fix-pin connection is Str20 with a maximum response ratio of 0.97.

Even though the structures that implement fix-pin connection generally have larger residual deformation than the structures with fix-fix connections, they have better re-centering capability after the SPD to be released. The releasing SPD connection after earthquake excitation stimulates the changing of residual deformation of the structures that implement fix-pin connection, as shown in Table 4.4 and Figure 4.14. Under earthquake excitation, the structures that implements fix-pin connection occur maximum strain is less than $1.44\varepsilon_y$ and the plastic area is less than 33%. The re-centering capability maybe related the quantity of the columns cross section part which remains behave elastic. The structures with the fix-pin connections have the maximum responses below the deformation limit in which there is small portion plastic strain. Based on the hysteresis loop observation in Figures (4.15D, 4.15E, and 4.15F), in the maximum response, the structural second stiffness remains stable.

While on the structures with fix-fix connections cases, there is small changing in their residual deformation. Based on the response maximum displacement ratio in Table 4.4, it occur maximum strain larger than $2.00\varepsilon_y$ (Performance 2a limit). In the possible reason for this phenomena, the cross section of the steel pipe column occurs an enormous amount of plastic strain due to the maximum responses of has exceeded the deformation limit. Based on the hysteresis loop observation in Figures (4.15A, 4.15B, and 4.15C), in the maximum response, the structural second stiffness starting decease significantly.

4.6 Conclusions

The seismic performance enhancement of integrated bridge pier with multiple steel pipes connected by friction damper was conducted successfully. As the result, it can realize several advantages including not only increases the seismic performance but also reduces the lateral load demand of the structure. The detail of the achievement results are explained below:

(a) The fix-pin connection implementation could increase the deformation capacity of the limit up to 1.63 times from the initial design of the structure.

(b) The structures which implement the fix-pin connection could produce second stiffness with 0.4 times smaller than the structure with the fix-fix connection and smaller resistance force at the same deformation point. However, it's initial stiffness and transition stiffness point slightly lower than the structure with the fix-fix connection.

(c) There was insignificant dissipated energy enhancement of the structure with the fix-fix connection which the best improvement achieved is 14%. Also, its damping ratio achievement at the deformation limit is 10.66%.

(d) Improving the dissipated energy of structure with fix-pin connections occurs the satisfied results which the best improvement achieved is 272%. Also, the damping ratio at the deformation limit is 22.28%.

(e) The structures that implement fix-pin connections had smaller deformation response ratio than the structures that adopt fix-fix connections. Even though the deformation value of the structure that implement fix-pin connection was slightly greater than the original one, the smaller deformation ratio was caused by the improvement of deformation limit capacity and the dissipated energy enhancement.

(f) Even though the structures that implement fix-pin connection generally had larger residual deformation than the structures with fix-fix connections, they had better re-centering capability after the SPD was released.

(g) In the best seismic performance enhancement of the structure (case Str18), the lateral seismic force demand could be reduced up to 22% from the original structural configuration.

Bibliography

[1] Abebe, D.Y., Jeong, J.S., Kim, J.W. and Choi, J.: Analytical Study on Large Deformation in Shear Panel Hysteresis Damper Using low Yield Point Steel, in *2013 NZSEE Conference*, Xx, pages 0–6, 2013.

[2] Bosco, M., Marino, E.M. and Rossi, P.P.: Modelling of steel link beams of short, intermediate or long length, Engineering Structures, volume 84, no. February:406–418, 2015.

[3] Caccese, V., Elgaaly, M. and Chen, R.: Experimental Study of Thin Steel-Plate Shear Walls under Cyclic Load, Journal of Structural Engineering, volume 119, no. 2:573–587, 1993.

[4] Chen, Z., Bian, G. and Huang, Y.: Hysteretic Behavior of Shear Panel Dampers under High Axial Compression Loading, Advanced Steel Construction, volume 9, no. 3:190–204, 2013.

[5] Chen, Z., Fan, H. and Bian, G.: Parametic Analysis of Shear Panel Dampers under High Axial Compression, Advanced Steel Construction, volume 11, no. 1:1–14, 2015.

[6] Chen, Z., Ge, H. and Usami, T.: Hysteretic Model of Stiffened Shear Panel Dampers, Journal of Structural Engineering, volume 132, no. 3:478–483, 2006.

[7] Clayton, P., Berman, J.W. and Lowes, L.: Seismic design and performance of self-centering steel plate shear walls, Journal of Structural Engineering, volume 1, no. JANUARY:22–30, 2011.

[8] El-Bahey, S. and Bruneau, M.: Bridge Piers with Structural Fuses and Bi-Steel Columns. I: Analytical Investigation, Journal of Bridge Engineering, volume 17, no. 1:36–46, 2012.

[9] Gu, Q., Conte, J.P. and Barbato, M.: OpenSees Command Language Manual: Response Sensitivity Analysis based on the Direct Differentiation Method (DDM) OpenSees Command Language Manual : DDM-Based Response Sensitivity Analysis Introduction, 2010.

[10] Hashimoto, K., Sugiura, K., Nishioka, T. and Tamba, Y.: Mechanical Behavior of Steel Pier Integrated Steel Pipes Subjected to Axial, Torsional and Cyclic Horizontal Load, Journal of JSCE, volume 70, no. 1:80–93, 2014.

[11] Hashimoto, K. et al.: Effect of Structural Parameters of Shear Panel Damper on Seismic Performance of Multi-pipe Integrated Bridge Pier, Journal of JSCE, volume 72, no. 1:75–91, 2016.

[12] Hashimoto, S., Abe, M. and Fujino, Y.: Damage Analysis of Hanshin Expressway Viaducts during 1995 Kobe Earthquake. III: Three-Span Continuous Girder Bridges, Journal of Bridge Engineering, volume 10, no. 1:61–68, 2005.

[13] Jacobsen S., L.: Steady forced vibrations as influenced by damping, Transactions, volume 52, no. 15:169–181, 1930.

[14] Japan Road Association: *Specifications for Highway Bridges: Part V Seismic Design*, Maruzen Co. Ltd., Tokyo, 2012.

[15] Kanaji, H. et al.: Experimental Study on Seismic Performance of an Integrated Column by Multi Steel Pipes with Hysteretic Damper, Journal of JSCE, volume 13, no. 49:59–72, 2006.

[16] Malakoutian, M., Berman, J.W. and Dusicka, P.: Seismic response evaluation of the linked column frame system, Earthquake Engineering and Structural Dynamics, volume 6, no. May 2013:795–814, 2012.

[17] Mazzoni, S., McKenna, F., Scott, M.H. and Fenves, G.L.: OpenSees Command Language Manual, 2007.

[18] Mehraein, M. and Saiidi, S.: Seismic Performance of Bridge Column-Pile-Shaft Pin Connections for Application Accelerated Bridge Costruction, Technical Report 2, University of Nevada, Reno, Reno, 2016.

[19] Mehrsoroush, A. and Saiidi, M.S.: Experimental and analytical seismic studies of bridge piers with innovative pipe pin column-footing connections and precast cap beams, Technical report, University of Nevada, Reno, Reno, 2014.

[20] Menegotto, G., Pinto, M. and Emilio, P.: Method of Analysis for Cyclically Loaded R.C. Plane Frames Including Changes in Geometry and Non-Elastic Behavior of Elements under Combined Normal Force and Bending, in *Proceedings of IABSE Symposium on Resistance and Ultimate Deformability of Structures Acted on by Well Defined Loads*, pages 15–22, Zurich, 1973.

[21] Nader, M., Maroney, P. and Eng, P.: Seismic Design for the Self Anchored Suspension Bridge–San Franciso Oakland Bay Bridge, IABSE Symposium Report, volume 102, no. 2014-09-01T00:00:00:1307–1314, 2014.

[22] Nakamura, R., Kanaji, H. and Kosaka, T.: Development and Design of New Steel Pipe Integrated Pier with Shear Link, Technical report, Hanshin Expressway Company Limited, Osaka, 2014.

[23] Roberts, T.M. and Ghomi, S.S.: Hysteretic characteristics of unstiffened plate shear panels, Thin-Walled Structures, volume 12, no. 2:145–162, 1991.

[24] Scott, M.H., Fenves, G.L., McKenna, F. and Filippou, F.C.: Software Patterns for Nonlinear Beam-Column Models, Journal of Structural Engineering, volume 134, no. 4:562–571, 2008.

[25] Scott, M.H. and Hamutçuoğlu, O.M.: Numerically Consistent Regularization of Force-based Frame Elements, International Journal for Numerical Methods in Engineering, volume 76, no. 10:1612–1631, 2008.

[26] Setiawan, A.F., Takahashi, Y., Kiyono, J. and Sawada, S.: Numerical Analysis of RC Columns Accompanied with Friction Damping Mechanism under Cyclic Loading, in *Procedia Engineering*, volume 171, pages 821–835, Denpasar, 2017.

[27] Shinohara, M., Kanaji, H., Oniki, K. and Sugiura, K.: Basic Properties of an Integrated Column by Multiple Steel Pipes with Hysteretic Shear Damper, Journal of JSCE, volume 58A:471–483, 2012.

[28] Shinohara, M., Kanaji, H., Oniki, O. and Kimura, M.: A Proposal of a Bridge Column Integrated by Multiple Steel Pipes with Directly-connected Piles and a Seismic Response Analysis, Journal of JSCE, volume 69, no. 3:312–325, 2013.

[29] Spacone, E., Filippou, F.C. and Taucer, F.F.: Fibre Beam-Column Model for Non-Linear Analysis of R/C Frames : Part II. Applications, Earthquake Engineering and Structural Dynamics, volume 25, no. January:727–742, 1996.

[30] Takahashi, Y., Takemoto, Y., Takeda, T. and Takagi, M.: Experimental study on thin steel shear walls and particular steel bracings under alternative horizontal load their stiffness is so rigid that structure designed by static analysis, Technical report, Ohbayashi-Gumi Ltd., Tokyo, 1973.

[31] Taucer, F.F. and Spacone, E.: Aa Fiber Beam-Column Element for Seismic Response Analysis of Reinforced Concrete Structures, Technical Report December 2014, Earthquake Engineering Research Center College of Engineering University of California, Berkeley, California, 1991.

[32] Thorburn, L.J., Kulak, G.L. and Montgomery, C.J.: Analysis of Steel Plate Shear Walls, Technical report, Department of Civil Engineering, The University of Alberta, Alberta, 1983.

[33] Zaghi, A.E. and Saiidi, S.: Seismic Design of Pipe-Pin Connections in Concrete Bridges, Technical Report January, University of Nevada, Reno, Reno, 2010.

[34] Zhang, C. et al.: The Lightweight Design of a Seismic Low-Yield-Strength Steel Shear Panel Damper, Materials, volume 9, no. 6:424, 2016.

Chapter 5

Development of a Shear Panel Damper Plus Gap

5.1 General Remarks

This chapter discusses the development of a shear panel damper plus gap (SPDG) device. The experimental study of half-scale of four SPDG specimens was conducted with cyclic loading protocol. Also, the numerical analysis was performed to calibrate the specimen parameter and to verify its behavior. There are two methods of numerical analysis for the SPDG specimens, including a spring model and a three-dimensional finite element (3D FE) model. In the spring model, the stiffness and strength factor of the proposed damper specimens were adjusted by matching the hysteresis loop skeleton of the experimental result. Furthermore, in the 3D FE simulation, the gap mechanism and the SPDG strength factor verification were conducted by monitoring the skeleton curve and stress distribution in the web panel of SPDG. As the result, under deformation load, the proposed SPDG device can achieve a sufficient flexibility under the gap length and sufficient energy dissipation over the gap length. Furthermore, in the 3D FE simulation, it was verified that the reduced stiffness and strength of web panel due to the free-side connection type which triggering the diagonal compression yielding mechanism.

5.2 Background

The high seismic performance of integrated bridge pier with multiple steel pipe columns connected by shear panel damper (SPD) has been developed and applied by Hanshin Expressway [17]. With the dissipated energy of SPD, the structure can absorb sufficient vibration energy due to severe earthquake excitation. So that the structural damage can be descended, the implication is the life-cycle-cost reduction [17]. As shown in Figure 5.1A, the shear panel damper device contains a web panel with low yield strength steel material, a flange with ordinary strength steel material connected to the side edges of the web panel. In the implementation, this damper device connected to the steel pipe columns by the joint member, as in Fig 5.1B. Some studies on such kinds structure have been conducted. The first, experimental study on the seismic performance of integrated steel pipes pier connected by hysterical dampers based on reference [14]. Also, the basic property of an integrated steel pipes pier with hysterical damper was suggested by reference [19]. In that study, the shape properties related the device performance was investigated. The other hand, the advisability of the direct connection system between the superstructure and the pier in the integrated bridge pier with multiple steel pipe columns connected by shear panel damper (SPD) needs to be studied more deeply. Because possibility of infirmity was the high degree of structural uncertainty could evoke the internal induction force of structural member and stress-induces-fatigue [20] of the SPD components due to the frequent lateral deformation of the daily load. The unhandled of the SPD's stress-induces-fatigue can propagate deterioration SPD in the lifetime. The deterioration of the SPD can reduce the seismic performance of the structure.

In term of the shear panel damper development sequence, it was started from the experimental study of thin steel shear wall damper by Takahashi et.al.[22], then the method of analysis was developed by Thorburn et.al. [24]. The study of the hysterical behavior of plate shear panels was proposed by reference [18], followed by experiments from the thin plate shear wall to find out more about cyclic behavior performed by reference [2]. Then, the hysterical parameter of shear panel damper under cyclic loading of SPD was proposed by the Chen et. al. [5]. Also, the SPD behavior which is subjected to axial load has been conducted by reference [3, 4]. More ever, the application of low-yield SPD steel materials for the seismic design was performed by reference [25] and for seismic design on large deformations was studied by reference [1]. Furthermore, the development of SPD with buckling restrainer was developed by [11]. Finally, the deformation capacity of SPD by considering the cyclic fatigue effect was determined by the reference [23]. However, based on the all of the predecessor research above, there was no research about the damper device that could solve its deterioration due to frequent lateral deformation of the pier during the lifetime.

This study discusses the development of a shear panel damper plus gap (SPDG) device. The experimental study of half-scale of four SPDG specimens was conducted with cyclic loading

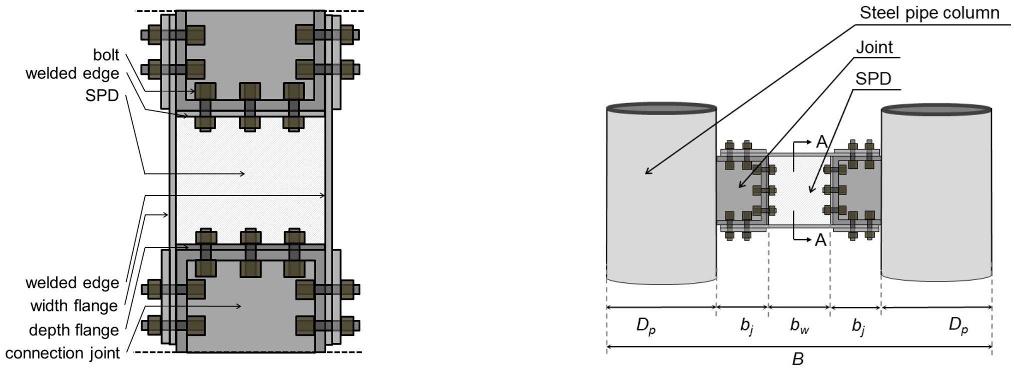

(A) (B)

FIGURE 5.1: (a) SPD components and (b) Steel pipe columns connected by SPD.

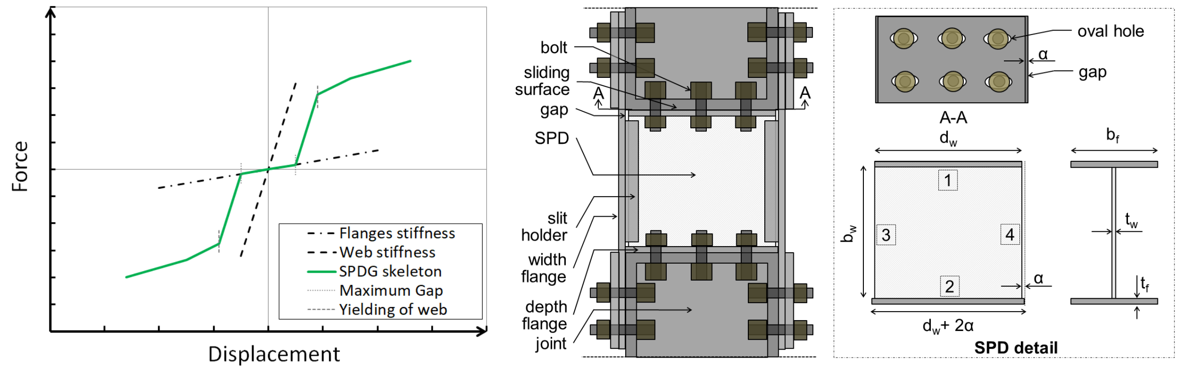

(A) (B)

FIGURE 5.2: A proposed SPDG device: (a) SPDG behavior and (b) SPDG components.

protocol. Also, the numerical analysis was performed to calibrate the specimen parameter and to verify its behavior. There are two methods of numerical analysis for the SPDG specimens, including a spring model and a three-dimensional finite element (3D FE) model. In the spring model, the stiffness and strength factor of the proposed damper specimens were adjusted by matching the hysteresis loop skeleton of the experimental result. Furthermore, in the 3D FE simulation, the gap mechanism and the SPDG strength factor verification were conducted by monitoring the skeleton curve and stress distribution in the web panel of SPDG. In this study, numerical analysis with spring model was conducted by Opensees software, while the 3D FE analysis was performed to verify the characteristics and mechanism of SPDG by using Abaqus software. As the result, under deformation load, the proposed SPDG device can achieve a sufficient flexibility under the gap length and sufficient energy dissipation over the gap length. Furthermore, in the 3D FE simulation result, it was verified that the reduced stiffness and strength of web panel due to the free-side connection type which triggering the diagonal compression yielding mechanism.

5.3 Shear Panel Damper

Shear panel damper consists of a low-yield strength steel web panel surrounded by ordinary-yield strength steel flanges around its edges, as shown in Figure 5.1. Due to the low-yield strength steel material of web panel, in a small deformation, it easily occurs yielding under shear deformation. Based on the reference [5], the device behavior was idealized as a bi-linear material with kinematic hardening. While the ultimate deformation capacity of SPD was determined by the reference [13]. So, the SPD hysteresis parameters are specified in Equation (5.1)-(5.9).

$$Q_n = \tau_w.b_w.t_w,\ \Delta = \gamma.b_w \tag{5.1}$$

$$\tau_u = \tau_f + \tau_w \tag{5.2}$$

$$\frac{\tau_w}{\tau_{wy}} = 0.918 + \frac{0.038}{R_w^2} \leq 1.2 \tag{5.3}$$

$$\frac{\tau_f}{\tau_{fy}} = 0.0287\,\frac{b_f}{b_w}.\frac{t_f}{t_w}\left(\frac{t_f}{t_w}4.\frac{d_w}{(n_L+1)\,R_w b_w}+2\right) \tag{5.4}$$

$$\tau_{wy} = \frac{\sigma}{\sqrt{3}} \tag{5.5}$$

$$R_w = \frac{b_w}{(n_L+1)\ t_w}\sqrt{\frac{12\,(1-\nu)\ \tau_y}{K\pi^2 E}} \tag{5.6}$$

$$K = 5.35 + 4.\left(\frac{b}{d}\right)^2 for.\left(\frac{d}{b}\right) \geq 1 \tag{5.7}$$

$$K = 5.35\,.\left(\frac{b}{d}\right)^2 + 4for.\left(\frac{d}{b}\right) < 1 \tag{5.8}$$

$$\begin{aligned}\overline{\frac{\gamma_u}{\gamma_y}} &= 20\ (\alpha \leq 0.8)\\ &= \tfrac{7.034}{(R_\tau+0.54)^{8.0}} + 4,\ (0.8 \leq \alpha \leq 1.5)\end{aligned} \tag{5.9}$$

With b is the component width, d is the component depth, t is the component thickness, n_L is the number of the stiffener flanges, E is the elastic modulus of steel material, Q_n is the shear force of the SPD, Δ is the displacement of the SPD, τ is shear stress of the steel material, γ_s is a shear strain of the steel material, and σ is an axial stress of the steel material.

TABLE 5.1: Specimen parameters of the experiment.

No	Spec.	Web (mm)			Depth flange (mm)		Width flange (mm)		Gap length (α, mm)		Friction force (KN)		Monitoring	Response type
		d_w	b_w	t_w	b_{f12}	t_{f12}	b_{f34}	t_{f34}	Top	Bot.	Top	Bot.		
1	Exp1	276	264	6	170	12	170	12	5.00	0.00	0.00	∞	MF1, MD1	Global
2	Exp2	276	264	6	170	12	170	12	4.00	0.00	50.00	∞	MF1, MD1, MD2	SPDG
3	Exp3	282	264	6	170	12	170	12	2.25	1.75	30.00	80.00	MF1, MD1, MD2, MD3	SPDG, SPD
4	Exp4	282	264	6	170	12	170	12	2.25	1.75	30.00	80.00	MF1, MD1, MD2, MD3	SPDG, SPD

Spec.: Specimen; Bot.: Bottom

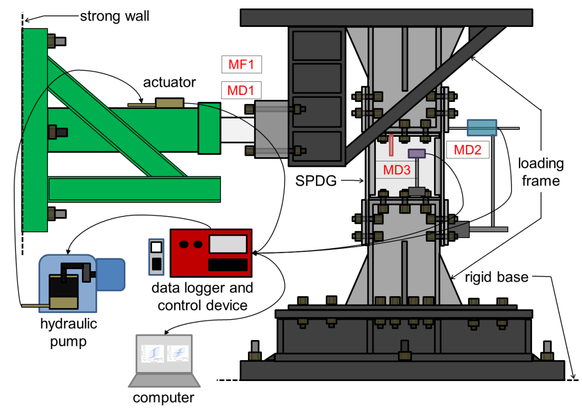

(A)

(B)

FIGURE 5.3: Experimental set up of SPDG: (a) illustration (b) real.

5.4 Experiment and Numerical Analysis of SPDG

In this study, to prevent the SPD deterioration due to the daily load which may be triggered by the cyclic fatigue of frequent lateral deformation, the seismic device named shear panel damper plus gap (SPDG) is introduced. The gap existence is expected to delay the web panel work under frequent lateral deformation in its range. While under severe seismic excitation, the deformation of the proposed seismic device over the gap length so that the web panel could contribute in absorbing the vibration energy, as illustrated in Figure 5.2A.

5.4.1 The components and behavior of SPDG specimen

The SPDG composed of a web panel component made of low-yield strength steel (named SY225) [21] with flanges connected along the bottom and top side (side 1 and 2) with fix connection in all degrees of freedom (DOF), while the side-edges (side 3 and 4) is just confined to the side flange's slit holder in the lateral degree of freedom (DOF), as shown in Figure 5.2B.

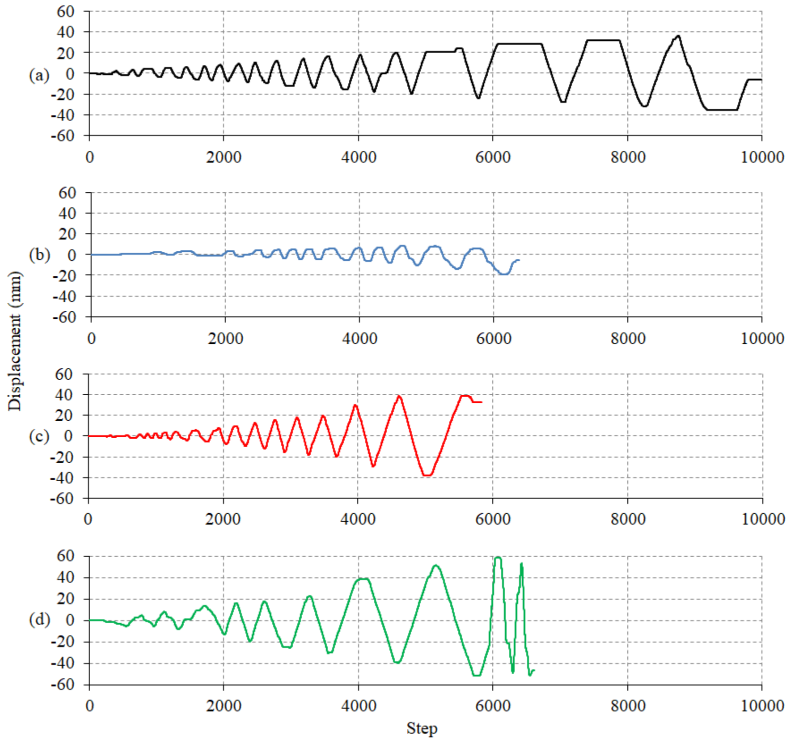

FIGURE 5.4: Experimental loading protocol with displacement control: (a) Exp1, (b) Exp2, (c) Exp3, and (d) Exp4.

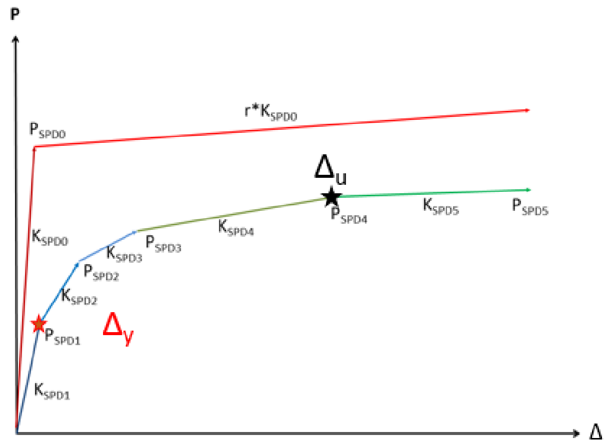

FIGURE 5.5: Illustration of SPDG parameters in the numerical model compared to the theoretical parameters.

Also, a gap is provided between the web panel and side flanges in the parallel direction of the plane. While the top and bottom side of the flanges are connected to the joint with bolts, whereby the bottom (side 2) is fixed in all directions of degrees of freedom whereas the top side (called the slip plane) is permitted to move in the shear loading direction. Furthermore, all the flanges of the SPDG are composed of ordinary-strength steel material (named SM570).

When the SPDG occurs deformation due to external shear forces, the side flanges will work

TABLE 5.2: Strength and stiffness factor definition of the SPD parameter to the experimental skeleton curve.

No	Comp.	Par. Id.	Eq.	Par. Id.	Eq.
1	SPD	FP_{SPD1}	P_{SPD1}/P_{SPD0}	K_{SPD1}	K_{SPD1}/K_{SPD0}
2		FP_{SPD2}	P_{SPD2}/P_{SPD1}	FK_{SPD2}	K_{SPD2}/K_{SPD1}
3		FP_{SPD3}	P_{SPD3}/P_{SPD1}	FK_{SPD3}	K_{SPD3}/K_{SPD1}
4		FP_{SPD4}	P_{SPD4}/P_{SPD1}	FK_{SPD4}	K_{SPD4}/K_{SPD1}
5		FP_{SPD5}	P_{SPD5}/P_{SPD1}	FK_{SPD5}	K_{SPD5}/K_{SPD1}
6	FD	FP_{FD}	P_{FD}/P_{SPD0}	K_{FD1}	40*P_{FD}
7		r	FK_{FD2}/K_{FD1}		

Comp.: Component; SPD: shear panel damper; FD: friction damper; Par. Id.: Parameter Identity; Eq.: Equation; FP: force factor; FK: stiffness factor; r: friction force ratio.

at the first time (called gap phase). In such conditions, the encounter surfaces between the top side flange and the joint (sliding surface) occur slip. When the sliding deformation is larger than the gap length, the side flange will push the web panel component. This state is the SPD starts to work (called the SPD phase). The main stiffness of web panel occurs in the deformation of the gap length up to the unloading stage. The re-loading stage is equal to the sequence of the loading stage which to be initiated with small stiffness due to the gap exists. In addition, this study also considers the friction effect due to confinement force at the sliding surface. The confinement force is inflicted by the pretension force of bolts. More ever, the experiment was conducted by applying 4 SPDG specimens, the SPDG specimen parameters are shown in Table 5.1.

5.4.2 Experiment set-up

The experiment of SPDG specimens was conducted with displacement control of quasi-static loading. The experimental equipment consists of an actuator, a mechanical dial gauge, a ray gauge, and loading frame. The actuator is horizontally supported by the strong wall, driving the shear force and measuring shear deformation (Δ_1) of SPD with the accuracy of 0.001 KN and 0.0005 mm respectively. While the mechanical dial-gauge that measures the SPDG displacement has 0.01 mm and a 100 mm of accuracy and deformation measurement capacity respectively. Also, the ray-gauge that installed in SPD component has a precision of 0.0001 mm and a 20 mm measurement capacity. In the experimental set-up, the bottom part of the loading frame connected to the strong pedestal and the top component connected to the actuator. While the loading set up is described as in Figure 5.3.

Furthermore, the parameters calibration of SPDG experiment was conducted with spring

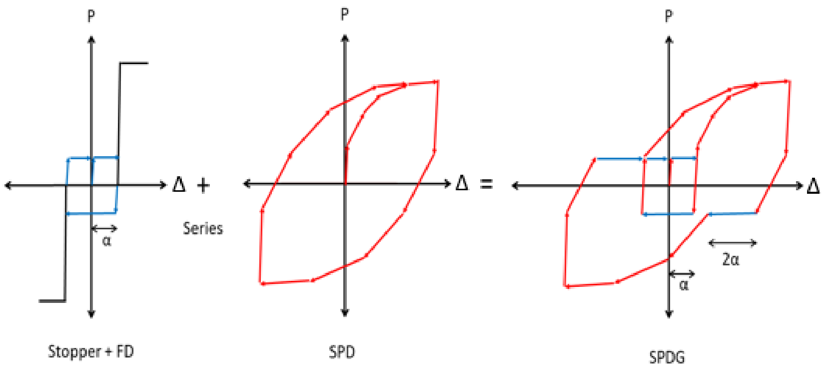

FIGURE 5.6: Idealization of SPDG material in the spring model.

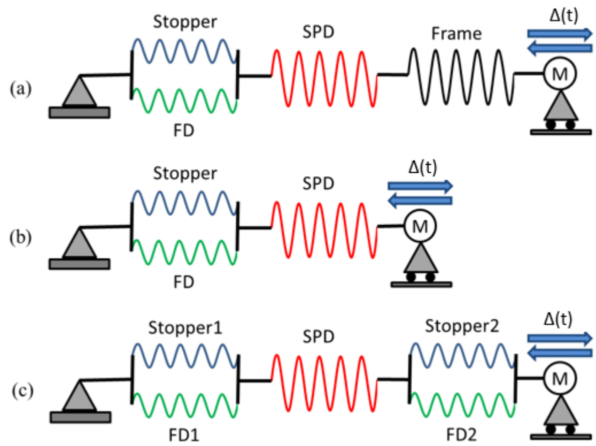

FIGURE 5.7: Element configuration of spring model: (a) Spring-Exp1, (b) Spring-Exp2, and (c) Spring-Exp3 and Spring-Exp4.

model in the dynamic analysis. In order the stability of dynamic analysis, experimental data displacement was smoothed with an exponential method. The smoothed displacement load protocol is presented in Figure 5.4. Also, to examine the mechanism of proposed seismic device, the 3D FE model was proposed.

5.4.3 Numerical analysis method of spring element model

The experimental parameters calibration was performed by finding the proper strength and stiffness factor of the matched skeleton curve to the determined SPD skeleton curve equation of the Chen et. al. [5]. The matched skeleton curve express the adjacent of the spring model to the experimental hysteresis loop. Furthermore, the strength and stiffness factor of SPDG compared to the determined SPD equation are illustrated and defined in Figure 5.5 and Table 5.2, respectively.

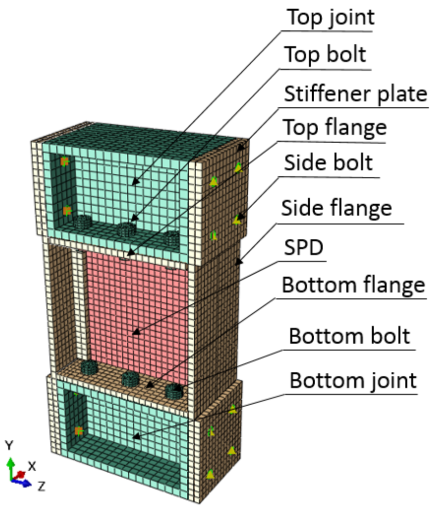

FIGURE 5.8: 3D FE model of SPDG.

In the numerical model, generally, the SPDG mechanism composes parallelly of stopper material and multi-linear material with kinematic hardening behavior [16] which are illustrated as in Figure 5.6. Also, the numerical model composes of spring elements and truss elements in Opensees software, the SPDG model configuration is presented in Figure 5.7. While the difference element configuration of the numerical model adapts the different scenario and measurement response method of each experimental specimen. More ever, the SPDG device parameters are considered to represent if the character of the hysteric curve between numerical models coincides with the experimental hysteretic curve. Furthermore, single point constraint with displacement excitation [16] was implemented to the SDOF structural model. In this dynamic analysis, at each step displacement of experimental loading protocol to be idealized equivalent to 0.1 seconds with analysis interval applied is 0.01 seconds.

5.4.4 3D FE modeling

In the verification of the SPDG mechanism, 3D FE simulation was also performed with monotonic loading using Abaqus software [8]. The side edges (side 3 and 4) of the SPDG web that is only confined by the slit holder of the side flanges might be influence the mechanical behavior of the sheer panel web. In the 3D FE analysis, the mechanical behavior of the ordinary SPD and SPDG was compared. The appropriate steel material parameters of SPD was investigated by matching the skeleton curve of an ordinary SPD model (named FE-01) to the SPD skeleton curve based on the determined Equations ((5.1)-(5.9)). Also, simulation of the FE-02 model was conducted to verify the effect of new proposed connection system between side edges and slit

TABLE 5.3: Part and element parameters of SPDG in the 3D FE model.

Model	Component	Element type	Comp. Num.	El. Qty.	Total
FE- 01	SPD + top and bottom flange	SC8R	1	1248	1248
	Side flange	SC8R	2	780	1560
	Stiffener plate	SC8R	4	196	784
	SPD joint	SC8R	2	936	1872
	Top and bottom bolt	Beam connector	12	1	12
	Side bolt	Beam connector	16	1	16
	Total				5492
FE-02	SPD + top and bottom flange	SC8R	1	1196	1196
	Side flange	SC8R	2	864	1728
	Stiffener plate	SC8R	4	196	784
	SPD joint	SC8R	2	936	1872
	Top and bottom bolt	C3D8R	12	640	7680
	Side bolt	Beam connector	16	1	16
	Total				13276
FE-Exp1	SPD + top and bottom flange	SC8R	1	1196	1196
	Side flange	SC8R	2	864	1728
	Stiffener plate	SC8R	4	196	784
	SPD joint	SC8R	2	936	1872
	Top and bottom bolt	C3D8R	6	640	3840
	Side bolt	Beam connector	16	1	16
	Total				9436
FE-Exp2	SPD + top and bottom flange	SC8R	1	1226	1226
	Side flange	SC8R	2	864	1728
	Stiffener plate	SC8R	4	196	784
	SPD joint	SC8R	2	936	1872
	Top and bottom bolt	C3D8R	12	640	7680
	Side bolt	Beam connector	16	1	16
	Total				13306

Comp. Num.: Component Number; El. Qty.: Element Quantity.

TABLE 5.4: Material parameters of SPDG in the 3D FE model.

No	Mat. Type	E (MPa)	σ^0 (MPa)	C_1	γ_1	$\sigma\|_0$ (MPa)	Q_∞ (MPa)	b
1	LY225	200000.0	225.0	2000.0	50.0	225.0	25.0	4.0
2	SM570	200000.0	345.0	2000.0	50.0	225.0	25.0	4.0

E: elastic modulus; σ^0: the evolution of the equivalent stress defining the size of the yield surface; C_1: kinematic hardening modulus; γ_1: the rate at which the kinematic hardening moduli decrease with increasing plastic deformation; $\sigma|_0$: the equivalent stress defining the size of the yield surface at zero plastic strain; Q_∞: the maximum change in the size of the yield surface; b: the rate at which the size of the yield surface changes as plastic straining develops.

holder of the side flange. To verify the effect of the gap and the friction surface the specimen models from the first to the second experimental scenarios (called FE-Exp1 and FE-Exp2) were also simulated by implementing 5.0 mm of the gap length. Furthermore, the geometric and

TABLE 5.5: Strength factor of the matched SPD parameter to the experimental skeleton curve.

No	Comp.	Par. Id.	Eq.	Factor of strength				
				Exp1	Exp2	Exp3	Exp4	Ave.
1	SPD	FP_{SPD1}	P_{SPD1}/P_{SPD0}	0.450	0.450	0.450	0.450	0.450
2		FP_{SPD2}	P_{SPD2}/P_{SPD1}	1.350	1.350	1.450	1.500	1.413
3		FP_{SPD3}	P_{SPD3}/P_{SPD1}	1.800	1.650	1.850	1.900	1.800
4		FP_{SPD4}	P_{SPD4}/P_{SPD1}	2.000	1.950	2.300	2.450	2.175
5		FP_{SPD5}	P_{SPD5}/P_{SPD1}	2.055	-	2.375	2.560	2.330
6	FD	FP_{FD}	P_{FD}/P_{SPD0}	0.060	0.060	0.060	0.060	0.060
7		r	K_{FD2}/K_{FD1}	0.005	0.005	0.005	0.005	0.005

TABLE 5.6: Stiffness factor of the matched SPD parameter to the experimental skeleton curve.

No	Comp.	Par. Id.	Eq.	Factor of stiffness				
				Exp1	Exp2	Exp3	Exp4	Ave.
1	SPD	K_{SPD1}	K_{SPD1}/K_{SPD0}	0.375	0.375	0.375	0.375	0.375
2		K_{SPD2}	K_{SPD2}/K_{SPD1}	0.150	0.150	0.150	0.125	0.144
3		K_{SPD3}	K_{SPD3}/K_{SPD1}	0.040	0.050	0.045	0.050	0.046
4		K_{SPD4}	K_{SPD4}/K_{SPD1}	0.015	0.020	0.033	0.030	0.024
5		K_{SPD5}	K_{SPD5}/K_{SPD1}	0.005	-	0.003	0.003	0.003
6	FD	K_{FD1}	40*P_{FD}	40	40	40	40	40

finite element model data are presented in Figure 5.8 and Table 5.3.

In the 3D FE simulation, the continuum shell element (SC8R) [9] was implemented to the web and SPD flanges. While the bolts that connect the top and the bottom side flanges to the joints were idealized as the hexahedral elements (C3D8R) [9]. Also, the beam connector type [6] attached the side flanges and the joints. The interaction between surfaces of the SPDG components was idealized as hard contact in the normal direction and penalty contact in the tangential direction by implementing perfect plastic friction behavior [6]. The steel material was idealized as a metal plasticity model with cyclic hardening [7], the input properties are presented as in Figure 5.3. The loading is performed by displacement control with the Newton algorithm [10]. The displacement load in the Z-axis direction was assigned to a reference point connected by rigid body interaction [6] with the top joint part. In addition, rigid body interactions were also applied to the bottom joint part connected to a reference point that was fixed in all of its DOF directions.

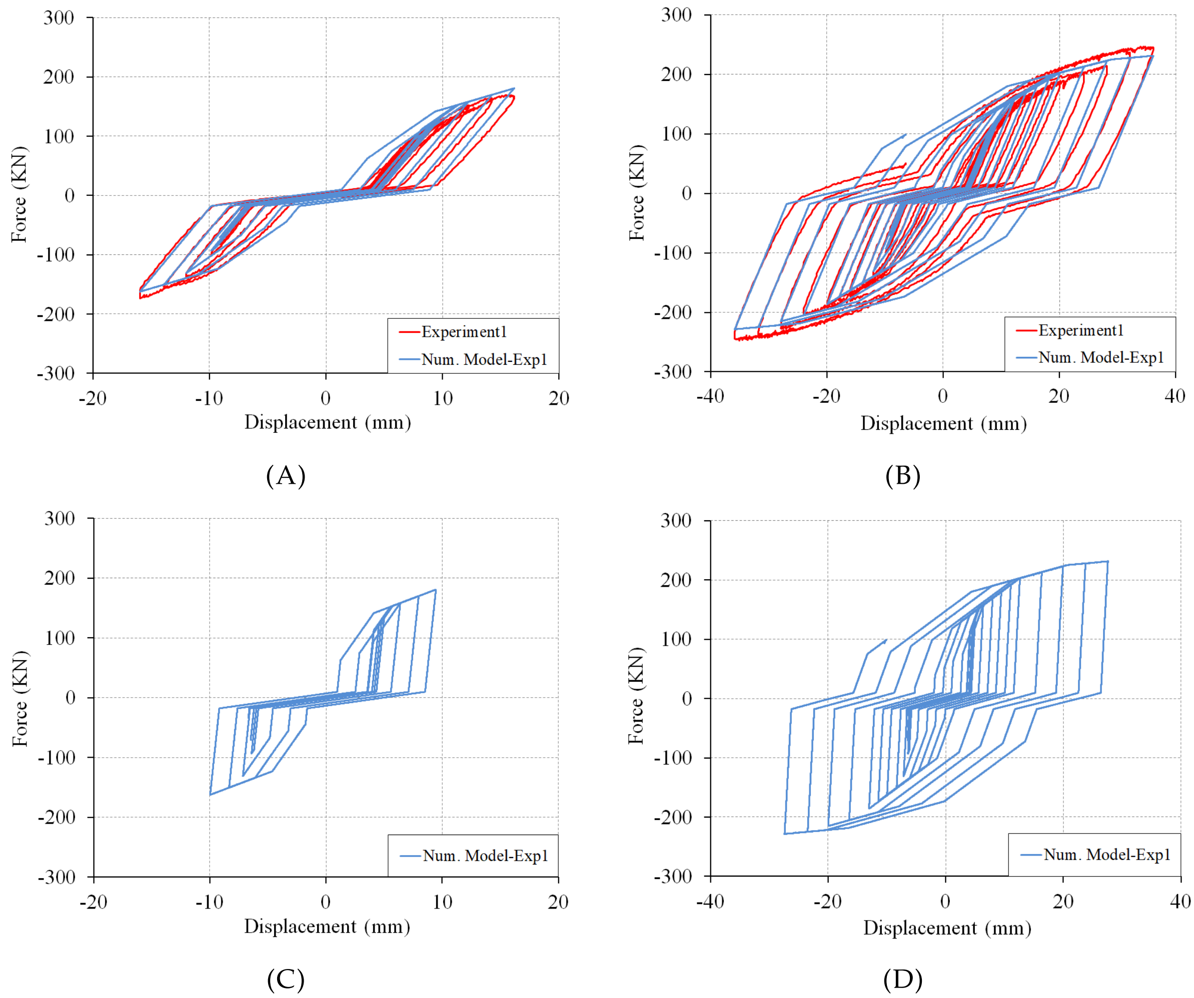

FIGURE 5.9: Hysteresis loop of experimental and numerical model Exp1: (a) small deformation of global response, (b) large deformation of global response, (c) small deformation of SPDG response, and (d) large deformation of SPDG response.

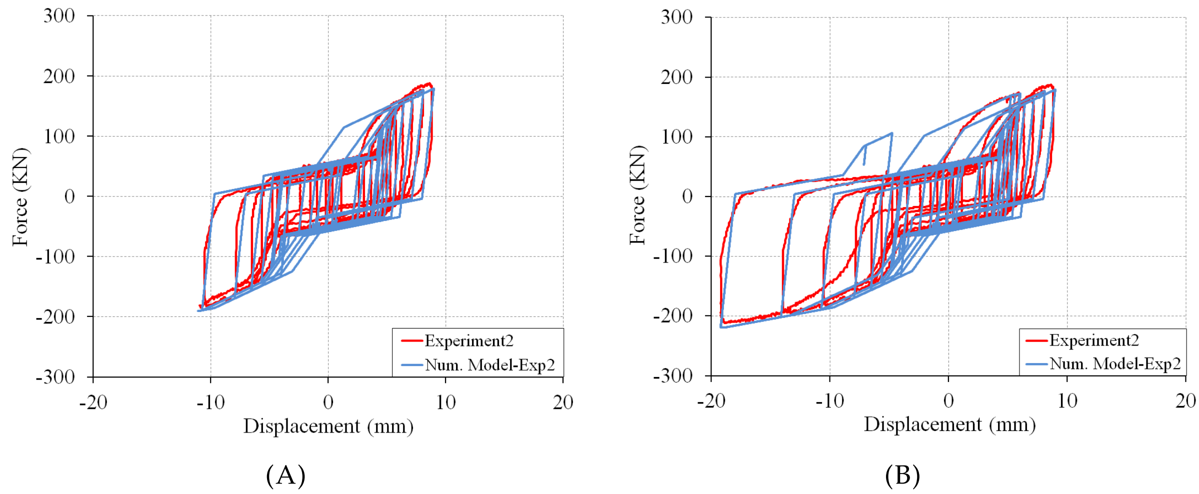

FIGURE 5.10: Hysteresis loop of experimental and numerical model Exp2: (a) small deformation of SPDG response and (b) large deformation of SPDG response.

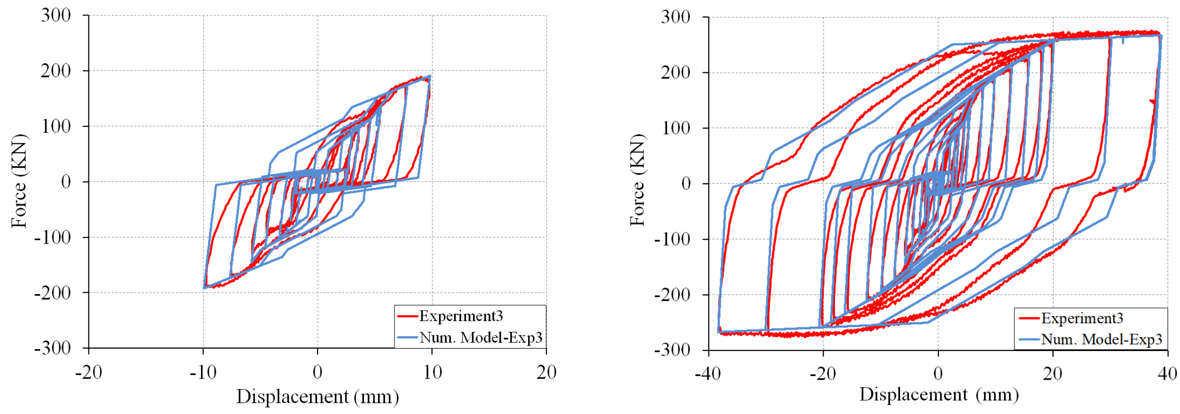

(A) (B)

FIGURE 5.11: Hysteresis loop of experimental and numerical model Exp3: (a) small deformation of SPDG response and (b) large deformation of SPDG response.

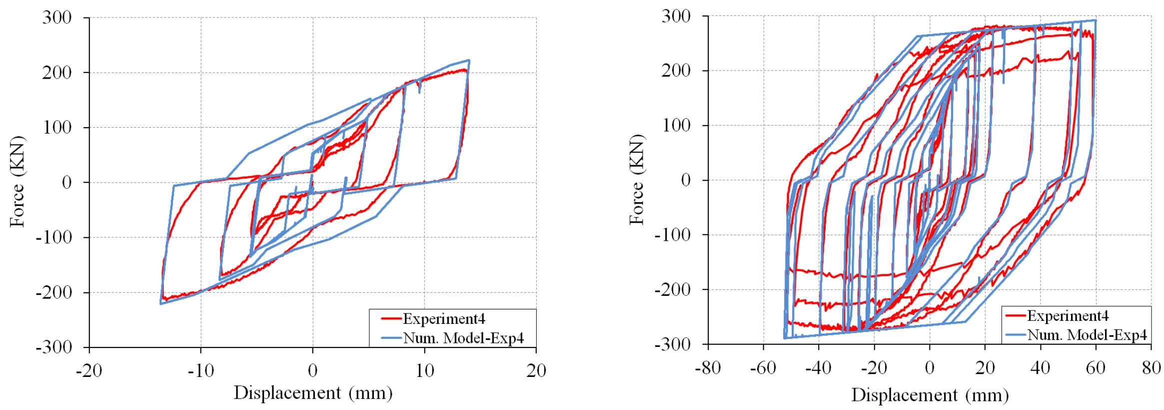

(A) (B)

FIGURE 5.12: Hysteresis loop of experimental and numerical model Exp4: (a) small deformation of SPDG response and (b) large deformation of SPDG response.

5.5 Results and Discussion

5.5.1 Experiment calibrated with spring model result

As the experimental calibrated by the spring model results, the proposed addition of gaps on the SPD device successfully realized. In Specimen 1 where no friction force is present on the sliding surface (side 1), the specimen stiffness at deformation which less than the gap length (5 mm) is much smaller than that of the SPDG main stiffness as shown in Figure 5.9. This initial stiffness is only produced by the side flanges on the 3 and 4 SPDG sides. Whereas in Specimen 2, 3, and 4 the initial stiffness of the structure is relatively similar to the SPDG main stiffness, due to the friction force of sliding surface as shown in Figures (5.10, 5.11, and 5.12). After the friction force is exceeded, the stiffness of these specimens drops to the stiffness of

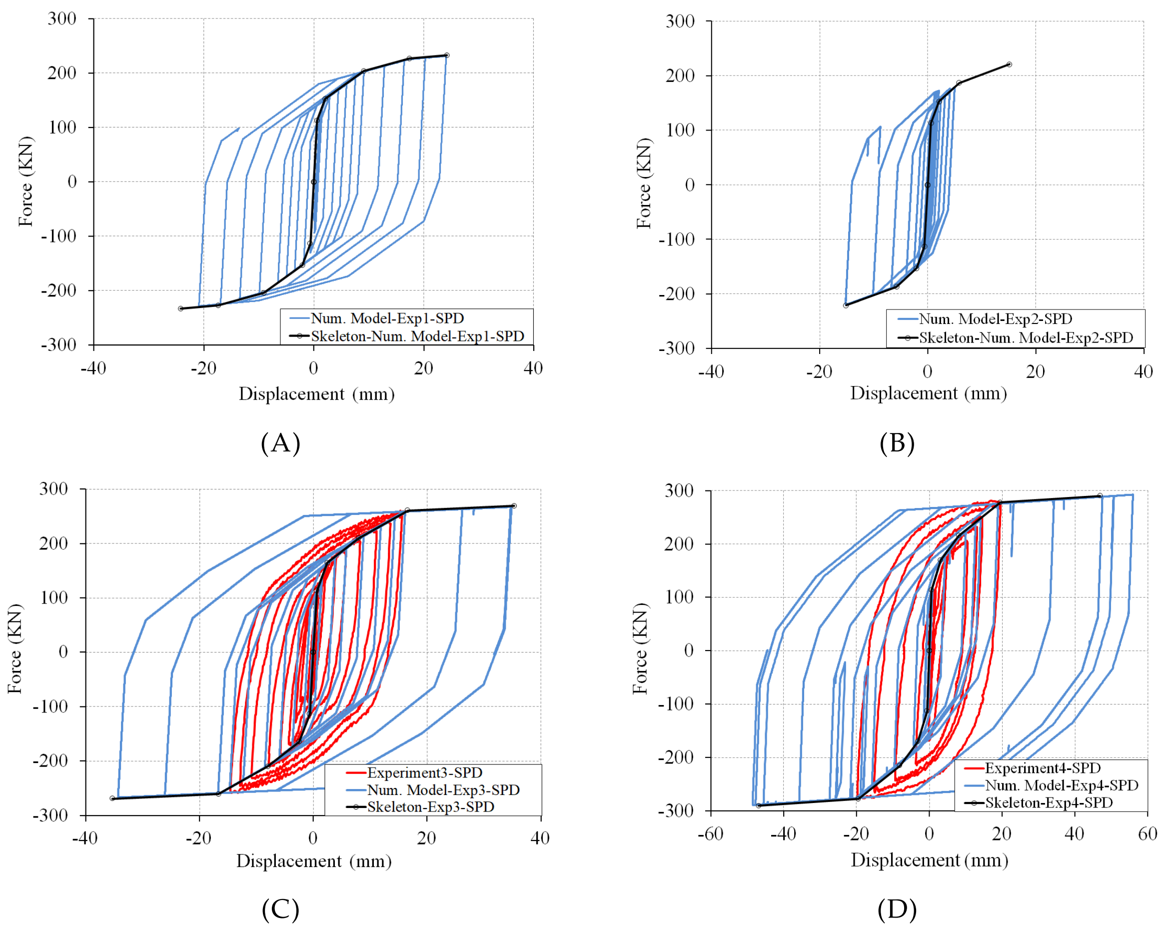

FIGURE 5.13: Hysteresis loop of experimental and numerical with the skeleton curve of web panel in the model: (a) SPD Exp1, (b) SPD Exp2, (c) SPD Exp3, and (d) SPD Exp4.

the side flanges and second stiffness of the friction force. In the post-slip state of friction force, there is second stiffness with isotropic hardening behavior as shown in Figures (5.10 and 5.11). After the SPDG deformation exceeds the gap length, the SPDG main stiffness will occur as the SPD component begins to work supporting the shear load. This phenomenon is shown in Figures (5.9A, 5.9C, 5.10A,5.11A, and 5.12A).

Based on the experimental hysteresis curve observation as shown in Figures (5.9, 5.10, 5.11, and 5.12), the best appropriate material approach of SPDG is with the multi-linear material. The transition stiffness of the SPDG device in the yielding state occurs gradually is a contrast with the ordinary SPD which can be idealized as bi-linear material. Based on reference studies [15], the presence of fix connection between the side edges of web panel (3 and 4 sides) and the vertical wings evokes a uniform stress distribution in the web panel surface than the implementation of the slit holder connection system. To produce a good similarity it is necessary to determine the factor of stiffness and strength. The parameter factors were determined by

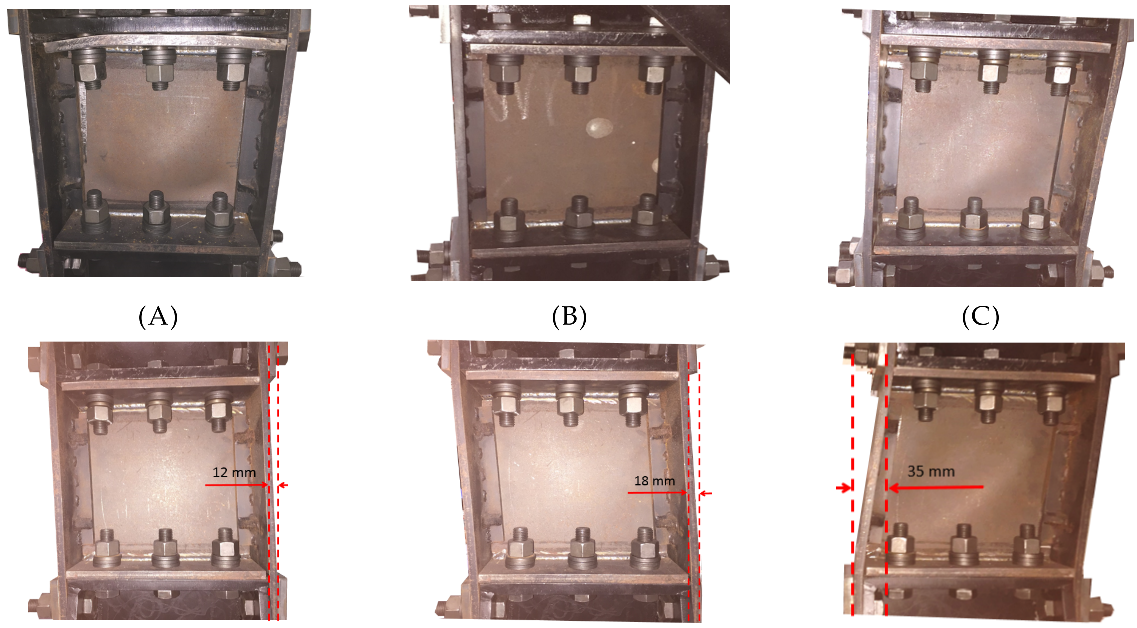

(A) (B) (C)

(D) (E) (F)

FIGURE 5.14: Deformed shape of the SPDG in the experiment test: (a) Exp1, (b) Exp2, (c) Exp3, (d) Exp4 (disp. = -12 mm), (e) Exp4 (disp. = -18 mm), and (f) Exp4 (disp. = 35 mm).

squeeze the skeleton curve to the experimental hysteresis loop as in Figure 5.13. The values and factors of stiffness and strength that matched are shown in Tables (5.5 and 5.6).

The SPDG device achieves stable stiffness and strength in the average ductility of 27.58. After the limit, the SPD components begin buckling and stiffness degradation. The appearance of buckling specimens is shown in Figures (5.14A,5.14C, and 5.14E), while the unbuckling specimen as shown in Figures (5.14D, and 5.14F). Also, after deformation exceeds the stable ductility limit (SPD starts buckling) the friction force on the slip surface also occurs degradation. The degradation of friction force occurs due to the sliding surface is not flat anymore, resulting in loss of contact. In numerical models, the degradation conditions can be simulated by aligning the friction force parameters with the term "update parameter" [12]. Based on the experimental observation in Table 5.7, the occurrence of initial buckling on SPD deformation (without gap) average 17.15 mm. Therefore the best approach to compare maximum SPDG ductility results is skeleton curve based on Approach-μ = 40.

5.5.2 3D FE verification result

As the 3D FE verification results, the SPDG mechanism could be simulated with good agreement result. The FE-01 model is used as a reference point for the 3D FE modeling to the SPD

TABLE 5.7: Matched numerical parameter of the SPD to the experimental skeleton curve.

No	State	Par. Id.	Matching value of the strength (KN)					Par. Id.	Matching value of displacement (mm)					μ	Δ(%)
			Exp1	Exp2	Exp3	Exp4	Ave.		Exp1	Exp2	Exp3	Exp4	Ave.		
1	Yield	P_{SPD1}	113.34	113.34	113.34	113.34	113.34	Δ_{SPD1}	0.62	0.62	0.62	0.62	0.62	1.00	0.22%
2	-	P_{SPD2}	153.01	153.01	164.34	170.01	160.09	Δ_{SPD2}	2.07	2.07	2.49	3.11	2.44	3.92	0.85%
3	-	P_{SPD3}	204.01	187.01	209.68	215.34	204.01	Δ_{SPD3}	9.07	5.80	8.02	8.08	7.74	12.45	2.69%
4	Buckle	P_{SPD4}	226.68	221.01	260.68	277.68	246.51	Δ_{SPD4}	17.36	15.13	16.63	19.49	17.15	27.58	5.96%
5	Max.	P_{SPD5}	232.91	-	269.18	290.15	264.08	Δ_{SPD5}	24.20	-	35.28	46.85	35.44	56.99	12.31%

μ: ductility; Δ(%): deformation ratio of SPD; Exp: specimen number of experiment; Ave.: Average; Max.: Maximum.

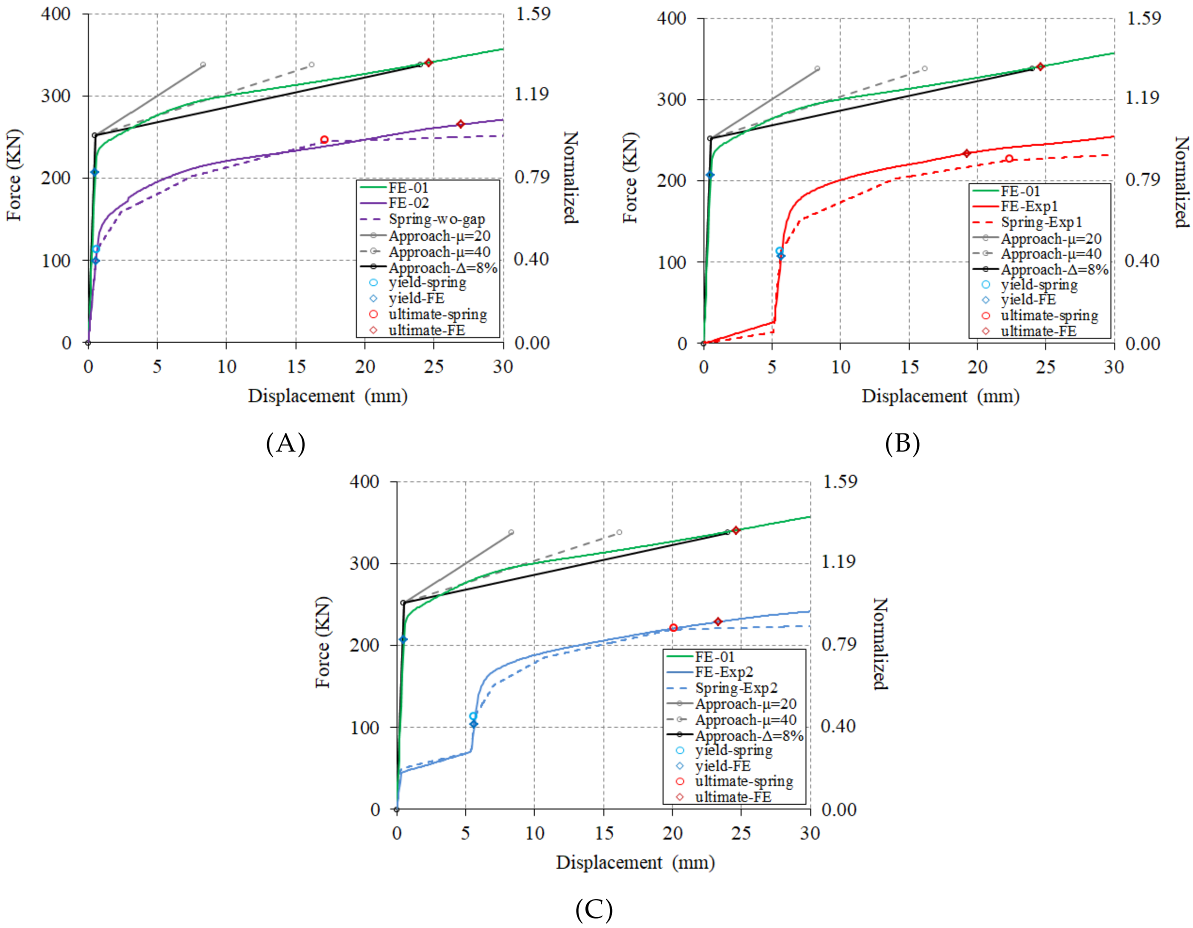

FIGURE 5.15: Skeleton curve comparison of the calibrated spring model, 3D FE model, and SPD constitutive approach [5]: (a) without gap and $FP_{FD} = \infty$, (b) with 5 mm gap and $FP_{FD} = 0\%$, and (c) with 5 mm gap and $FP_{FD} = 20\%$.

constitutive of analytical approach [5]. Also, the mechanism of gaps existence to the specimen behavior that could obtain small stiffness below the gap length reach a good agreement between 3D FE model and calibrated experiment result with spring model. Furthermore, the effect of web panel confined by slit holder on the side edges 3 and 4 can be investigated in the

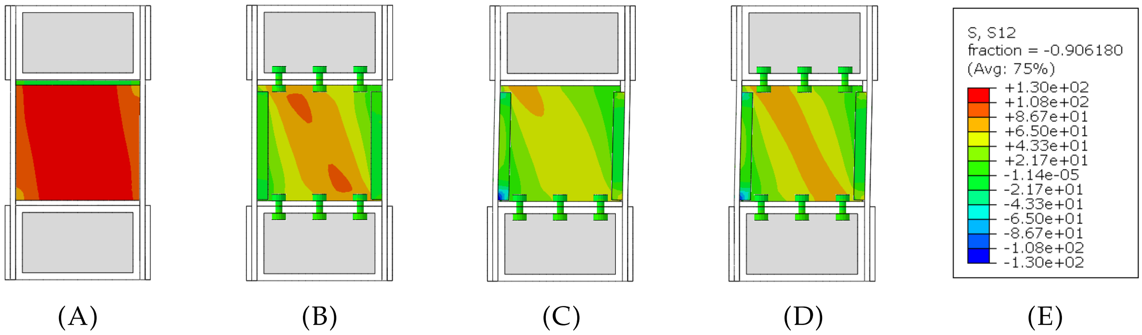

FIGURE 5.16: Shear stress of: (a) FE-01 (disp. = 0.51 mm), (b) FE-02 (disp. = 0.53 mm), (c) FE-Exp1 (disp. = 5.66 mm), (d) FE-Exp2 (disp. = 5.63 mm), and (e) stress contour scale.

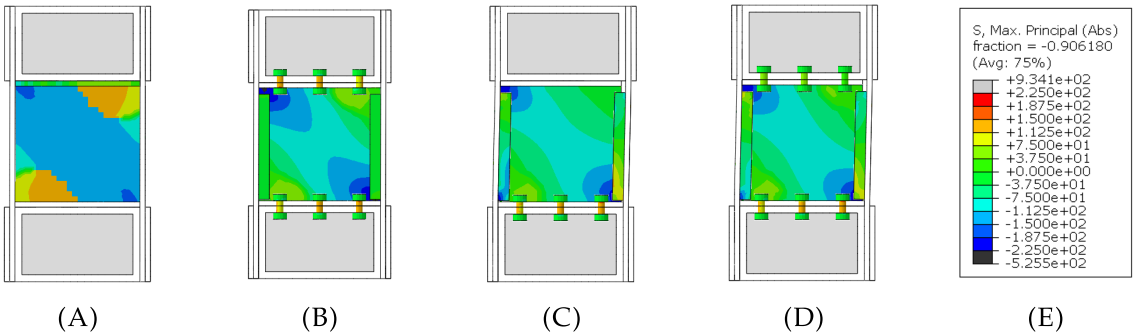

FIGURE 5.17: Absolute maximum principle stress of: (a) FE-01 (disp. = 0.51 mm), (b) FE-02 (disp. = 0.53 mm), (c) FE-Exp1 (disp. = 5.66 mm), (d) FE-Exp2 (disp. = 5.63 mm), and (e) stress contour scale.

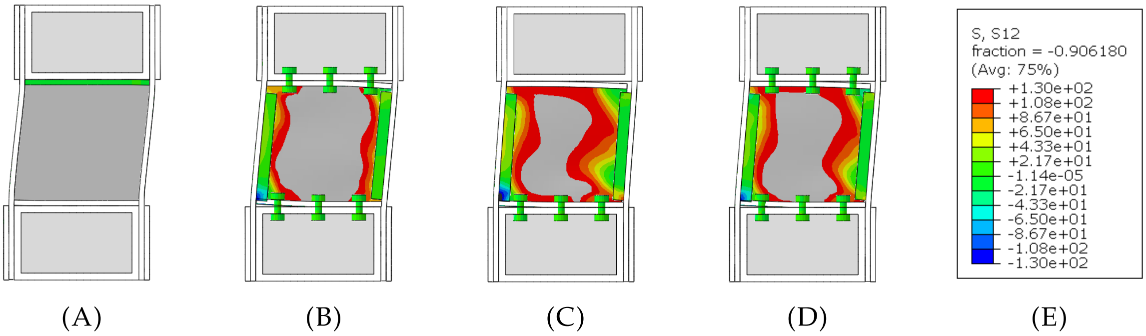

FIGURE 5.18: Shear stress of: (a) FE-01 (disp. = 24.61 mm), (b) FE-02 (disp. = 26.93 mm), (c) FE-Exp1 (disp. = 19.28 mm), and (d) FE-Exp2 (disp. = 23.33 mm), and (e) stress contour scale.

skeleton curve as well as stress distribution visualization on the web panel.

Based on the calibration of the FE-01 model, the shear yielding state of SPD is near to the formulation approach [5]. The skeleton curve comparison can be observed in Figure 5.15. In the post-yield state, the skeleton curve of the FE-01 model tends to coincide with the curve of Approach-μ = 40 curve and Approach-Δ = 8%. As the result of Figures (5.16A and 5.17A, and 5.18A), the web component of the FE-01 model dominated shear stress and distributed uniform entire shear panel web plain. The shear stress dominance of FE-01 model is indicated by the maximum principal and minimum principal stress not exceeding the yielding stress, as

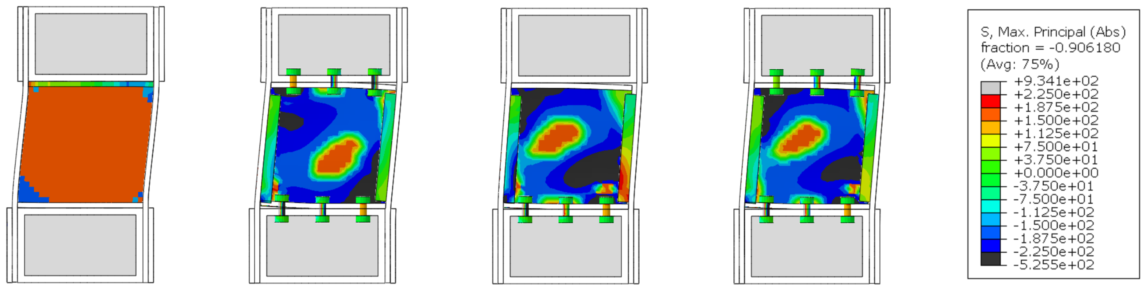

(A) (B) (C) (D) (E)

FIGURE 5.19: Absolute maximum principle stress of: (a) FE-01 (disp. = 24.61 mm), (b) FE-02 (disp. = 26.93 mm), (c) FE-Exp1 (disp. = 19.28 mm), and (d) FE-Exp2 (disp. = 23.33 mm), and (e) stress contour scale.

shown in Figure 5.19A. In addition, the FE-01 model is not experiencing buckling on a large deformation.

However, the difference yield strength between the proposed SPDG and the ordinary SPD occurs due to the yield mode of web panel in the SPDG system dominated by diagonal compression stress rather than the shear stress. In the the FE-02 model, the shear yield stress distributed un-uniformly in SPD plain, as shown in Figures (5.16B, 5.17B, and 5.18B). In the small deformations, the minimum principal stress of web panel part has exceeded the yielding limit as shown in Figure 5.19B.

The gap existence that can delay the SPD work is captured in the distribution of shear stress occurring before and after the deformation beyond the length of each gap, as shown in Figure 5.16B with Figure 5.16C and Figure 5.17B with Figure 5.17C. Also, by monitoring the skeleton curve of 3D FE model, the gap existence that can reduce the initial stiffness of the SPDG device was observed. Furthermore, the friction force implementation effect causes the SPD work to be equivalent to that friction force in the deformation below the gap length, as shown in Figure 5.16D. Based on the Figures (5.15B and 5.15C), FE-Exp1 and FE-Exp2 skeleton curves have an adjacent pattern with spring model skeleton curves (Spring-Exp1 and Spring-Exp2) of experimental data calibration with numerical analysis. The slight difference in stiffness below the gap length might be due to the bolt connections idealization influence on the side flanges as elastic beam connector. Also, the elastic-perfect plastic with kinematic hardening idealization in the post-slip friction surface could influence this difference.

5.6 Conclusions

The study of shear panel damper plus gap (SPDG) was conducted with experimental and numerical. As the results, the proposed specimen can obtain small stiffness under gap length and sufficient energy dissipation under large deformation. Some important points are:

(a) At the deformation below the gap length, the existence of the gap produced a significant stiffness reduction. The SPDG device had a high potential applied to connect multiple steel pipe columns to reduce the deterioration due to frequent lateral deformation of bridge pier.

(b) In the numerical analysis verification, the spring model and 3D FE model had a good agreement with the experiment results.

(c) The stiffness and strength factor of the SPD part were defined to this device due to the stiffness and strength reduction. This phenomena occurred due to the yield mode of web panel in the SPDG system dominated by diagonal compression stress rather than the shear stress.

(d) The implementation of ductility limit 40.0, the SPDG had an agreement with soundness 3 based on the reference [17].

Bibliography

[1] Abebe, D.Y., Jeong, J.S., Kim, J.W. and Choi, J.: Analytical Study on Large Deformation in Shear Panel Hysteresis Damper Using low Yield Point Steel, in *2013 NZSEE Conference*, Xx, pages 0–6, 2013.

[2] Caccese, V., Elgaaly, M. and Chen, R.: Experimental Study of Thin Steel-Plate Shear Walls under Cyclic Load, Journal of Structural Engineering, volume 119, no. 2:573–587, 1993.

[3] Chen, Z., Bian, G. and Huang, Y.: Hysteretic Behavior of Shear Panel Dampers under High Axial Compression Loading, Advanced Steel Construction, volume 9, no. 3:190–204, 2013.

[4] Chen, Z., Fan, H. and Bian, G.: Parametic Analysis of Shear Panel Dampers under High Axial Compression, Advanced Steel Construction, volume 11, no. 1:1–14, 2015.

[5] Chen, Z., Ge, H. and Usami, T.: Hysteretic Model of Stiffened Shear Panel Dampers, Journal of Structural Engineering, volume 132, no. 3:478–483, 2006.

[6] Dassault Systèmes Simulia: Abaqus CAE User's Manual, in *Abaqus 6.12*, page 1174, 2012.

[7] Dassault Systèmes Simulia: Analysis User's Manual Volume 2: Analysis, in *Abaqus 6.12*, volume II, 2012.

[8] Dassault Systèmes Simulia: Analysis User's Manual Volume 3: Materials, in *Abaqus 6.12*, volume III, 2012.

[9] Dassault Systèmes Simulia: Analysis User's Manual Volume 4, in *Abaqus 6.12*, volume IV, pages 29.3.8–10, 2012.

[10] Dassault Systèmes Simulia: Analysis User's Manual: Volume 5:Prescribed Conditions, Constraints & Interactions, in *Abaqus 6.12*, volume IV, page 831, 2012.

[11] Deng, K., Pan, P., Li, W. and Xue, Y.: Development of a buckling restrained shear panel damper, Journal of Constructional Steel Research, volume 106:311–321, 2015.

[12] Gu, Q., Conte, J.P. and Barbato, M.: OpenSees Command Language Manual: Response Sensitivity Analysis based on the Direct Differentiation Method (DDM) OpenSees Command Language Manual : DDM-Based Response Sensitivity Analysis Introduction, 2010.

[13] Hashimoto, K. et al.: Effect of Structural Parameters of Shear Panel Damper on Seismic Performance of Multi-pipe Integrated Bridge Pier, Journal of JSCE, volume 72, no. 1:75–91, 2016.

[14] Kanaji, H. et al.: Experimental Study on Seismic Performance of an Integrated Column by Multi Steel Pipes with Hysteretic Damper, Journal of JSCE, volume 13, no. 49:59–72, 2006.

[15] Liu, Y., Aoki, T. and Shimoda, M.: Strain Distribution Measurement of a Shear Panel Damper Developed for Bridge Structure, Journal of Structures, volume 11:1–11, 2013.

[16] Mazzoni, S., McKenna, F., Scott, M.H. and Fenves, G.L.: OpenSees Command Language Manual, 2007.

[17] Nakamura, R., Kanaji, H. and Kosaka, T.: Development and Design of New Steel Pipe Integrated Pier with Shear Link, Technical report, Hanshin Expressway Company Limited, Osaka, 2014.

[18] Roberts, T.M. and Ghomi, S.S.: Hysteretic characteristics of unstiffened plate shear panels, Thin-Walled Structures, volume 12, no. 2:145–162, 1991.

[19] Shinohara, M., Kanaji, H., Oniki, K. and Sugiura, K.: Basic Properties of an Integrated Column by Multiple Steel Pipes with Hysteretic Shear Damper, Journal of JSCE, volume 58A:471–483, 2012.

[20] Susmel, L.: A unifying approach to estimate the high-cycle fatigue strength of notched components subjected to both uniaxial and multiaxial cyclic loadings, Fatigue and Fracture of Engineering Materials and Structures, volume 27, no. 5:391–411, 2004.

[21] Suzuki, T. et al.: Seismic control divices using LYS, Technical report, Nippon Steel, Tokyo, 1998.

[22] Takahashi, Y., Takemoto, Y., Takeda, T. and Takagi, M.: Experimental study on thin steel shear walls and particular steel bracings under alternative horizontal load their stiffness is so rigid that structure designed by static analysis, Technical report, Ohbayashi-Gumi Ltd., Tokyo, 1973.

[23] Tamai, H. and Kasai, K.: Deformation Capacity of Shear Panel Steel Damper and Its Reflection To Aij Fatigue Design Requirements, Journal of Disaster Research, volume 11, no. 1:125–135, 2016.

[24] Thorburn, L.J., Kulak, G.L. and Montgomery, C.J.: Analysis of Steel Plate Shear Walls, Technical report, Department of Civil Engineering, The University of Alberta, Alberta, 1983.

[25] Zhang, C. et al.: The Lightweight Design of a Seismic Low-Yield-Strength Steel Shear Panel Damper, Materials, volume 9, no. 6:424, 2016.

Chapter 6

Integrated Multiple Steel Pipes Bridge Pier Connected by SPDG

6.1 General Remarks

This chapter discusses the implementation shear panel damper plus gap (SPDG) on the integrated multiple steel pipes bridge pier. The additional gap expected to delay the SPD work in the small deformation range. Consequently, the structure could realize sufficient flexibility and deterioration avoidance of the seismic device under the frequent lateral deformation due to daily load. In this study, the behavior and the properties of the SPDG based on the experiment and numerical analysis study based on the Chapter 5 were implemented in a numerical model. As the result, the proposed structure capable to generate expected behavior and to achieve high seismic performance (called Performance Level IIa) under severe earthquake excitation (called Level 2). Furthermore, the friction part could reduce the structural internal force and the stress of the SPD under Level 1 of earthquake excitation.

6.2 Background

The advisability of the direct connection system between the superstructure and the pier in the integrated bridge pier with multiple steel pipe columns connected by shear panel damper (SPD) needs to be studied more deeply. A possibility of infirmity was the high degree of structural uncertainty could evoke the internal induction force of structural member and stress-induces-fatigue [3] of the SPD components due to the frequent lateral deformation of the daily load. The un-handled of the SPD stress-induces-fatigue propagates deterioration upon the lifetime. The deterioration can reduce the seismic performance of the structure. Also, the internal inducted force that produces additional stress in the superstructure element members requires the larger dimension of its cross-section. The other hand, in the superior side, the enhanced of dissipated energy and seismic performance such kind bridge pier was successfully conducted in the Chapter 4. The structure could achieve high seismic performance (Performance IIa under Level 2 of seismic excitation). Furthermore, it could achieve not only more sensitive deformation of SPD but also larger deformation limit than the old system one.

This thesis part discussed the implementation shear panel damper plus gap (SPDG) in the integrated bridge pier with multiple steel pipe columns. Following the structural concept in the Chapter 3, the additional gap in the SPD device is expected to improve the structural flexibility under small deformation. So, the seismic device deterioration which triggered by the frequent lateral deformation of daily load can be reduced. In this study, the typical bridge pier following the Chapter 4 was selected to examine the advisability of the SPDG device implementation. By proposing 50 mm of gap length in the global response of the pier, the numerical analysis including static and dynamic was performed to examine the structural behavior and structural performance by following the simulation in the Chapter 5. Also, there are four structural variables which consider the friction force of sliding surface in the SPDG. As the result, the proposed structure could achieve the intended structural behavior and structural performance. Furthermore, the appropriate friction force on the sliding surface of SPDG resulted in sufficient flexibility under small deformation, better force reduction under Level 1 of earthquake excitation. Finally, the proposed structure could remain on the Performance IIa under Level 2 of seismic excitation.

6.3 Integrated Bridge Pier with Multiple Steel Pipe Columns Connected by SPDG

6.4 Methodology

In this study, the investigation of the structural behavior and performance was conducted by numerical analysis including static and dynamic. The numerical model of the structure considering the non-linearity follows the Chapter 4, as illustrated in Figure 6.1. The components, behavior, performance, and parameter inputs of shear panel damper plus gap (SPDG)

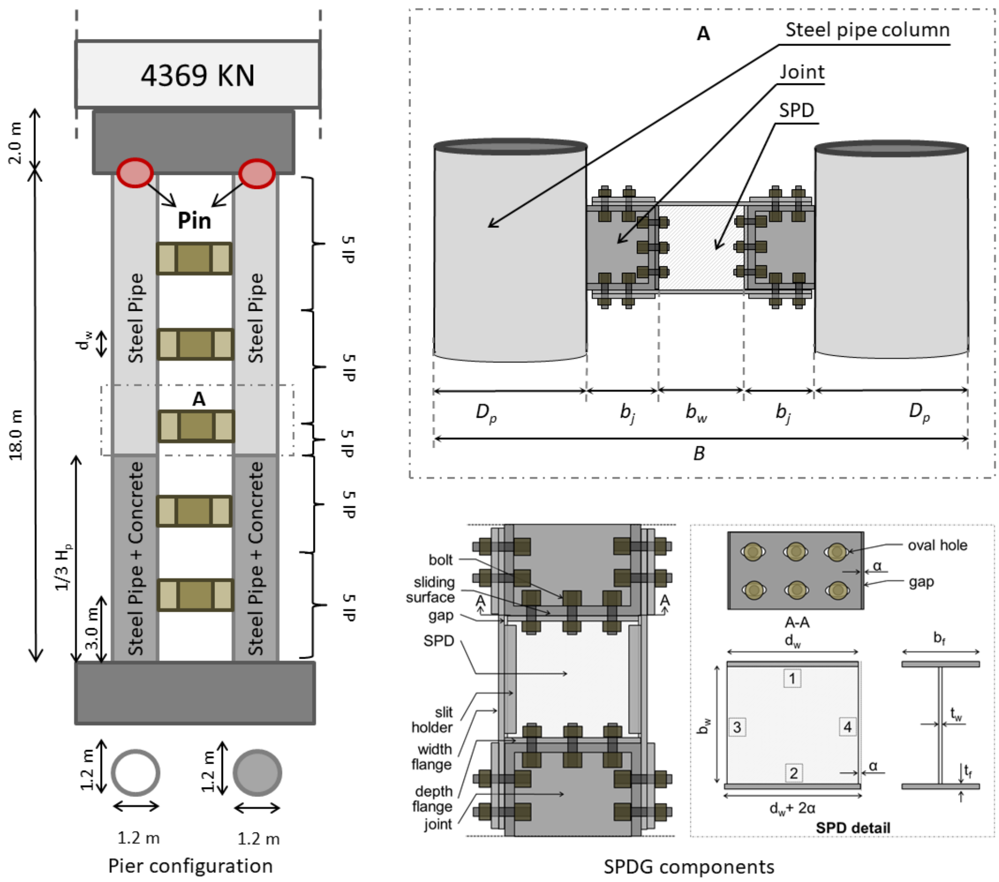

FIGURE 6.1: Integrated steel pipes bridge pier connected by SPDG.

follow the experimental and numerical analysis result of the Chapter 5. Also, the limit state of the SPD strain is $40\gamma_y$ for the benchmark structural model (Str18). The changing of the strain limit instead of the Chapter 4 because of $40\gamma_y$ shear strain limit still below the 8% shear strain limit of the reference [2]. There are four types of the proposed structure that implement gap 50.0 mm considering different friction force values on the sliding surfaces, as shown in the Table 6.1. While the components and parameter inputs of steel pipe columns follow the study in the Chapter 4. The seismic performance target of the proposed structure is IIa following the reference [2] which the limit state of the steel pipe columns sectional strain is $2\varepsilon_y$.

6.4.1 Numerical modeling of the structures

The numerical modeling and structural idealization follow the method of Chapter 4. The structural model Str18 that obtained the best optimum dissipated energy and seismic performance was taken as the basic comparison. In the structural idealization, there are several

TABLE 6.1: SPDG parameters in the numerical model.

No	Str. Name	Gap (mm)	Fric. force (%*P_{SPD0})	SPD dimension (mm) t_w	d_w	b_w	t_f	b_f
1	Str0	0.0	-	18	800-540, incr. -65	540-800, incr. 65	Min(2*t_w, 50)	200
2	Str1	50.0	0.00%	22	600-400, incr. -50	400-600, incr. 50	Min(2*t_w, 50)	200
3	Str2	50.0	10.00%	22	600-400, incr. -51	400-600, incr. 51	Min(2*t_w, 50)	200
4	Str3	50.0	20.00%	22	600-400, incr. -52	400-600, incr. 52	Min(2*t_w, 50)	200
5	Str4	50.0	30.00%	22	600-400, incr. -53	400-600, incr. 53	Min(2*t_w, 50)	200

changing of the hysterical damper component configuration due to the replacement of the SPD to be the SPDG. In the SPDG device case, it to be idealized as a series and a parallel combination of link element and truss element, as shown in Figure 6.2A. Also, the idealization of the SPDG is shown on the Figure 6.2B. The link element represents the SPD part and stopper part (gap) while the truss element represents the friction damper part. Furthermore, the parameter of the SPDG was defined following Chapter 5, as shown in Table 6.1. The SPD of Str0 was idealized as the bi-linear material which is implemented in the Chapter 4, while the SPDG of Str1-Str4 were modeled as the multi-linear material which following Chapter 5.

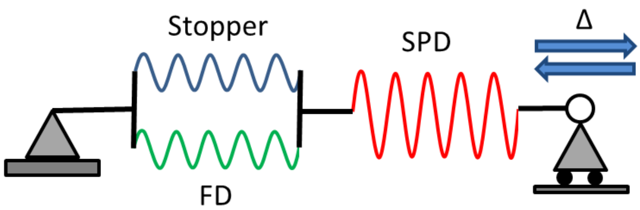

(A)

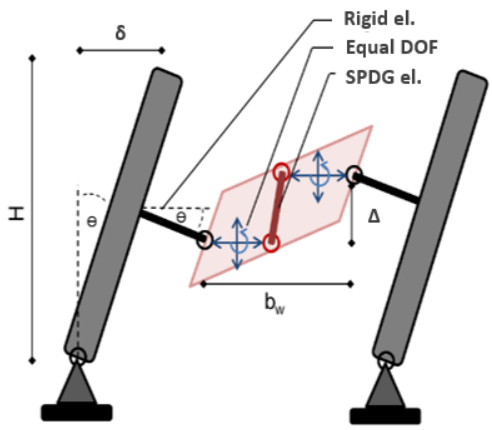

(B)

FIGURE 6.2: The SPDG idealization in the numerical model: (A) SPDG element configuration and (B) SPDG implementation in the pier structure.

6.4.2 The structural behavior and performance verification method

Generally, the structural behavior and performance verification method follow the study in Chapter 4. Static pushover analysis was conducted to examine the deformation limit capacity of the structure, while static cyclic analysis to calculate and optimize energy dissipation of the structure. Furthermore, dynamic analysis to verify the structural seismic performance of the structure. In this study, the structural performance also to be examined under Level 1 of seismic excitation. The Level 1 of seismic excitation that might occur frequently during lifetime of the bridge could induce a deterioration. Under deterioration which might be triggered by small earthquake occurrence, the proposed seismic device performance need to be examined. There are three Level 1 of ground motion excitation input based on the reference [1] were implemented in the dynamic analysis. All ground motion excitation inputs including Level 1 and Level 2 are shown in Figures (A.4-A.6) with the responses spectra are shown in Figures (A.7-A.9). In the output-target of the structural seismic performance verification, the maximum response and the residual deformation of the structures with the proposed gap and the difference friction force parameters were compared to check their influence.

6.5 Results and Discussion

6.5.1 The structural behavior

As the initial stiffness monitoring under the gap range (in this case 50 mm), the initial stiffness of the proposed structure are varied depends on the friction force implementation. While after the deformation over the gap range, the structural stiffness will equal with the main stiffness, as shown in Figure 6.3. Furthermore, the stiffness ratios of the proposed structures to the structural benchmark (Str0) are shown in the Table 6.2. The larger friction force evokes the smaller structural flexibility in the gap range. So, the most flexible structure could be achieved by neglecting the friction force. The friction force application of 0%-20%P_SPD0 could achieve sufficient structural stiffness reduction. For example, the implementation friction force 20%P_SPD0 resulted in 0.53 times stiffness compared to the benchmark. More ever, the considering friction force of SPDG resulted hysteresis loop under gap range compared to the without gap and without considering friction force, as shown in Figures (6.3A, 6.3E, 6.3I, 6.3M, and 6.3Q). While in the deformation limit cases, the displacements that observed from the occurring yield of steel pipe column are around the 200 mm. Meanwhile the displacement limit of the Performance IIa

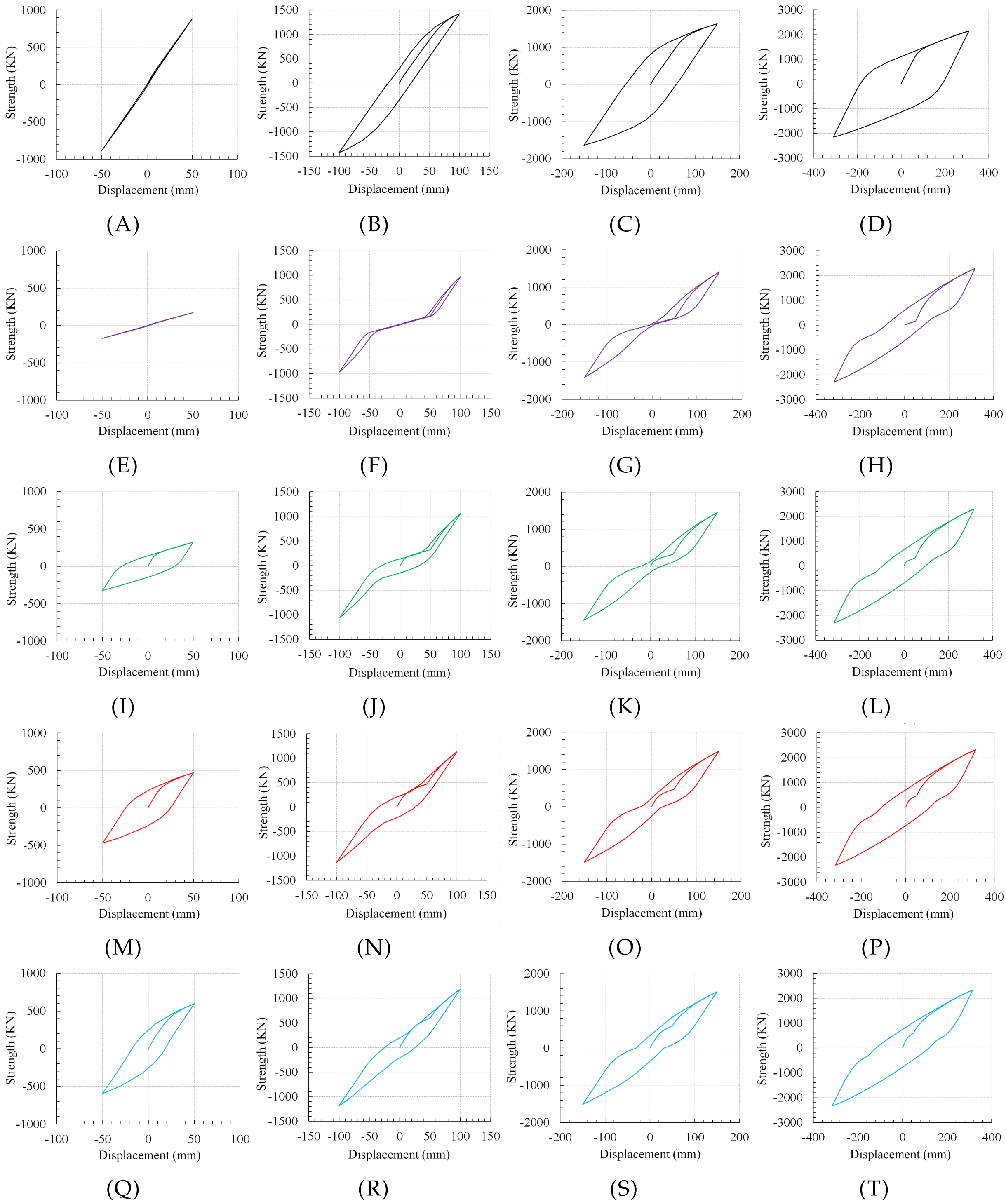

FIGURE 6.3: Hysteresis loops at displacement 50 mm, 100 mm, 150 mm, and Performance 2a deformation limit of: (A-D) Str0, (E-H) Str1, (I-L) Str2, (M-P) Str3, and (Q-T) Str4.

(the sectional strain of steel pipe column is $2\varepsilon_y$) are about 310 mm as shown in Table 6.3 and Figures (6.3D, 6.3H, 6.3L, 6.3P, and 6.3T).

TABLE 6.2: Hysteresis loops at displacement 50 mm, 100 mm, 150 mm, and Performance 2a deformation limit of: (A-D) Str0, (E-H) Str1, (I-L) Str2, (M-P) Str3, and (Q-T) Str4.

No	Str. Name	K_n/K_0	Dissipated Energy (KJ)	h_{eq}	$\delta_{y_{SPD}}$ *(mm)*	$\delta_{max}/\delta_{y_{SPD}}$	Earth-quake no.
1	Str0	1.00	1.08	0.39%	58.40	0.86	1-III
2	Str1	0.19	0.26	0.47%	75.70	1.40	1-III
3	Str2	0.37	22.23	21.91%	69.90	0.62	1-III
4	Str3	0.53	30.96	20.88%	64.10	0.59	1-III
5	Str4	0.67	30.27	16.17%	58.00	0.70	1-III

TABLE 6.3: The parameters of the structural behavior below the deformation limit of Performance 2a and the structural performance under Level 2 of earthquake excitation.

No	Str. Name	Dissipated Energy (KJ)	h_{eq}	δ_{ε_y} *(mm)*	$\delta_{2\varepsilon_y}$ *(mm)*	$\delta_{max}/\delta_{2\varepsilon_y}$	Earth-quake no.	δ_{res1} (mm)	δ_{res2} (mm)	Earth-quake no.
1	Str0	1034.65	24.67%	191.60	310.00	0.78	2-II-II-1	58.00	3.01	2-II-III-1
2	Str1	631.85	13.85%	211.50	317.50	1.19	2-II-III-1	32.92	31.12	2-II-III-1
3	Str2	672.56	14.69%	207.90	316.50	1.05	2-II-III-1	22.54	22.72	2-II-III-1
4	Str3	710.82	15.47%	204.20	315.70	1.00	2-II-III-1	20.55	18.35	2-II-III-1
5	Str4	742.96	16.15%	202.00	314.80	0.96	2-II-III-1	19.95	15.52	2-II-III-1

6.5.2 The dissipated energy of the structure

As the dissipated energy observation, the appearance of the gap in the SPDG will reduce the dissipated energy of the structure. Based on the observation of Table 6.3, the structure without the gap (Str0) has dissipated energy larger than the structure with the gap. The gap presence makes the hysteresis loop of the structures slimmer than the structure without the gap. The particular composition each SPD and SPDG that contribute producing dissipated energy also demonstrate this difference quantity of dissipated energy, as shown in Figure 6.4. While the larger friction force could produce the larger energy dissipation. The friction force that contributes to produce energy dissipation to be evidenced with the SPDG hysteresis loops, as shown in Figures (6.4B-6.4E).

The implementation of the gap in the SPD device could delay the dissipated energy enrichment of the SPD part in its deformation. It can be seen in Figure 6.5, the Str1 starts to achieve dissipated energy about in 80 mm of deformation, while the Str0 produce dissipated energy about in 60 mm deformation. These occurrences due to yield deformation of the SPDG and SPD is about 80 mm and 60 mm respectively. The occurrence of small equal damping ratio of Str0 and Str1 in the small deformation raised by the open-close-strain phenomena of a concrete-filled material of the bottom steel pipe columns.

Below the gap range (50.0 mm), dissipated energy generated due friction force consideration of SPDG . In small deformation, event though its energy dissipation seemly equal with the SPD as shown Figure 6.5A, the equal damping ratio difference was investigated, as shown in Figure 6.5B. Furthermore, the implementation friction force with 10% of the SPDG theoretical yield strength produces larger damping ratio than the implementation of the 20% and 30%. The Str2, Str3, and Str4 capable enrich equal damping ratio about 23%, 21%, and 16% in the 30 mm, 50 mm, and 50 mm of deformation respectively. This occurs because the larger of friction force needs the larger deformation to reach yield point.

6.5.3 The structural performance verification

The friction force consideration could produce significant seismic response reduction of the structure under Level 1 seismic excitation. The structure that implements SPDG without considering friction force (Str1) has the largest displacement response than the others, then followed by the structure with SPD (Str0). While the structure that implements SPDG considering the friction (Str2, Str3, and Str4) have smaller displacement response than Str1 and Str2, as shown in Figure 6.6. Both of Str0 and Str1 do not have equal hysterical damping in this deformation range. The response difference caused the diversity of the natural period of the structure. The hysterical damping of the SPDG friction part leads the response reduction of the structures which implement SPDG considering the friction force.

Under the Level 2 of earthquake excitation, the implementation gap in the structure increases the structural response. The maximum deformation that not exceeds the deformation limit occurs on Str0, Str3, and Str4, as shown Table 6.3. While the maximum deformation response of the structure which implement SPD is the smallest, as shown in Figure 6.7. This phenomenon caused by the decreasing of the dissipated energy of the structure. However, the appearance of the friction force gives better seismic response reduction due to larger dissipated energy. The sequent of seismic responses from smaller to larger is Str4, Str3, Str2, and Str1 respectively.

The application of gap in the SPDG results in the influence to residual deformation of the structure under Level 2 of earthquake excitation. Based on the Table 6.3 and Figure 6.8, the structures with SPDG result in smaller residual deformation than the structure with SPD. This occurrence may be due to the hysteresis loop characteristic of the SPD is more perfect-plastic than the SPDG. While after the SPD and SPDG to be released (in the last 5 seconds), the structure with SPD has the best re-centering capability than the others. Based on the Chapter 4, the structure with SPD (Str0) is designed with 90% of yield stiffness limit which the maximum

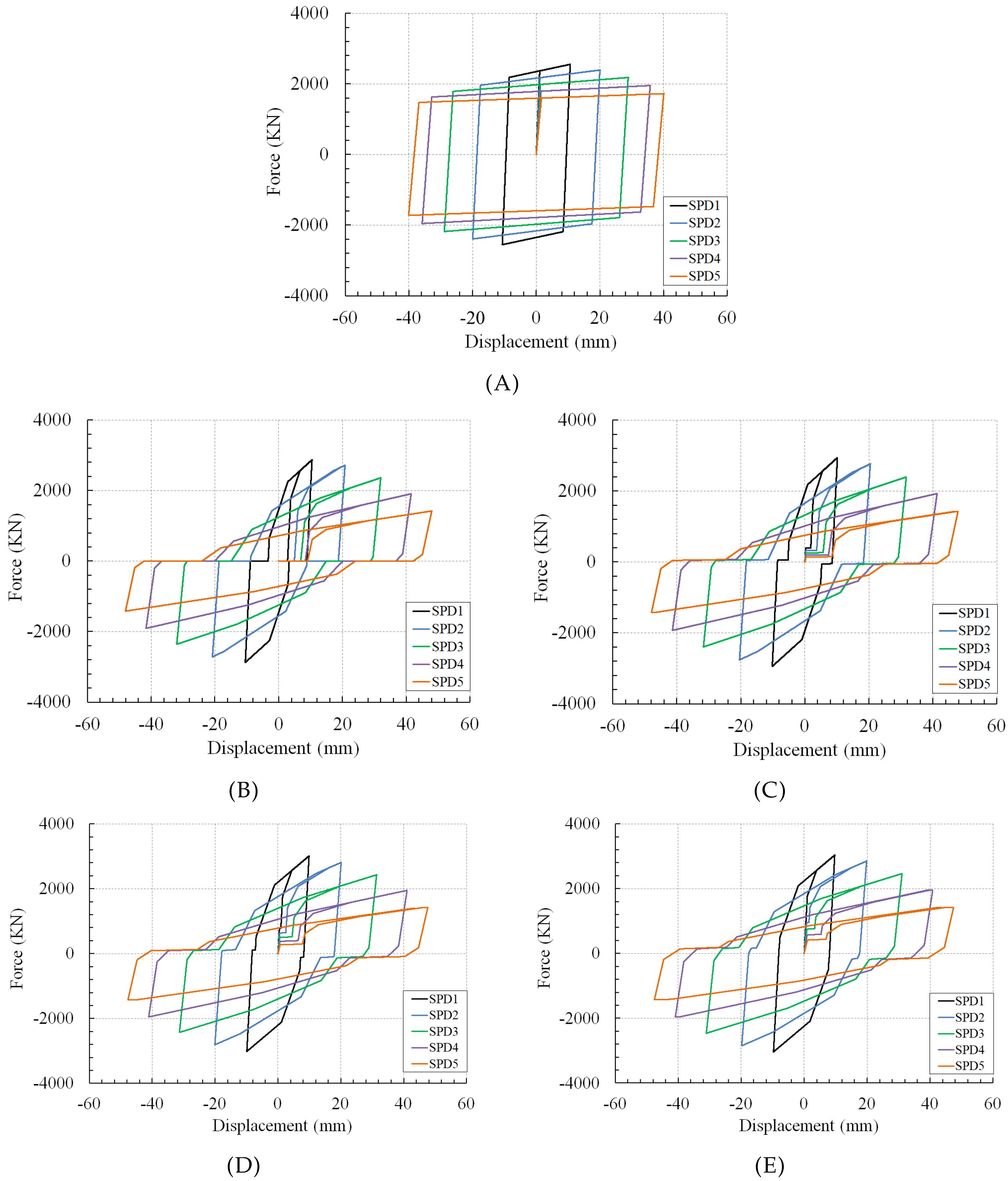

FIGURE 6.4: The SPD hysteresis loops of: (A) Str0, (B) Str1, (C) Str2, (D) Str3, and (E) Str14.

strain of the column parts less than $1.44\varepsilon_y$. In this case, the structure with SPDG use displacement limit $2\varepsilon_y$ of the maximum columns strain. So that the influence of the maximum strain response of the columns to the re-centering capability is significant. Also, in the case of the structure that implements SPDG, the re-centering capability remains proportional with the ratio of maximum displacement response to the displacement limit. It can be said that the larger

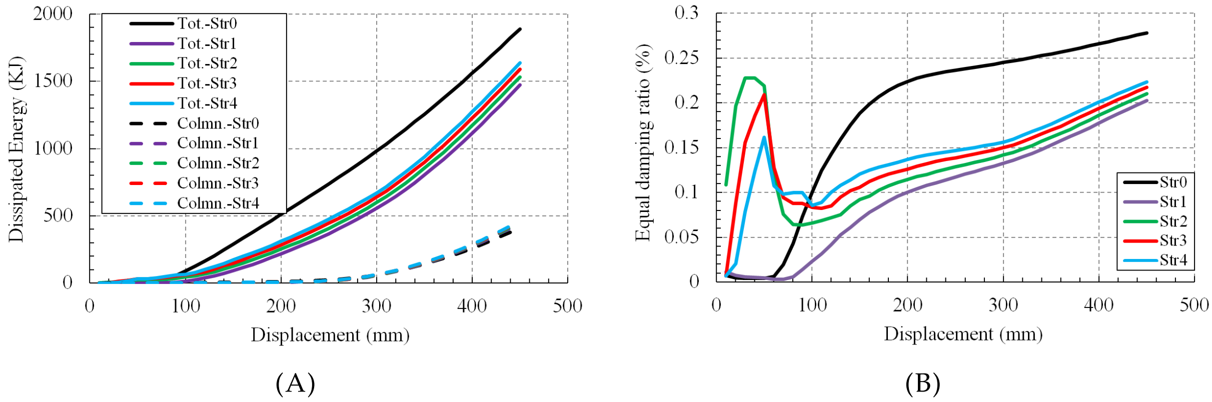

FIGURE 6.5: The dissipated energy comparison: (A) the dissipated energy composition, and (B) the equal damping.

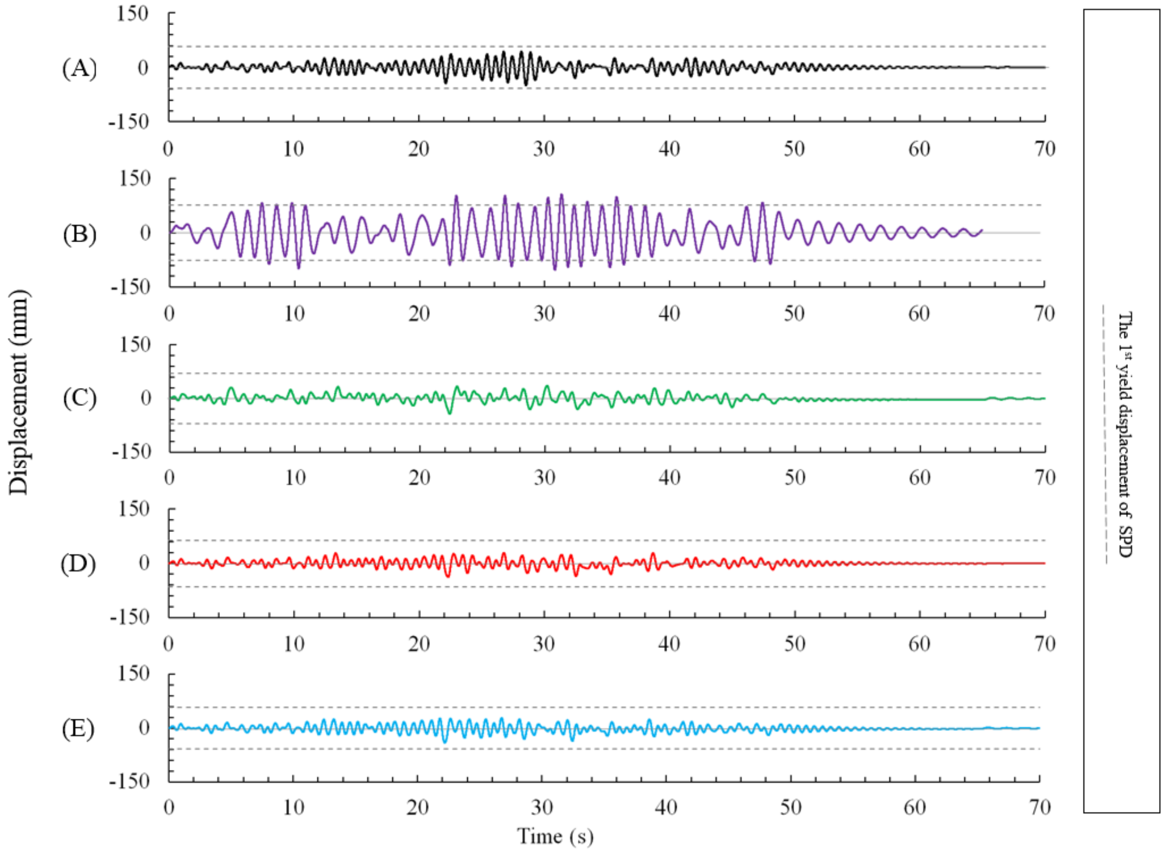

FIGURE 6.6: The largest displacement response of the structure under seismic Level 1 excitation.

friction force proportion of SPDG results in the larger energy dissipation. Also, the larger energy dissipation could obtain the smaller of maximum structural response. Finally, the larger maximum structural response could achieve the larger residual deformation.

Finally, the force resistant reduction of SPDG friction force consideration is observed clearly. Based on the Figures (6.9A, 6.10A, 6.11A, 6.12A, and 6.13A), the implementation friction force

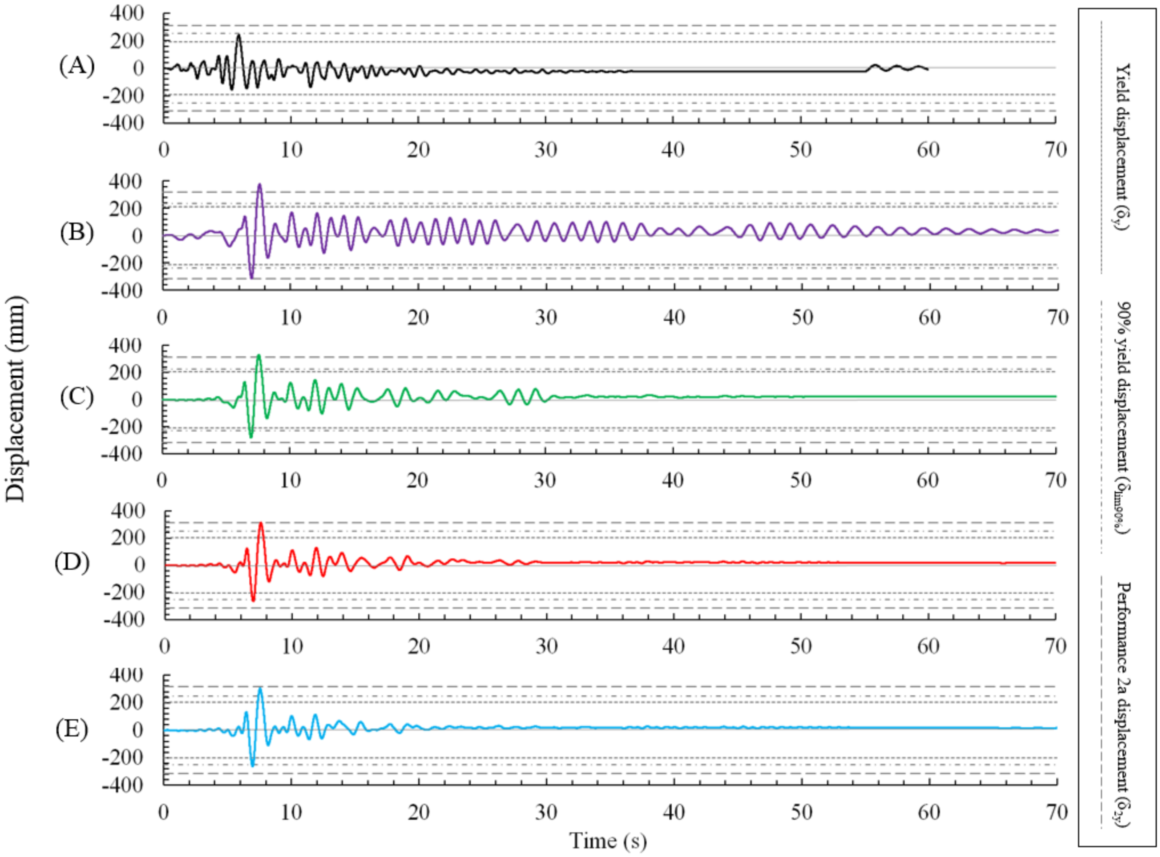

FIGURE 6.7: The largest displacement response of the structure under Level 2 of seismic excitation.

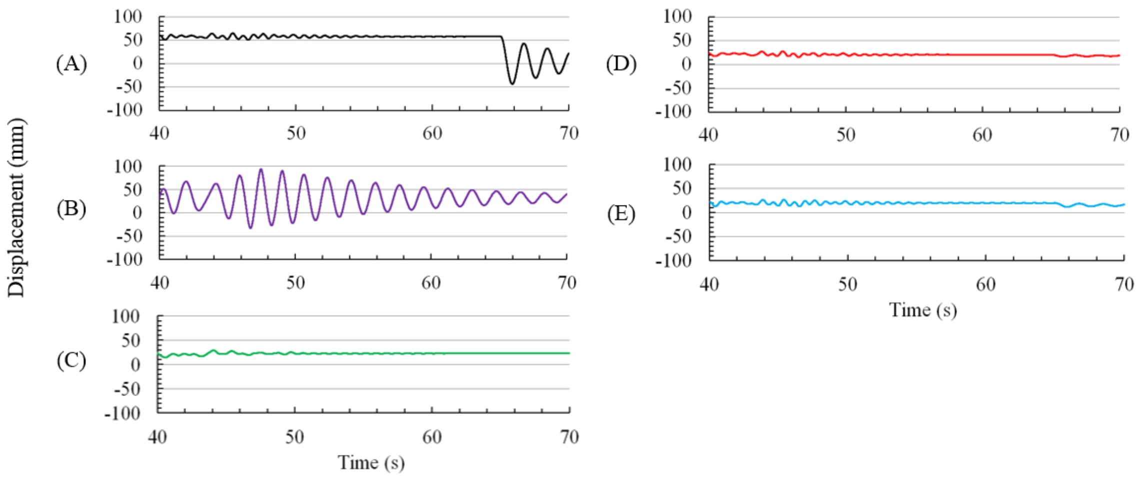

FIGURE 6.8: The residual displacement of the structure under Level 2 of seismic excitation.

with 10% and 20% of the SPDG yield strength produce significant reduction force of seismic excitation. So that the maximum deformation response of its less than the yield deformation limit of SPD devices. Consequently, seismic response reduction in the Level 1 could give the

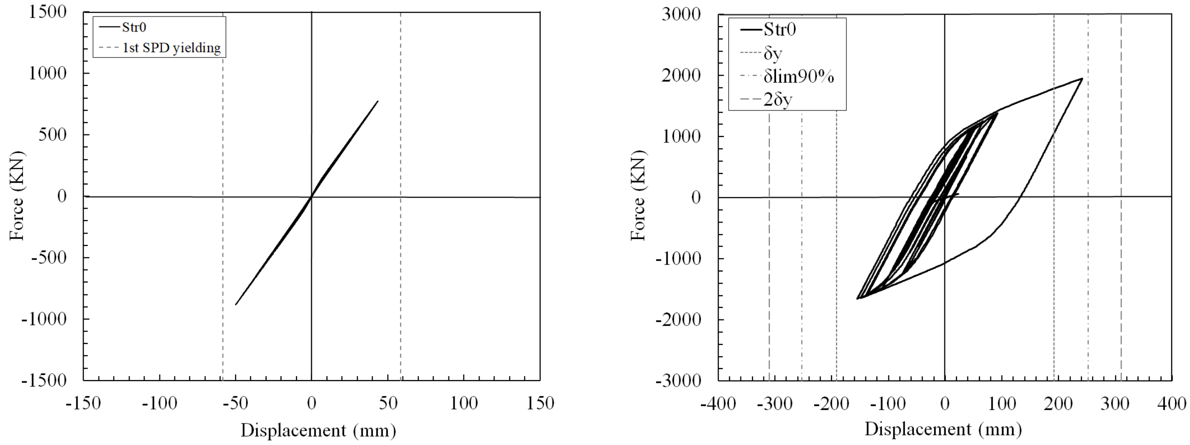

(A) (B)

FIGURE 6.9: The force and displacement seismic response of Str0 under earthquake excitation: (A) Level 1 and (B) Level 2.

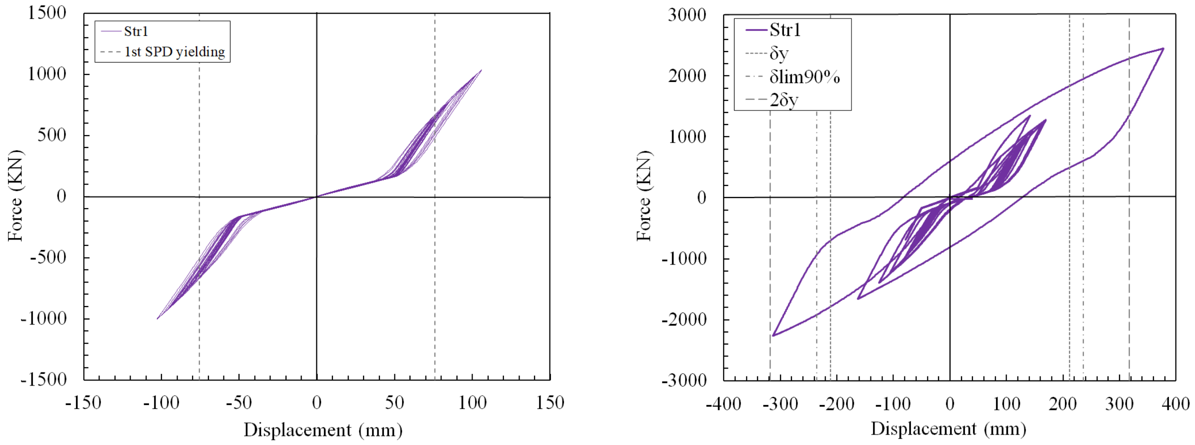

(A) (B)

FIGURE 6.10: The force and displacement seismic response of Str1 under earthquake excitation: (A) Level 1 and (B) Level 2.

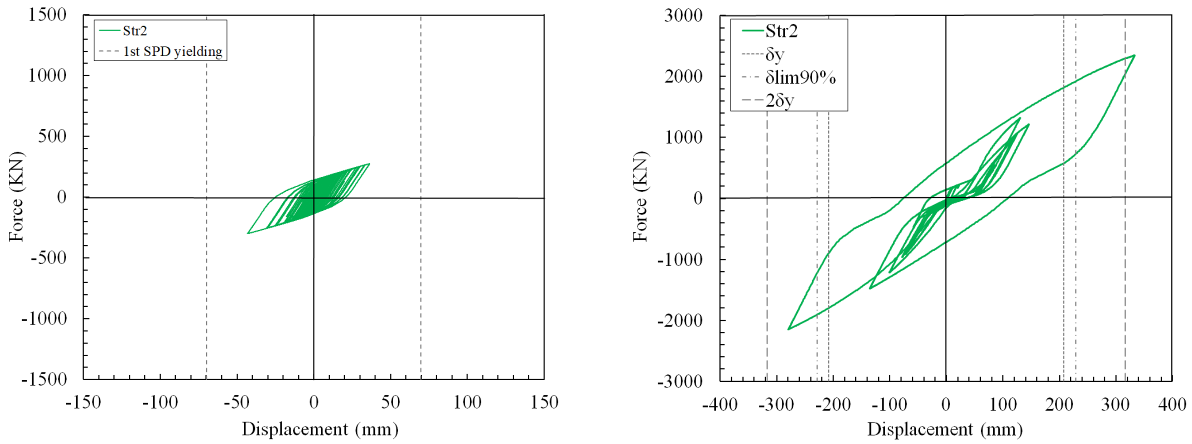

(A) (B)

FIGURE 6.11: The force and displacement seismic response of Str2 under earthquake excitation: (A) Level 1 and (B) Level 2.

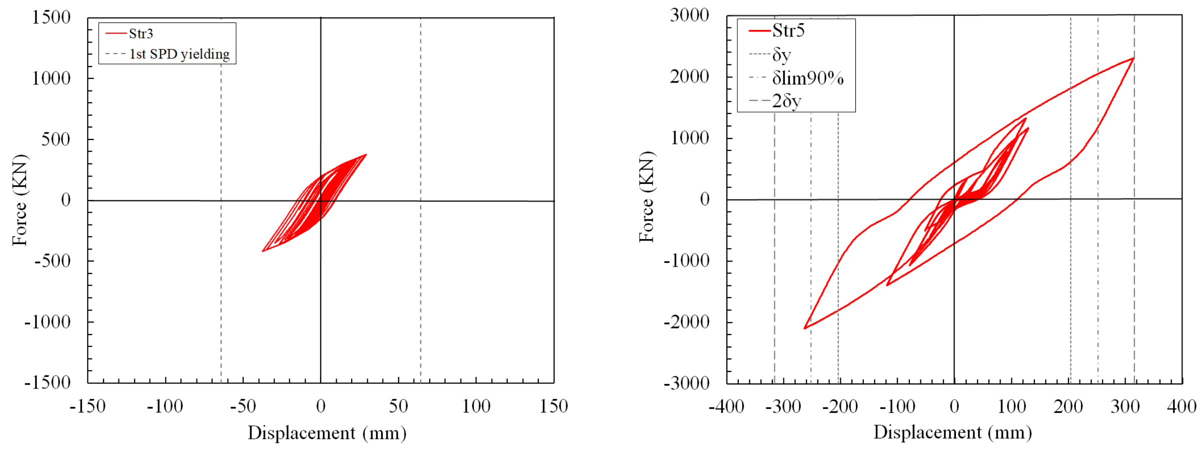

(A) (B)

FIGURE 6.12: The force and displacement seismic response of Str3 under earthquake excitation: (A) Level 1 and (B) Level 2.

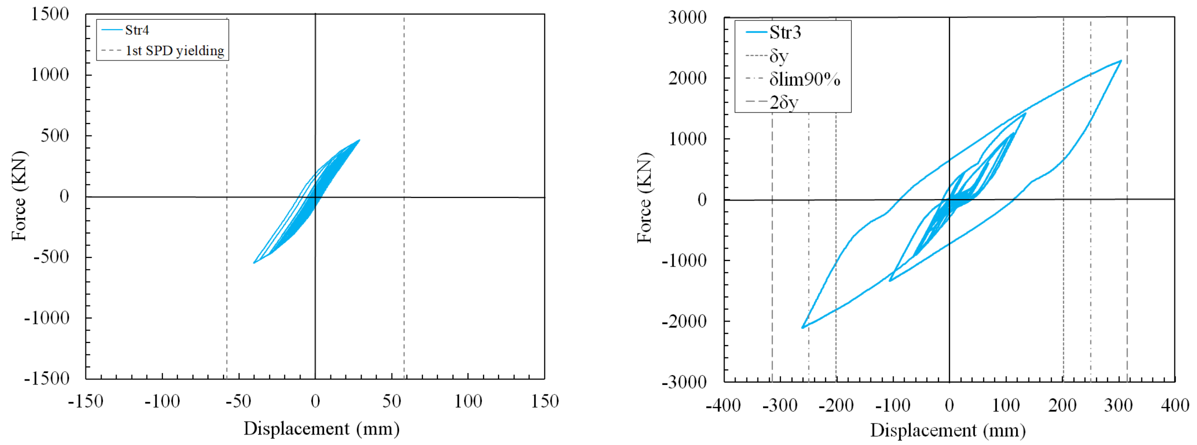

(A) (B)

FIGURE 6.13: The force and displacement seismic response of Str4 under earthquake excitation: (A) Level 1 and (B) Level 2.

advantage to increase N-value of high-cyclic fatigue. While under Level 2 of earthquake excitation, the implementation the gap with and without considering the friction force induced larger resisting force compared to the benchmark structure, as shown in Figures (6.9B, 6.10B, 6.11B, 6.12B, and 6.13B)

6.6 Conclusions

The proposal of SPDG implementation to the integrated multiple steel pipes bridge pier was successfully conducted in the numerical analysis. The implementation of the gap by considering the friction effect to the proposed structure generated some advantages and consequences:

(a) The implementation of the gap could increase structural flexibility, the result the shear panel stress due to frequent lateral load in the small deformation range was reduced. The reduced shear stress of SPD under frequent lateral load could reduce the deterioration of SPD.

(b) The appropriate friction force appearance that produced sufficient energy dissipation in the small deformation significantly reduced the structural response under Level 1 of the seismic excitation. The reduced structural response under Level 1 of seismic excitation also could descend the shear panel stress.

(c) The gap existence of the SPD decreased the dissipated energy in the limit state range of the structural performance target. Consequently, the implementation of the gap in the SPDG generated larger structural response under severe (Level2) seismic excitation.

(d) In the best performance, the structural model with the gap that considering 20 percent of P_{SPD0} friction force had sufficient flexibility in the small deformation, achieved sufficient dissipated energy and significant seismic force reduction in the small deformation, and realized Performance 2a under Level 2 of seismic excitation.

(e) The structure with SPDG resulted in smaller residual deformation under Level 2 of earthquake excitation than the structure with SPD. While after the SPD and SPDG to be released (in the last 5 seconds), the structure with SPDG did not has better re-centering capability than the structure with SPD.

Bibliography

[1] Japan Road Association: *Specifications for Highway Bridges: Part V Seismic Design*, Maruzen Co. Ltd., Tokyo, 2012.

[2] Nakamura, R., Kanaji, H. and Kosaka, T.: Development and Design of New Steel Pipe Integrated Pier with Shear Link, Technical report, Hanshin Expressway Company Limited, Osaka, 2014.

[3] Susmel, L.: A unifying approach to estimate the high-cycle fatigue strength of notched components subjected to both uniaxial and multiaxial cyclic loadings, Fatigue and Fracture of Engineering Materials and Structures, volume 27, no. 5:391–411, 2004.

Chapter 7

Conclusions and Recommendations

7.1 Conclusions

In Chapter 1, The importance of high seismic performance bridge pier was outlined. Then, a high seismic performance concept of the integrated bridge pier connected by hysterical damper was introduced in the case both of RC pier and steel pipe pier. Also, its deficiency and the improvement were explained for the improvement chance. The improvement including developing the numerical model and dissipated energy optimization of the existing proposed structure. Furthermore, the deterioration of the seismic device of the bridge structure specifically on the using of high damping rubber bearing was discussed. The additional gap on the hysterical damper was proposed as a solution for the integrated multiple column bridge pier connected by the hysterical damper.

In Chapter 2, The numerical analysis and dissipated energy optimization of integrated triple columns connected by friction dampers were successfully performed. With this basic of concept and method, the high seismic performance bridge pier connected by hysterical damper could be developed.

In Chapter 3, A high seismic performance concept of the integrated bridge pier with triple RC columns connected by friction dampers plus gap also was developed. With numerical analysis verification, the structural system could obtain not only near to elastic behavior under Level 2 of seismic excitation but also could to produce flexible stiffness under frequent lateral deformation of daily load.

In Chapter 4, The seismic performance enhancement of the integrated bridge pier with multiple steel pipe columns was successfully conducted. By optimizing dissipated energy capacity with not only redistributes SPD's strength and stiffness at along the pier height but also proposes the pin connection of the top pier and head pier, the seismic performance of structure could be upgraded from the Performance IIb to the Performance IIa under Level 2 of seismic excitation.

In Chapter 5, The SPDG was successfully developed by experimental study and verified by numerical analysis. Hence, the SPDG could produce small stiffness under gap range. Furthermore, considering of friction force on the friction surface capable to produce dissipated energy under gap range.

In Chapter 6, The implementation of SPDG to the integrated bridge pier with multiple steel pipe columns was carried out by numerical analysis. With appropriate friction force consideration, the proposed structure not only capable to produce Performance IIa under Level 2 of seismic excitation but also capable to realize sufficient flexibility under frequent lateral deformation and significant force reduction under Level 1 of earthquake excitation.

7.2 Recommendations

Some recommendations for the future studies about this research topic are expected to enrich the knowledge also capable to be implemented in the real bridge pier structure development.

1. The dissipated optimization of the proposed structure also need to consider the damage index.
2. Related to the construction and maintenance method, the better practice of integrated bridge pier configuration may be the implementation of the two-layer columns rather than the three-layer columns. Also, it's beneficial is the better consideration for bi-directions of seismic resistance.
3. In the consideration of pier and superstructure interaction influence and torsional effect, three-dimensional analysis of the full model structure that considering bi-direction earthquake excitation analysis needs to be conducted.
4. The reliability analysis of such kind structure needs to be conducted in the safety factor determination for structural design application.
5. Life-cycle cost analysis under high seismic environment needs to be studied to examine the advisability of the structure.
6. To achieve the better energy dissipation enrichment of the SPDG specimen, the improvement is needed from the free vertical edge of web panel to be the fix vertical edge.

7. In the verification of the proposed integrated bridge pier with multiple columns connected by hysterical damper plus gap, an experimental study needs to be conducted.

Appendix A

Seismic Excitation Input

A.1 Spectra Coefficient

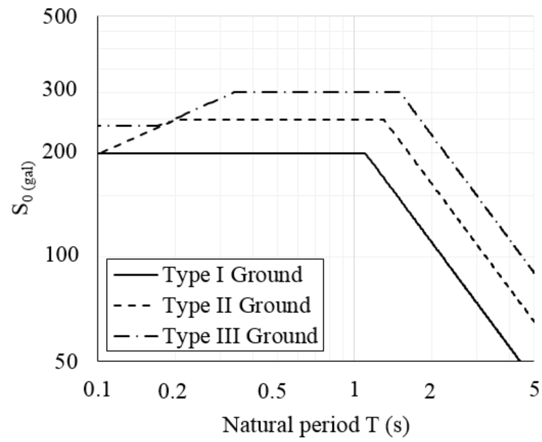

FIGURE A.1: Spectra coefficient of seismic design Level 1 [1]

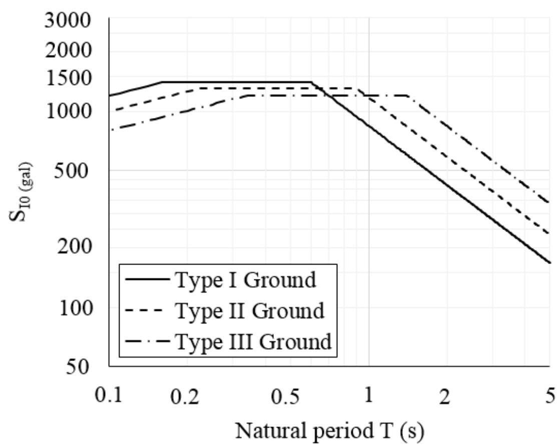

FIGURE A.2: Spectra coefficient of seismic design Level 2 Type I [1]

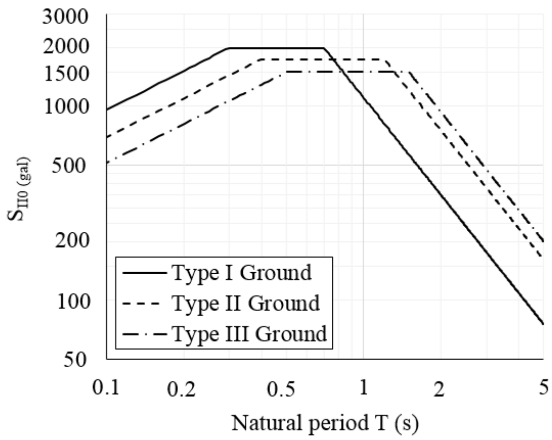

FIGURE A.3: Spectra coefficient of seismic design Level 2 Type II [1]

A.2 Ground Motion Input

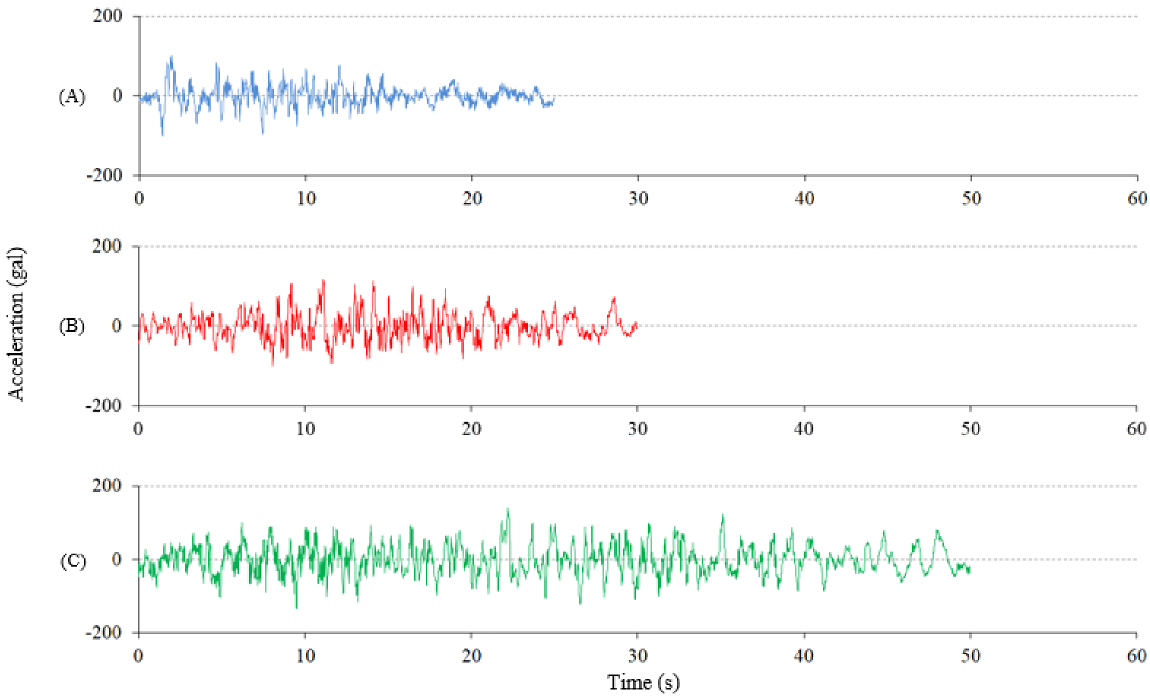

FIGURE A.4: Ground motion excitation input Level 1; a) Ground I, b) Ground II, and c) Ground III [1].

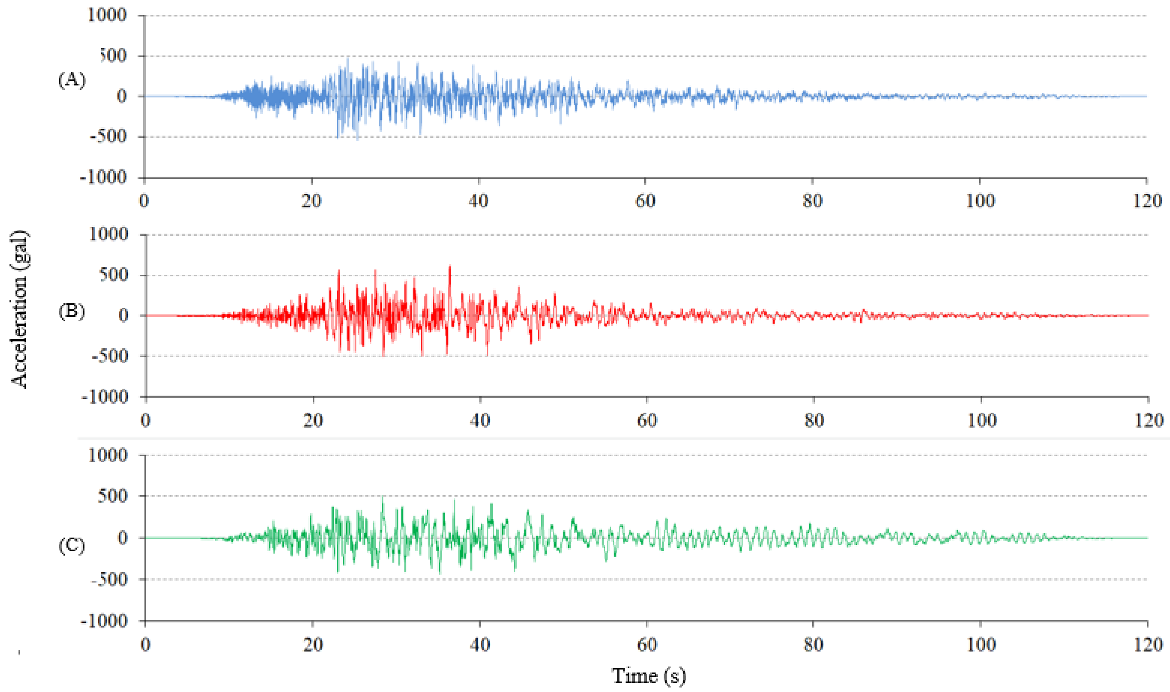

FIGURE A.5: Ground motion excitation input Level 2 Type I; a) Ground I-1, b) Ground II-1, and c) Ground III-1 [1].

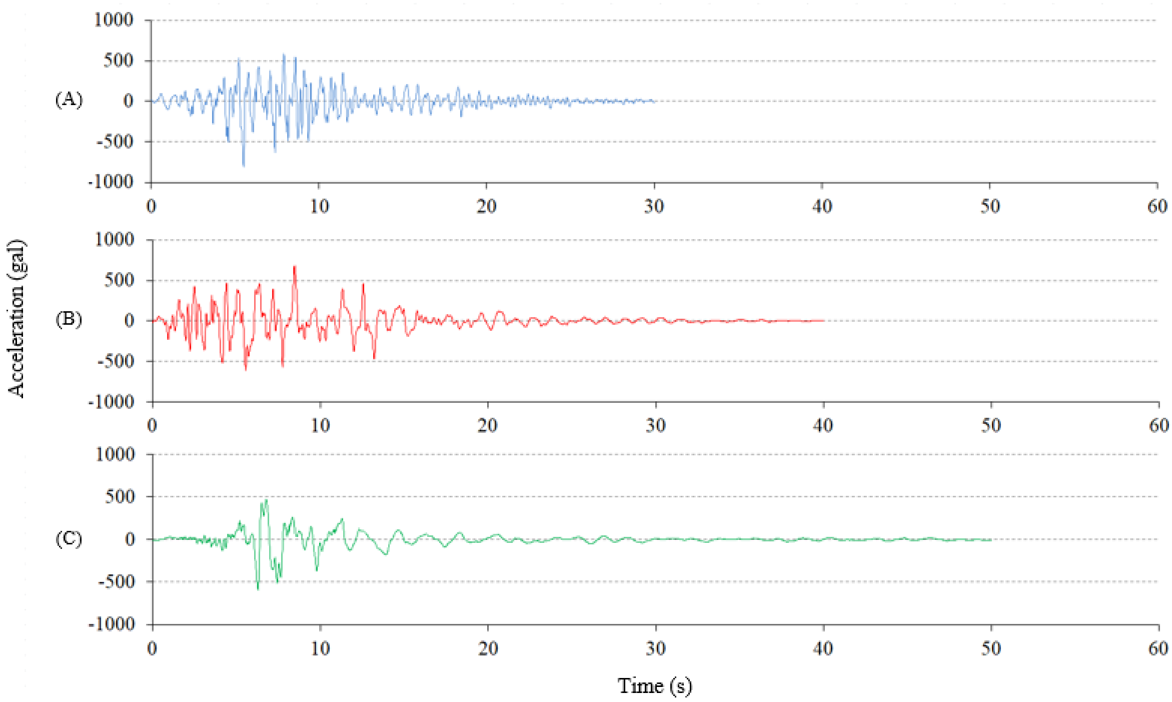

FIGURE A.6: Ground motion excitation input Level 2 Type II; a) Ground I-1, b) Ground II-1, and c) Ground III-1 [1].

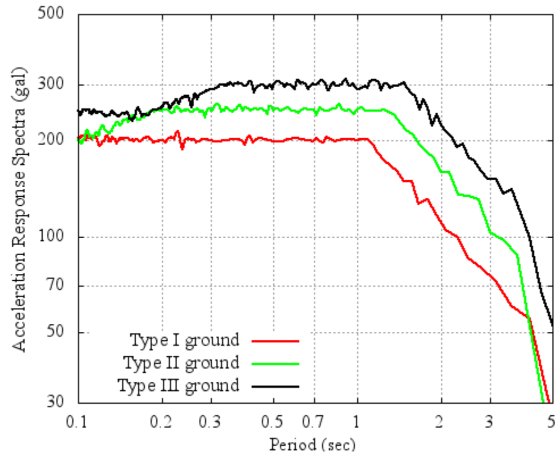

FIGURE A.7: Spectra coefficient of seismic design Level 1 [1]

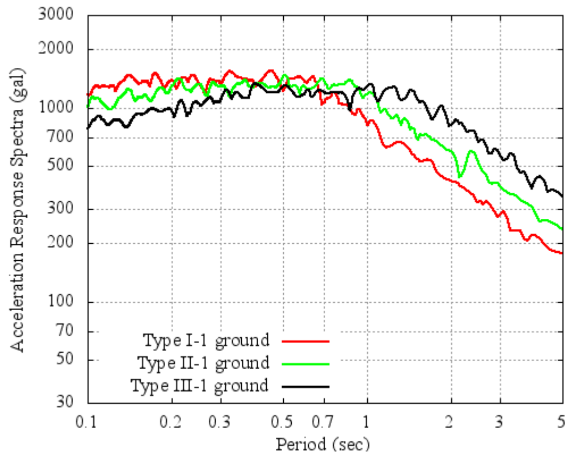

FIGURE A.8: Spectra coefficient of seismic design Level 2 Type I [1]

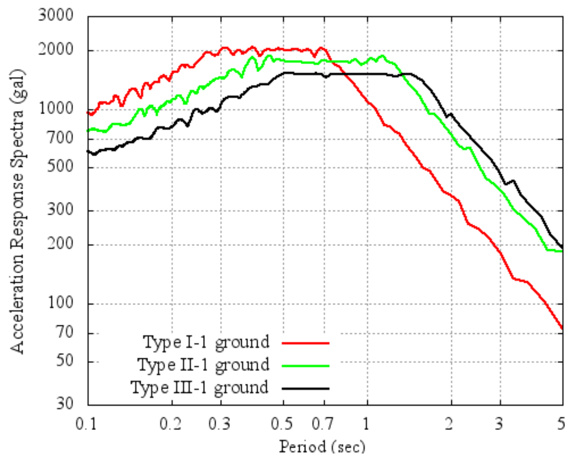

FIGURE A.9: Spectra coefficient of seismic design Level 2 Type II [1]

Bibliography

[1] Japan Road Association: *Specifications for Highway Bridges: Part V Seismic Design*, Maruzen Co. Ltd., Tokyo, 2012.

Appendix B

The Soundness of Element Members

B.1 Elements soundness

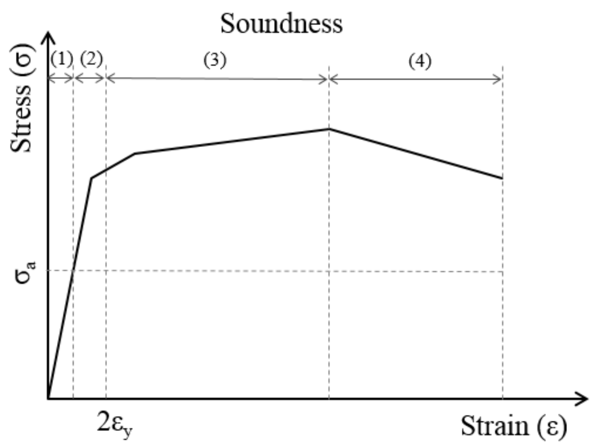

FIGURE B.1: Soundness of the steel pipe member [1].

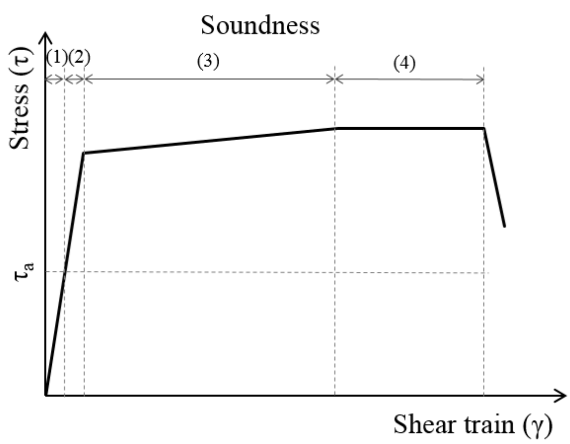

FIGURE B.2: Soundness of the steel SPD member [1].

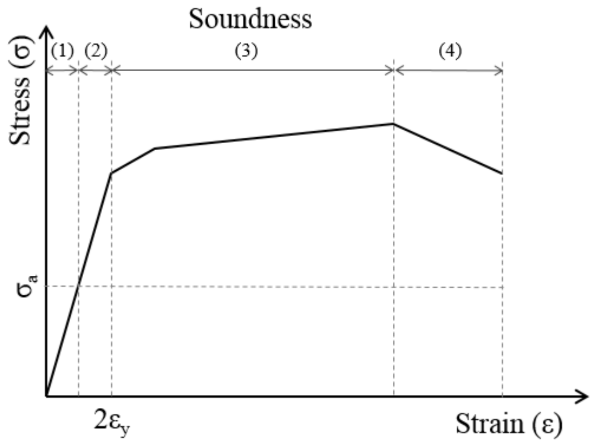

FIGURE B.3: Soundness of the steel joint member [1].

Bibliography

[1] Nakamura, R., Kanaji, H. and Kosaka, T.: Development and Design of New Steel Pipe Integrated Pier with Shear Link, Technical report, Hanshin Expressway Company Limited, Osaka, 2014.